

Université du Québec
Institut national de la recherche scientifique
Centre Énergie, Matériaux et Télécommunications

**Advanced Wireless Channel Identification and Parameter Estimation
Techniques for 5G-and-Beyond Radio Interface Technologies**

Par
Souheib Ben Amor

Mémoire présenté pour l'obtention du grade de
Doctorat en philosophie, Ph.D.
en télécommunications

Jury d'évaluation

Examineur externe	Prof. Mohamed Ibnkahla Carleton University
Examineur externe	Prof. Georges Kaddoum ÉTS
Examineur interne	Prof. Tayeb Denidni INRS
Directeur de recherche	Prof. Sofiene Affes INRS
Co-directeur de recherche	Prof. Faouzi Bellili University of Manitoba

To my parents
To Fay

Remerciements

Tout d'abord, je remercie les membres du jury qui ont accepté d'évaluer ce travail.

Ensuite, je tiens à manifester l'expression de mes respects les plus distingués à mon superviseur Prof. Sofiène Affes pour toute aide qu'il m'a apportée. Je lui adresse ma plus vive gratitude et ma profonde reconnaissance pour la confiance qu'il m'a accordée et ses conseils fructueux qui m'ont permis de réaliser ce travail dans les meilleures conditions d'encadrement.

Je tiens également à remercier Prof. Faouzi Bellili pour son assistance et ses conseils.

Je remercie aussi Dorra, Oussama, et mes camarades de l'INRS pour leurs encouragements et leur soutien tout au long de ces quatre années.

Mes vifs remerciements à ma famille et aux gens sans lesquels ce projet n'aurait jamais été mené à bien.

Résumé

Dans cette thèse, nous nous intéressons au développement de nouvelles techniques d'identification des canaux sans fil et d'estimation des paramètres du canal pour les technologies d'interface radio 5G et au-delà. Les propriétés physiques des canaux sans fil peuvent avoir des effets indésirables vu que les signaux transmis subissent toujours plusieurs réflexions, diffractions, etc. Ces derniers se traduisent par exemple par la présence de copies multiples du même signal avec des atténuations, des distorsions, des retards et des déphasages différents du côté du récepteur. Dans un tel scénario, les interférences entre ces copies peuvent conduire à une combinaison destructrice au niveau du récepteur rendant une communication fiable impossible. Par conséquent, il est essentiel que le récepteur connaisse les paramètres caractérisant le canal sans fil via des techniques d'estimation pour pouvoir détecter le signal transmis. Plus précisément, nous proposons des solutions d'estimation conjointe de plusieurs paramètres offrant ainsi de meilleures performances. En premier lieu, on s'intéresse à l'estimation conjointe du délai de propagation et de la direction d'arrivée (DdA) qui sont principalement utilisés à des fins de localisation. Ensuite, nous abordons l'estimation conjointe des décalages temporels et fréquentiels pour assurer la synchronisation dans les réseaux coopératifs. Enfin, les coefficients du canal et la variance du bruit sont utilisés pour acquérir une estimation précise du rapport signal à bruit (RSB). Les techniques développées doivent bien fonctionner selon les scénarios variés tel qu'un environnement à faible RSB ou des utilisateurs à mobilité élevée. Pour garantir des performances élevées, les techniques proposées reposent sur l'approche du maximum de vraisemblance (MV) et qui ont été adaptées en fonction des scénarios pour assurer une complexité de calcul raisonnable. Comme le montrent les résultats des simulations, les solutions proposées fonctionnent mieux que les benchmarks en termes de précision au niveau des composants et rapportent un meilleur débit au niveau lien.

Mots-clés Modules sensoriels, estimation des paramètres du canal, estimation assistée par les données, estimation autodidacte, localisation, synchronisation, probabilité maximale, débit au niveau lien, OFDM.

Abstract

In this thesis, we are interested in the development of new wireless channel identification and parameter estimation techniques for 5G-and-beyond radio interface technologies. Since the physical properties of wireless channels may have undesirable effects as the transmitted signals always undergo multiple reflections, diffraction etc. The latter result for example in the presence of multiple copies of the same signal with different attenuation, distortion, delays, and phase shift at the receiver side. In such scenario, the interference between these copies may lead to a destructive combination at the receiver making it impossible to ensure a reliable communication. Hence, it is crucial for the receiver to be aware of the parameters charactering the wireless channel via estimation techniques to be able to detect the transmitted signal. More specifically, we provide solutions for joint estimation of several parameters, thereby offering better performance. The channel parameters investigated in this thesis can be categorized into three categories: the joint propagation delay and direction of arrival (DoA) estimation which are mainly used for localization purposes. Next, we have the joint estimation of the timing and frequency offsets which are required for the synchronization in cooperative networks. We also investigate the channel coefficient and the noise variance to acquire an accurate estimate of the signal-to-noise (SNR) ratio. The developed technique should perform well in various scenarios such as low SNR environments or high mobility users. To ensure high performance, the proposed techniques rely on maximum likelihood (ML) approach. The developed techniques are adapted depending on the scenarios to ensure a reasonable computational complexity. As shown in simulation results, the proposed solutions perform better than the benchmarks in terms component level accuracy and link-level throughput. Finally, we provide a summary of other contributions achieved during the PhD program including the participation in the evaluation process of IMT-2020.

Keywords Sensory modules, channel parameter estimation, data-aided, non-data-aided, localization, synchronization, maximum likelihood, link-level throughput, OFDM, IMT-2020, WP 5D.

Table des matières

Remerciements	v
Résumé	vii
Abstract	ix
Table des matières	xi
Liste des figures	xv
Liste des tableaux	xix
Liste des abréviations	xxi
1 Extended Summary	1
1.1 Background and motivation	1
1.2 Motivations	2
1.3 Thesis contributions	3
1.3.1 ML-Type EM-Based Estimation of Fast Time-Varying Frequency-Selective Channels Over SIMO OFDM Transmissions	4
1.3.2 Multi-Node ML Time and Frequency Synchronization for Distributed MIMO-Relay Beamforming over Time-Varying Flat-Fading Channels	7
1.3.3 Maximum Likelihood Joint Angle and Delay Estimation from Multipath and Multicarrier Transmissions With Application to Indoor Localization Over IEEE 802.11ac Radio	10
1.3.4 Other Contributions within this Thesis	13
1.4 Concluding remarks	15
2 Résumé long	17
2.1 Contexte et motivation	17
2.2 Motivations	18
2.3 Contributions de la thèse	20
2.3.1 Estimation EM de type ML des canaux sélectifs en fréquence à variation temporelle rapide pour des transmissions SIMO OFDM	20
2.3.2 Synchronisation du temps et de la fréquence au sens maximum de vraisemblance pour la formation de faisceaux dans un système de relais MIMO distribués sur des canaux à évanouissement plat variant dans le temps	24

2.3.3	Estimation au sens maximum de vraisemblance conjointe des angles d'arrivées et des délais de propagation pour des transmissions multi-trajets et multi-porteuses avec des applications pour la localisation à l'intérieur via la radio IEEE 802.11ac	27
2.3.4	Autres contributions dans cette thèse	31
2.4	Conclusion	33
3	Thesis Overview	35
3.1	Background and preliminaries	36
3.1.1	Adopted algorithms and mathematical tools	36
3.1.2	Channel parameter estimation	38
3.1.3	Evaluation methods	38
3.2	Thesis organization	40
4	ML-Type EM-Based Estimation of Fast Time-Varying Frequency-Selective Channels Over SIMO OFDM Transmissions	43
4.1	Introduction	44
4.2	System model	47
4.3	New NDA ML-EM estimator	49
4.4	Proposed hybrid ML-EM estimator	54
4.4.1	Initialization with new DA ML	54
4.4.2	Reduction of pilot subcarriers	56
4.4.3	Extreme slow-up of pilot insertion rate	57
4.5	Simulation results	59
4.6	Conclusion	70
5	Multi-Node ML Time and Frequency Synchronization for Distributed MIMO-Relay Beamforming over Time-Varying Flat-Fading Channels	71
5.1	Introduction	72
5.2	System model	75
5.3	Joint TD and CFO ML estimator	78
5.3.1	TCC Case	78
5.3.2	TVC Case	80
5.3.3	Cramer rao lower bound (CRLB)	84
5.3.4	Joint synchronization and Doppler spread estimation	85
5.4	Distributed MIMO-relay beamforming	85
5.5	Simulation results	89
5.5.1	Component-level simulations	90
5.5.2	Link-level simulations	93
5.6	Conclusion	97
5.7	Appendices	99
6	Maximum Likelihood Joint Angle and Delay Estimation from Multipath and Multicarrier Transmissions With Application to Indoor Localization Over IEEE 802.11ac Radio	101
6.1	Introduction	102
6.2	Overview of related works	104
6.3	System model	106

6.4	Derivation of the concentrated likelihood function (CLF)	108
6.5	Global maximization of the CLF	110
6.5.1	Pincus' theorem and the IS concept	110
6.5.2	Approximation of the CLF and appropriate choice for $\bar{\mathcal{G}}(\boldsymbol{\alpha}, \boldsymbol{\tau})$	112
6.6	Special case of single-carrier systems	116
6.7	Generation of the required realizations	117
6.8	Implementation details	122
6.8.1	Local generation of the required realizations	122
6.8.2	Estimations of the TDs and AoAs	124
6.9	Estimating the number of paths	127
6.10	Simulation results	128
6.10.1	Impact of parameters ρ_0 and ρ_1	128
6.10.2	AoA and TD estimation accuracies: multi-carrier case	131
6.10.3	AoA and TD estimation accuracies: single-carrier case	136
6.10.4	Complexity assessment	139
6.11	Conclusion	140
6.12	Appendices	140
7	Other Contributions within this Thesis	145
7.1	Evaluation of radio interface technology (RIT) and set of RITs (SRITs) candidates to the new ITU-R WP 5D IMT-2020 (5G) standards within the CEG ¹ and ISED ² mandates	146
7.1.1	Introduction	146
7.1.2	Simulation process	147
7.2	Contributions to students' mentoring within this thesis	155
7.2.1	Blind maximum likelihood jade in multipath environment using importance sampling	155
7.2.2	Terahertz propagation performance evaluation for indoor environment	156
7.2.3	Synchronization of UAV swarms for indoor applications under obstacle-avoidance restrictions	156
7.2.4	Implementation of D2D communication between multiple IoT devices	156
7.2.5	Online indoor localization techniques of mobile units over non-line-of-sight transmission links	157
8	Conclusion and Future Work	159
8.1	Major research contributions	159
8.2	Future research directions	161
8.2.1	Channel coefficient estimation	161
8.2.2	Multi-node time and frequency synchronization with multiple destination nodes	161
8.2.3	Joint azimuth, elevation and, delay estimation	162
8.3	List of publications	162
8.3.1	Technical reports	162
8.3.2	Submitted/accepted journal papers	163
8.3.3	Accepted conference papers	163
	Références	165

1. Canadian Evaluation Group
2. Innovation, Science, and Economic Development Canada

Liste des figures

1.1	Usage scenarios of IMT for 2020 and beyond [1].	2
1.2	Link-level per-carrier throughput vs. the per-carrier SNR of the advocated new hybrid ML-EM (with $N_p = 4$) at multiple RI values, the SISO DA LS in [2] (i.e., $N_r = 1$), and its proposed SIMO DA ML extension (with $N_p = 8$) with $N_c = 3$, $N_r = 2$, and $\lambda = 0.5$ at: (a) $v = 60$ km/h, (b) $v = 120$ km/h, and (c) $v = 240$ km/h.	7
1.3	Link-level throughput vs SNR for ML TVC-PD at a refreshment rate $P = 100$ and different Doppler frequencies for: (a) $K = 1$, (b) $K = 2$, (c) $K = 4$, and (d) $K = 8$	10
1.4	CDF of the position error e_z for both IS-ML and UMP: (a) covariance-based localization procedure (b) covariance-free localization procedure.	14
2.1	Scénarios d'utilisation de l'IMT pour 2020 et au-delà [1].	18
2.2	Link-level per-carrier throughput vs. the per-carrier SNR of the advocated new hybrid ML-EM (with $N_p = 4$) at multiple RI values, the SISO DA LS in [2] (i.e., $N_r = 1$), and its proposed SIMO DA ML extension (with $N_p = 8$) with $N_c = 3$, $N_r = 2$, and $\lambda = 0.5$ at: (a) $v = 60$ km/h, (b) $v = 120$ km/h, and (c) $v = 240$ km/h.	23
2.3	Débit du niveau lien vs. RSB pour MV CVT-DP à un taux de rafraîchissement $P = 100$ et différentes fréquences Doppler pour: (a) $K = 1$, (b) $K = 2$, (c) $K = 4$, et (d) $K = 8$	27
2.4	FDC de l'erreur de position e_z pour EP MV et UMP: (a) procédure de localisation basée sur la covariance (b) procédure de localisation sans covariance.	31
4.1	Channel path gain estimates versus time index over the first $N_c = 3$ OFDM blocks with the SISO DA LS (8 pilots) and SISO RDM (4 pilots) initialization techniques at $SNR = 30$ dB for $N_r = 1$ and multiple values of λ	57
4.2	Data structure and processing tasks for different estimation approaches: (a) SISO DA LS [2] or its proposed SIMO DA ML extension, (b) the new NDA ML-EM, and (c) the advocated new hybrid ML-EM solution (i.e., combines both new NDA ML-EM and DA ML versions).	58
4.3	MSE of the advocated new hybrid ML-EM vs the number of ICIC iterations for QPSK and 64-QAM modulations with $v = 300$ km/h, $N_c = 3$, $N_r = 2$, and $N_p = 8$ at: (a) $SNR = 10$ dB, and (b) $SNR = 30$ dB.	61
4.4	MSE of the advocated new hybrid ML-EM, the SISO DA LS in [2] (i.e., $N_r = 1$), and its proposed SIMO DA ML extension vs. the per-carrier SNR for different numbers of receiving antennas with QPSK, $N_c = 3$ and $N_p = 8$ at: (a) $v = 60$ km/h, and (b) $v = 300$ km/h.	62

4.5	MSE of the advocated new hybrid ML-EM, the SISO DA LS in [2] (i.e., $N_r=1$), and its proposed SIMO DA ML extension vs. the per-carrier SNR with QPSK, $N_c=3$, $N_r=2$, and $N_p=8$ at: (a) $v=60$ km/h, and (b) $v=300$ km/h.	63
4.6	MSE of the advocated new hybrid ML-EM vs. the per-carrier SNR for different values of RI with QPSK, $N_c=3$, $N_r=2$, and $N_p=8$ at: (a) $v=60$ km/h, (b) $v=300$ km/h, and (c) $v=600$ km/h.	64
4.7	MSE of the advocated new hybrid ML-EM vs. the per-carrier SNR for different regularization factors of RDM at initialization with QPSK, $N_r=2$, and $N_c=3$ at: (a) $v=60$ km/h, and (b) $v=300$ km/h.	65
4.8	Performance of the advocated new hybrid ML-EM, the SISO DA LS in [2] (i.e., $N_r=1$), and its proposed SIMO DA ML extension vs. the per-carrier SNR with QPSK, $N_c=3$ and $N_r=2$ in terms of: (a) MSE at $v=60$ km/h, (b) BER at $v=60$ km/h, (c) MSE at $v=300$ km/h, and (b) BER at $v=300$ km/h.	66
4.9	Link-level per-carrier throughput vs. the per-carrier SNR of the advocated new hybrid ML-EM with $N_c=3$, $N_r=2$, and $N_p=8$ at: (a) $v=60$ km/h, and (b) $v=300$ km/h.	67
4.10	Link-level per-carrier throughput vs. the per-carrier SNR of the advocated new hybrid ML-EM, the SISO DA LS in [2] (i.e., $N_r=1$), and its proposed SIMO DA ML extension with $N_c=3$, $N_r=2$, and $\lambda=0.5$ at: (a) $v=60$ km/h, and (b) $v=300$ km/h.	68
4.11	Link-level per-carrier throughput vs. the per-carrier SNR of the advocated new hybrid ML-EM (with $N_p=4$) at multiple RI values, the SISO DA LS in [2] (i.e., $N_r=1$), and its proposed SIMO DA ML extension (with $N_p=8$) with $N_c=3$, $N_r=2$, and $\lambda=0.5$ at: (a) $v=60$ km/h, (b) $v=120$ km/h, and (c) $v=240$ km/h.	69
5.1	System model for the distributed MIMO-relay beamforming scheme illustrated during the DT (data transmission) cycles.	75
5.2	Block diagram of the DF receiver at the k^{th} relay.	77
5.3	Block diagram of the DF transceiver at the k^{th} relay.	86
5.4	Processing and data signaling structure of the two-hop MIMO-relay beamforming scheme assuming ideal (inactive) first-hop communication.	87
5.5	CRLB and NMSE vs SNR of the ML TVC, ML TCC, and SAGE techniques vs the SNR with $F_{D_k}=15$ Hz and <i>uniform Jakes'</i> model for: (a) the TDs and (b) the CFOs.	90
5.6	CRLB and NMSE vs SNR of the ML TVC, ML TCC, and SAGE techniques vs the SNR with $F_{D_k}=100$ Hz and <i>uniform Jakes'</i> model for: (a) the TDs and (b) the CFOs.	91
5.7	CRLB and NMSE vs F_{D_k} of the ML TVC, ML TCC, and SAGE techniques with $SNR=10$ dB and <i>uniform Jakes'</i> model for: (a) the TDs, and (b) the CFOs.	92
5.8	CRLB and NMSE vs the number of pilot symbols L_{sync} of the ML TVC, ML TCC, and SAGE techniques with $SNR=10$ dB, $F_{D_k}=100$ Hz, and <i>uniform Jakes'</i> model for: (a) the TDs, and (b) the CFOs.	93
5.9	Link-level throughput vs SNR for ML TVC-PD at $K=2$ relays and a refreshment rate $P=100$ for: (a) $\{F_{D_k}\}_{k=1}^K=15$ Hz, and (b) $\{F_{D_k}\}_{k=1}^K=100$ Hz.	95
5.10	Link-level throughput vs SNR for ML TVC-PD and ML TVC-DE at $K=2$ relays, $\{F_{D_k}\}_{k=1}^K=100$ Hz, and a refreshment rate $P=100$ for: (a) $\{F_{D_k}\}_{k=1}^K=15$ Hz, and (b) $\{F_{D_k}\}_{k=1}^K=100$ Hz.	96
5.11	Link-level throughput vs SNR for ML TVC-PD at $K=2$ relays and a refreshment rate $P=100$ for: (a) $\{F_{D_k}\}_{k=1}^K=15$ Hz, and (b) $\{F_{D_k}\}_{k=1}^K=100$ Hz.	97
5.12	Link-level throughput vs SNR for ML TVC-PD at a refreshment rate $P=100$ and different Doppler frequencies for: (a) $K=1$, (b) $K=2$, (c) $K=4$, and (d) $K=8$	98

5.13	CDF of the minimum of absolute value of $\text{diag}\{\mathbf{\Omega}(\tau_k)\}$ for: (a) multiple modulation orders, and (b) multiple sequence lengths.	100
6.1	CCDF of the magnitude of the ratio between the off-diagonal and diagonal entries of the matrix $\mathbf{D}^H \mathbf{D}$, using $M + 1 = 245$ subcarriers and a ULA configuration of $P = 6$ receiving antenna elements.	114
6.2	Marginal and conditional pdfs illustrated in a single-carrier system, ULA, $P = 5$, $\bar{Q} = 2$ and SNR = 30 dB: (a) marginal pdf of τ , (b) marginal pdf of α , (c) conditional pdf of α given $\tau_1^{(r)}$, and (d) conditional pdf of α given $\tau_2^{(r)}$	118
6.3	Pseudo-pdfs in a single-carrier system illustrated for $\bar{Q} = 2$ and SNR = -5 dB: (a) marginal CDF of τ , (b) marginal pdf of τ , (c) local pdf of τ around $\bar{\tau}_1$, (d) local pdf of τ around $\bar{\tau}_2$, (e) local CDF of τ around $\bar{\tau}_1$, and (f) local CDF of τ around $\bar{\tau}_2$	120
6.4	The mean value of $\rho(Q)$ for different values of \bar{Q} , SNR = -10 dB, ULA with $P = 5$ receiving antennas.	128
6.5	labelInTOC	129
6.6	labelInTOC	130
6.7	Error Probability on detecting the number of paths for a multicarrier-carrier system employing $M + 1 = 245$ subcarriers at SNR = 0 dB with $P = 5$ and $\rho_1 = 4$	131
6.8	RMSE for the TDs and AoAs with $M + 1 = 245$ subcarriers, for large angular and delay separations.	132
6.9	RMSE for the TDs and AoAs with $M = 245$ subcarriers, for paths with closely-spaced angles and large delay separations and vice versa.	133
6.10	Constellation of the location estimates in the XY plane for: (a) UMP with weighting matrix, (b) UMP without weighting matrix, (c) IS ML with weighting matrix, (d) IS ML without weighting matrix.	135
6.11	CDF of the position error e_z for both IS-ML and UMP: (a) covariance-based localization procedure (b) covariance-free localization procedure.	136
6.12	RMSE for the TDs and AoAs with $M = 128$ samples for <i>large</i> angular and delay separations.	137
6.13	RMSE for the TDs and AoAs with $M = 128$ samples for paths with closely-spaced angles and large delay separations and vice versa.	138
7.1	INRS Professor Sofiène Affes and his two students Oussama Ben Smida and Souheib Ben Amor (2nd to 4th from the right), accompanied by Venkatesh Sampath from Ericsson Canada (right) and Serge Bertuzzo from Bell Canada (left), at the ITU meeting in Geneva in February 2020. [3]	154
7.2	Next steps for the development of IMT-2020 radio interface Recommendations [4]	155
7.3	BS receiving RSSI values from multiple nodes: (a) Network topology and (b) RSSI values displayed at the BS	157
7.4	Real-world demo using Arduino rovers	157

Liste des tableaux

1.1	Technologies covered by the CEG for WP 5D	15
2.1	Technologies couvertes par le CEG pour WP 5D	32
4.1	Channel parameters	60
5.1	Simulation parameters	93
6.1	Complexity assessment of the considered JADE algorithms (cf. Table 6.2).	137
6.2	Definition of the Complexity Analysis Parameters in Table 6.1	139
7.1	5th percentile user spectral efficiency	148
7.2	Average spectral efficiency	149
7.3	Traffic channel link data rates normalized by bandwidth.	149
7.4	Technologies covered by the CEG for WP 5D	150
7.5	Compliance template for technical performance requiring evaluation by simulation for 3GPP NR RIT technology	152
7.6	Compliance template for technical performance requiring evaluation by simulation for 3GPP SRIT technology	153
7.7	Compliance template for technical performance requiring evaluation by simulation for ETSI-DECT SRIT technology	153

Liste des abréviations

3GPP	3 rd Generation Partnership Project
AoA	Angle of Arrival
AP	Access Point
AIC	Akaike Information Criterion
BPSK	Binary Phase Shift Keying
BEM	Basis Expansion Model
CDF	Cumulative Distribution Function
CCDF	Complementary Cumulative Distribution Function
CEG	Canadian Evaluation Group
CFO	Carrier Frequency Offset
CLF	Compressed Likelihood Function
CRLB	Cramer-Rao Low Bound
DA	Data-Aided
DFT	Discrete Fourier Transform
DECT	Digital European cordless telecommunications
DOA	Direction of Arrival
EM	Expectation Maximization
ESPRIT	Estimation of Signal Parameters via Rotational Invariance Techniques
ETSI	European Telecommunications Standards Institute
FFt	Fast Fourier Transform
ICI	Intercarrier Interference
ICIC	Intercarrier Interference Cancellation
iid	Independent and identically distributed
IML	Iterative Maximum likelihood
IMT	International Mobile Telecommunications
IS	Importance Sampling
ITU	International Telecommunication Union
JADE	Joint Angular and Delay Estimation
LLF	Log-Likelihood Function
LS	Least Squares
MAP	Maximum a posteriori probability
MDL	Minimum Description Length
MIMO	Multiple Input Multiple Output
ML	Maximum likelihood
MRC	Maximum Ratio Combining
MU	Mobile Unit
MUSIC	Multiple Signal Classification
NDA	Non-Data-Aided

OFDM	Orthogonal Frequency-Division Multiplexing
PDF	Probability Density Function
RI	Refreshment Interval
RIT	Radio Interface Technology
RRC	Root Raised Cosine
RDM	Regularized DA ML
RMSE	Root Mean Square Error
QAM	Quadrature Amplitude Modulation
QPSK	Quadrature Phase Shift Keying
SAGE	Space-Alternating Generalized Expectation Maximization
SIC	Successive Interference Cancellation
SISO	Single Input Single Output
SI-JADE	Shift Invariance-JADE
SIMO	Single Input Single Output
TD	Time Delay
TDOA	Time Difference of Arrival
TCC	Time Constant Channel
TST-MUSIC	Time-Space-Time MUSIC
TVC	Time Varying Channel
SNR	Signal to Noise Ratio
UMP	Unitary Matrix Pencil
WP 5D	Working Party 5D

Chapitre 1

Extented Summary

1.1 Background and motivation

Every 10 years, wireless communications go through a technological shift that brings more use cases and opportunities. The 1G was marked by the introduction of analog telecommunications that support voice only. During the 90s, the second generation introduced digital standards allowing new services such as roaming and short message service (SMS). In the year 2000, the International Telecommunication Union (ITU) issued the International Mobile Telecommunications (IMT)-2000 which is a globally coordinated definition of 3G covering key issues such as frequency spectrum use and technical standards. This generation introduced the notion of smartphones for the first time and proposed new sorts of applications such as web browsing and email access. As new cases surface and become more data hungry, there was a need for new technologies. The 4G, under the banner of IMT-Advanced, was put on the table in 2010 and brought new concepts such as “all IP”, multimedia data (video and music) and faster mobile broadband. In the past decade, a lot of research efforts were carried out to prepare for the next generation of wireless communications. The new generation, with the first recommendations aimed to be released in 2021 under the banner of IMT-2020, is promising much faster connection, more reliability and higher connection density along with a lower latency. These features vary depending on the application. Indeed, 5G is aiming to provide more than enhanced broadband services and encompass new ones. As shown in fig. 1.1, 5G relies on three main pillars. The first one being an enhanced mobile broadband (eMMB) allowing a more reliable and faster connections when compared to the existing long term evolution (LTE)

technology. The second one is the massive machine type communications (mmtc) which covers

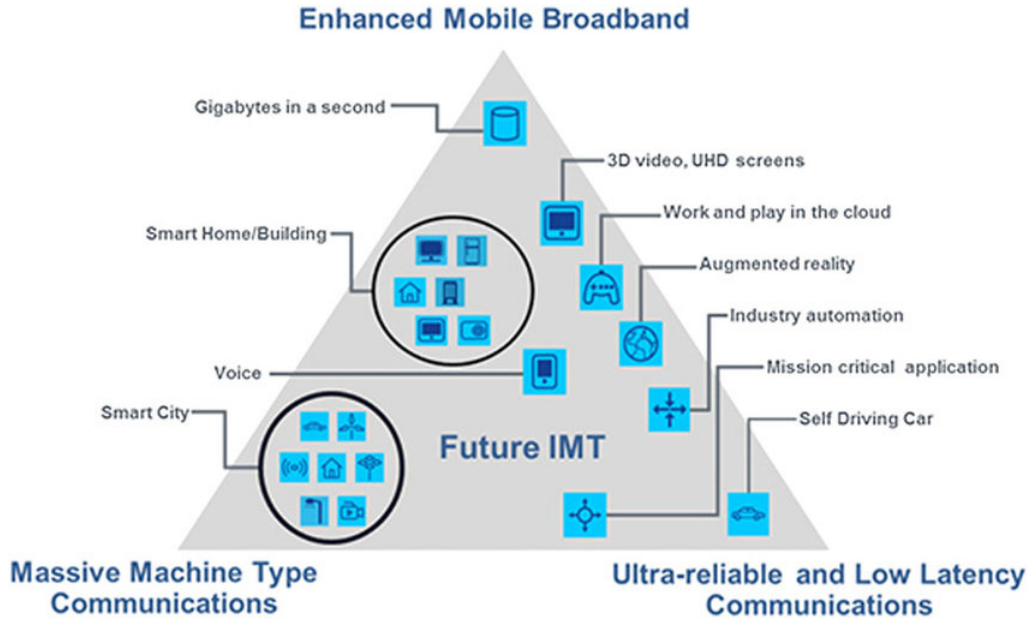


Figure 1.1 – Usage scenarios of IMT for 2020 and beyond [1].

applications like the internet of things applications, smart homes and factories. The third one is the ultra-reliable low latency communications (URRLC) for applications requiring extreme reliability and latency below 0.1ms.

1.2 Motivations

The physical properties of wireless channels may have undesirable effects as the transmitted signals always undergo multiple reflections, diffraction etc. The latter result for example in the presence of multiple copies of the same signal with different attenuation, distortion, delays, and phase shift at the receiver side. In such scenario, the interference between these copies may lead to a destructive combination at the receiver making it impossible to ensure a reliable communication. Hence, it is crucial for the receiver to be aware of the parameters characterizing the wireless channel via estimation techniques to be able to detect the transmitted signal. Indeed, it needs information regarding the carrier frequency, timing, and phase offsets to ensure a full synchronization between the transmitter and the receiver. While the direction of arrival (DoA) can be used for localization purposes, channel tracking and noise variance estimation are useful in computing the signal-to-noise (SNR) ratio which is useful for the adaptive modulation, coding, and handoff scheme. Estimation

techniques can be categorized in different ways depending on the approach, the type of input data, etc. For example, depending on the type of input, estimation techniques can be categorized into four main categories: the data-aided (DA) approaches where the transmitted symbols are assumed to be perfectly known at the receiver. Generally, they provide highly-accurate estimates at a significant cost, however, in terms of overhead; *ii*) the blind or non-data-aided (NDA) approaches where the receiver does not have *a priori* information about the transmitted data. Therefore, NDA techniques do not incur any overhead but come with reduced accuracy. *iii*) Some NDA parameter estimation approaches available in the literature (e.g., see [5]-[6]), occasionally or intermittently, operate an initialization step at much less frequent pilot insertion instants (by an order or two of magnitude). Referred to as hybrid (i.e., combine NDA and DA), these techniques very often perform much better than full NDA approaches (i.e., with random initialization). While at the same time they require negligible overhead amounts compared to DA solutions [7]; *iv*) The code aided (CA) approach can be seen as a middle ground solution between the NDA and DA estimation schemes. Indeed, rather than relying on perfectly known or completely unknown symbols, CA estimation takes advantage of the soft information delivered by the decoder at each decoding iteration. As shown in [8], this kind approach provides a significant improvement compared to the NDA counterpart. However, its performance is strictly related to coding rate. While it is able to reach near DA performance at mid-range SNR, it is only the case for low rate configurations that come with high redundancy and eventually lower link-level throughput. The developed techniques can also be categorized by the adopted approach. Indeed, some techniques focus on estimating one specific parameter while assuming the rest to be known. Such techniques provide high accuracy in ideal cases but may suffer from performance deterioration in real scenarios where the remaining parameters are obtained using additional estimators. This may increase the overall complexity and makes the performance strongly dependent on other solutions' accuracy. Joint estimation, however, provides estimates for two or multiple channel parameters at the same time providing a higher accuracy and in certain cases lower computational complexity since a limited number of estimations techniques is involved.

1.3 Thesis contributions

In this thesis, we aim to develop new advanced joint estimation techniques for channel parameters ranging from channel quality parameters including channel coefficients and the noise variance, to the

synchronization parameters including timing and frequency offsets, and the localization parameters such as joint propagation delay and DoA estimation. The developed techniques rely mainly on the maximum likelihood (ML) approach which is renowned to exhibit high performance. The main contributions of this thesis are:

1.3.1 ML-Type EM-Based Estimation of Fast Time-Varying Frequency-Selective Channels Over SIMO OFDM Transmissions

Overview of related works

Orthogonal frequency-division multiplexing (OFDM) showed its effectiveness in current 4G. A scalable variety of CP-OFDM is already included in 5G new radio (NR) standards by the 3rd Generation Partnership Project (3GPP) [9]. The adopted waveform will include multiple sub-carrier spacings that depend on the type of deployments and service requirements. Moreover, when coupled with the large-scale antenna technology OFDM is poised to enable the 1000-fold increase in capacity that is required over the next few years. Despite its attractive features such as robustness to frequency selective channels and spatial diversity, OFDM-type radio interface technologies (RITs) are already very sensitive to channel time variations since the latter break the crucial orthogonality between the subcarriers thereby introducing the so-called inter-carrier interference (ICI). Accurate channel estimation, hence, becomes a daunting task at very high mobility [10].

So far, several channel estimation techniques have been reported in the literature. They can be categorized in two major categories: *i*) the data-aided (DA) approaches where the transmitted symbols are assumed to be perfectly known at the receiver. They provide highly-accurate channel estimates at a significant cost, however, in terms of overhead; *ii*) the blind or non-data-aided (NDA) approaches where the receiver has no *a priori* information about the transmitted data. Therefore, NDA techniques do not incur any overhead at the cost, however, of reduced accuracy. Some NDA parameter estimation approaches available in the literature (mainly proposed by the authors' group e.g., see [5]-[6]), occasionally or intermittently, operate an initialization step at much less frequent pilot insertion instants (by an order or two of magnitude). Referred to as hybrid (i.e., combine NDA and DA), these techniques very often perform much better than full NDA approaches (i.e., with random initialization). While at the same time they require negligible overhead amounts compared to DA solutions [7]. Hence, we shall advocate a hybrid approach in this work.

For fast time-varying channels, most of the DA techniques rely on a basis expansion model (BEM) to estimate the equivalent discrete-time channel taps [11]-[12]. In fact, BEM methods such as Karhunen-Loeve BEM were designed with low mean square error (MSE) [11]. They are, however, sensitive to statistical channel mismatch. The complex-exponential BEM, also proposed in [11], does not make use of the channel statistics but suffers from large modeling errors. The polynomial BEM (P-BEM) investigated in [13] yields accurate channel estimates, but only at low Dopplers. In [2], the complex gain variations of each path was approximated by a polynomial function of time then estimated by least squares (LS) technique. This solution offers accurate performance even at high Doppler. However, it requires that the number of paths to be smaller than the inserted pilot symbols in each OFDM time slot. Moreover, it was derived in the single-input single-output (SISO) case and its extension to single-input multiple-output (SIMO) systems has never been addressed.

Under the NDA category, time-varying channel estimation was also investigated in [14]. The authors used the discrete Legendre polynomial BEM along with the space alternating generalized expectation maximization (EM)-maximum a posteriori probability (SAGE-MAP) technique to estimate the time-domain channel coefficients of OFDM channels. In [15], we used EM to estimate the channel gains over a SISO configuration. However, both techniques have been tailored for multi-carrier SISO systems and, hence, do not exploit the potential diversity gain achievable by multi-antenna systems. Moreover, they require the number of pilots to be greater than the number of channel paths. In [16], the instantaneous SNR estimation problem was investigated using the EM approach, yet still over SISO configurations only. In [17] and [18], both the EM and LS techniques were again leveraged, respectively, to estimate the SNR over single-carrier SIMO systems. In [19],[20], iterative channel estimation with Kalman filtering and QR detection was first investigated under SISO multi-carrier channels and later generalized to MIMO OFDM systems. Its performance was further enhanced in [21] by exploiting the statistics of the channel estimation errors in an iterative estimation process. However, Kalman filter-based techniques require perfect knowledge of the Doppler as well as the power-delay profile. Moreover, a high number of pilots per OFDM block is needed to obtain accurate estimates, thereby affecting the overall throughput of the system.

Contribution

In this contribution, we develop an iterative EM-based ML estimator of fast time-varying channels over SIMO OFDM-type radio interfaces. By relying on the polynomial approximation of the

multipath channel gains [2] and resorting to the powerful EM technique [22] instead of the LS approach, our solution offers a more accurate ML-type acquisition of the polynomial expansion coefficients and the resulting time-varying channel gains. To avoid local convergence that is inherent to iterative algorithms, we initialize the EM algorithm with a SIMO DA ML version developed in this work for that sole purpose. We show that the latter boils down to applying SISO DA LS in [2] over each receive antenna. Besides, coming back to our key contribution here, our new SIMO NDA ML-EM solution, it yields as a byproduct MAP-based soft estimates of the unknown symbols. The latter are leveraged to devise a dedicated ICI cancellation (ICIC) scheme that works side by side with the EM-based time-varying estimator according to the turbo principle (e.g., see [8]). Furthermore, we introduce an alternative SIMO regularized DA ML (RDM) initialization procedure that can still apply when the number of paths exceeds the number of available pilot observations. This desirable feature renders the proposed solution robust to any rapid variations in the propagation environment where the number of paths can change unpredictably due to the mobile users motion. Hence, we investigate the possibility of reducing the number of pilots in each OFDM block down below the number of channel paths without significantly affecting the performance. By doing so, we are able to reduce the overhead and eventually increase the throughput quite significantly. Simulation results show that the proposed hybrid ML-EM estimator (i.e., combines all new NDA ML-EM and DA ML or RDM versions) converges within few iterations, thereby providing very accurate estimates of all multipath channel gains. Most importantly, this increased estimation accuracy translates into very significant BER and link-level per-carrier throughput gains over the best representative benchmark solution available so far for the problem at hand, the SISO DA LS technique in [2] with its new generalization here to SIMO systems. We see from Figs. 1.2 (a) and (b) that the per-carrier throughput increases with hybrid ML-EM at low to medium Doppler once the refreshment interval RI jumps from 1 to 5. It follows that the pilot subcarriers are no longer required at the current OFDM blocks and can be used to carry data instead. Pilot insertion rate can be slowed down significantly, by at least as much as 20 times (pilot to data or overhead ratio can become as low as 0.16%), while still reporting some noticeable throughput gains instead of losses, more so at high per-carrier SNR. Whereas SISO DA LS in [2] and its proposed SIMO DA ML extension still require the same amount of pilots to provide reliable channel estimates. Therefore, no additional throughput gains can be achieved.

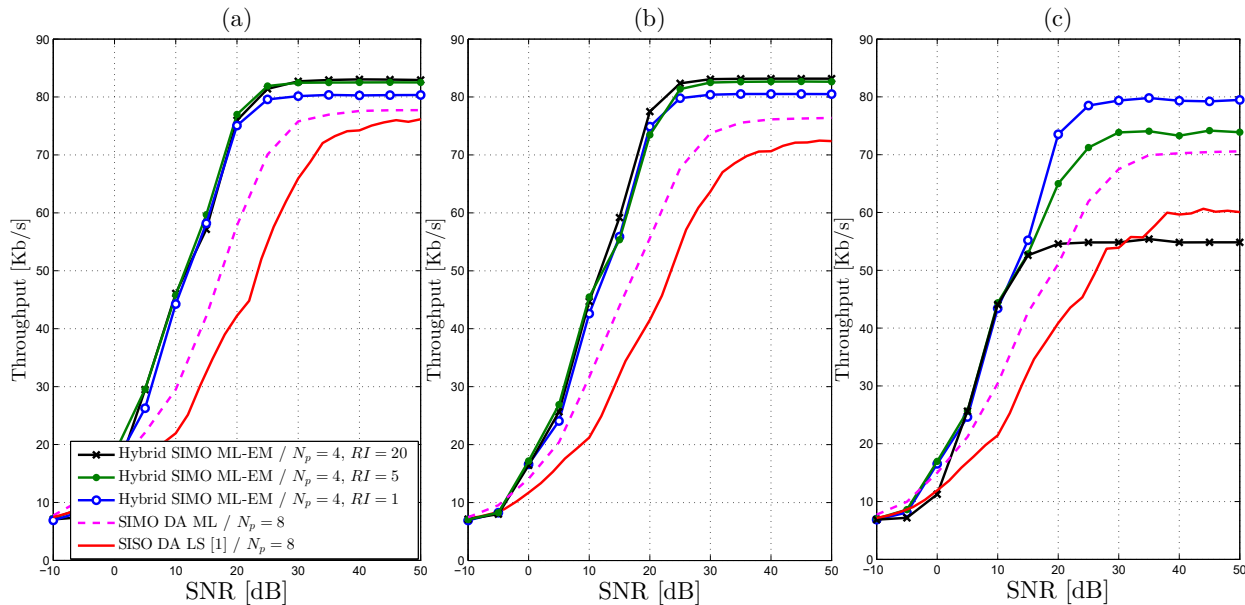


Figure 1.2 – Link-level per-carrier throughput vs. the per-carrier SNR of the advocated new hybrid ML-EM (with $N_p = 4$) at multiple RI values, the SISO DA LS in [2] (i.e., $N_r = 1$), and its proposed SIMO DA ML extension (with $N_p = 8$) with $N_c = 3$, $N_r = 2$, and $\lambda = 0.5$ at: (a) $v = 60$ km/h, (b) $v = 120$ km/h, and (c) $v = 240$ km/h.

1.3.2 Multi-Node ML Time and Frequency Synchronization for Distributed MIMO-Relay Beamforming over Time-Varying Flat-Fading Channels

Overview of related works

Spatial diversity is a well-known concept allowing to combat the channel fading and increase the overall throughput of communication systems. Such attracting advantage can be achieved through multiple solutions. Cooperative networks provide a distributed solution that avoids some of the difficulties related to traditional MIMO systems [23], [24]. Indeed, in many situations, some user equipments are not able to embed multiple antenna sensors due to size and power limitations. As such, users can cooperate with each other to form a virtual antenna array. However, some challenges need to be addressed to ensure constructive cooperation between the relays. One major problem in cooperative relaying systems is multi-node synchronization, both in time and frequency. The latter is crucial for the proper implementation of energy-, spectrum-, and area-efficient distributed MIMO-relay beamforming between a given source-destination link having coverage limitations.

There are two basic approaches to alleviate the effect of time-varying channel (TVC) distortions in time, frequency, phase, and amplitude: the closed-loop and the open-loop compensation procedures. In the closed-loop approach, the destination performs the estimation of all the syn-

chronization parameters along with the channel coefficients. Those estimates are later fed to an equalization block to combat time and frequency asynchronism as proposed in [25],[26]. To their credentials, closed-loop approaches exhibit less overhead as the interaction among the relay nodes is kept to minimal while the destination coordinates the synchronization process. However, it may be difficult for wireless networks without the adequate infrastructure to handle highly-complex multi-dimensional estimation algorithms. In open-loop approaches, however, the source signal to be relayed is shifted in the temporal and frequency domains before transmission, as proposed in [27]. By doing so, we ensure that replicas of the same transmitted signal, originating from different relay nodes, arrive at the same time and combine constructively at the receiver. In this scenario, less complex estimation algorithms can be considered at the nodes with minimal signaling from the destination.

As far as the estimation of the synchronization parameters is concerned, multiple techniques exist in the open literature [28]. On one hand, the works in [29]-[30] investigate time delay (TD) synchronization while neglecting the carrier frequency offset's (CFO) effect. On the other hand, the solutions introduced in [31]-[32] deal with multiple CFOs while neglecting the TD effect. Other techniques perform joint estimation of all parameters at the destination in closed-loop cooperative networks [25],[33],[34]. Although they could work well in practice, they suffer from high computational complexity since they require solving a multi-dimensional problem that increases with the number of relaying nodes. Moreover, the synchronization task might become very costly in terms of overhead. Indeed, after estimating the TDs and CFOs, the destination node needs to feed them back to the relays. Such a step leads to an additional overhead problem along with quantization errors since the estimated values are quantized before their feedback phase.

Alternative solutions can be considered by relying on distributed collaborative beamforming (DCBF) schemes [35]. Many of these techniques focus on the optimal design of the beamformer's weights while assuming perfect synchronization that leave them extremely vulnerable in practice to phase, frequency, and time offsets. Many other techniques focus, on the other hand, on combating the misalignment effect at the destination caused by such offsets. In [36], the authors proposed a phase compensation solution based on an iterative bit-feedback approach. In [37], a solution for frequency synchronization in wireless sensor networks (WSN)s using a round trip synchronization method was proposed. In [38], a distributed synchronization method was proposed for dense wireless networks using a correlation-based joint TD and CFO estimator. Yet, all the above-mentioned techniques rely on the simplifying time-constant channel (TCC) assumption. In contrast, a broad

range of applications require that the terminals act as relaying nodes and, at the same time, fifth-generation (5G) communication systems are expected to support reliable communications at very high velocities reaching 500 Km/h (e.g., in high-speed trains) [39]. For such systems, the conventional TCC assumption leads to severe performance losses. Recently, some other works on DCBF [40], [41] had tackled the challenging problem of multi-node synchronization under TVCs using enhanced versions of one-bit feedback technique. However, they have only addressed phase compensation while assuming perfect TD and CFO estimation.

Contribution

Motivated by these facts, we develop in this chapter a new decentralized ML synchronization technique along with a distributed MIMO-relay beamforming design that tackles the challenging TVC case over multi-node relaying transmissions. The proposed ML TVC solution builds upon a very useful approximation of the channel covariance matrix by a two-ray propagation model. It provides accurate ML estimates of the TDs and CFOs at a reduced computational cost because it does not require any matrix inversion. We also develop an iterative version, referred to as ML TVC-DE (Doppler estimate), that accounts for the practical need to estimate at each relay node the Doppler spread upon which relies the initial version referred to hereafter as ML TVC-PD (perfect Doppler). Simulation results show significant synchronization accuracy improvement over previous distributed multi-node synchronization techniques assuming TCCs. The latter translates into noticeable gains in terms of useful (i.e., after accounting for incurred overhead) link-level throughput, more so at higher Doppler or with more distributed MIMO-relay beamforming nodes. In Fig. 1.3, we report noticeable and constantly increasing throughput gains of ML TVC over TCC-based SAGE and ML TCC at both medium and high SNR levels when increasing the number of relays from 1 to 8. At higher Doppler values (i.e., $F_{D_k} = 200$ Hz or $F_{D_k} = 300$ Hz), the relative throughput gains of ML TVC over SAGE and ML TCC become even more significant, again more so when the number of relays also increases. These key observations come as a solid confirmation of the very important performance benefits of the proposed distributed MIMO-relay beamforming and multi-node synchronization schemes.

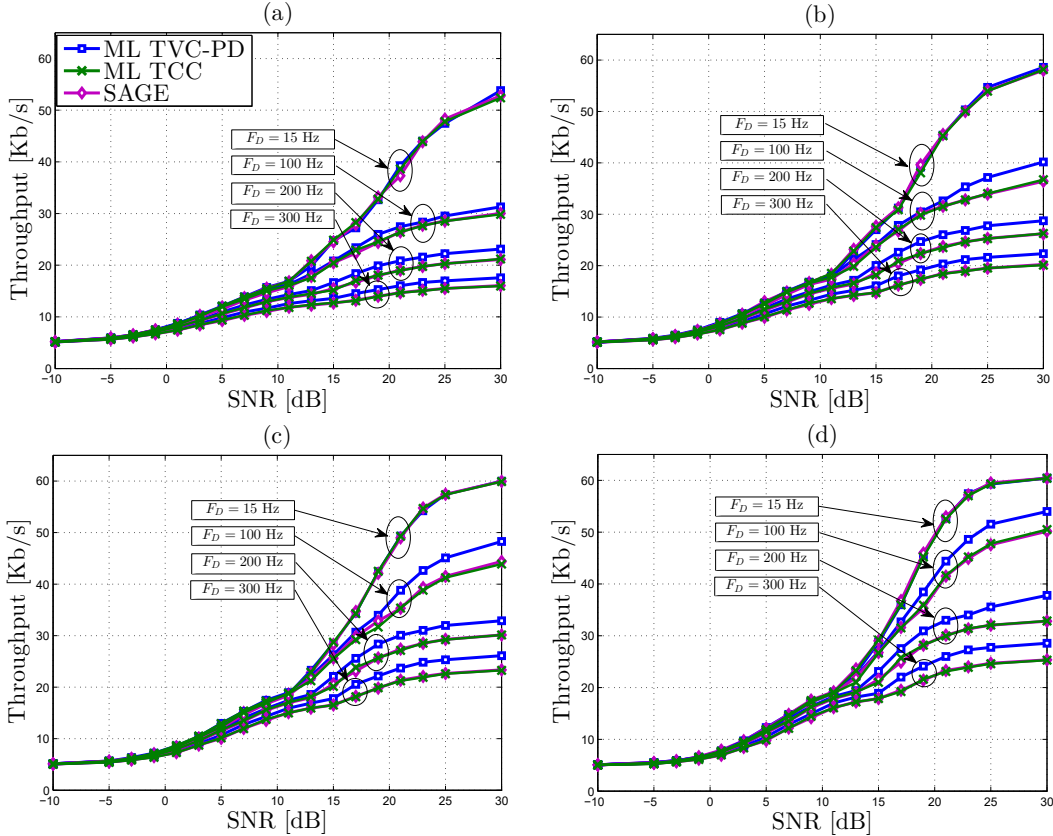


Figure 1.3 – Link-level throughput vs SNR for ML TVC-PD at a refreshment rate $P = 100$ and different Doppler frequencies for: (a) $K = 1$, (b) $K = 2$, (c) $K = 4$, and (d) $K = 8$.

1.3.3 Maximum Likelihood Joint Angle and Delay Estimation from Multipath and Multicarrier Transmissions With Application to Indoor Localization Over IEEE 802.11ac Radio

Overview of related works

In parametric multipath propagation models, a source signal impinges on an antenna array through a number of rays, each described by an angle-of-arrival (AoA), a time delay (TD), and a path gain. The joint angle and delay estimation (JADE) problem consists then in jointly estimating all the AoAs and their corresponding TDs from a finite number of received samples. The JADE problem arises in many practical situations ranging from military applications (e.g., radar and sonar) to broadband wireless communication systems. Typically, the power to characterize each path with its own angle and delay endows the system with stronger sensorial capabilities leading, for instance, to more robust beamforming techniques [42] and enhanced equalization performance

[43]. Moreover, as location-aware services for handhelds are likely to be in high demand for future wireless communication systems, the information about the AoAs and the TDs can be used to design highly-accurate localization techniques [44]-[45]. In this context, in order to cope with dense multipath environments, the so-called *fingerprinting* paradigm which recasts source localization into a pattern recognition problem was envisaged in [46]-[47]. In particular, it was recently shown that *fingerprinting* with location signatures that are characterized by the AoAs and TDs of each candidate location leads to substantial improvements against location signatures that are characterized by the received signal strength (RSS) [48]. In fact, contrarily to the RSS which varies substantially over a wavelength distance (due to constructive and destructive multipath interference), the AoAs together with the associated TDs form a unique fingerprint for each location [47]. Hence, accurate and low-cost estimation of such multipath parameters can be used along with the *fingerprinting* paradigm to develop very efficient localization algorithms. Alternatively, if multiple access points (APs) are available, they can cooperate to localize a mobile user by using the estimated time difference of arrivals (TDoA)s and AoAs (see [49] and [50] for more details).

Unlike JADE, the separate (or disjoint) estimation of either time delays or directions of arrivals (DoA)s has been heavily investigated for decades now. For prior works on DoA-only and TD-only estimation, see [51], [52] and [53], [54] and references therein, respectively. In comparison with disjoint estimation techniques which first estimate the delays and then the corresponding angles, the joint estimation of these space-time parameters (i.e., JADE) is more accurate in cases where multiple rays have nearly equal delays or angles [42]. Moreover, contrarily to JADE, the number of estimated angles in DoA-only estimation schemes must be smaller than the number of antennae. Thus DoA-only estimators would require large-size antenna arrays in highly dense multipath environments.

So far, a number of JADE techniques have been reported in the literature, except the unitary matrix pencil (UMP)-based approach proposed recently [49], all the existing solutions are geared toward single-carrier systems. Roughly speaking, they can be broadly categorized into two major categories: subspace-based and ML-based estimators. Most of subspace-based techniques are built upon the well-known MUSIC and ESPRIT algorithms [55]-[56]. In practice, subspace-based approaches are more attractive due to their reduced computational load. However, they are usually suboptimal and suffer from severe performance degradation (both in terms of resolution and estimation accuracy) for low SNR levels and/or closely-spaced paths. ML approaches, however, are

known to enjoy higher accuracy and enhanced resolution capabilities. Yet, despite their promising advantages, their computational complexity has been often considered as the major culprit for a widespread reluctance of designers to their implementation in practice.

In the specific JADE context, to the best of our knowledge, only two ML estimators have been so far introduced but only for narrowband signals. The very first ML solution was proposed by Wax *et al.* in [57] which is *iterative* in nature and thus will be referred to, hereafter, as the iterative ML (IML) estimator. The other ML solution introduced later in [58] is also *iterative* and based on the space-alternating generalized expectation maximization (SAGE) algorithm. However, like any *iterative* approach, the performance of these two ML estimators is closely tied to the initial knowledge about the unknown parameters, i.e., they will not converge to the global maximum of the log-likelihood function (LLF) if their initial guesses are not reliable. Besides, for both *iterative* ML estimators, a fixed sampling grid is selected to serve as a possible set of all candidate estimates for the unknown TDs and AoAs. Then, by assuming all true (unknown) parameters to be exactly on the selected grid, IML and SAGE attempt to maximize the LLF iteratively. Consequently, they suffer from the inevitable off-grid problem which arises in practical situations where some of the true TDs and/or AoAs do not lie on the sampling grid. For accurate estimation, it is compulsory to use a densely-sampled grid since it reduces the gap between the true parameters and their nearest points on the grid. However, as “there is no free lunch”, the cost of a dense grid sampling is the excessive increase in computational complexity.

Contribution

The proposed estimator builds upon the global maximization theorem of Pincus [59] and the importance sampling (IS) concept [60]. In particular, owing to a very accurate approximation of the concentrated likelihood function (CLF), we transform the original *multi-dimensional* optimization problem into multiple *two-dimensional* optimization ones resulting thereby in tremendous computational savings. Even more, the underlying two-dimensional optimization problems are totally disjoint and, as such, they can be performed separately in practice. From this perspective, the new IS-based ML estimator lends itself to a very attractive parallel computing implementation that can be efficiently executed on nowadays multiprocessor platforms.

The combination of Pincus’ theorem and IS concept has been previously applied to many fundamental estimation problems. To the best of our knowledge, however, this elegant combination was first

pioneered by S. Kay and S. Saha in [61] in the context of multiple frequencies estimation. There, it was shown for the very first time that joint ML estimation of multiple frequencies boils down to the computation of sample mean estimates from a number of realizations generated according to a carefully designed importance function (or pseudo-pdf). Pincus' theorem along with the IS concept were later on applied by S. Kay *et al.* to the estimation of chirp signals' parameters [62], sources' DOAs estimation with antenna arrays [52], as well as, joint angle and Doppler estimation in [63]. They were also successfully applied in the context of joint CFO and channel estimation under: *i*) single-user OFDMA communications [64], and *ii*) multiuser multiple-input multiple-output (MIMO)-OFDM communications with optimal training sequences design [65]. More recently, these powerful tools were leveraged in the context of TDoA-based source localization [66], non-data-aided (NDA) timing recovery [67], as well as, time delays acquisition in multipath environments [54]. Computer simulations show the superiority of the proposed IS-based ML estimator over state-of-the-art ML-type and subspace-based JADE techniques in terms of estimation accuracy, resolution capabilities, and computational complexity. Real-world channel measurements collected using IEEE 802.11ac standard's setup parameters in an indoor environment were also used to investigate the online localization capabilities of the proposed algorithm.

As seen from Fig. 1.4 (a), both UMP and IS ML techniques yield remarkably small localization errors which are smaller than 10 cm at all times, when used with the covariance-based localization procedure. Fig. 1.4 (b) depicts the Cumulative distribution function (CDF) when the more practical covariance-free localization procedure is applied using the TDoA and AoA estimates provided by each algorithm. There, it is seen that IS-ML still provides a localization error smaller than 10 cm in 90% of the cases (and never exceed 15 cm) while UMP localization errors are higher than 70 cm in 10% of the cases.

1.3.4 Other Contributions within this Thesis

Evaluation of Radio Interface Technology (RIT) and Set of RITs (SRITs) Candidates ITU-R WP 5D for IMT-2020 (5G) within the CEG¹ and ISED² Mandates

One of the strongest driving forces for wireless technology evolution today is 5G, also known as IMT-2020 [1], which promises to encompass several radio interface technologies (RITs) or sets

1. Canadian Evaluation Group

2. Innovation, Science, and Economic Development Canada

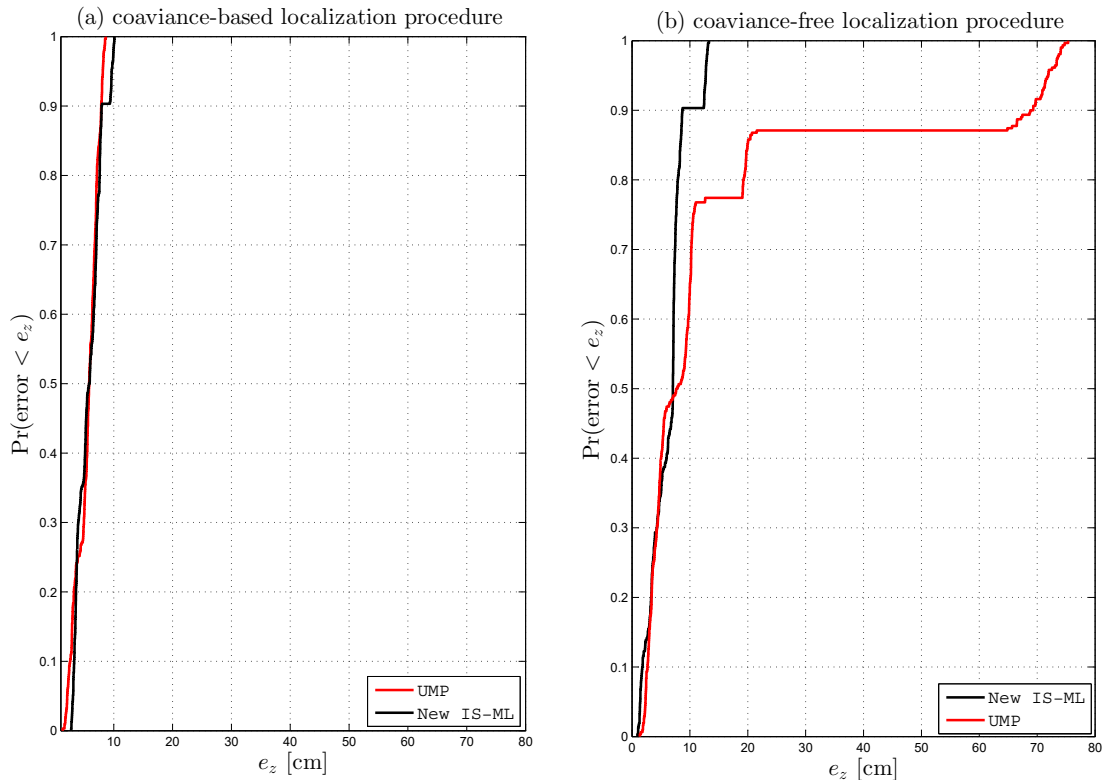


Figure 1.4 – CDF of the position error e_z for both IS-ML and UMP: (a) covariance-based localization procedure (b) covariance-free localization procedure.

thereof (SRITs), including 3GPP and ETSI/DECT among others. These IMT-2020 standard candidates, made available very recently for evaluation, are to be assessed for compliance to minimum requirements [68],[69].

Multiple key features are to be assessed such as packet throughput, cell spectrum efficiency, packet loss rate, and latency. These features will give valuable insights to identify i) areas where enhancements can be made, ii) introduce these enhancements and evaluate them, iii) support equipment manufacturers and operators in their standardization effort to integrate these enhancements if deemed valuable. The comparison of the selected 5G technologies is performed on a fair basis using a common simulation platform.

It is from this perspective that the Wireless Lab team, mandated by Innovation, Science and Economic Development Canada (ISED) and the Canadian Evaluation Group (CEG), has worked on developing a common simulation platform to evaluate the 3GPP and ETSI/DECT RIT candidates for 5G. The characteristics chosen for evaluation by simulation include 5th percentile user spectral efficiency, average spectral efficiency, connection density, reliability, and mobility [68]. The obtained

results were included in the final report of the CEG contribution to the working party 5D (WP 5D) meetings.

Contribution

Multiple standard candidates were submitted to WP 5D for evaluation. In Table 1.1, we provide a summary of the performance criteria evaluated for each submitted technology. To be approved, each candidate needs to fulfill the minimum requirements of each of the evaluation criteria mentioned above. The meeting WP 5D #35e reviewed the results of Step 4 (Evaluation of candidate RITs or

Table 1.1 – Technologies covered by the CEG for WP 5D

IMT-2020 SUBMISSION							
Proponent	3GPP		China	South Korea	TSDSI	ETSI-DECT	NuFront
Document Reference	RIT [70]	SRIT [71]	[72]	[73]	[74]	[75]	[76]
Status	Evaluated	Evaluated	Not evaluated (WP 5D has determined that the 3GPP evaluation applies to this candidate)	Not evaluated (WP 5D has determined that the 3GPP evaluation applies to this candidate)	Not evaluated (After de-activation of certain features, TSDSI RIT became sufficiently similar to 3GPP RIT)	Partial evaluation (only the DECT component RIT)	Partial evaluation
Average spectral efficiency	✓	✓				N/A	Missing data
5% spectral efficiency	✓	✓				N/A	Missing data
Mobility	✓	✓				N/A	Missing data
Reliability	✓	N/A				✓	Missing data
Connection density	✓	✓				Missing data	Missing data

SRITs by independent evaluation groups). It was agreed during the meeting that the 3GPP RIT and SRIT proposals, China, Korea, and TSDSI are considered as qualified RIT/SRITs of Step 6. Hence, they were forwarded to further consideration in Step 7. In Step 7:

- The RITs and SRITs proposed by 3GPP, China and Korea are grouped into the technology identified in ITU as “3GPP 5GSRIT” and “3GPP 5GRIT” as developed by 3GPP. Both technologies passed Step 7.
- The TSDSI RIT also passed Step 7 as “TSDSI RIT”.
- The WG Technology Aspects failed to reach an agreement on how to summarize the Step 4 results for ETSI-DECT and Nufront submissions. In the closing plenary of WP 5D Meeting #35e (23 June – 9 July), the meeting agreed on option 2 (Fig. 7.2) and provide a one-time extension on an exception basis for both candidates

1.4 Concluding remarks

In this thesis, we proposed multiple joint estimation techniques to acquire the information of key channel parameters. Mainly, we made four contributions. First, we proposed an ML estimator

that builds upon the global maximization theorem of Pincus [59] and the IS concept [60]. In the second contribution, we developed a new decentralized ML synchronization technique along with a distributed MIMO-relay beamforming design that tackles the challenging TVC case over multi-node relaying transmissions. The proposed ML TVC solution builds upon a very useful approximation of the channel covariance matrix by a two-ray propagation model. In the third contribution, we develop an iterative EM-based ML estimator of fast time-varying channels over SIMO OFDM-type radio interfaces. We also introduce an alternative SIMO RDM initialization procedure that can still apply when the number of paths exceeds the number of available pilot observations. In the fourth contribution, we covered the evaluation by simulation of 3GPP RIT and SRIT and we are currently pursuing the same process with re-evaluation of DECT and NuFront. Our work during this project was included in the CEG final report submitted to the WP 5D 34th meeting. The research during the PhD program has resulted in three journals and seven conference papers (cf. section 8.4).

Chapitre 2

Résumé long

2.1 Contexte et motivation

Tous les 10 ans, la communication sans fil subit un changement technologique qui apporte plus de cas d'utilisations et d'opportunités. La 1G a été marquée par l'introduction des télécommunications analogiques qui ne supportent que la voix. Au cours des années 90, la deuxième génération a introduit des normes numériques introduisant ainsi de nouveaux services tels que l'itinérance et le service de messages courts. En 2000, l'union internationale des télécommunications a publié l'International Mobile Telecommunications-2000 (IMT-2000) qui est une définition bâtie sur un consensus mondial de la 3G couvrant des problématiques clés telles que le spectre de fréquences utilisé et les normes techniques. Cette génération introduit pour la première fois la notion de téléphone intelligent et propose de nouveaux types d'applications tels que la navigation web et l'accès aux courriels électroniques. À mesure que de nouveaux cas font surface et deviennent de plus en plus gourmands en données, une nouvelle technologie était nécessaire. La 4G, sous la bannière IMT-Advanced, a été mise sur la table en 2010 et a apporté des nouveaux concepts tels que le tout IP, les données multimédias (vidéo et musique) et un débit mobile plus rapide. Au cours de la dernière décennie, de nombreuses recherches ont été menées pour préparer la prochaine génération de communications sans fil. Cette génération, avec les premières recommandations destinées à être publiées en 2021 sous la bannière IMT-2020, promet une connexion beaucoup plus rapide avec plus de fiabilité et aussi une densité de connexion plus élevée et une latence plus faible. Ces fonctionnalités varient en fonction de l'application. En effet, la 5G vise à fournir plus que juste des services à haut débit améliorés mais

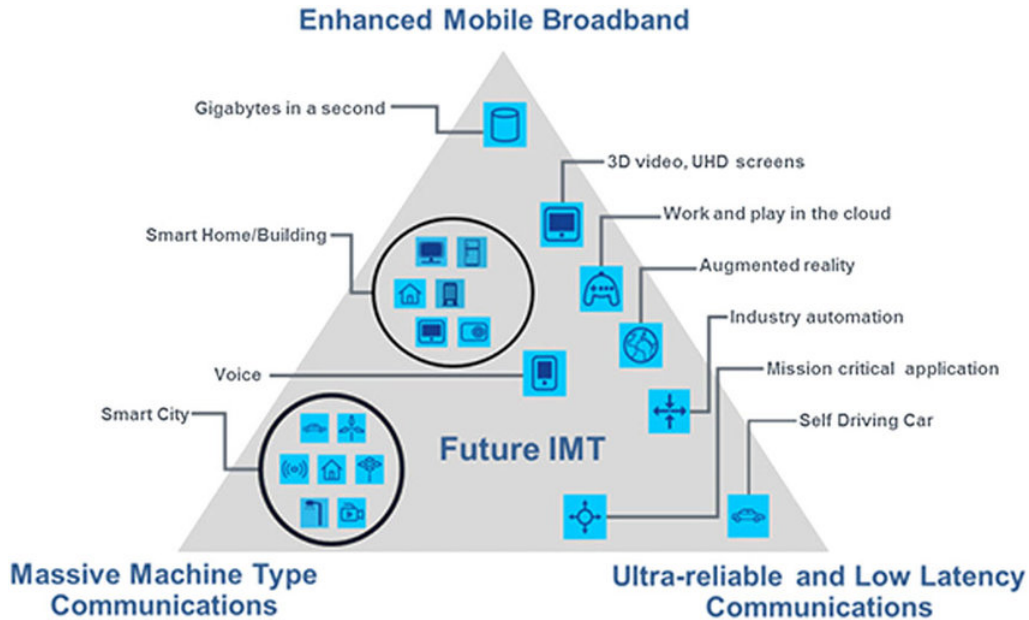


Figure 2.1 – Scénarios d’utilisation de l’IMT pour 2020 et au-delà [1].

elle englobe de nouveaux scénarios d’utilisation. Comme le montre la figure 2.1, la 5G repose sur 3 piliers principaux. Le premier étant le haut débit mobile amélioré permettant des connexions plus fiables et plus rapides par rapport à la technologie “LTE” existante. Le second couvre les communications massives de type machine qui couvrent des applications telles que les applications Internet des objets, les maisons et les usines intelligentes. Le troisième est dédié aux communications ultra fiables à faible latence nécessitant une fiabilité extrême et une latence inférieure à 0,1 ms.

2.2 Motivations

Les propriétés physiques des canaux sans fil peuvent avoir des effets indésirables car les signaux transmis subissent toujours de multiples réflexions, diffractions, etc. Ces dernières résultent par exemple de la présence de plusieurs copies du même signal avec des atténuations, des distorsions, des retards et des déphasages différents au niveau du côté récepteur. Dans un tel scénario, les interférences entre ces copies peuvent conduire à une combinaison destructrice au niveau du récepteur rendant une communication fiable impossible. Par conséquent, il est crucial que le récepteur connaisse les paramètres caractérisant le canal sans fil via des techniques d’estimation pour pouvoir détecter le signal transmis. En effet, il a besoin des informations concernant les décalages temporels, de la fréquence porteuse et de la phase pour assurer une synchronisation complète entre l’émetteur

et le récepteur. Alors que la direction d'arrivée (DdA) peut être utilisée à des fins de localisation, les coefficients de canal et la variance du bruit sont utiles pour calculer le RSB qui est utile pour la modulation adaptative et le codage. Les techniques d'estimation peuvent être catégorisées de différentes manières selon l'approche, le type de données d'entrée, etc. Par exemple, selon le type de données d'entrée, les techniques d'estimation peuvent être classées en quatre catégories principales: les approches assistées par les données (AD) où les symboles transmis sont supposés être parfaitement connus au niveau du récepteur. En général, ces techniques fournissent des estimations très précises, cependant, elles réduisent le débit avec la transmission de symboles connus; *ii*) les approches autodidactes où le récepteur n'a pas d'informations *a priori* sur les données transmises. Par conséquent, les techniques autodidactes n'entraînent aucune réduction sur le débit, cependant, elles ont une précision réduite par rapport aux techniques AD ; *iii*) certaines approches autodidactes disponibles dans la littérature (par exemple, voir [5] - [6]) opèrent occasionnellement ou par intermittence une étape d'initialisation à des instants d'insertion des pilotes beaucoup moins fréquente. Ces techniques, appelées hybrides (c'est-à-dire combinant autodidacte et DA), fonctionnent très souvent mieux que les approches complètement autodidactes (c'est-à-dire avec une initialisation aléatoire). En même temps, elles nécessitent un nombre de symboles pilotes négligeable par rapport aux solutions AD [7] ; *iv*) l'approche assistée par codage (AC) peut être vue comme une solution intermédiaire entre les schémas d'estimation autodidacte et AD. En effet, plutôt que de s'appuyer sur des symboles parfaitement connus ou totalement inconnus, l'estimation CA profite des informations délivrées par le décodeur à chaque itération de décodage. Comme le montre [8], ce type de techniques apporte une amélioration significative par rapport aux solutions autodidactes en termes de précision d'estimation. Cependant, ses performances sont strictement liées au taux de codage. Bien qu'il soit capable d'atteindre des performances quasi-AD à moyen RSB, ceci n'est possible que pour des taux de codage faibles conduisant ainsi à une redondance élevée et un débit de niveau lien moins élevé. Les techniques développées peuvent également être catégorisées selon l'approche adoptée. En effet, certaines techniques se concentrent sur l'estimation d'un paramètre spécifique tout en supposant que le reste soit parfaitement connu. Ces techniques offrent une précision élevée dans le cas idéal, mais peuvent souffrir d'une détérioration des performances dans des scénarios réels où le reste des paramètres sont obtenus à l'aide d'autres estimateurs. Ceci peut augmenter la complexité globale vu que des estimateurs supplémentaires sont inclus. Elle rend également la précision de la solution proposée étroitement liée à la précision des autres techniques. Cependant, l'estimation conjointe fournit des estimations pour deux ou plusieurs paramètres de canal en même

temps, offrant ainsi une précision plus élevée et, dans certains cas, une complexité de calcul faible car moins de techniques d'estimation sont impliquées.

2.3 Contributions de la thèse

À travers cette thèse, nous visons à développer de nouvelles techniques avancées d'estimation conjointe des paramètres du canal tels que les paramètres de qualité de canal comme les coefficients du canal et la variance du bruit, les paramètres de synchronisation, y compris les décalages temporels et fréquentiels, et aussi les paramètres de localisation tels que les délais de propagation et les DdA. Les techniques développées reposent principalement sur l'approche du maximum de vraisemblance (MV) qui est réputée pour ses performances élevées. Les principales contributions de cette thèse sont:

2.3.1 Estimation EM de type ML des canaux sélectifs en fréquence à variation temporelle rapide pour des transmissions SIMO OFDM

Revue de littérature

Le multiplexage orthogonal par répartition en fréquence (OFDM) a montré son efficacité dans la 4G. Une variété évolutive de CP-OFDM est déjà incluse dans les nouvelles normes radio de la 5G par le projet de partenariat de 3e génération (PP3G) [9]. La forme d'onde adoptée comprendra plusieurs espacements de sous-porteuses qui dépendent du type de déploiement et des exigences de service. De plus, lorsqu'il est couplé à la technologie d'antenne à grande échelle, l'OFDM est prêt à permettre l'augmentation de 1000 fois de la capacité requise au cours des prochaines années. Malgré ses caractéristiques attrayantes telles que la robustesse aux canaux sélectifs en fréquence et la diversité spatiale, les technologies d'interface radio (TIR) de type OFDM sont très sensibles aux variations du canal dans le domaine temporel puisque ces dernières influencent l'orthogonalité entre les sous-porteuses introduisant ainsi ce que l'on appelle l'interférence inter-porteuse (IIP). Ainsi, l'estimation précise des canaux devient une tâche difficile à très haute mobilité [10].

Jusqu'à présent, plusieurs techniques d'estimation du canal ont été rapportées dans la littérature. Ils peuvent être classés en deux grandes catégories: *i*) les approches assistées par les données (AD) où

les symboles transmis sont supposés être parfaitement connus au niveau du récepteur. Ils fournissent des estimations très précises des canaux à un coût important, cependant, en termes d'«overhead»; *ii*) les approches autodidactes où le récepteur n'a pas d'informations *a priori* sur les données transmises. Par conséquent, les techniques autodidactes n'entraînent aucun surcoût en termes d'«overhead». Cependant, elles ont une précision réduite par rapport aux techniques AD. Certaines approches d'estimation des paramètres autodidactes disponibles dans la littérature (voir [5] - [6]) opèrent occasionnellement ou par intermittence une étape d'initialisation à des instants d'insertion pilote beaucoup moins fréquente. Ces techniques, appelées hybrides (c'est-à-dire combinant autodidacte et DA), fonctionnent très souvent bien mieux que les approches autodidactes (c'est-à-dire avec une initialisation aléatoire). Alors qu'en même temps, ils nécessitent des «overheads» négligeables par rapport aux solutions AD [7]. Par conséquent, nous préconiserons une approche hybride dans ce travail.

Pour les canaux rapides variant dans le temps, la plupart des techniques AD s'appuient sur un modèle d'expansion de base (MEB) pour estimer les coefficients du canal [11] - [12]. En fait, les méthodes BEM telles que Karhunen-Loeve MEB ont été conçues avec une erreur quadratique moyenne (EQM) faible [11]. Ils sont cependant sensibles au décalage statistique des canaux. Le MEB complexe-exponentiel, proposé aussi dans [11], n'utilise pas les statistiques de canal mais souffre de grandes erreurs de modélisation. Le polynôme MEB (P-MEB) étudié dans [13] donne des estimations précises des coefficients du canal, mais uniquement dans des scénarios à Doppler faible. Dans [2], les variations des gains complexes de chaque trajet ont été approximées par une fonction polynomiale dans le temps puis estimations par la technique des moindres carrés (MC). Cette solution offre des performances précises même à un Doppler élevé. Cependant, il nécessite que le nombre de chemins soit inférieur aux nombres de symboles pilotes insérés dans chaque bloque OFDM. De plus, il a été dérivé dans le cas du système à entrée unique et sortie unique (SISO) et son extension aux systèmes à entrée multiple sortie unique (SIMO) n'a jamais été abordée.

Dans la catégorie autodidacte, l'estimation du canal variant dans le temps a été également étudiée dans [14]. Les auteurs ont utilisé le polynôme discret de Legendre MEB avec la technique de MEGAE -maximum a posteriori (MEG-MAP) pour estimer les coefficients du canal dans le domaine temporel. Dans [15], nous avons utilisé espérance maximisation (EM) pour estimer les gains du canal sur une configuration SISO. Cependant, les deux techniques ont été développées aux systèmes SISO multi-porteuses et, par conséquent, n'exploitent pas le gain de diversité qui peut être atteint par les systèmes multi-antennes. De plus, ils exigent aussi que le nombre de pilotes soit supérieur au

nombre de trajets du canal. Dans [16], le problème d'estimation instantanée du RSB a été étudié en utilisant l'approche EM, mais toujours sur des configurations SISO uniquement. Dans [17] et [18], les techniques EM et LS ont de nouveau été utilisées respectivement pour estimer le RSB sur des systèmes SIMO à une seule porteuse. Dans [19], [20], l'estimation itérative du canal avec filtre de Kalman et détection QR a d'abord été étudiée sous les canaux multi-porteuses SISO et ensuite généralisée aux systèmes OFDM à entrées multiples et sorties multiples (MIMO). Ses performances ont été encore améliorées dans [21] en exploitant les statistiques des erreurs d'estimation de canal dans un processus d'estimation itératif. Cependant, les techniques basées sur les filtres de Kalman nécessitent une parfaite connaissance du Doppler. De plus, un nombre élevé de pilotes par bloc OFDM est nécessaire pour obtenir des estimations précises affectant ainsi le débit global du système.

Contribution

Dans cette contribution, nous développons un estimateur MV itératif basé sur EM des canaux rapides variant dans le temps sur des interfaces radio de type SIMO OFDM. En s'appuyant sur l'approximation polynomiale des gains du canal multi-trajet en [2] et en recourant à la puissante technique EM [22] au lieu de l'approche LS, notre solution offre une acquisition plus précise des gains de canal variant dans le temps. Pour éviter la convergence locale inhérente aux algorithmes itératifs, nous initialisons l'algorithme EM avec une version SIMO DA MV qui est développée dans ce travail dans ce seul but. Nous montrons que ce dernier se résume à appliquer SISO DA LS de [2] sur chaque antenne réceptrice. En outre, pour revenir à notre contribution clé ici, notre nouvelle solution SIMO autodidacte MV-EM donne comme sous-produit des estimations des symboles inconnus. Ces derniers sont utilisés pour concevoir un schéma d'annulation IIP dédié (AIIP) qui fonctionne côte à côte avec l'estimateur basé sur EM selon le principe turbo (par exemple, voir [8]). De plus, nous introduisons une autre procédure d'initialisation, SIMO DA MV régularisée (DMR) qui peut s'appliquer lorsque le nombre de chemins dépasse le nombre de symboles pilotes disponibles. Cette caractéristique rend la solution proposée robuste à toute variation rapide de l'environnement de propagation où le nombre de trajets peut changer en raison du mouvement des utilisateurs mobiles. Ainsi, nous montrons la possibilité de réduire le nombre de pilotes dans chaque bloc OFDM en dessous du nombre de chemins de canal sans affecter de manière significative les performances de la solution globale, ce qui nous permet de réduire l'«overhead» et par la suite d'augmenter le débit de manière assez significative. Les résultats des simulations montrent que l'estimateur hybride ML-

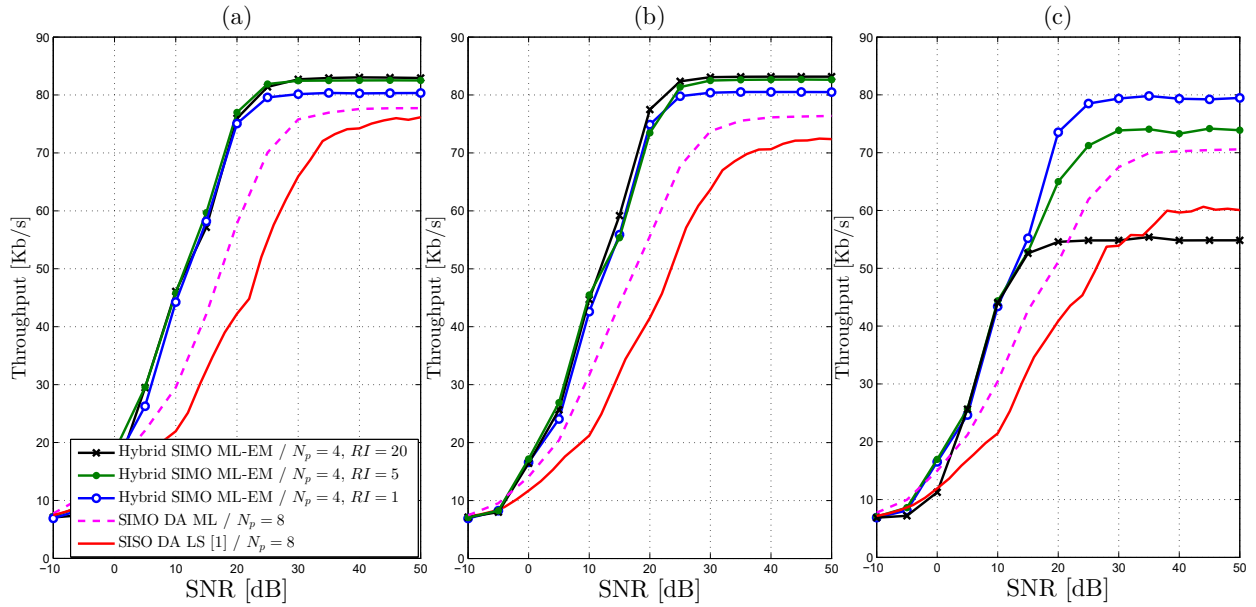


Figure 2.2 – Link-level per-carrier throughput vs. the per-carrier SNR of the advocated new hybrid ML-EM (with $N_p = 4$) at multiple RI values, the SISO DA LS in [2] (i.e., $N_r = 1$), and its proposed SIMO DA ML extension (with $N_p = 8$) with $N_c = 3$, $N_r = 2$, and $\lambda = 0.5$ at: (a) $v = 60$ km/h, (b) $v = 120$ km/h, and (c) $v = 240$ km/h.

EM proposé (c'est-à-dire combine toutes les nouvelles versions autodidacte MV-EM et DA MV ou DMR) converge en quelques itérations, fournissant ainsi des estimations très précises de tous les gains de canaux à trajets multiples. Plus important encore, cette précision d'estimation accrue se traduit par des gains très significatifs du taux d'erreur binaire (TEB). Ceci permet d'avoir un gain en débit par porteuse au niveau lien par rapport à la meilleure solution de référence disponible à ce jour pour le problème en question. La technique en question est la SISO DA MC, développée [2], avec sa nouvelle généralisation ici aux systèmes SIMO. Nous voyons à travers les Figures 2.2 (a) et (b) que le débit par porteuse augmente avec le MV-EM hybride pour des Doppler faible et moyen quand l'intervalle de rafraîchissement RI passe de 1 à 5. Il s'ensuit que les sous-porteuses pilotes ne sont plus nécessaires au niveau des blocs OFDM actuels et peuvent être utilisées pour transporter des données à la place. Le taux d'insertion du pilote peut être considérablement ralenti, d'au moins jusqu'à 20 fois (le rapport pilote / données ou le rapport d'« overhead » peut devenir aussi bas que 0,16 %), tout en signalant des gains de débit notables au lieu de pertes, d'autant plus à des niveaux élevés -porteur RSB. Alors que SISO AD MC de [2] et son extension SIMO AD MV nécessitent toujours le même nombre de pilotes pour fournir des estimations de canal fiables. Par conséquent, aucun gain de débit supplémentaire ne peut être obtenu.

2.3.2 Synchronisation du temps et de la fréquence au sens maximum de vraisemblance pour la formation de faisceaux dans un système de relais MIMO distribués sur des canaux à évanouissement plat variant dans le temps

Revue de littérature

La diversité spatiale est un concept bien connu permettant de lutter contre l'évanouissement des canaux et d'augmenter le débit global des systèmes de communication. Un tel avantage peut être obtenu grâce à de multiples solutions. Les réseaux coopératifs fournissent une solution distribuée qui évite certaines des difficultés liées aux systèmes entrées multiples et sorties multiples (MIMO) traditionnels [23], [24]. En effet, dans de nombreuses situations, certains équipements utilisateurs ne sont pas en mesure d'intégrer plusieurs capteurs d'antenne en raison de limitations en taille et puissance. Dans ce cas, les utilisateurs peuvent coopérer les uns avec les autres pour former un réseau d'antennes virtuel. Cependant, certains défis doivent être abordés pour garantir une coopération constructive entre les relais. Un problème majeur dans ces systèmes de relais coopératifs est la synchronisation multi-nœuds, à la fois en temps et en fréquence. Ce dernier est crucial pour assurer une efficacité en énergie, en spectre et en surface lors de la mise en œuvre de la formation de faisceaux à relais MIMO distribué dans le cas d'une liaison source-destination donnée ayant des limites de couverture.

Il existe deux approches pour atténuer l'effet des distorsions en temps, fréquence, phase et amplitude d'un canal variant dans le temps (CVT), on nomme: les procédures de compensation en boucle fermée et en boucle ouverte. Dans l'approche en boucle fermée, la destination effectue l'estimation de tous les paramètres de synchronisation avec les coefficients de canal. Ces estimations sont ensuite transmises à un bloc d'égalisation pour lutter contre l'asynchronisme en temps et en fréquence comme proposé dans [25], [26]. Les approches en boucle fermée présentent moins d'« overhead » car l'interaction entre les nœuds de relais est maintenue au minimum tandis que la destination coordonne le processus de synchronisation. Cependant, il peut être difficile pour les réseaux sans fil sans infrastructure adéquate de gérer des algorithmes d'estimation multidimensionnel très complexes. Dans les approches en boucle ouverte, cependant, le signal source à relayer est décalé dans les domaines temporel et fréquentiel avant transmission, comme proposé dans [27]. Ainsi, les répliques du même signal transmis, provenant de différents relais, arrivent au même moment et se combinent de manière constructive au niveau du récepteur. Dans ce scénario, des algorithmes d'es-

timation moins complexes peuvent être envisagés dans les nœuds avec une signalisation minimale de la destination.

En ce qui concerne l'estimation des paramètres de synchronisation, plusieurs techniques existent dans la littérature ouverte [28]. D'une part, les travaux de synchronisation [29] - [30] enquêtent sur le décalage temporel (DT) en négligeant l'effet du décalage fréquentiel (DF). D'un autre côté, les solutions introduites dans [31] - [32] traitent l'estimation conjointe de plusieurs DFs en négligeant l'effet des DTs. D'autres techniques effectuent une estimation conjointe de tous les paramètres à la destination dans les réseaux coopératifs en boucle fermée [25], [33], [34]. Bien qu'ils puissent bien fonctionner dans la pratique, ils souffrent d'une complexité de calcul très élevée car ils nécessitent la résolution un problème multidimensionnel qui augmente avec le nombre de relais. De plus, la tâche de synchronisation peut devenir très coûteuse en termes d'«overhead». En effet, après avoir estimé les DTs et les DFs, la destination doit les renvoyer aux relais. Cette dernière résulte en un «overhead» supplémentaire sans oublier des erreurs de quantification puisque les valeurs estimations sont quantifiées avant leur phase de rétroaction.

Des solutions alternatives peuvent être envisagées en s'appuyant sur des schémas de formation de faisceaux collaboratifs distribués (FFCD) [35]. Beaucoup de ces techniques se concentrent sur la conception optimale des poids du formateur de faisceaux tout en supposant une synchronisation parfaite qui les rend extrêmement vulnérables en pratique aux décalages de phase, de fréquence et de temps. D'autres techniques se concentrent en revanche sur la lutte contre l'effet de désalignement à destination qui est provoqué par de tels décalages. Dans [36], les auteurs ont proposé une solution de compensation de phase basée sur une approche itérative de retour de bits. Dans [37], une solution de synchronisation de fréquence dans les réseaux de capteurs sans fil utilisant une méthode de synchronisation aller-retour a été proposée. Dans [38], une méthode de synchronisation distribuée a été proposée pour les réseaux sans fil denses en utilisant un estimateur conjoint de DTs et DFs qui est basé sur la corrélation. Pourtant, toutes les techniques mentionnées ci-dessus reposent sur l'hypothèse simplificatrice d'un canal statique (CS). En revanche, une large gamme d'applications nécessite que les terminaux agissent comme des relais et, dans le même temps, les systèmes de communication de la 5G devraient prendre en charge des communications fiables à des vitesses très élevées atteignant 500 km / h (par exemple, en train à grande vitesse) [39]. Pour de tels systèmes, l'hypothèse conventionnelle du CS conduit à de graves pertes de performances. Récemment, d'autres travaux sur FFCD [40], [41] avaient abordé le problème difficile de la synchronisation multi-nœuds sous CVT en utilisant des versions améliorées de la technique de rétroaction à un bit. Cependant,

ils n'ont abordé que la compensation de phase en supposant une estimation parfaite du DTs et du DFs.

Contribution

Motivés par ces faits, nous développons dans ce chapitre une nouvelle technique de synchronisation décentralisée au sens MV avec une conception de formation de faisceau à relais MIMO distribuée qui aborde le cas difficile du CVT pour des transmissions de relais multi-nœuds. La solution MV CVT proposée repose sur une approximation très utile de la matrice de covariance de canal par un modèle de propagation à deux raies. Elle fournit des estimations précises de type MV des DTs et des DFs à un coût de calcul réduit car elle ne nécessite aucune inversion de matrice. Nous développons également une version itérative, appelée MV CVT-ED (avec estimation du Doppler), qui tient en compte de la nécessité pratique d'estimer à chaque relai l'étalement Doppler sur lequel repose la version initiale appelée ci-après MV CVT-DP (Doppler parfait). Les résultats des simulations montrent une amélioration significative de la précision de la synchronisation par rapport aux précédentes techniques de synchronisation distribuée à plusieurs relais en supposant des CSs. Ceci se traduit par des gains notables en termes de débit au niveau lien (c'est-à-dire en tenant en compte de l'«overhead»), plus encore à Doppler plus élevé ou avec des un nombre de nœuds plus important. Dans la figure 2.3, nous rapportons des gains de débit notables de MV CVT par rapport aux techniques MEGAE et MV CS à des niveaux RSB moyens et élevés lors de l'augmentation du nombre de relais de 1 à 8 . À des valeurs Doppler plus élevées (c'est-à-dire, $F_{D_k} = 200$ Hz ou $F_{D_k} = 300$ Hz), les gains de débit de MV CVT par rapport à MEGAE et MV CT deviennent encore plus significatifs, encore plus lorsque le nombre de relais augmente. Ces observations clés sont une solide confirmation des avantages de performance des schémas de formation de faisceaux et de synchronisation multi-nœuds à relais MIMO distribués proposés.

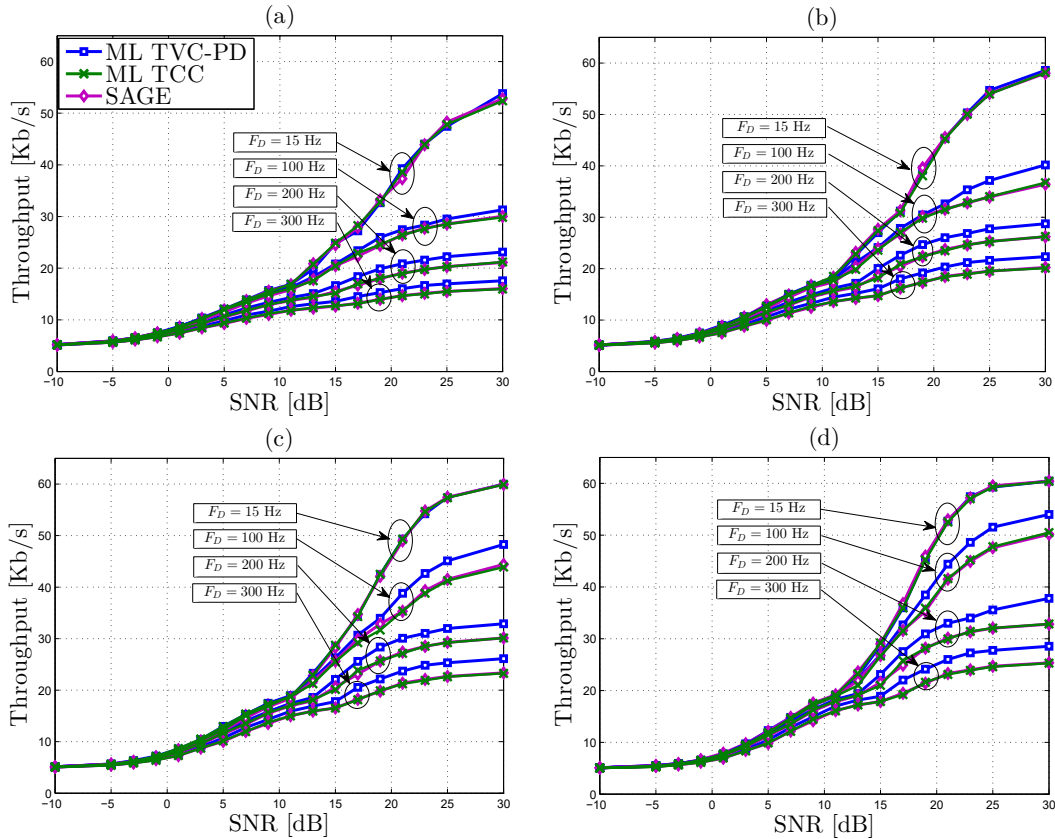


Figure 2.3 – Débit du niveau lien vs. RSB pour MV CVT-DP à un taux de rafraîchissement $P = 100$ et différentes fréquences Doppler pour: (a) $K = 1$, (b) $K = 2$, (c) $K = 4$, et (d) $K = 8$.

2.3.3 Estimation au sens maximum de vraisemblance conjointe des angles d'arrivées et des délais de propagation pour des transmissions multi-trajets et multi-porteuses avec des applications pour la localisation à l'intérieur via la radio IEEE 802.11ac

Revue de littérature

Dans les modèles de propagation à trajets multiples, un signal source est reçu par un réseau d'antennes via un certain nombre de trajets, chacun étant décrit par un angle d'arrivée (AdA), un retard temporel (RT) et un gain de trajet. Le problème d'estimation conjoint des AdA et des RT (ECAR) consiste alors à estimer conjointement tous les AoAs et leurs RTs correspondants à partir d'un nombre fini d'échantillons reçus. Le problème ECAR se pose dans de nombreuses situations pratiques allant des applications militaires (par exemple, radar et sonar) aux systèmes de communication sans fil à large bande. En général, la capacité de caractériser chaque trajet avec son

angle et son délai fournit au système des capacités sensorielles plus fortes menant, par exemple, à des techniques de formation de faisceau plus robustes [42] et à des performances d'égalisation améliorées [43]. De plus, comme les services de géolocalisation seront probablement très demandés pour les futurs systèmes de communication sans fil, les informations sur les AdAs et les RTs peuvent être utilisées pour concevoir des techniques de localisation hautement précises [44]; [45]. Dans ce contexte, afin de faire face à des environnements à trajets multiples denses, le paradigme d' *empreinte digitale* qui refond la localisation des sources en un problème de reconnaissance de formes a été envisagé dans [46] - [47]. En particulier, il a été récemment montré que l' *empreinte digitale* avec des signatures de localisation qui sont caractérisées par les AdAs et les RTs pour chaque emplacement candidat conduit à des améliorations par rapport aux signatures de localisation qui sont caractérisées par la puissance du signal reçu (PSR) [48]. En fait, contrairement au PSR qui varie sensiblement sur une distance de longueur d'onde (en raison d'interférences de trajets multiples constructives et destructives), les AdAs avec les RTs associés forment une empreinte digitale unique pour chaque emplacement [47]. Par conséquent, une estimation précise et peu coûteuse de ces paramètres de trajets multiples peut être utilisée avec le paradigme d' *empreinte digitale* pour développer des algorithmes de localisation très efficaces. Alternativement, si plusieurs points d'accès (PA) sont disponibles, ils peuvent coopérer pour localiser un utilisateur mobile en utilisant le décalage horaire d'arrivée (DHA) et AdAs (voir [49] an [50] pour plus de détails) .

Contrairement à ECRA, l'estimation séparée (ou disjointe) des retards ou des AdAs fait l'objet de nombreuses recherches depuis des décennies. Pour des travaux antérieurs sur l'estimation ADAs uniquement et RTs uniquement, voir respectivement [51], [52] et [53], [54]. En comparaison avec les techniques d'estimation disjointes qui estiment d'abord les retards puis les angles correspondants, l'estimation conjointe de ces paramètres spatio-temporels (c'est-à-dire ECRA) est plus précise dans les cas où plusieurs trajets ont des RTs ou AdAs presque égaux [42] . De plus, contrairement à ECRA, le nombre d'angles estimés dans les schémas d'estimation DOA uniquement doit être inférieur au nombre d'antennes. Ainsi, les estimateurs AdAs uniquement nécessiteraient des réseaux d'antennes de grande taille dans des environnements à trajets multiples très denses.

Jusqu'à présent, plusieurs techniques ECRA ont été rapportées dans la littérature, à l'exception de l'approche basée sur le «matrix pencil» unitaire (MPU) proposée récemment dans [49], toutes les solutions existantes sont orientées vers des systèmes à porteuse unique. Principalement, elles peuvent être classées en deux grandes catégories: les estimateurs sous-espace et MV. La plupart des

techniques sous-espaces sont construites sur les algorithmes MUSIC et ESPRIT [55] - [56]. En pratique, les approches sous-espace sont plus attrayantes en raison de leur complexité de calcul réduite. Cependant, ils sont généralement sous-optimaux et souffrent d'une dégradation des performances (à la fois en termes de résolution et de précision d'estimation) pour des niveaux de RSB faibles et/ou des trajets très rapprochés. Les approches MV, cependant, sont connus par leur haute précision et une capacité de résolution améliorée. Pourtant, malgré leurs avantages prometteurs, leur complexité de calcul a souvent été considérée comme un principal inconvénient.

Dans le contexte JADE spécifique, à notre connaissance, seuls deux estimateurs MV ont été introduits jusqu'à présent, mais uniquement pour les signaux à bande étroite. La toute première solution MV a été proposée par Wax *et al.* dans [57] qui est de nature *itérative* et sera donc appelée, ci-après, l'estimateur itératif MV (IMV). L'autre solution MV introduite plus tard dans [58] est également *itérative* et basée sur l'algorithme de maximisation d'espérance généralisée en alternance d'espace (MEGAE). Cependant, comme toute approche *itérative*, la performance de ces deux estimateurs MV est étroitement liée à la connaissance initiale des paramètres inconnus, c'est-à-dire qu'ils ne convergeront pas vers le maximum global de la fonction log-vraisemblance (FLV) si leurs estimations initiales ne sont pas fiables. En outre, pour les deux estimateurs MV *itératifs*, une grille d'échantillonnage fixe est sélectionnée pour servir l'ensemble de toutes les estimations candidates pour les RTs et les AdAs inconnus. Ensuite, en supposant que tous les vrais paramètres (inconnus) sont exactement sur la grille sélectionnée, IMV et MEGAE tentent de maximiser la FLV de manière itérative. Par conséquent, ils souffrent du problème inévitable qui se pose dans des situations pratiques où certains des vrais RTs et/ou AdAs ne se trouvent pas sur la grille d'échantillonnage. Ainsi, pour une estimation précise, il est obligatoire d'utiliser une grille à échantillonnage dense pour réduire l'écart entre les vrais paramètres et leurs points les plus proches sur la grille. Cependant, le coût d'un échantillonnage en grille dense est l'augmentation excessive de la complexité de calcul.

Contribution

L'estimateur proposé s'appuie sur le théorème de maximisation globale de Pincus [59] et le concept d'échantillonnage préférentiel (EP) [60]. En particulier, grâce à une approximation très précise de la fonction de vraisemblance concentrée (FVC), nous transformons le problème d'optimisation *multidimensionnel* original en plusieurs problèmes d'optimisation *bidimensionnels*, ce qui se traduit par une réduction de la complexité de calcul. De plus, les problèmes d'optimisation bidi-

mensionnelle sont totalement disjoints et peuvent être exécutés séparément dans la pratique. Dans cette perspective, le nouvel estimateur MV basé sur les EP peut compter sur une implémentation en parallèle qui peut être exécutée efficacement sur les plates-formes multiprocesseurs actuelles.

La combinaison du théorème de Pincus et du concept EP a déjà été appliquée à de nombreux problèmes d'estimation fondamentaux. A notre connaissance, cependant, cette combinaison a été appliquée pour la première fois par S. Kay et S. Saha dans [61] dans le contexte de l'estimation de fréquences multiples. Là, il a été montré pour la toute première fois que l'estimation conjointe MV de fréquences multiples se résume au calcul d'estimations moyennes d'échantillons à partir d'un certain nombre de réalisations générées selon une fonction d'importance soigneusement conçue. Le théorème de Pincus et le concept EP ont été appliqués plus tard par S. Kay *et al.* pour l'estimation des paramètres des signaux de type chirp [62], estimation AdAs des sources avec des réseaux d'antennes [52], ainsi que l'angle d'articulation et du Doppler dans [63]. Cette approche a également été appliquée avec succès dans le contexte de l'estimation conjointe du canal et du décalage fréquentiel sous: *i*) communications OFDMA mono-utilisateur [64], et *ii*) communications MIMO-OFDM multi-utilisateurs [65]. Plus récemment, ces outils puissants ont été mis à profit dans le contexte de la localisation de source basée sur DHA [66], de l'estimation de RT autodidacte dans [67], ainsi que l'acquisition des RTs dans les environnements à trajets multiples [54]. Les simulations numériques montrent la supériorité de l'estimateur MV basé sur l'EP proposé par rapport aux techniques ECRA de type MV et sous-espace en termes de précision d'estimation, de capacité de résolution et de complexité de calcul. Des mesures de canal réelles collectées à l'aide des paramètres de configuration de la norme IEEE 802.11ac dans un environnement intérieur ont également été utilisées pour étudier les capacités de localisation en ligne de l'algorithme proposé.

Comme le montre la Figure 2.4 (a), les techniques UMP et EP MV produisent des erreurs de localisation remarquablement petites, inférieures à 10 cm à tout moment, lorsqu'elles sont utilisées avec la procédure de localisation basée sur la covariance. La figure 2.4 (b) représente la fonction de distribution cumulative (FDC) lorsqu'une procédure de localisation sans covariance (plus pratique) est appliquée en utilisant les estimations DHA et AdAs fournies par chaque algorithme. Là, on voit qu'EP MV fournit toujours une erreur de localisation inférieure à 10 cm dans 90 % des cas (et ne dépasse jamais 15 cm) tandis que les erreurs de localisation UMP sont supérieures à 70 cm dans 10 % des cas.

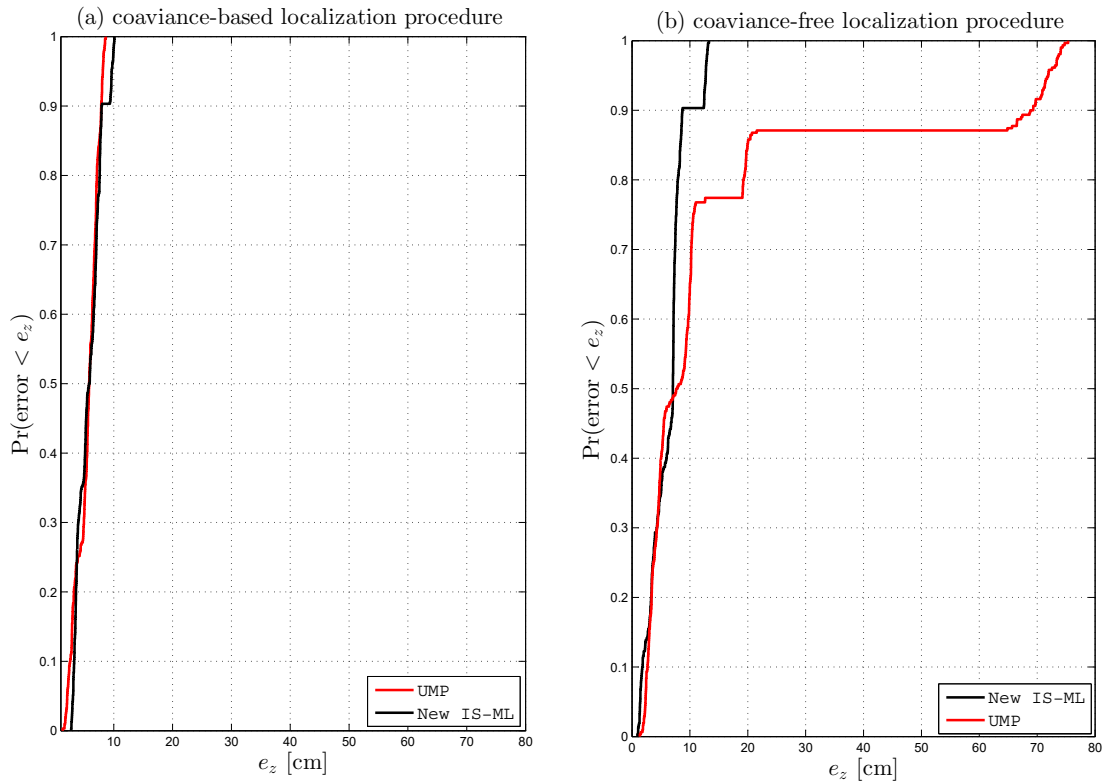


Figure 2.4 – FDC de l’erreur de position e_z pour EP MV et UMP: (a) procédure de localisation basée sur la covariance (b) procédure de localisation sans covariance.

2.3.4 Autres contributions dans cette thèse

Évaluation des technologies d’interface radio (TIR)s et des ensembles de TIR (ETIR)s pour IMT-2020 (5G) dans le cadre du mandat du CEG

La 5G, également connue sous le nom d’IMT-2020 [1], est l’une des forces motrices les plus puissantes de l’évolution de la technologie sans fil, qui promet d’englober plusieurs TIRs, y compris 3GPP et ETSI-DECT. Ces candidats IMT-2020, mis à disposition très récemment pour évaluation, doivent être évalués pour assurer leur conformité aux exigences minimales [68], [69].

Plusieurs caractéristiques clés doivent être évaluées telles que le débit des paquets, l’efficacité du spectre cellulaire, le taux de perte de paquets et la latence. Ces fonctionnalités donneront des informations précieuses pour identifier i) les domaines où des améliorations peuvent être apportées, ii) introduire ces améliorations et les évaluer, iii) soutenir les fabricants et les opérateurs d’équipement dans leurs efforts de normalisation pour intégrer ces améliorations si elles sont jugées utiles.

La comparaison des technologies 5G doit être déployée sur une base équitable, en utilisant une plateforme de simulation commune.

C’est dans cette perspective que l’équipe du Wireless Lab, mandatée par Innovation, Sciences et Développement économique Canada (ISDE) et le groupe canadien d’évaluation, a travaillé sur développement d’une plateforme de simulation commune pour évaluer les candidats 3GPP et l’ETSI-DECT RIT. Les caractéristiques choisies pour l’évaluation par simulation comprennent le 5e centile de l’efficacité spectrale de l’utilisateur, l’efficacité spectrale moyenne, la densité de connexion, la fiabilité et la mobilité [68]. Les résultats obtenus ont été inclus dans le rapport final de la contribution du CEG aux réunions du groupe de travail 5D (WP 5D).

Contribution

Plusieurs candidats ont été soumis au WP 5D pour évaluation. Dans le tableau 2.1, nous fournissons un résumé des critères de performance évalués pour chaque technologie soumise. Pour être approuvé, chaque candidat doit satisfaire aux exigences minimales de chacun des critères d’évaluation mentionnés ci-dessus. La réunion WP 5D # 35e a examiné les résultats de l’étape 4 (évaluation

Table 2.1 – Technologies couvertes par le CEG pour WP 5D

Candidat Document Référence	Soumission IMT-2020						
	3GPP RIT [70]	SRIT [71]	Chine [72]	Corée du Sud [73]	TSDSI [74]	ETSI-DECT [75]	NuFront [76]
Status	Évalué	Évalué	Non évalué (WP 5D a déterminé que l’évaluation 3GPP s’applique à ce candidat)	Non évalué (WP 5D a déterminé que l’évaluation 3GPP s’applique à ce candidat)	Not evaluated (After de-activation of certain features, TSDSI RIT became sufficiently similar to 3GPP RIT)	Évaluation partielle (uniquement la composante DECT TIR)	Évaluation partielle
Efficacité spectrale moyenne	✓	✓				N/A	Données manquantes
5% d’efficacité spectrale	✓	✓				N/A	Données manquantes
Mobilité	✓	✓				N/A	Données manquantes
Fiabilité	✓	N/A				✓	Données manquantes
Densité de connexion	✓	✓				Données manquantes	Données manquantes

des candidats TIRs ou ETIRs par des groupes d’évaluation indépendants). Il a été convenu au cours de la réunion que les propositions de 3GPP TIR et ETIR, Chine, Corée et TSDSI passent l’étape 6. Par conséquent, elles ont été transmises pour un examen plus approfondi à l’étape 7. À l’étape 7:

- Les TIRs et ETIRs proposés par 3GPP, la Chine et la Corée sont regroupés dans la même technologie identifiée à l’UIT comme “3GPP 5GETIR” et “3GPP 5GTIR” et telle que développée par 3GPP. Les deux technologies ont passé l’étape 7.
- TSDSI TIR a également passé l’étape 7 en tant que “TSDSI RIT”.
- le «WG Technology Aspects» n’a pas réussi à parvenir à un accord sur la manière de résumer les résultats de l’étape 4 pour les soumissions ETSI-DECT et Nufront. Lors de la séance

plénière de clôture de la réunion WP 5D # 35e (23 juin - 9 juillet), la réunion a approuvé l'option 2 et a accordé une prolongation unique à titre exceptionnel pour les deux candidats.

2.4 Conclusion

Dans cette thèse, nous avons proposé plusieurs techniques d'estimation conjointe pour acquérir les informations sur des paramètres clés du canal sans-fil. Principalement, nous avons fait quatre contributions. Tout d'abord, nous avons proposé un estimateur MV qui s'appuie sur le théorème de maximisation globale de Pincus [59] et le concept EP [60]. Dans la deuxième contribution, nous avons développé une nouvelle technique de synchronisation MV décentralisée avec une conception de formation de faisceaux MIMO-relais distribuée qui s'adapte au cas difficile du CVT sur des transmissions de relais multi-nœuds. La solution ML CVT proposée repose sur une approximation très utile de la matrice de covariance de canal par un modèle de propagation à deux raies. Dans la troisième contribution, nous développons un estimateur MV itératif basé sur l'EM de canaux rapides variant dans le temps sur des interfaces radio de type SIMO OFDM. Nous avons également introduit une procédure alternative d'initialisation SIMO DMR qui peut encore s'appliquer lorsque le nombre de chemins dépasse le nombre d'observations pilotes disponibles. Dans la quatrième contribution, nous avons couvert l'évaluation par simulation de TIR et ETIR 3GPP. Nous poursuivons actuellement le même processus avec la réévaluation de DECT et NuFront. Nos travaux au cours de ce projet ont été inclus dans le rapport final du CEG soumis à la 34e réunion du WP 5D. La recherche au cours du programme de doctorat a abouti à trois revues et sept articles de conférence (cf. section 7.4).

Chapitre 3

Thesis Overview

Every 10 years, wireless communications go through a technological shift that brings more use cases and opportunities. The 1G was marked by the introduction of analog telecommunications that support voice only. During the 90s, the second generation introduced digital standards allowing new services such as roaming and short message service (SMS). In the year 2000, the ITU issued the IMT-2000 which is a globally coordinated definition of 3G covering key issues such as frequency spectrum use and technical standards. This generation introduced the notion of smartphones for the first time and proposed new sorts of applications such as web browsing and email access. As new cases surface and become more data hungry, there was a need for new technologies. The 4G, under the banner of IMT-Advanced, was put on the table in 2010 and brought new concepts such as “all IP”, multimedia data (video and music) and faster mobile broadband. In the past decade, a lot of research efforts were carried out to prepare for the next generation of wireless communications. The new generation, with the first recommendations aimed to be released in 2021 under the banner of IMT-2020, is promising much faster connection, more reliability and higher connection density along with a lower latency. These features vary depending on the application. Indeed, 5G is aiming to provide more than enhanced broadband services and encompass new ones. 5G relies on three main pillars. The first one being an enhanced mobile broadband (eMBB) allowing a more reliable and faster connections when compared to the existing LTE technology.

3.1 Background and preliminaries

3.1.1 Adopted algorithms and mathematical tools

Within this thesis, we used multiple algorithmic approaches and mathematical tool to achieve high performance while keep a practical computational Complexity.

Maximum Likelihood Estimation

Maximum likelihood (ML) estimates are obtained by maximizing the likelihood function (LF). The latter measures how well the statistical model is fitting the observations for a specific value of the unknown parameter. It is one of the most widely used approaches to obtain practical estimates. The ML estimator (MLE) is known to be asymptotically efficient. In other words, it can reach the Cramer Rao low bound (CRLB) (3.4) for a large number of data samples [77]. In general, to obtain the ML estimates of a vector parameter $\boldsymbol{\delta}$, we need to maximize LF, $p(\mathbf{y}; \boldsymbol{\delta})$, over the allowable range of $\boldsymbol{\delta}$. To obtain the MLE estimate, the straightforward approach is to perform a grid search over all possible values of $\boldsymbol{\delta}$. However, a grid search approach has certain drawbacks. For example, there is the inevitable off-grid problem which arises in practical situations where $\boldsymbol{\delta}$ is not on the sampling grid. Moreover, grid search can be computationally infeasible especially when $\boldsymbol{\delta}$ is multi-dimensional. In such cases, we can use iterative maximization solutions such as Newton Raphson or the expectation-maximization (EM). Other non-iterative optimization solution can be envisioned based on Pincus theorem and Monte Carlo method.

Expectation-Maximization

The EM algorithm is an iterative optimization technique that can be used to find maximum of the likelihood function when the model depends on unobserved variables. At each iteration, the algorithm alternates between two steps. The first step is an expectation (E) step where the expectation of the log-likelihood is evaluated using the ML EM estimate of the previous iteration. In the second step, the MLE are obtained by maximizing the expected log-likelihood found on the E step and will serve as input for the next iteration. The Algorithm keeps iterating until it converges or reaches the maximum number of iterations. As each EM iteration requires the MLE of the previous

step, hence an initialization technique is required to trigger the EM algorithm, and which can have an impact on the overall performance. Indeed, if the initialization technique provides poor initial estimates, the EM algorithm can converge to local maximum instead leading to poor performances.

Pincus Theorem

The Pincus' theorem can be used to finding the global maximum of any objective function. The latter, in its most general form, states [59]:

Theorem: Let S be the closure of a bounded domain in an n -dimensional Euclidean space \mathbb{R}^n and denote the elements in S as $\mathbf{x} = [x_1, x_2, \dots, x_n]^T$. Let $F(\mathbf{x})$ be a *continuous* function on S that attains its global maximum on S at a point $\mathbf{z} = [z_1, z_2, \dots, z_n]^T \in S$. Then, z_i ($i = 1, \dots, n$) is given by:

$$z_i = \lim_{\rho \rightarrow +\infty} \frac{\int \dots \int x_i e^{\rho F(\mathbf{x})} dx_1 \dots dx_n}{\int \dots \int e^{\rho F(\mathbf{x})} dx_1 \dots dx_n}. \quad (3.1)$$

Importance Sampling

In some cases, we aim to evaluate $\mathbb{E}\{X\}$ where the pdf exhibits approximately null values outside a certain region. Random sampling from the distribution of X could fail to have even one point inside the region of interest. To obtain some samples from that region, we can perform sampling from a distribution that overweights the important region, hence the name of the technique: importance sampling. Having oversampled the important region, we have to adjust the estimate to account for the fact of using different distribution. Assume that we aim to compute the statistical expectation, $\hat{x} = \mathbb{E}\{X\}$. If we are able to generate R realizations, $\{x^{(r)}\}_{r=1}^R$ using the pdf, $f(x)$, it will be very accurate to approximate the expectation by its sample mean estimate as follows:

$$\hat{x} = \frac{1}{R} \sum_{r=1}^R x^{(r)}. \quad (3.2)$$

Clearly, as the number of realizations R increases, the variance of the sample mean estimate above decreases. If $f(x)$ is extremely non-linear, it cannot be practically used to generate the required realizations. To sidestep this problem, we can resort to the importance sampling concept. In this case vectors X can be alternatively regarded as distributed according to $g(x)$ and the statistical

expectation in (3.3) is equivalently interpreted as an expected value of the transformed random variable [62]:

$$\hat{x} = \frac{1}{R} \sum_{r=1}^R \frac{f(x^{(r)})}{g(x^{(r)})} x^{(r)}. \quad (3.3)$$

3.1.2 Channel parameter estimation

To ensure a reliable communication, the transceiver must gain knowledge about key channel parameters. The latter can be categorized into three categories:

- Localization parameters such as the propagation delay and DoA are used to estimate the MT position.
- Synchronization parameters such as the timing offset and frequency offset that stems from the hardware impairments of local oscillators.
- Channel quality parameters such as the SNR and Ricean K-factor.

Multiple approaches to predict these parameters are available and categorized into four categories:

- Data aided (DA) techniques: These solutions rely on pilot symbols. They provide higher accuracy at a significant cost, however, in terms of overhead.
- Non data aided (NDA): In this case, the receiver does not have *a priori* information about the transmitted data. Therefore, NDA techniques do not incur any overhead at the cost, however, of reduced accuracy.
- Hybrid approach (i.e., combine NDA and DA): These techniques occasionally or intermittently operate an initialization step at much less frequent pilot insertion. Very often they perform much better than full NDA approaches (i.e., with random initialization).
- Code aided (CA): The CA estimation takes advantage of the soft information delivered by the decoder at each decoding iteration. Therefore, CA techniques provide lower overhead, however, its performance is depended on multiple factors such as the coding scheme and the coding rate.

3.1.3 Evaluation methods

To assess the performance of new estimation techniques, we can use different evaluation approaches such as:

Component-level simulation

In the component-level simulations, the evaluation focus mainly on evaluating the accuracy of an estimation technique. Metrics such as the mean square error (MSE), root mean square error (RMSE) are usually used to assess accuracy performances against other techniques from the literature and/or the Cramer Rao low bound (CRLB). The latter is defined as:

$$\text{CRLB}(\boldsymbol{\delta}) = \mathbf{I}^{-1}(\boldsymbol{\delta}), \quad (3.4)$$

where $\boldsymbol{\delta}$ is the vector of channel parameters to estimate. $\mathbf{I}(\boldsymbol{\delta})$ refers to the Fisher information matrix (FIM) whose entries are expressed by:

$$[\mathbf{I}(\boldsymbol{\delta})]_{i,l} = -\text{E} \left\{ \frac{\partial^2 L(\mathbf{y}; \boldsymbol{\delta})}{\partial \delta_i \partial \delta_l} \right\} \quad (3.5)$$

where $L(\mathbf{y}; \boldsymbol{\delta}) = \log(p(\mathbf{y}; \boldsymbol{\delta}))$ and $p(\mathbf{y}; \boldsymbol{\delta})$ is pdf of the received vector \mathbf{y} and parametrized by $\boldsymbol{\delta}$. At the component-level, the computational complexity of the estimation technique can be also assessed in terms of the total number of addition and multiplication operations.

Link-level simulation

At the link-level simulation, the estimation technique is integrated into a transceiver to assess its performances in terms of bit error rate (BER), symbol error rate (SER), frame error rate (FER), and link-level throughput. Usually, the link-level simulations includes features such as:

- channel coding,
- high modulation order,
- adaptive modulation,
- multi-carrier SISO, SIMO, MIMO systems,
- Etc.

The link-level simulation can reveal some insights that cannot be observed at the component-level. Indeed, an improvement in accuracy does not always guarantee a gain in terms of FER or link-level throughput.

System-level simulation

The system-level simulation includes more complex scenarios that includes the deployment of specific network architecture with multiple base stations (BSs) and mobile stations (MTs). Usually, system-level simulation is used to assess the performance of:

- interference cancellation techniques,
- cooperative networks,
- scheduling algorithms,
- Etc.

It can also be used to assess the performance of channel estimation techniques. Indeed, the output of the link-level simulation is fed directly to the system-level simulator to evaluate metrics such the average spectral efficiency and 5th percentile user spectral efficiency.

Real data simulation

Real data evaluation can be performed in two different ways. For the first option, the estimation solution is embedded directly into transceiver. The latter assess the robustness of the proposed solution to hardware impairments. The second option is to conduct measurement campaigns where the received signal or the channel state information (CSI) is captured in different scenarios and later used to assess the performance of the estimation technique.

3.2 Thesis organization

The remainder of the thesis is structured as follows: In chapter 4, we focus on the problem of fast time-varying frequency-selective (i.e., multipath) channel estimation over SIMO OFDM-type transmissions. We do so by tracking the variations of each complex gain coefficient using a polynomial-in-time expansion. To that end, we derive the log-likelihood function (LLF) both in the DA and NDA cases. The DA ML estimates over fast SIMO OFDM channels are derived here for the first time in closed-form expressions and hereby shown to be limited to applying over each receive antenna the DA LS estimator tailored in [2] to fast SISO OFDM channels. This DA ML is used to initialize periodically, over a relatively large number of data blocks (i.e., with further reduced and

relatively close-to-negligible pilot overhead compared to DA ML), a new EM ML-type solution we developed here in the NDA case to iteratively maximize the LLF. We also introduce an alternative RDM initialization solution no longer requesting - in contrast to DA ML - more per-carrier pilot frames than the number of paths to further reduce overhead without incurring significant performance losses. Simulation results show that the proposed hybrid ML-EM estimator (i.e., combines all new NDA ML-EM and DA ML or RDM versions) converges within few iterations, thereby providing very accurate estimates of all multipath channel gains. Most importantly, this increased estimation accuracy translates into very significant BER and link-level per-carrier throughput gains over the best representative benchmark solution available so far for the problem at hand, the SISO DA LS technique in [2] with its new generalization here to SIMO systems.

While chapter 4 focuses on the channel quality aspect, chapter 5 investigates maximum likelihood (ML) time delay (TD) and carrier frequency offset (CFO) synchronization in multi-node decode-and-forward (DF) cooperative relaying systems operating over time-varying channels (TVCs). This new synchronization scheme is embedded into a distributed MIMO-relay beamforming transceiver structure to avoid the drawbacks of multidimensional ML estimation at the destination and to minimize the overhead cost. By accounting for a perfect Doppler spread value, the new synchronization solution delivers accurate TD and CFO estimates. For real-world operation, however, this new technique can be jointly implemented with any Doppler spread estimator in a new iterative scheme using a time-constant channel (TCC) based synchronization method at the initialization step. The resulting TD and CFO estimates along with the channel estimates are then fed into a distributed MIMO-relay beamforming transceiver of K single-antenna nodes, for pre-compensation at each node of the transmitted signals, to ensure constructive maximum ratio combining (MRC) at the destination. Simulation results show significant synchronization accuracy improvement over previous distributed multi-node synchronization techniques assuming TCCs. The latter translates into noticeable gains in terms of useful link-level throughput, more so at higher Doppler or with more relaying nodes.

In chapter 6, we apply the IS technique along with the ML concept to the JADE problem over both OFDM and single-carrier transmissions. More specifically, we propose a new *non-iterative* ML estimator that enjoys guaranteed global optimality and enhanced high-resolution capabilities for both single- and multi-carrier models. The new ML approach succeeds in transforming the original *multi-dimensional* optimization problem into multiple *two-dimensional* ones thereby resulting in

huge computational savings. Moreover, it does not suffer from the off-grid problems that are inherent to most existing JADE techniques. By exploiting the sparsity feature of a carefully designed pseudo-pdf that is intrinsic to the new estimator, we also propose a novel approach that enables the accurate detection of the unknown number of paths over a wide range of practical signal-to-noise ratios (SNRs). Computer simulations show the distinct advantage of the new ML estimator over state-of-the-art JADE techniques both in the single- and multi-carrier scenarios. Most remarkably, they suggest that the proposed IS-based ML JADE is statistically efficient as it almost reaches the Cramér-Rao lower bound (CRLB) even in the adverse conditions of low SNR levels. Using real-world channel measurements collected from four access points (APs) with IEEE 802.11ac standard's setup parameters in an indoor environment, we also show that the proposed ML estimator achieves a localization performance below 15 cm accuracy.

In chapter 7, we provide a summary of other contributions achieved during the PhD program including the participation in the evaluation process of IMT-2020. In the latter, we provide details about the valuation process. The evaluation by simulation covers 3GPP RIT and SRIT and we are currently pursuing the same process with re-evaluation of DECT and NuFront. Next, we summarize the most significant conclusions drawn at the end of last WP 5D # 35e meeting.

In chapter 8, we draw some concluding remarks and provide some insights on potential future work related to each of the contributions mentioned in this thesis.

Chapitre 4

ML-Type EM-Based Estimation of Fast Time-Varying Frequency-Selective Channels Over SIMO OFDM Transmissions

Souheib Ben Amor, Sofène Affes, Faouzi Bellili, and Dush Nalin Jayakody

IEEE Access, vol. 7, no. 1, October 2019.

Abstract

This chapter investigates the problem of fast time-varying frequency-selective (i.e., multipath) channel estimation over single-input multiple-output orthogonal frequency-division multiplexing (SIMO OFDM)-type transmissions. We do so by tracking the variations of each complex gain coefficient using a polynomial-in-time expansion. To that end, we derive the log-likelihood function (LLF) both in the data-aided (DA) and non-data-aided (NDA) cases. The DA maximum likelihood (ML) estimates over fast SIMO OFDM channels are derived here for the first time in closed-form expressions and hereby shown to be limited to applying over each receive antenna the DA least squares (LS) estimator tailored in [2] to fast SISO OFDM channels. This DA ML is used to initialize periodically, over a relatively large number of data blocks (i.e., with further reduced and relatively

close-to-negligible pilot overhead compared to DA ML), a new expectation maximization (EM) ML-type solution we developed here in the NDA case to iteratively maximize the LLF. We also introduce an alternative regularized DA ML (RDM) initialization solution no longer requesting - in contrast to DA ML - more per-carrier pilot frames than the number of paths to further reduce overhead without incurring significant performance losses. Simulation results show that the proposed hybrid ML-EM estimator (i.e., combines all new NDA ML-EM and DA ML or RDM versions) converges within few iterations, thereby providing very accurate estimates of all multipath channel gains. Most importantly, this increased estimation accuracy translates into very significant BER and link-level per-carrier throughput gains over the best representative benchmark solution available so far for the problem at hand, the SISO DA LS technique in [2] with its new generalization here to SIMO systems.

4.1 Introduction

Orthogonal frequency-division multiplexing (OFDM) showed its effectiveness in current 4th generation wireless technology (4G). A scalable variety of CP-OFDM is already included in 5th generation (5G) new radio (NR) standards by the 3rd Generation Partnership Project (3GPP) [9]. The adopted waveform will include multiple sub-carrier spacings that depend on the type of deployments and service requirements. Moreover, when coupled with the large-scale antenna technology OFDM is poised to enable the 1000-fold increase in capacity that is required over the next few years. Despite its attractive features such as robustness to frequency selective channels and spatial diversity, OFDM-type radio interface technologies (RITs) are already very sensitive to channel time variations since the latter break the crucial orthogonality between the subcarriers thereby introducing the so-called inter-carrier interference (ICI). Accurate channel estimation, hence, becomes a daunting task at very high mobility [10].

So far, a number of channel estimation techniques have been reported in the literature. They can be categorized in two major categories: *i*) the data-aided (DA) approaches where the transmitted symbols are assumed to be perfectly known at the receiver. They provide highly-accurate channel estimates at a significant cost, however, in terms of overhead; *ii*) the blind or non-data-aided (NDA) approaches where the receiver has no *a priori* information about the transmitted data. Therefore, NDA techniques do not incur any overhead at the cost, however, of reduced accuracy. Some NDA

parameter estimation approaches available in the literature (mainly proposed by the authors' group e.g., see [5]-[6]) occasionally or intermittently operate an initialization step at much less frequent pilot insertion instants (by an order or two of magnitude). Referred to as hybrid (i.e., combine NDA and DA), these techniques very often perform much better than full NDA approaches (i.e., with random initialization). While at the same time they require negligible overhead amounts compared to DA solutions [7]. Hence, we shall advocate a hybrid approach in this work.

For fast time-varying channels, most of the DA techniques rely on a basis expansion model (BEM) to estimate the equivalent discrete-time channel taps [11]-[12]. In fact, BEM methods such as Karhunen-Loeve BEM were designed with low mean square error (MSE) [11]. They are, however, sensitive to statistical channel mismatch. The complex-exponential BEM, also proposed in [11], does not make use of the channel statistics but suffers from large modeling errors. The polynomial BEM (P-BEM) investigated in [13] yields accurate channel estimates, but only at low Dopplers. In [2], the complex gain variations of each path was approximated by a polynomial function of time then estimated by least squares (LS) technique. This solution offers accurate performance even at high Doppler. However, it requires that the number of paths to be smaller than the inserted pilot symbols in each OFDM time slot. Moreover, it was derived in the single-input single-output (SISO) case and its extension to single-input multiple-output (SIMO) systems has never been addressed.

Under the NDA category, time-varying channel estimation was also investigated in [14]. The authors used the discrete Legendre polynomial BEM along with the space alternating generalized expectation maximization (EM)-maximum a posteriori probability (SAGE-MAP) technique to estimate the time-domain channel coefficients of OFDM channels. In [15], we used EM to estimate the channel gains over a SISO configuration. However, both techniques have been tailored for multi-carrier SISO systems and, hence, do not exploit the potential diversity gain achievable by multi-antenna systems. Moreover, they require the number of pilots to be greater than the number of channel paths. In [16], the instantaneous SNR estimation problem was investigated using the EM approach, yet still over SISO configurations only. In [17] and [18], both the EM and LS techniques were again leveraged, respectively, to estimate the SNR over single-carrier SIMO systems. In [19],[20], iterative channel estimation with Kalman filtering and QR detection was first investigated under SISO multi-carrier channels and later generalized to multiple-input multiple-output (MIMO) OFDM systems. Its performance was further enhanced in [21] by exploiting the statistics of the channel estimation errors in an iterative estimation process. However, Kalman filter-based techniques require perfect knowledge of the Doppler as well as the power-delay profile. Moreover,

a high number of pilots per OFDM block is needed to obtain accurate estimates thereby affecting the overall throughput of the system.

In this paper, we develop an iterative EM-based maximum likelihood (ML) estimator of fast time-varying channels over SIMO OFDM-type radio interfaces. By relying on the polynomial approximation of the multipath channel gains [2] and resorting to the powerful EM technique [22] instead of the LS approach, our solution offers a more accurate ML-type acquisition of the polynomial expansion coefficients and the resulting time-varying channel gains. To avoid local convergence that is inherent to iterative algorithms, we initialize the EM algorithm with a SIMO DA ML version developed in this work for that sole purpose. We show that the latter boils down to applying SISO DA LS in [2] over each receive antenna. Besides, coming back to our key contribution here, our new SIMO NDA ML-EM solution, it yields as a byproduct MAP-based soft estimates of the unknown symbols. The latter are leveraged to devise a dedicated ICI cancellation (ICIC) scheme that works side by side with the EM-based time-varying estimator according to the turbo principle (e.g., see [8]). Furthermore, we introduce an alternative SIMO regularized DA ML (RDM) initialization procedure that can still apply when the number of paths exceeds the number of available pilot observations. This desirable feature renders the proposed solution robust to any rapid variations in the propagation environment where the number of paths can change unpredictability due the motion of mobile users. Hence we investigate the possibility of reducing the number of pilots in each OFDM block down below the number of channel paths without significantly affecting the performance. By doing so, we are able to reduce the overhead and eventually increase the throughput quite significantly.

The rest of the paper is organized as follows: In Section 4.2, we introduce the system model. In Section 4.3, we derive a new NDA EM-based ML solution for the underlying estimation problem. In Section 4.4, we develop a new DA ML version of this estimator over fast SIMO OFDM channels and demonstrate that it amounts to applying the SISO DA LS estimator in [2] separately over each receive antenna. The latter is only run for the initialization of our NDA ML-EM solution at relatively rare pilot insertion instants, resulting in the ultimately proposed new hybrid ML-EM estimator of fast time-varying OFDM channels. In Section 4.5, we use exhaustive computer simulations to assess and confirm the superior performance of the proposed channel estimator not only in terms of component-level channel identification accuracy, but also in terms of much more compelling yet rarely adopted link-level throughput. Finally, we draw out some concluding remarks in Section 4.6.

The notations adopted in this paper are as follows. Vectors and matrices are represented in

lower- and upper-case bold fonts, respectively. Moreover, $\{\cdot\}^T$ and $\{\cdot\}^H$ denote the conjugate and Hermitian (i.e., transpose conjugate) operators. The Euclidean norm of any vector is denoted as $\|\cdot\|$. For any matrix \mathbf{X} , $[\mathbf{X}]_q$ and $[\mathbf{X}]_{l,k}$ denote its q^{th} column and $(l, k)^{\text{th}}$ entry, respectively. For any vector \mathbf{x} , $\text{diag}\{\mathbf{x}\}$ refers to the diagonal matrix whose elements are those of \mathbf{x} . Moreover, $\{\cdot\}^*$, $\angle\{\cdot\}$, and $|\cdot|$ return the conjugate, angle, and modulus of any complex number, respectively. Finally, $\mathbb{E}\{\cdot\}$ stands for the statistical expectation, j is the pure imaginary number (i.e., $j^2 = -1$), and the notation \triangleq is used for definitions.

4.2 System model

Consider a SIMO OFDM system with N_r receiving antenna elements, N subcarriers, and a cyclic prefix (CP) of a length N_{cp} . The wireless link between the transmitter and the $\{r^{\text{th}}\}_{r=1}^{N_r}$ antennas is modeled as a multipath fading channel as follows:

$$h_r(t, \tau) = \sum_{l=1}^{L_r} \alpha_{l,r}(t) \delta(\tau - \tau_{l,r} T_s), \quad (4.1)$$

where L_r is the number of paths of the r^{th} wireless link. For each path, the delay $\tau_{l,r}$ is normalized by the sampling period T_s and the complex gain $\alpha_{l,r}(t)$ is modeled by a Rayleigh random variable with zero mean and a variance $\sigma_{l,r}^2$. The multipath power profile (i.e., the channel) is assumed to be normalized (i.e., $\sum_{l=1}^{L_r} \sigma_{l,r}^2 = 1$). For each of the N_r links, we approximate the sampled complex gain of the l^{th} path within the duration of N_c consecutive OFDM blocks, $\boldsymbol{\alpha}_{l,r} = [\alpha_{l,r}(-N_{cp}T_s), \dots, \alpha_{l,r}(N_b N_c - N_{cp} - 1)]^T$, by a polynomial of order $N_c - 1$ as follows [2]:

$$\alpha_{l,r}(pT_s) \approx \sum_{d=1}^{N_c} c_{d,l,r} p^{(d-1)} + \zeta_{l,r}[p], \quad (4.2)$$

where $p \in [-N_{cp}, -N_{cp} + 1, \dots, N_b N_c - N_{cp} - 1]$. Moreover, $\mathbf{c}_{l,r} = [c_{1,l,r}, c_{2,l,r}, \dots, c_{N_c,l,r}]^T$ gathers the approximating polynomial coefficients corresponding to the l^{th} path between the transmitter and the r^{th} receiving antenna while $\zeta_{l,r}[p]$ is the approximation error. $T = N_b T_s$ denotes the OFDM block duration where $N_b = N + N_{cp}$. At the destination, after removing the CP and applying a N -point fast Fourier transform (FFT), the collected OFDM symbols at each local approximation window of N_c OFDM blocks (i.e., $k = 1, 2, \dots, N_c$), over the r^{th} antenna element, can be written

as follows:

$$\tilde{\mathbf{y}}_{k,r} = \mathbf{H}_{k,r} \mathbf{a}_k + \mathbf{w}_{k,r}, \quad (4.3)$$

where $\tilde{\mathbf{y}}_{k,r} = [y_{k,r}[1], y_{k,r}[2], \dots, y_{k,r}[N]]^T$ is the received k^{th} OFDM block, and $\mathbf{w}_{k,r} = [w_{k,r}[1], w_{k,r}[2], \dots, w_{k,r}[N]]^T$ is the complex white Gaussian noise vector with covariance $\sigma^2 \mathbf{I}_N$ where \mathbf{I}_N is the N -dimensional identity matrix. The N transmitted symbols during the k^{th} OFDM block, $\mathbf{a}_k = [a_k[1], a_k[2], \dots, a_k[N]]^T$, are generated randomly from a M -ary constellation alphabet, denoted \mathcal{C}^M , and are assumed equally likely, i.e., $\{P_r(a_m) = \frac{1}{M}\}_{a_m \in \mathcal{C}^M}$. The $N \times N$ matrix, $\mathbf{H}_{k,r}$, is the channel frequency response whose elements are given by:

$$[\mathbf{H}_{k,r}]_{m,n} = \frac{1}{N} \sum_{l=1}^{L_r} \left[e^{-j2\pi(\frac{n-1}{N} - \frac{1}{2})\tau_{l,r}} \sum_{q=0}^{N-1} \alpha_{k,l,r}(qT_s) e^{j2\pi\frac{n-m}{N}q} \right], \quad (4.4)$$

where $\{\alpha_{k,l,r}(qT_s)\}_{q=kN_b}^{kN_b+N-1}$ are the samples corresponding to the l^{th} path within the duration of the k^{th} OFDM block over the r^{th} receiving antenna. As shown in [2], with the above approximation [2], the polynomial coefficients, $\mathbf{c}_{l,r}$ can be obtained using the time average of the channel gain over the effective duration of each OFDM time slot ($\{\bar{\alpha}_{k,l,r} = \frac{1}{N} \sum_{q=kN_b}^{kN_b+N-1} \alpha_{k,l,r}(qT_s)\}_{k=0}^{N_c-1}$) as follows:

$$\mathbf{c}_{l,r} = \mathbf{T}^{-1} \bar{\boldsymbol{\alpha}}_{l,r}, \quad (4.5)$$

where $\bar{\boldsymbol{\alpha}}_{l,r} = [\bar{\alpha}_{1,l,r}, \bar{\alpha}_{2,l,r}, \dots, \bar{\alpha}_{N_c,l,r}]^T$ and \mathbf{T} is a $(N_c \times N_c)$ matrix given by:

$$\mathbf{T} = \begin{pmatrix} 1 & \frac{N-1}{2} & \frac{(N-1)(2N-1)}{6} \\ 1 & \frac{N-1}{2} + N_b & \frac{(N-1)(2N-1)}{6} + (N-1)N_b + N_b^2 \\ 1 & \frac{N-1}{2} + 2N_b & \frac{(N-1)(2N-1)}{6} + 2(N-1)N_b + 4N_b^2 \end{pmatrix}.$$

Using these coefficients, the samples of the complex gain of each channel path over the interval $[-N_{cp}, \dots, N_b N_c - N_{cp} - 1]$, $\mathbf{c}_l = [c_{1,l,r}, c_{2,l,r}, \dots, c_{N_c,l,r}]$, can be obtained as follows:

$$\boldsymbol{\alpha}_{l,r} = \mathbf{S}^T \mathbf{c}_{l,r}, \quad (4.6)$$

where \mathbf{S} is a $(N_c \times N_b N_c)$ matrix whose elements are given by:

$$\left\{ \{[\mathbf{S}]_{d,p'} = (p' - N_{cp} - 1)^{d-1}\}_{p'=1}^{N_b N_c} \right\}_{d=1}^{N_c}. \quad (4.7)$$

The channel gains can be estimated using (4.6) from the channel coefficient estimates whose estimation in (4.5) ultimately requires an estimate for the channel gain time averages vector $\bar{\alpha}_{l,r}$.

In [2], $\bar{\alpha}_{l,r}$ is estimated by SISO DA LS over N_p per-carrier pilot frames inserted in each OFDM block in the case of SISO systems (i.e., $N_r = 1$). Two more processing blocks of i) iterative ICIC and ii) frequency-domain smoothing (to take advantage of the previous $N_c - 1$ estimates of $\{\bar{\alpha}_{k,l,1}\}_{k=0}^{N_c-2}$) then follow to improve estimation accuracy and speed up convergence. However, increasing performance requires a relatively large number of pilot symbols per block. Moreover, the LS solution requires the number of per-carrier pilot frames to be greater than the number of paths at each antenna element.

In the following, we address the problem of estimating $\bar{\alpha}_{l,r}$ in SIMO systems (i.e., $N_r \geq 1$) using all data symbols available at each OFDM block, not only pilots. By doing so, we develop a new ML-type EM solution that is able to significantly improve performance while keeping the same overhead or otherwise reducing it. Accuracy can be further enhanced as in [2] by suppressing the ICI components from the received signal.

4.3 New NDA ML-EM estimator

We start by stacking the received samples at the output of all the antenna elements, $\left\{ \left\{ \left\{ y_{k,r}(n) \right\}_{n=1}^N \right\}_{k=0}^{N_c-1} \right\}_{r=1}^{N_r}$, into vectors $\left\{ \left\{ \mathbf{y}_k(n) = [y_{k,1}(n), y_{k,2}(n), \dots, y_{k,N_r}(n)]^T \right\}_{n=1}^N \right\}_{k=0}^{N_c-1}$. We also define $\bar{\varphi}_k = [\bar{\varphi}_{k,1}^T, \bar{\varphi}_{k,2}^T, \dots, \bar{\varphi}_{k,N_r}^T]$ as the vectors containing all the time averages of the channel gains of all $\{L_r\}_{r=1}^{N_r}$ paths with $\{\bar{\varphi}_{k,r} = [\bar{\alpha}_{k,1}, \bar{\alpha}_{k,2}, \dots, \bar{\alpha}_{k,L_r}]^T\}_{r=1}^{N_r}$. The probability density function (pdf) of the received samples $\left\{ \left\{ \mathbf{y}_k(n) \right\}_{n=1}^N \right\}_{k=0}^{N_c-1}$ conditioned on the transmitted symbol $a_k[n]$ and parametrized by $\psi_k = [\bar{\varphi}_k^T, \sigma^2]^T$, is expressed as follows:

$$p(\mathbf{y}_k(n) | a_k[n] = a_m; \psi_k) = \frac{1}{(2\pi\sigma^2)^{N_r}} \exp \left\{ \frac{-1}{2\sigma^2} \sum_{r=1}^{N_r} |y_{k,r}(n) - a_m [\mathbf{H}_{k,r}]_{n,n}|^2 \right\}, \quad (4.8)$$

where:

$$[\mathbf{H}_{k,r}]_{n,n} = \frac{1}{N} \sum_{l=1}^{L_r} \left[e^{-j2\pi \left(\frac{n-1}{N} - \frac{1}{2} \right) \tau_{l,r}} \sum_{q=0}^{N-1} \alpha_{l,k,r}(qT_s) \right], \quad (4.9)$$

Note that, for the time being, we absorb the effect of the ICI in the additive noise and we also assume that normalized delays, $\{\tau_{l,r}\}_{l=1}^{L_r}$, are perfectly known to the receiver. The n^{th} diagonal

element of the matrix $\mathbf{H}_{k,r}$ in (4.9) can then be written as follows:

$$[\mathbf{H}_{k,r}]_{n,n} = \bar{\varphi}_{k,r}^T \mathbf{F}_{n,r}, \quad (4.10)$$

where $\mathbf{F}_{n,r}$ is a vector containing the elements of the m^{th} row of the $(N \times L_r)$ matrix \mathbf{F}_r which is defined as:

$$[\mathbf{F}_r]_{m,l} = e^{-j2\pi(\frac{m-1}{N}-\frac{1}{2})\tau_{l,r}}. \quad (4.11)$$

By injecting (4.10) back into (4.8), we obtain the following result:

$$p(\mathbf{y}_k(n)|a_k[n] = a_m; \boldsymbol{\psi}_k) = \frac{1}{(2\pi\sigma^2)^{N_r}} \exp\left\{-\frac{1}{2\sigma^2} \sum_{r=1}^{N_r} \left| y_{k,r}(n) - a_m \bar{\varphi}_{k,r}^T \mathbf{F}_{n,r} \right|^2\right\}. \quad (4.12)$$

Now, by averaging (4.12) over the alphabet, the pdf of the received samples can be written as follows:

$$p(\mathbf{y}_k(n); \boldsymbol{\psi}_k) = \sum_{m=1}^M P_r(a_m) p(\mathbf{y}_k(n)|a_k[n] = a_m; \boldsymbol{\psi}_k). \quad (4.13)$$

As mentioned earlier, the transmitted symbols are generated from a normalized M -ary constellation (i.e., PAM, PSK or QAM). It follows that:

$$p(\mathbf{y}_k(n); \boldsymbol{\psi}_k) = \frac{1}{M(2\pi\sigma^2)^{N_r}} \sum_{m=1}^M \exp\left\{-\frac{1}{2\sigma^2} \sum_{r=1}^{N_r} \left| y_{k,r}(n) - a_m \bar{\varphi}_{k,r}^T \mathbf{F}_{n,r} \right|^2\right\}. \quad (4.14)$$

It is obvious at this stage that maximizing (4.14) with respect to $\boldsymbol{\psi}_k$ is analytically intractable. Thus, we will resort to the EM concept to find the maximum of the multidimensional likelihood function (LF). First, we define the log-LF (LLF), $\mathcal{L}(\boldsymbol{\psi}_k|a_k[n] = a_m) \triangleq \ln(p(\mathbf{y}_k(n)|a_k[n] = a_m; \boldsymbol{\psi}_k))$, of $\mathbf{y}_k(n)$ conditioned on the transmitted symbol $a_k[n]$ for the k^{th} OFDM symbol which can be written as:

$$\begin{aligned} \mathcal{L}(\boldsymbol{\psi}_k|a_k[n] = a_m) = & -N_r \ln(2\pi\sigma^2) - \frac{1}{2\sigma^2} \left(\sum_{r=1}^{N_r} |y_{k,r}(n)|^2 \right. \\ & \left. + \left| a_m \bar{\varphi}_{k,r}^T \mathbf{F}_{n,r} \right|^2 - 2\Re\left\{ y_{k,r}(n)^* a_m \bar{\varphi}_{k,r}^T \mathbf{F}_{n,r} \right\} \right). \end{aligned} \quad (4.15)$$

During the “expect step (E-STEP)” of the EM algorithm, we compute the expectation of the LLF in (4.15) over all possible transmitted symbols, $\{a_m\}_{m=1}^M$, using the previous estimates of the underlying unknown parameters. Then, the resulting expectation is maximized with respect to the unknown coefficient $\boldsymbol{\psi}_k$ during the “Maximization step (M-STEP)”. Starting with an initial guess, $\widehat{\boldsymbol{\psi}}_k^{(0)}$, of the channel estimates, the cost function to be maximized during the M-STEP at the i^{th} EM iteration is given by:

$$\mathcal{Q}(\boldsymbol{\psi}_k | \widehat{\boldsymbol{\psi}}_k^{(i-1)}) = \sum_{n=1}^N E_{a_m} \left\{ \mathcal{L}(\boldsymbol{\psi}_k | a_k[n] = a_m) \middle| \mathbf{y}_k(n); \widehat{\boldsymbol{\psi}}_k^{(i-1)} \right\}, \quad (4.16)$$

where $E_{a_m} \{ \cdot \}$ denotes the expectation over all possible transmitted symbols $\{a_m\}_{m=1}^M$ and $\widehat{\boldsymbol{\psi}}_k^{(i-1)} = [\widehat{\boldsymbol{\varphi}}_k^{(i-1)T}, \widehat{\sigma}_k^2]^{(i-1)T}$ contains the estimates of $\boldsymbol{\psi}_k$ and the noise variance at the $(i-1)^{\text{th}}$ EM iteration.

The expression in (4.16) can be further simplified as follows:

$$\mathcal{Q}(\boldsymbol{\psi}_k | \widehat{\boldsymbol{\psi}}_k^{(i-1)}) = -NN_r \ln(2\pi\sigma^2) - \frac{1}{2\sigma^2} \left(\sum_{r=1}^{N_r} Z_{k,r} + \sum_{n=1}^N \gamma_{n,k}^{(i-1)} |\bar{\boldsymbol{\varphi}}_{k,r}^T \mathbf{F}_{n,r}|^2 - 2\beta_{n,k,r}^{(i-1)} \right), \quad (4.17)$$

where¹:

$$Z_{k,r} = \sum_{n=1}^N |y_{k,r}(n)|^2, \quad (4.18)$$

$$\gamma_{n,k}^{(i-1)} = E_{a_m} \left\{ |a_m|^2 | \mathbf{y}_k(n); \widehat{\boldsymbol{\psi}}_k^{(i-1)} \right\}, \quad (4.19)$$

$$\beta_{n,k,r}^{(i-1)} = E_{a_m} \left\{ \Re \left\{ y_{k,r}(n)^* a_m \bar{\boldsymbol{\varphi}}_{k,r}^T \mathbf{F}_{n,r} \right\} | \mathbf{y}_k(n); \widehat{\boldsymbol{\psi}}_k^{(i-1)} \right\}. \quad (4.20)$$

Using the Bayes formula, the a posteriori probability of a_m , $P_{m,n,k}^{(i-1)} = P_r(a_m | \mathbf{y}_k(n); \widehat{\boldsymbol{\psi}}_k^{(i-1)})$, at the $(i-1)^{\text{th}}$ iteration is given by:

$$P_r(a_m | \mathbf{y}_k(n); \widehat{\boldsymbol{\psi}}_k^{(i-1)}) = \frac{P_r(a_m) P(\mathbf{y}_k(n) | a_m; \widehat{\boldsymbol{\psi}}_k^{(i-1)})}{P(\mathbf{y}_k(n); \widehat{\boldsymbol{\psi}}_k^{(i-1)})}. \quad (4.21)$$

Since the transmitted symbols are equiprobable (i.e., $P_r(a_m) = \frac{1}{M}$), we have the following result:

$$P(\mathbf{y}_k(n); \widehat{\boldsymbol{\psi}}_k^{(i-1)}) = \frac{1}{M} \sum_{n=1}^N P(\mathbf{y}_k(n) | a_m; \widehat{\boldsymbol{\psi}}_k^{(i-1)}). \quad (4.22)$$

1. For the particular case of normalized-energy constant-envelope constellations, note that we have $\gamma_{n,k}^{(i-1)} = 1$.

Exploiting the fact that $\bar{\varphi}_{k,r} = \Re\{\bar{\varphi}_{k,r}\} + \Im\{\bar{\varphi}_{k,r}\}$ and $\mathbf{F}_{n,r} = \Re\{\mathbf{F}_{n,r}\} + \Im\{\mathbf{F}_{n,r}\}$, the cost function in (4.17) can be written as follows:

$$\begin{aligned} \mathcal{Q}(\psi_k | \hat{\psi}_k^{(i-1)}) = & -NN_r \ln(2\pi\sigma^2) - \frac{1}{2\sigma^2} \left(\sum_{r=1}^{N_r} Z_{k,r} + \sum_{n=1}^N \gamma_{n,k}^{(i-1)} \right) \\ & \times \left(\mathbf{F}_{n,r}^H \mathbf{G}_{1,k,r} \mathbf{F}_{n,r} + \Im\{\mathbf{F}_{n,r}\}^T \mathbf{G}_{2,k,r} \Re\{\mathbf{F}_{n,r}\} \right. \\ & \left. + \Re\{\mathbf{F}_{n,r}\}^T \mathbf{G}_{3,k,r} \Im\{\mathbf{F}_{n,r}\} \right) - 2 \sum_{m=1}^M P_{m,n,k}^{(i-1)} \eta_{k,n,r}^{(m)}, \end{aligned} \quad (4.23)$$

where:

$$\begin{aligned} \mathbf{G}_{1,k,r} &= \Re\{\bar{\varphi}_{k,r}\} \Re\{\bar{\varphi}_{k,r}\}^T + \Im\{\bar{\varphi}_{k,r}\} \Im\{\bar{\varphi}_{k,r}\}^T, \\ \mathbf{G}_{2,k,r} &= \Re\{\bar{\varphi}_{k,r}\} \Im\{\bar{\varphi}_{k,r}\}^T - \Im\{\bar{\varphi}_{k,r}\} \Re\{\bar{\varphi}_{k,r}\}^T, \\ \mathbf{G}_{3,k,r} &= \Im\{\bar{\varphi}_{k,r}\} \Re\{\bar{\varphi}_{k,r}\}^T - \Re\{\bar{\varphi}_{k,r}\} \Im\{\bar{\varphi}_{k,r}\}^T, \\ \eta_{k,n,r}^{(m)} &= \Re\{y_{k,r}(n)^* a_m \mathbf{F}_{n,r}^T\} \Re\{\bar{\varphi}_{k,r}\} - \Im\{y_{k,r}(n)^* a_m \mathbf{F}_{n,r}^T\} \Im\{\bar{\varphi}_{k,r}\}. \end{aligned} \quad (4.24)$$

As per the M-STEP, we differentiate the cost function in (4.23) with respect to $\Re\{\bar{\varphi}_{k,r}\}$ and $\Im\{\bar{\varphi}_{k,r}\}$ and set the result to zero to obtain the following results:

$$\begin{aligned} \sum_{n=1}^N \gamma_{n,k}^{(i-1)} \left(\mathbf{J}_{1,n,r} \Re\{\bar{\varphi}_{k,r}\} - \mathbf{J}_{2,n,r} \Im\{\bar{\varphi}_{k,r}\} \right) &= \sum_{n=1}^N \boldsymbol{\mu}_{1,n,k,r}, \\ \sum_{n=1}^N \gamma_{n,k}^{(i-1)} \left(\mathbf{J}_{1,n,r} \Im\{\bar{\varphi}_{k,r}\} + \mathbf{J}_{2,n,r} \Re\{\bar{\varphi}_{k,r}\} \right) &= - \sum_{n=1}^N \boldsymbol{\mu}_{2,n,k,r}, \end{aligned}$$

where:

$$\begin{aligned} \mathbf{J}_{1,n,r} &= \Re\{\mathbf{F}_{n,r}\} \Re\{\mathbf{F}_{n,r}\}^T + \Im\{\mathbf{F}_{n,r}\} \Im\{\mathbf{F}_{n,r}\}^T, \\ \mathbf{J}_{2,n,r} &= \Re\{\mathbf{F}_{n,r}\} \Im\{\mathbf{F}_{n,r}\}^T - \Im\{\mathbf{F}_{n,r}\} \Re\{\mathbf{F}_{n,r}\}^T, \\ \boldsymbol{\mu}_{1,n,k,r} &= \sum_{m=1}^M P_{m,n,k}^{(i-1)} \Re\{y_{k,r}(n)^* a_m \mathbf{F}_{n,r}^T\}, \\ \boldsymbol{\mu}_{2,n,k,r} &= \sum_{m=1}^M P_{m,n,k}^{(i-1)} \Im\{y_{k,r}(n)^* a_m \mathbf{F}_{n,r}^T\}. \end{aligned}$$

Now, using the identity $\bar{\varphi}_{k,r} = \Re\{\bar{\varphi}_{k,r}\} + j\Im\{\bar{\varphi}_{k,r}\}$ leads to:

$$\sum_{n=1}^N (\mathbf{J}_{1,n,r} + j\mathbf{J}_{2,n,r}) \gamma_{n,k}^{(i-1)} \bar{\varphi}_{k,r} = \sum_{n=1}^N \boldsymbol{\mu}_{1,n,r} - j\boldsymbol{\mu}_{2,n,r}. \quad (4.25)$$

Hence, the i^{th} EM update for time average of the channel gains at the i^{th} iteration can be obtained as follows:

$$\hat{\varphi}_{k,r}^{(i)} = \left(\sum_{n=1}^N \gamma_{n,k}^{(i-1)} (\mathbf{J}_{1,n,r} + j\mathbf{J}_{2,n,r}) \right)^{-1} \sum_{n=1}^N \left(\sum_{m=1}^M P_{m,n,k}^{(i-1)} y_{k,r}^*(n) a_m \mathbf{F}_{n,r}^T \right)^H. \quad (4.26)$$

Similarly, by differentiating the cost function in (4.23) with respect to σ^2 and setting the result to zero, we obtain the following update for the noise variance:

$$\hat{\sigma}^2^{(i)} = \frac{\sum_{r=1}^{N_r} Z_{k,r} + \sum_{n=1}^N \left| \mathbf{F}_{n,r}^T \hat{\varphi}_{k,r}^{(i-1)} \right|^2 \gamma_{n,k}^{(i-1)} - 2\beta_{n,k,r}^{(i-1)}}{2NN_r}. \quad (4.27)$$

Finally, after \mathcal{I}_{EM} iterations of the EM algorithm, the channel estimates, corresponding to N_c consecutive OFDM symbols over the r^{th} antenna element, are obtained as follows:

$$\hat{\boldsymbol{\alpha}}_{l,r} = \mathbf{S}^T \hat{\mathbf{c}}_{l,r} = \mathbf{S}^T \mathbf{T}^{-1} \hat{\boldsymbol{\alpha}}_{l,r}^{(\mathcal{I}_{\text{EM}})}, \quad (4.28)$$

where $\hat{\boldsymbol{\alpha}}_{l,r}^{(\mathcal{I}_{\text{EM}})} = [\hat{\alpha}_{1,l,r}^{(\mathcal{I}_{\text{EM}})}, \hat{\alpha}_{2,l,r}^{(\mathcal{I}_{\text{EM}})}, \dots, \hat{\alpha}_{N_c,l,r}^{(\mathcal{I}_{\text{EM}})}]^T$ is the EM-based ML vector estimate of the complex channel gain time averages of the l^{th} path over N_c OFDM data symbols. The channel gain estimates in (4.28) can be further improved by implementing an iterative ICIC technique. Indeed, the channel and symbol estimates provided by the EM algorithm can be used to reconstruct then remove the ICI components from the received signal and the resulting samples can be re-injected once again as new inputs to the EM algorithm to enhance accuracy. In this way, the entire process can be repeated \mathcal{I}_{ICI} iterations until no additional improvements can be achieved. ICIC requires decoding the data symbols to be able to reduce the ICI level. Instead of implementing the successive interference cancellation (SIC) at the output of each antenna element as in [2], we make use of the symbols' posteriors, $P_{m,n,k}^{(\mathcal{I}_{\text{EM}})}$, already provided by the EM algorithm and decode the data symbols according to the MAP criterion as follows:

$$\hat{a}_k^{(s)}[n] = \underset{a_m \in \mathcal{C}^M}{\operatorname{argmax}} \left| a_m - \sum_{m'=1}^M P_{m',n,k}^{(\mathcal{I}_{\text{EM}})} a_{m'} \right|^2, \quad (4.29)$$

where $\hat{a}_k^{(s)}[n]$ is the detected symbol corresponding to the n^{th} subcarrier of each k^{th} OFDM block after s ICIC iterations. At each s^{th} ICIC iteration, the detected symbols are used to remove the ICI component from the original received signal so as to provide the EM algorithm with less-ISI-corrupted observations. The later is given by:

$$\tilde{\mathbf{y}}_{k,r}^{(s+1)} = \tilde{\mathbf{y}}_{k,r} - (\hat{\mathbf{H}}_{k,r}^{(s,\mathcal{I}_{EM})} - \text{diag}\{\hat{\mathbf{h}}_{k,r}^{(d,s,\mathcal{I}_{EM})}\})\hat{\mathbf{a}}_k^{(s)}, \quad (4.30)$$

where $\hat{\mathbf{h}}_{k,r}^{(s,\mathcal{I}_{EM})}$ is a vector containing the diagonal elements of $\hat{\mathbf{H}}_{k,r}^{(s,\mathcal{I}_{EM})}$. The latter is the estimate of channel frequency response at the convergence of the EM technique.

4.4 Proposed hybrid ML-EM estimator

Due to its iterative nature, NDA ML-EM requires an initial starting point. One straightforward solution is to settle on a random initial guess. By doing so, the proposed solution preserves its full NDA characteristic. However, with random initialization, the algorithm's convergence to a local minimum becomes extremely high. Hence, we develop a SIMO DA ML version of this estimator for the sole purpose of providing relatively reliable initial values that ensure global convergence of the NDA ML-EM solution. We will show later in this section that this initialization step can be applied at relatively rare pilot insertion instants, giving rise to the ultimately proposed new hybrid ML-EM estimator of fast time-varying OFDM channels.

4.4.1 Initialization with new DA ML

As mentioned above, NDA ML-EM requires a good initial guess in order to return accurate estimates of the channel gains. An intuitive solution for obtaining those initial values is to use the pilot symbols injected at the subcarrier positions $\{p_1, p_2, \dots, p_{N_p}\}$ within each OFDM block. In the SIMO system, the received N_p subcarriers at each OFDM block, $\mathbf{y}_{k,r}^{(p)} = [y_{k,r}(p_1), y_{k,r}(p_2), \dots, y_{k,r}(p_{N_p})]^T$, corresponding to the pilot positions (by neglecting the ICI) are given by:

$$\tilde{\mathbf{y}}_{k,r}^{(p)} = \text{diag}\{\mathbf{a}_k^{(p)}\}\mathbf{h}_{k,r}^{(p)} + \mathbf{w}_{k,r}^{(p)}, \quad (4.31)$$

where $\mathbf{a}_k^{(p)} = [a_k^{(p)}(1), a_k^{(p)}(2), \dots, a_k^{(p)}(N_p)]^T$ are the transmitted pilots within the k^{th} OFDM block. The channel frequency response and noise component corresponding to the pilot indices are given by $\mathbf{h}_{k,r}^{(p)} = [[\mathbf{H}_{k,r}]_{p_1,p_1}, [\mathbf{H}_{k,r}]_{p_2,p_2}, \dots, [\mathbf{H}_{k,r}]_{p_{N_p},p_{N_p}}]^T$ and $\mathbf{w}_{k,r}^{(p)} = [w_{k,r}(p_1), w_{k,r}(p_2), \dots, w_{k,r}(p_{N_p})]^T$, respectively. By stacking the received pilot samples at the output of the antenna elements into vectors, $\{\mathbf{y}_k^{(p)}(p_n) = [y_{k,1}(p_n), y_{k,2}(p_n), \dots, y_{k,N_r}(p_n)]^T\}_{n=1}^{N_p}$, we rewrite (4.31) as follows:

$$\mathbf{y}_k^{(p)} = \mathbf{A}_k^{(p)} \mathbf{F}^{(p)} \bar{\boldsymbol{\varphi}}_k + \mathbf{w}_k^{(p)}, \quad (4.32)$$

where $\mathbf{w}_k^{(p)} = [\mathbf{w}_{k,1}^{(p)T}, \mathbf{w}_{k,2}^{(p)T}, \dots, \mathbf{w}_{k,N_r}^{(p)T}]^T$ and $\mathbf{A}_k^{(p)}$ is a diagonal matrix given by:

$$\mathbf{A}_k^{(p)} = \mathbf{I}_{N_r} \otimes \text{diag}\{\mathbf{a}_k^{(p)}\}. \quad (4.33)$$

The matrix $\mathbf{F}^{(p)}$ is a $(N_r N_p \times L)$ block-diagonal matrix ($L = \sum_{r=1}^{N_r} L_r$) defined as follows:

$$\mathbf{F}^{(p)} = \text{blkdiag}\{\mathbf{F}_1^{(p)}, \mathbf{F}_2^{(p)}, \dots, \mathbf{F}_{N_r}^{(p)}\}. \quad (4.34)$$

in which $\mathbf{F}_r^{(p)}$ contains the rows of the matrices \mathbf{F}_r that corresponds to the pilot symbols' indices (i.e., $\left\{ \{[\mathbf{F}_r^{(p)}]_{m,l} = [\mathbf{F}_r]_{p_m,l}\}_{m=1}^{N_p} \right\}_1^{L_r}$). The pdf in the DA case is given by:

$$p(\mathbf{y}_k^{(p)} | \mathbf{a}_k^{(p)}; \boldsymbol{\psi}_k) = \frac{1}{(2\pi\sigma^2)^{N_r N_p}} \exp\left\{ \frac{-1}{2\sigma^2} \left(\mathbf{y}_k - \mathbf{A}_k^{(p)} \mathbf{F}^{(p)} \bar{\boldsymbol{\varphi}}_k \right)^H \left(\mathbf{y}_k - \mathbf{A}_k^{(p)} \mathbf{F}^{(p)} \bar{\boldsymbol{\varphi}}_k \right) \right\}. \quad (4.35)$$

The corresponding LLF is given by:

$$\mathcal{L}(\boldsymbol{\psi}_k) = -N_r N_p \ln(2\pi\sigma^2) - \frac{1}{2\sigma^2} \left(\mathbf{y}_k - \mathbf{A}_k^{(p)} \mathbf{F}^{(p)} \bar{\boldsymbol{\varphi}}_k \right)^H \left(\mathbf{y}_k - \mathbf{A}_k^{(p)} \mathbf{F}^{(p)} \bar{\boldsymbol{\varphi}}_k \right). \quad (4.36)$$

By differentiating (4.36) with respect to $\bar{\boldsymbol{\varphi}}_k$, we obtain the following initial ML-based DA estimates:

$$\hat{\boldsymbol{\varphi}}_k^{(0)} = \left(\mathbf{F}^{(p)H} \mathbf{A}_k^{(p)H} \mathbf{A}_k^{(p)} \mathbf{F}^{(p)} \right)^{-1} \mathbf{F}^{(p)H} \mathbf{A}_k^{(p)H} \mathbf{y}_k. \quad (4.37)$$

Due to the linearity of the observation model in (4.31) and the Gaussianity of the noise, the new SIMO DA ML estimator reduces in the SISO case to the DA LS estimator in [2], making the former a generalized extension of the latter to SIMO configurations. More importantly, we reveal that the solution in (4.37) requires the inversion of a block-diagonal matrix whose computation can therefore be decoupled across the receive antennas by separately inverting the N_r antenna-specific

blocks $\left\{ \mathbf{F}_r^{(p)H} \text{diag}\{\mathbf{a}_k^{(p)}\} \{\mathbf{a}_k^{(p)}\}^H \mathbf{F}_r^{(p)} \right\}_{r=1}^{N_r}$. Hence, we prove that the SIMO DA ML solution actually boils down to applying the SISO DA LS in [2] at the output of each receive antenna. Another point worth mentioning here is that the number of pilots N_p required to obtain initial estimates has to be larger than the number of paths L_r . The initial estimate of the noise variance can also be obtained by differentiating (4.36) with respect to σ^2 as follows:

$$\widehat{\sigma^2}^{(0)} = \frac{1}{2N_p N_r} \left\| \mathbf{y}_k - \mathbf{A}_k^{(p)} \mathbf{F}^{(p)} \widehat{\boldsymbol{\varphi}}_k^{(0)} \right\|^2. \quad (4.38)$$

4.4.2 Reduction of pilot subcarriers

Usually, the solution in (4.37) requires that $N_p \geq \max\{L_r\}_{r=1}^{N_r}$ otherwise the system of equations is underdetermined and the matrix $\mathbf{F}_r^{(p)H} \text{diag}\{\mathbf{a}_k^{(p)}\} \{\mathbf{a}_k^{(p)}\}^H \mathbf{F}_r^{(p)}$ is no longer invertible. In this case, the overall throughput will be strongly dependant on the number of paths $\max\{L_r\}_{r=1}^{N_r}$. Now since the ML-EM solution relies on those estimates only to trigger the iteration process, we can settle for less reliable initial estimates by reducing the number of pilots per OFDM blocks. Taking into account the fact that the SIMO DA ML solution in (4.37) corresponds to an ill-posed problem, we opt for a regularization technique to solve this problem. One attracting solution is the Tikhonov regularization [78] which allows us to obtain the initial estimates as follows:

$$\widehat{\boldsymbol{\varphi}}_k^{(0)} = \left(\mathbf{F}^{(p)H} \mathbf{A}_k^{(p)H} \mathbf{A}_k^{(p)} \mathbf{F}^{(p)} + \lambda \mathbf{I}_L \right)^{-1} \mathbf{F}^{(p)H} \mathbf{A}_k^{(p)H} \mathbf{y}_k. \quad (4.39)$$

The factor λ is a regularization factor, when set to zero, the solution in (4.39) becomes equivalent to the one in (4.37). Mainly, the RDM is developed to improve the conditioning of the problem by adding a regularization factor to the non-invertible matrix, $\mathbf{F}_r^{(p)H} \text{diag}\{\mathbf{a}_k^{(p)}\} \{\mathbf{a}_k^{(p)}\}^H \mathbf{F}_r^{(p)}$.

In Fig. 4.1, we show the effect of the regularization factor on the performance of the RDM estimator. On one hand, if chosen too small (i.e., $\lambda = 10e^{-16}$), the solution in (4.39) is close to the original one given in (4.37). At this point, the RDM may suffer from the same instability issues as the original DA ML solution. On the other hand, if chosen too large (i.e., $\lambda = 4$), the provided solution will start moving away from the original problem defined in (4.35). It is worth mentioning that the range of values over which RDM provides acceptable initial values is conveniently large. Hence, an exhaustive search for the optimal regularization factor is not required. Note also that other regularization techniques can be envisioned such as the least absolute shrinkage and selection

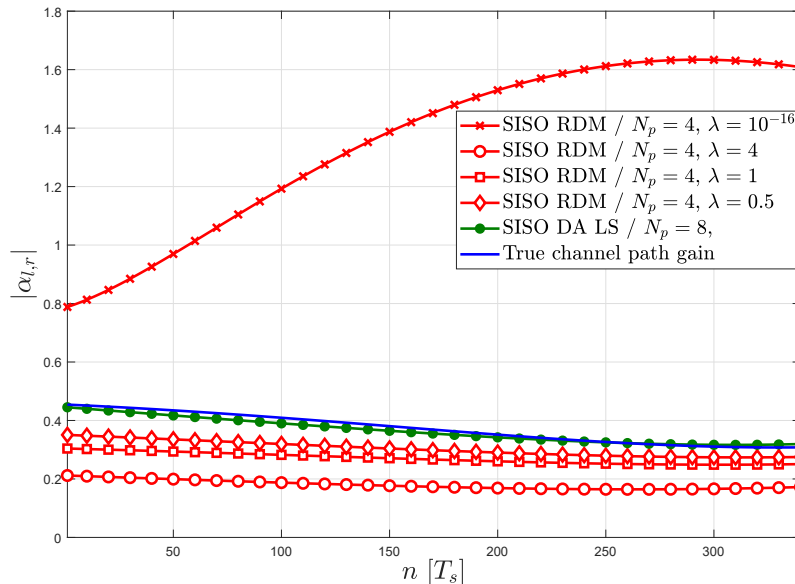


Figure 4.1 – Channel path gain estimates versus time index over the first $N_c = 3$ OFDM blocks with the SISO DA LS (8 pilots) and SISO RDM (4 pilots) initialization techniques at $SNR = 30$ dB for $N_r = 1$ and multiple values of λ .

operator (LASSO) technique [79]. However, the latter, unavailable in a closed-form solution, is usually found using optimization methods such as quadratic programming or convex optimization. Such solution introduces additional computational complexity whereas the Tikhonov regularization keeps the computational burden approximately the same of the original SIMO DA ML.

4.4.3 Extreme slow-up of pilot insertion rate

As mentioned earlier, an initial guess is always required to trigger NDA ML-EM. However, depending on the receiver mobility, the EM technique may use the estimates of the previous OFDM block channel gains as initial candidates for the current one. In the following, we discuss the possibility of reducing the total number of per-carrier pilot frames and, hence, the overhead to achieve higher per-carrier throughput. As depicted in Fig. 4.2, we show an example of pilots insertion and processing tasks for all possible channel estimation techniques. In the DA case, i.e., Fig.4.2 (a), the estimation relies on known per-carrier pilot frames at the receiver side. In this configuration, the DA techniques provide better estimation performance at the expense of significant overhead. Indeed, some subcarriers at each OFDM block are used as pilots for estimation purposes while $(N - N_p)$ remaining ones carry the useful data. Such approach relies on a trade-off between overhead and es-

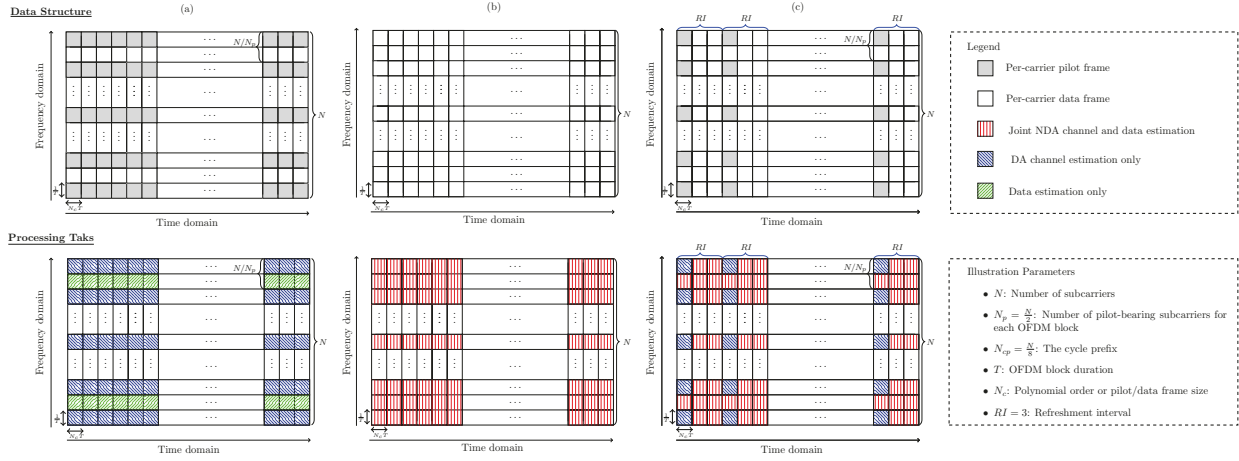


Figure 4.2 – Data structure and processing tasks for different estimation approaches: (a) SISO DA LS [2] or its proposed SIMO DA ML extension, (b) the new NDA ML-EM, and (c) the advocated new hybrid ML-EM solution (i.e., combines both new NDA ML-EM and DA ML versions).

timation performance since the estimation accuracy increases with the number of pilots. In the full NDA case, i.e., Fig.4.2 (b), the estimation technique uses only the per-carrier data frames to estimate the channel gains. Such technique enjoys zero overhead but suffers from performance degradation especially in high mobility scenarios. With the new hybrid ML-EM, i.e., Fig.4.2 (c), the initialization technique (SIMO DA ML or its SIMO RDM equivalent at a low number of pilot subcarriers) is performed only once each RI consecutive N_c OFDM blocks to trigger the NDA estimation process. Since the channel, even a fast time-varying one, varies relatively slowly with respect to the high sampling or processing rates that characterize new radio access technologies, more so at low and moderate mobilities, there is no need for frequent initialization at each N_c OFDM blocks. Instead, the EM technique relies on the same estimates provided by NDA ML-EM during the previous N_c OFDM blocks. In other words, the first N_c OFDM blocks of a sequence of $RI N_c$ blocks will be initialized using the DA LS technique. And each of the remaining $(RI - 1) N_c$ OFDM blocks will be initialized with the channel gain estimates of their predecessors. Thus, the number of inserted pilots can be significantly reduced (by an order or two of magnitude as will be shown later).

Note that the choice of RI , called hereafter as the refreshment interval, might vary depending on some key parameters. Indeed, from an estimation accuracy point of view, RI depends mainly on the Doppler frequency and the average per-carrier SNR. From a per-carrier throughput point of view, performance deterioration is expected at higher RI values in high mobility scenarios. However, such deterioration can have a negligible impact if not any, on decoding performance. Indeed, with the adoption of adaptive modulation, QPSK is adopted at low per-carrier SNR values since it is more

robust to estimation errors. At high per-carrier SNR values, the estimation error is less severe and higher modulation orders can be considered since they perform well even with low pilot numbers.

By taking into account all the features mentioned above, the hybrid channel estimation technique can be summarized in Algorithm 1. Note that the “*initialization*” condition mentioned in

Algorithm 1 Joint hybrid ML-EM channel and data estimation

```

for  $k = 1$  to  $N_c$  do
    if initialization then
        if  $N_p \geq \max\{L_r\}_{r=1}^{N_r}$  then
            Estimate  $\hat{\varphi}_k^{(0)}$  using (4.37)
        else
            Estimate  $\hat{\varphi}_k^{(0)}$  using (4.39)
        end if
    else
        Use  $\hat{\varphi}_k^{(k-1)}$  as initial guess
    end if
    Estimate  $\hat{\sigma}^2^{(0)}$  using (4.38)
end for
while  $s < \mathcal{I}_{ICI}$  do
    for  $k = 1$  to  $N_c$  do
        while  $i < \mathcal{I}_{EM}$  do
            Estimate  $\hat{\varphi}_k^{(i)}$  using (4.26)
            Estimate the noise variance  $\hat{\sigma}^2^{(i)}$  using (4.27)
        end while
        Decode the data  $\hat{\mathbf{a}}_k$  using (4.29)
    end for
    Construct the channel frequency response using  $\{\hat{\alpha}_{l,r}^{(\mathcal{I}_{EM})}\}_{l=1}^{L_r}$  as in (4.4)
    Remove the ICI component using  $\{\hat{\mathbf{a}}_k\}_{k=1}^{N_c}$  as in (4.30)
end while

```

Algorithm 1 controls the rate at which the SIMO RDM is run during the initialization phase.

4.5 Simulation results

In this section, we assess the performance of the new EM-based ML time varying channel estimator *i*) at the component level in terms of the mean square error (MSE) of the channel gains (averaged over all antennas), and *ii*) in terms of link-level bit error rate (BER) and per-carrier throughput. In all simulations, we consider a SIMO OFDM RIT with $N = 128$ subcarriers, a cyclic prefix $N_{cp} = 16$, and a central frequency $f_c = 5$ GHz. The sampling period is $T_s = 0.5 \mu s$.

The channel between the transmitter and each r^{th} antenna element is modeled by a multipath Rayleigh fading channel where the individual complex path gains, $\{\alpha_{l,r}(t)\}_{l=1}^{L_r}$, follow a uniform Jake's model. We assume, without loss of generality, that the links between the source and the N_r receiving antennas have the same channel parameters used in [2] listed in Table 4.1. Unless specified otherwise, the initialization step is executed at each OFDM block (i.e., $RI = 1$).

Table 4.1 – Channel parameters

Path Number	1	2	3	4	5	6
Average Power [dB]	-7.219	-4.219	-6.219	-10.219	-12.219	-14.219
Normalized Delay	0	0.4	1	3.2	4.6	10

We start by investigating the effect of the number of EM iterations on the estimation accuracy. To do so, we plot in Fig. 4.3 the MSE of our proposed estimator (referred to hereafter as hybrid ML-EM) along with the MSE lower bound (LB) derived in [2] against R_{EM} at two different per-carrier SNR levels and high Doppler (i.e., $F_D T = 0.1$). The latter translates into a receiver speed of $v = 300$ km/h ($v = \frac{F_D v_c}{f_c}$, v_c being the speed of light).

Obviously, at a fixed per-carrier SNR level, the convergence rate of the hybrid ML-EM technique (\mathcal{I}_{EM}) is affected by the ICI level corrupting the received samples. In fact, the EM technique is able to converge much faster when the ICI level is reduced with an ICIC technique. For instance, when using QPSK modulation, ML-EM is able to provide the same accuracy either with 1 or 5 EM iterations when ICIC is applied. However, for high modulation order (i.g., 64-QAM) that are usually more sensitive to ICI component, the same technique requires at least 3 EM iterations to converge when ICIC is not implemented.

In Fig. 4.4, we investigate the influence of the number of receiving antenna elements on the estimation performance. We compare the hybrid ML-EM estimator to the DA LS technique and the LB both derived in [2] in the SISO case and to the generalized DA ML versions proposed here in the SIMO case. We observe a clear advantage of hybrid ML-EM at both low (i.e., $F_D T = 0.02$ or equivalently $v = 60$ km/h) and high (i.e., $F_D T = 0.01$ or $v = 300$ km/h) Dopplers even in the SISO case. As the number of antenna elements increases, hybrid ML-EM exhibits a better estimation accuracy especially at low and medium per-carrier SNR levels. Since hybrid ML-EM takes advantage of the diversity gain of multi-antenna systems, it is able to improve the channel estimates per-antenna. Moreover, the noise variance estimate in (4.27), provided by hybrid ML-EM is a more accurate as it is averaged over many antenna branches. At high per-carrier SNR, however,

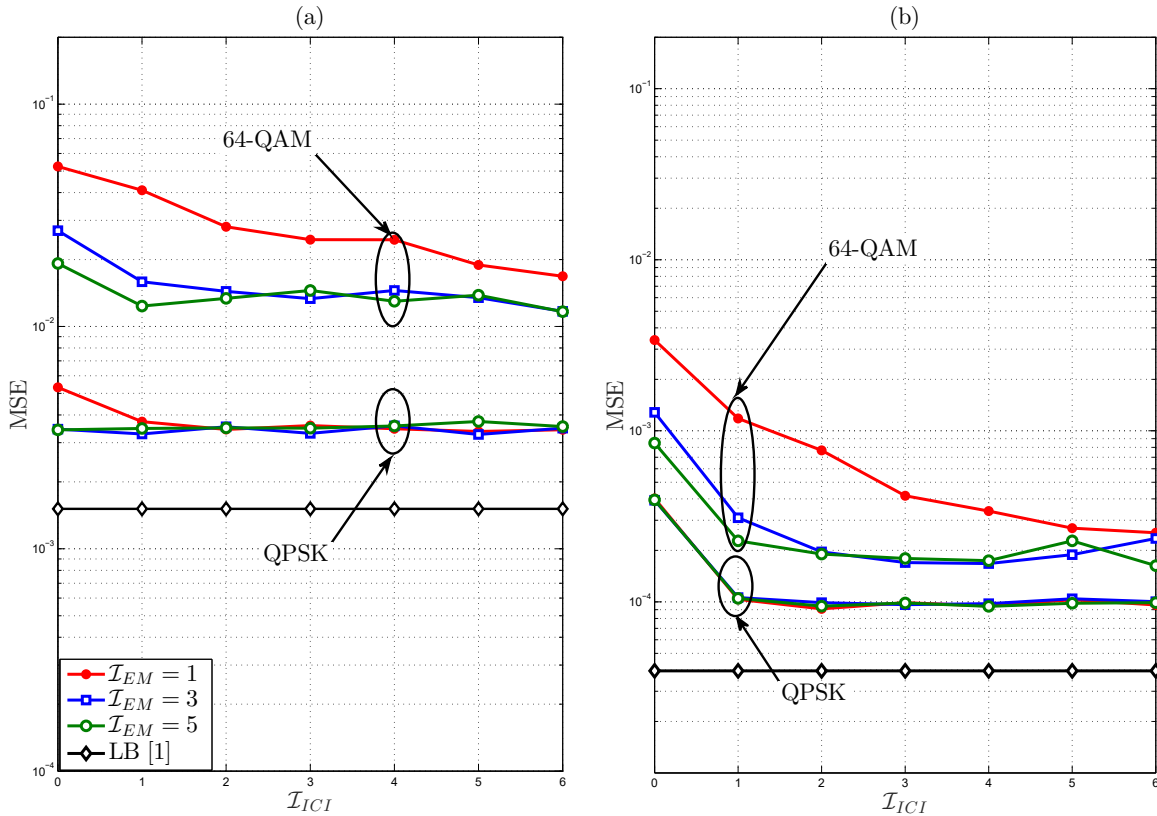


Figure 4.3 – MSE of the advocated new hybrid ML-EM vs the number of ICIC iterations for QPSK and 64-QAM modulations with $v = 300$ km/h, $N_c = 3$, $N_r = 2$, and $N_p = 8$ at: (a) $SNR = 10$ dB, and (b) $SNR = 30$ dB.

we observe that increasing the number of antennas has almost no effect on the estimation accuracy performance. This is due to the noise level being lower than the ICI components. At such per-carrier SNR levels, the channel estimation accuracy is dictated mainly by ICIC capabilities of the proposed design.

In Fig. 4.5, we evaluate the performance of the proposed technique at low and high mobilities against the DA LS technique and the LB both derived in [2] in the SISO case and to the generalized DA ML versions proposed here in the SIMO case. We observe a clear advantage of the hybrid ML-EM technique at both low and high Dopplers. We also observe that the ICIC block enhances the performance of both techniques. However, hybrid ML-EM benefits from much larger gains and approaches the LB at high per-carrier SNR values. Moreover, we notice that the ICIC block provides enhanced performances only at high per-carrier SNR values. This behavior stems from the fact that noise level at low and medium SNRs is much higher than the ICI component. Hence, the estimator performance is dictated by the noise level. At high per-carrier SNR, the ICI level becomes

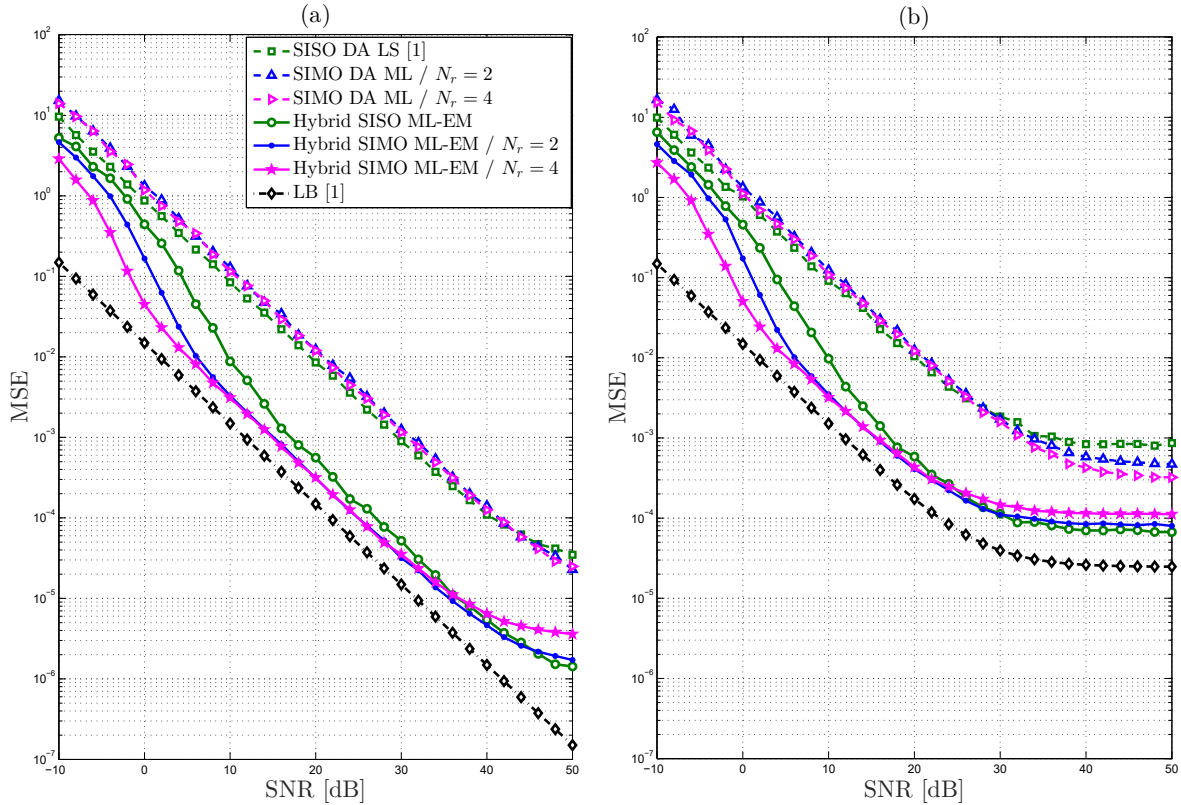


Figure 4.4 – MSE of the advocated new hybrid ML-EM, the SISO DA LS in [2] (i.e., $N_r = 1$), and its proposed SIMO DA ML extension vs. the per-carrier SNR for different numbers of receiving antennas with QPSK, $N_c = 3$ and $N_p = 8$ at: (a) $v = 60$ km/h, and (b) $v = 300$ km/h.

comparable to the noise level it follows that more ICIC iterations are required to provide better estimation accuracy.

In Fig. 4.6, we investigate the effect of the refreshment interval RI on the estimation accuracy of the proposed technique at low and high mobilities. At low Doppler (i.e., at velocity $v = 60$ km/h), the hybrid ML-EM technique exhibits the same performance when initialized with DA ML at each OFDM block (i.e., $RI = 1$) or with less recurrent initialization (i.e., $RI = 20$). However, at high Doppler (i.e., at velocity $v = 600$ km/h), we observe a significant deterioration when hybrid ML-EM is initialized at the rates of 5 or 20. This is hardly surprising because the channel varies slowly at low Doppler and the estimates provided during the previous N_c OFDM blocks become adequate initial guesses for the current N_c blocks. At high Doppler, however, the channel varies rapidly in time and the estimates of the previous blocks can no longer be considered as good candidates to trigger the estimation process during the following blocks.

In Fig. 4.7, we investigate the impact of the regularization factor λ in initialization with SIMO

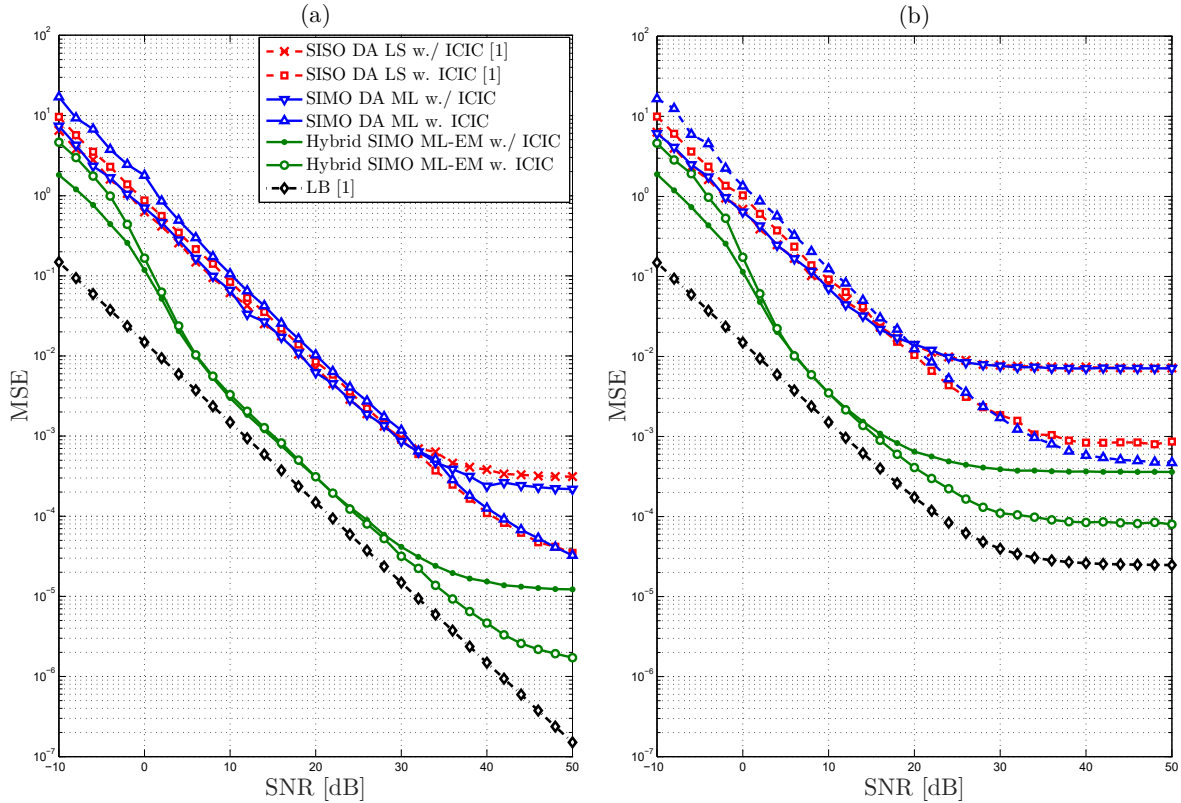


Figure 4.5 – MSE of the advocated new hybrid ML-EM, the SISO DA LS in [2] (i.e., $N_r = 1$), and its proposed SIMO DA ML extension vs. the per-carrier SNR with QPSK, $N_c = 3$, $N_r = 2$, and $N_p = 8$ at: (a) $v = 60$ km/h, and (b) $v = 300$ km/h.

RDM on the performance of the proposed hybrid ML-EM technique. With an arbitrarily small regularization factor (i.e., $\lambda = 10^{-16}$), its performance deteriorates since its initialization with SIMO RDM suffers from the same instability issues of the SISO DA LS technique in [2] or its proposed SIMO DA ML extension. By increasing λ , its performance improves and approaches the estimation accuracy achieved with $N_p = 8$ pilot tones. The latter corresponds to an overdetermined problem. However, for higher values of λ , the performance of hybrid ML-EM starts to deteriorate again since the SIMO RDM initialization solution departs significantly from the original one defined in (4.36) and becomes less sensitive to the received samples.

In Fig. 4.8, we assess the robustness of the proposed technique to the number of available per-carrier pilot frames. We see that the gap between the two techniques increases by reducing the number of pilots per OFDM block from $N_p = 16$ to $N_p = 8$, more so at high Dopplers. Indeed, both SISO DA LS in [2] and its proposed SIMO DA ML extension deteriorate in MSE performance by reducing N_p while the advocated hybrid ML-EM exhibits exactly the same performance at medium-

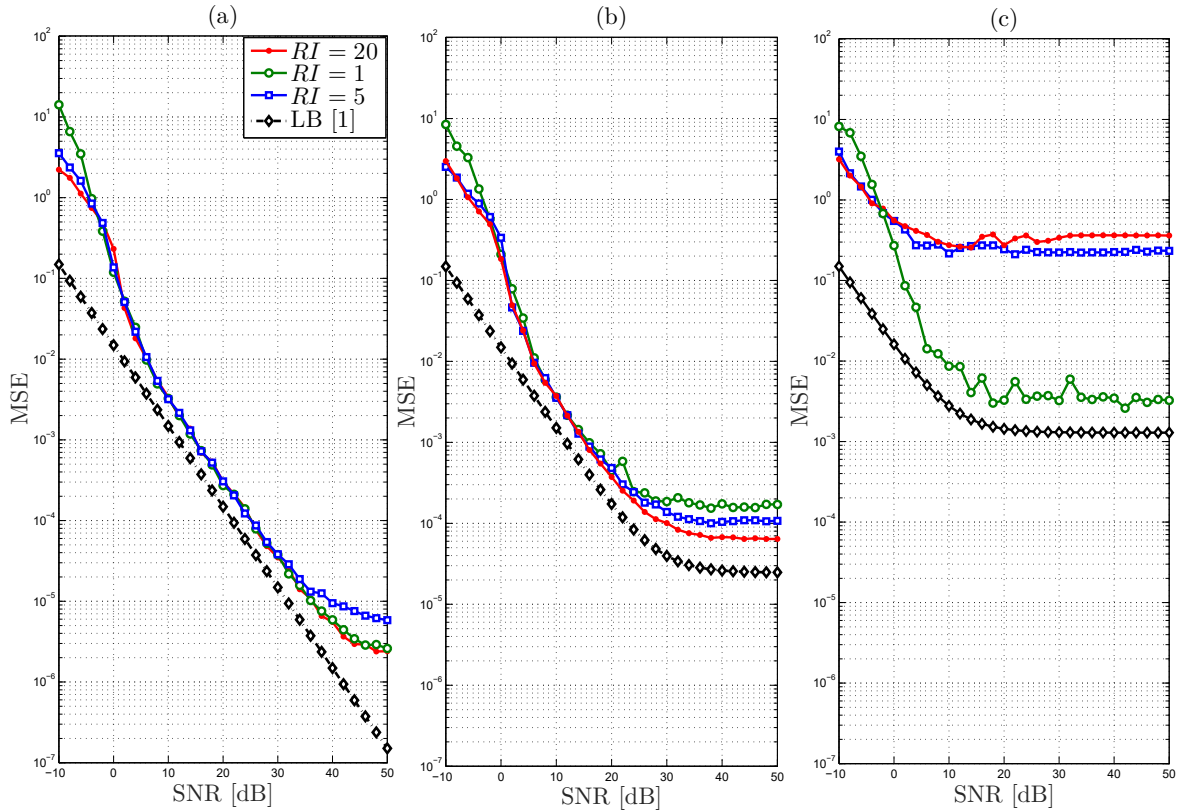


Figure 4.6 – MSE of the advocated new hybrid ML-EM vs. the per-carrier SNR for different values of RI with QPSK, $N_c = 3$, $N_r = 2$, and $N_p = 8$ at: (a) $v = 60$ km/h, (b) $v = 300$ km/h, and (c) $v = 600$ km/h.

to-high per-carrier SNR thresholds. Actually, hybrid ML-EM performs nearly the same in BER² as the proposed SIMO DA ML extension, yet with less pilots. Consequently, the new technique can achieve a higher per-carrier throughput by reducing the overhead by half. The number of pilots can even be further reduced to $N_p = 4$ (up to 75% reduction), below the number of paths. In this configuration, both SISO DA LS in [2] and its proposed SIMO DA ML extension cannot provide reliable estimates. Whereas, the advocated hybrid ML-EM solution still works properly when initialized instead with SIMO RDM. As can be seen in Figs. 4.8 (a) and (c), the new technique exhibits approximately the same MSE performance, except for some negligible deterioration at high SNRs. Yet the latter does not affect the BER performance. Indeed, the proposed hybrid ML-EM performs nearly the same in BER regardless of the different numbers of pilots considered in Figs. 4.8 (b) and (d).

2. In the proposed SIMO DA ML extension and its SIMO RDM variant, we implement maximum ratio combining (MRC) over the N_r antenna branches prior to passing the resulting MRC output through an iterative SIC decoder as in SISO DA LS in [2]. Whereas we implement the MAP decoder in (30) with the advocated hybrid SIMO ML-EM solution or the proposed SIMO NDA ML version.

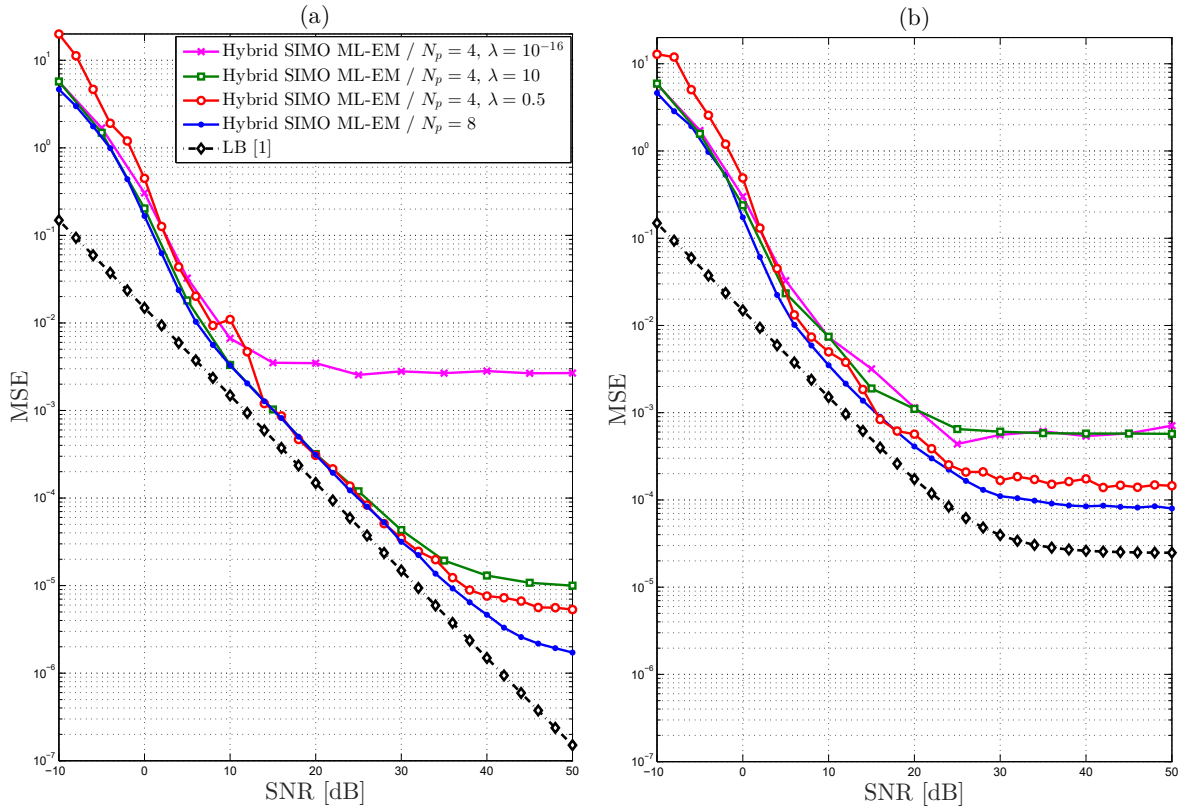


Figure 4.7 – MSE of the advocated new hybrid ML-EM vs. the per-carrier SNR for different regularization factors of RDM at initialization with QPSK, $N_r = 2$, and $N_c = 3$ at: (a) $v = 60$ km/h, and (b) $v = 300$ km/h.

In Fig. 4.9, we plot the link-level per-carrier throughput curves of hybrid ML-EM. For a given modulation order M , please note that the per-carrier throughput can be obtained from the symbol error rate (SER) as follows:

$$\text{Throughput} = \frac{1}{T} \log_2(M)(1 - \text{SER})(1 - \Delta), \quad (4.40)$$

where Δ is the overhead ratio computed as:

$$\Delta = \frac{N_p}{N RI}, \quad (4.41)$$

which becomes negligible at large values of RI . The latter cannot be, however, increased indefinitely as the hybrid ML-EM technique requires more frequent up-to-date initial estimates in the case of high mobility.

We see from Fig. 4.9 (a) that QPSK transmissions, among the considered modulations, provide

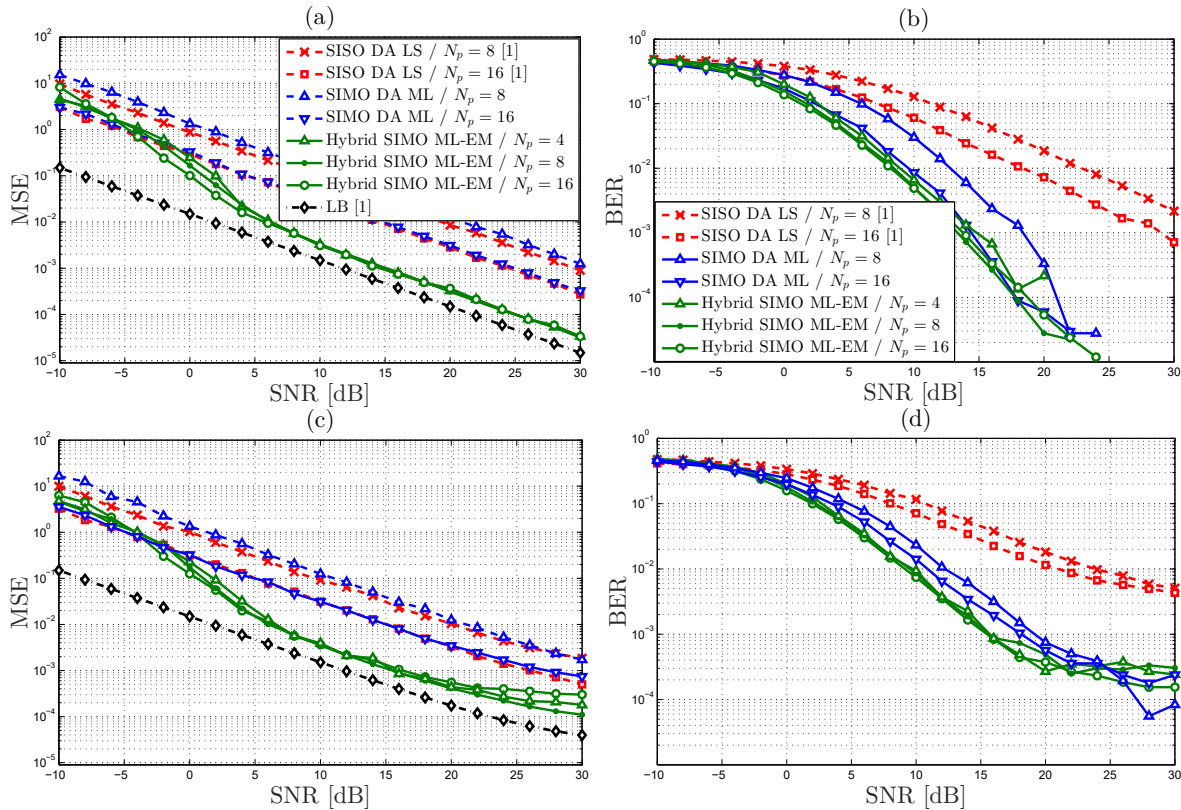


Figure 4.8 – Performance of the advocated new hybrid ML-EM, the SISO DA LS in [2] (i.e., $N_r = 1$), and its proposed SIMO DA ML extension vs. the per-carrier SNR with QPSK, $N_c = 3$ and $N_r = 2$ in terms of: (a) MSE at $v = 60$ km/h, (b) BER at $v = 60$ km/h, (c) MSE at $v = 300$ km/h, and (d) BER at $v = 300$ km/h.

higher per-carrier throughput at per-carrier SNR values below 4 dB. When the per-carrier SNR ranges between 4 and 14 dB, 16-QAM becomes more suitable whereas 64-QAM dominates when the per-carrier SNR exceeds 14 dB. The resulting per-carrier throughput curve assuming an adaptive (i.e., SNR-dependent) modulation is depicted by the black curve. In Fig. 4.9 (b), we show the performance of the hybrid ML-EM technique at a higher normalized Doppler $F_D T = 0.1$. In this scenario, QPSK, 16-QAM, and 64-QAM modulations provide higher per-carrier throughput over the same SNR ranges reported above at low Doppler. We also observe that both 16- and 64-QAM transmissions suffer from some performance degradation when compared to the low mobility scenario. Indeed, at lower Doppler values, the hybrid technique provides accurate estimates since the channel varies slowly during the same period. Hence, the decoder at the destination is able to accurately decode the transmitted symbols. In the case of high mobility, the channel varies rapidly during the same period, leading to a more severe degradation of the channel estimates. The latter affects the decoding process, especially at higher-order modulations which are more sensitive to

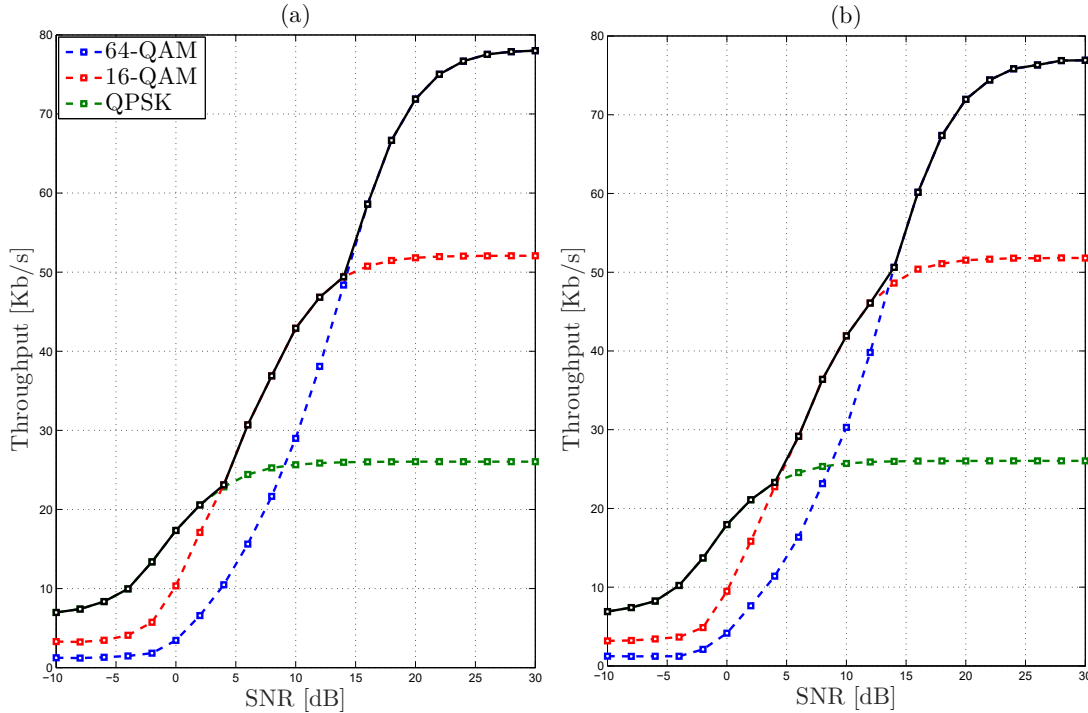


Figure 4.9 – Link-level per-carrier throughput vs. the per-carrier SNR of the advocated new hybrid ML-EM with $N_c = 3$, $N_r = 2$, and $N_p = 8$ at: (a) $v = 60$ km/h, and (b) $v = 300$ km/h.

phase shifts.

In Fig. 4.10, we plot the link-level per-carrier throughput curves of the hybrid ML-EM, the SISO DA in [2], and the proposed SIMO DA ML extension assuming an adaptive (i.e., SNR-dependent) modulation scheme. Here, we report a clear advantage in throughput performance of the hybrid ML-EM technique, especially at higher mobility (i.e., $F_D T = 0.1$) and modulation orders (i.e., 16- and 64-QAM). As reported previously, the SISO DA LS technique in [2] and its proposed SIMO DA ML extension provide less reliable channel estimates since both operate only at pilot symbols. These estimates lead to higher BER when injected later at the data samples in the MRC-SIC decoding process. Moreover, from Fig. 4.10 (b), we observe that the performance of both SISO DA in [2] and its proposed SIMO DA ML extension significantly deteriorates when the number of pilots reduces by half from 16 to 8. Such losses stem from the fact that poor channel gain estimates result in less reliable ICIC, especially at higher modulation orders. Even though the proposed SIMO DA ML extension takes advantage of antenna diversity, it still exhibits the same behaviour as the SISO DA LS original version in [2] since the quality of channel estimates also deteriorates when the number of pilots decreases. On the other hand, the advocated hybrid ML-EM maintains approximately the

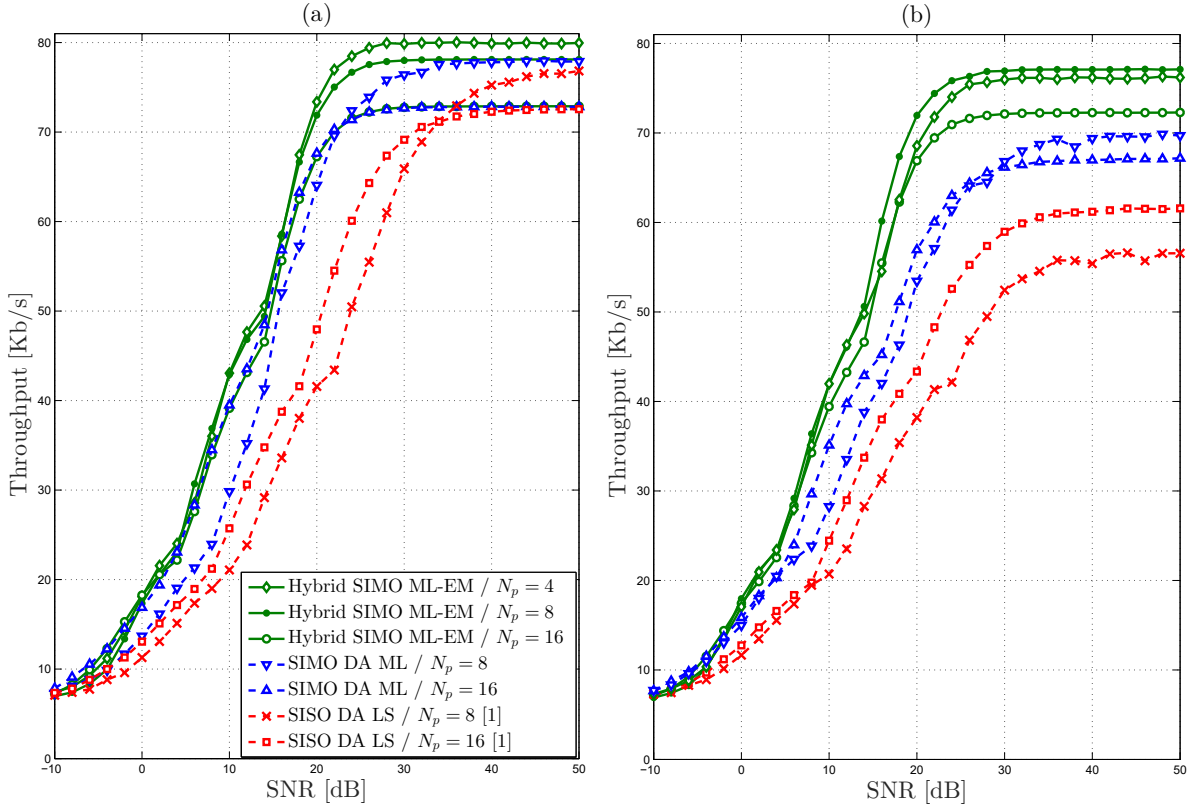


Figure 4.10 – Link-level per-carrier throughput vs. the per-carrier SNR of the advocated new hybrid ML-EM, the SISO DA LS in [2] (i.e., $N_r = 1$), and its proposed SIMO DA ML extension with $N_c = 3$, $N_r = 2$, and $\lambda = 0.5$ at: (a) $v = 60$ km/h, and (b) $v = 300$ km/h.

same performance in terms of MSE whether initialized with $N_p = 4, 8$ or 16 Per-carrier pilot frame. Hence, it exhibits higher link-level per-carrier throughputs, more so at medium or high per-carrier SNR levels, with best performance achieved when $N_p = 4$ pilots.

In Fig. 4.11, we plot the link-level per-carrier throughput curves of the advocated hybrid ML-EM - when operated at multiple refreshment rates - and both SISO DA LS in [2] and its proposed SIMO DA ML extension to assess more thoroughly their robustness to mobility. We see from Figs. 4.11 (a) and (b) that the per-carrier throughput increases with hybrid ML-EM at low to medium Doppler once the refreshment interval RI jumps from 1 to 5 . This is hardly surprising since the channel varies slowly in time and, hence, the channel coefficients of the previous OFDM blocks act as extremely reliable initial guesses for the current OFDM blocks. It follows that the pilot subcarriers are no longer required at the current OFDM blocks and can be used to carry data instead. Pilot insertion rate can be slowed down significantly, by at least as much as 20 times (pilot to data or overhead ratio can become as low as 0.16%), while still reporting some noticeable

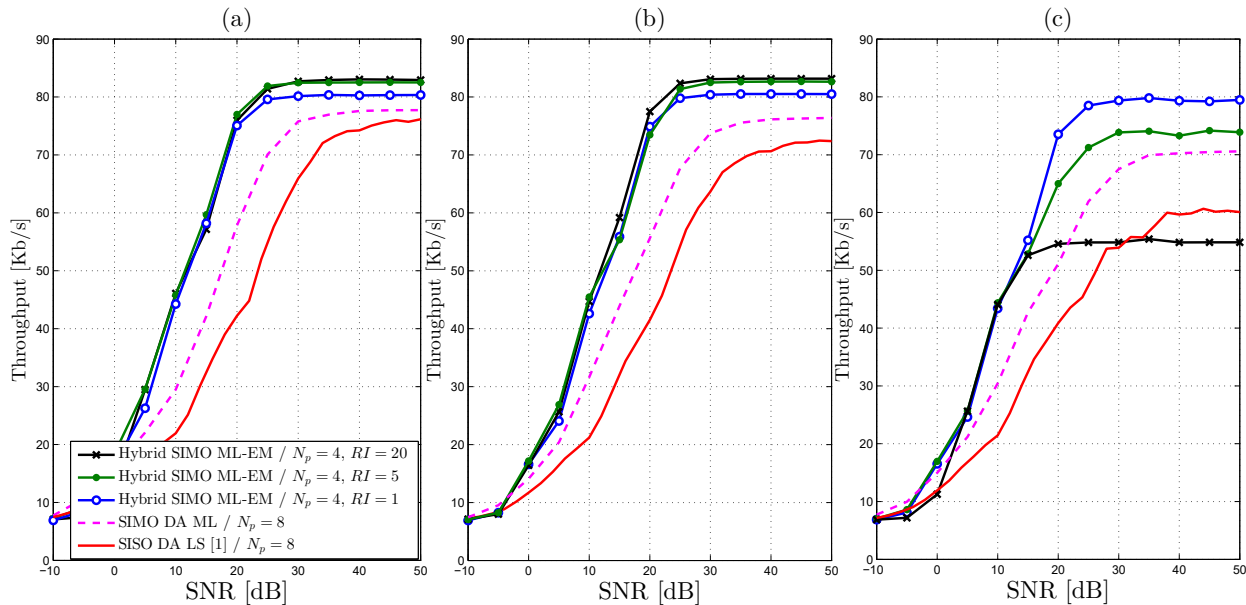


Figure 4.11 – Link-level per-carrier throughput vs. the per-carrier SNR of the advocated new hybrid ML-EM (with $N_p = 4$) at multiple RI values, the SISO DA LS in [2] (i.e., $N_r = 1$), and its proposed SIMO DA ML extension (with $N_p = 8$) with $N_c = 3$, $N_r = 2$, and $\lambda = 0.5$ at: (a) $v = 60$ km/h, (b) $v = 120$ km/h, and (c) $v = 240$ km/h.

throughput gains instead of losses, more so at high per-carrier SNR! Whereas SISO DA LS in [2] and its proposed SIMO DA ML extension still require the same amount of pilots to provide reliable channel estimates. Therefore, no additional throughput gains can be achieved. At high Doppler, however, the channel varies more rapidly and more frequent initialization is needed. As can be observed in Fig. 4.11 (c), we start to measure increasingly significant per-carrier throughput losses as the refreshment interval RI increases. Yet, most importantly, our new hybrid ML-EM technique still outperforms both SISO DA LS in [2] and its proposed SIMO DA ML extension in all considered scenarios, more so over increasingly faster time-varying channels. Here, we have to reduce RI at least from 20 to 5 among three tested values, or ultimately to 1 in order to secure the highest reported gains in throughput achievable among the three RI -dependent scenarios. Actually, one can reach the maximum achievable throughput performance after offline optimization³ of the refreshment interval RI against mobility.

3. To obtain the optimal value of RI , the performance of the new hybrid ML-EM can be evaluated offline in different scenarios over multiple combinations of the average per-carrier SNR, Doppler, and RI values. However, this ad hoc offline optimization step is beyond the scope of this work.

4.6 Conclusion

In this paper, we addressed the problem of time-varying channel estimation over SIMO OFDM transmissions in multipath propagation environments. The proposed approach is based on a polynomial approximation of the complex path gains and takes advantage of all the observation - both at pilot and non-pilot positions - to enhance the channel estimation capabilities. To do so, we develop a new SIMO DA ML estimator - which turns out to be a generalized extension of the SISO DA LS estimator in [2] - for the sole purpose of initializing at relatively rare pilot insertion instants (pilot to data or overhead ratio can be as low as 0.16%) of another new SIMO NDA ML version when operated at the remaining data samples, resulting in the ultimately advocated new hybrid ML-EM estimator of fast time-varying OFDM channels. Moreover, by further developing a new regularized DA ML (RDM) variant of either SISO DA LS in [2] or its proposed SIMO DA ML extension, we were able to further reduce the number of pilots and break the strict requirement of more pilots than paths in [2], and, hence, decrease the overhead and increase the per-carrier throughput. We show through exhaustive simulations that the proposed hybrid ML-EM solution outperforms both SISO DA LS in [2] and its proposed SIMO DA ML extension in terms of component-level channel identification accuracy. The latter translates into significant gains in terms of link-level BER and per-carrier throughput performances, especially at medium-to-high per-carrier SNR values more so at relatively higher Doppler or faster SIMO OFDM channel variations.

Chapitre 5

Multi-Node ML Time and Frequency Synchronization for Distributed MIMO-Relay Beamforming over Time-Varying Flat-Fading Channels

Souheib Ben Amor, Sofène Affes, Faouzi Bellili, Usa Vilaipornsawai, Liqing Zhang, and Peiying Zhu
IEEE Transactions on Communications, vol. 67, no. 4, April 2019.

Abstract

In this chapter, we investigate maximum likelihood (ML) time delay (TD) and carrier frequency offset (CFO) synchronization in multi-node decode-and-forward (DF) cooperative relaying systems operating over time-varying channels (TVCs). This new synchronization scheme is embedded into a distributed multiple input multiple output (MIMO)-relay beamforming transceiver structure to avoid the drawbacks of multidimensional ML estimation at the destination and to minimize the overhead cost. By accounting for a perfect Doppler spread value, the new synchronization solution delivers accurate TD and CFO estimates. For real-world operation, however, this new technique can be jointly implemented with any Doppler spread estimator in a new iterative scheme using a time-constant channel (TCC) based synchronization method at the initialization step. The resulting

TD and CFO estimates along with the channel estimates are then fed into a distributed MIMO-relay beamforming transceiver of K single-antenna nodes, for pre-compensation at each node of the transmitted signals, to ensure constructive maximum ratio combining (MRC) at the destination. Simulation results show significant synchronization accuracy improvement over previous distributed multi-node synchronization techniques assuming TCCs. The latter translates into noticeable gains in terms of useful link-level throughput, more so at higher Doppler or with more relaying nodes.

5.1 Introduction

Spatial diversity is a well-known concept allowing to combat the channel fading and increase the overall throughput of communication systems. Such attracting advantage can be achieved through multiple solutions. Cooperative networks provide a distributed solution that avoids some of the difficulties related to traditional multiple input multiple output (MIMO) systems [23], [24]. Indeed, in many situations, some user equipments are not able to embed multiple antenna sensors due to size and power limitations. As such, users can cooperate with each other to form a virtual antenna array. However, some challenges need to be addressed to ensure constructive cooperation between the relays. One major problem in cooperative relaying systems is multi-node synchronization, both in time and frequency. The latter is crucial for the proper implementation of energy-, spectrum-, and area-efficient distributed MIMO-relay beamforming between a given source-destination link having coverage limitations.

There are two basic approaches to alleviate the effect of time-varying channel (TVC) distortions in time, frequency, phase, and amplitude: the closed-loop and the open-loop compensation procedures. In the closed-loop approach, the destination performs the estimation of all the synchronization parameters along with the channel coefficients. Those estimates are later fed to an equalization block to combat time and frequency asynchronism as proposed in [25],[26]. To their credentials, closed-loop approaches exhibit less overhead as the interaction among the relay nodes is kept to minimal while the destination coordinates the synchronization process. However, it may be difficult for wireless networks without the adequate infrastructure to handle highly-complex multi-dimensional estimation algorithms. In open-loop approaches, however, the source signal to be relayed is shifted in the temporal and frequency domains before transmission, as proposed in [27]. By doing so, we ensure that replicas of the same transmitted signal, originating from different

relay nodes, arrive at the same time and combine constructively at the receiver. In this scenario, less complex estimation algorithms can be considered at the nodes with minimal signaling from the destination.

As far as the estimation of the synchronization parameters is concerned, multiple techniques exist in the open literature [28]. On one hand, the works in [29]-[30] investigate time delay (TD) synchronization while neglecting the carrier frequency offset's (CFO) effect. On the other hand, the solutions introduced in [31]-[32] deal with multiple CFOs while neglecting the TD effect. Other techniques perform joint estimation of all parameters at the destination in closed-loop cooperative networks [25],[33],[34]. Although they could work well in practice, they suffer from high computational complexity since they require solving a multi-dimensional problem that increases with the number of relaying nodes. Moreover, the synchronization task might become very costly in terms of overhead. Indeed, after estimating the TDs and CFOs, the destination node needs to feed them back to the relays. Such a step leads to an additional overhead problem along with quantization errors since the estimated values are quantized before their feedback phase.

Alternative solutions can be considered by relying on distributed collaborative beamforming (DCBF) schemes [35]. Many of these techniques focus on the optimal design of the beamformer's weights while assuming perfect synchronization that leave them extremely vulnerable in practice to phase, frequency, and time offsets. Many other techniques focus on the other hand on combating the misalignment effect at the destination caused by such offsets. In [36], the authors proposed a phase compensation solution based on an iterative bit-feedback approach. In [37], a solution for frequency synchronization in wireless sensor networks (WSN) using a round trip synchronization method was proposed. In [38], a distributed synchronization method was proposed for dense wireless networks using a correlation-based joint TD and CFO estimator. Yet, all the above-mentioned techniques rely on the simplifying time-constant channel (TCC) assumption. In contrast, a broad range of applications require that the terminals act as relaying nodes and, at the same time, fifth-generation (5G) communication systems are expected to support reliable communications at very high velocities reaching 500 Km/h (e.g., in high-speed trains) [39]. For such systems, the conventional TCC assumption leads to severe performance losses. Recently, some other works on DCBF [40], [41] had tackled the challenging problem of multi-node synchronization under TVCs using enhanced versions of one-bit feedback technique. However, they have only addressed phase compensation while assuming perfect TD and CFO estimation.

Motivated by these facts, we develop in this paper a new decentralised maximum likelihood (ML)

synchronization technique along with a distributed MIMO-relay beamforming design that tackles the challenging TVC case over multi-node relaying transmissions. The proposed ML TVC solution builds upon a very useful approximation of the channel covariance matrix by a two-ray propagation model. It provides accurate ML estimates of the TDs and CFOs at a reduced computational cost because it does not require any matrix inversion. We also develop an iterative version, referred to as ML TVC-DE (Doppler estimate), that accounts for the practical need to estimate at each relay node the Doppler spread upon which relies the initial version referred to hereafter as ML TVC-PD (perfect Doppler). Simulation results show significant synchronization accuracy improvement over previous distributed multi-node synchronization techniques assuming TCCs. The latter translates into noticeable gains in terms of useful (i.e., after accounting for incurred overhead) link-level throughput, more so at higher Doppler or with more distributed MIMO-relay beamforming nodes.

The rest of the paper is organized as follows. In Section 5.2, we introduce the system model. In Section 5.3, we derive the new ML solution of the underlying estimation problem. The pre-compensation procedure and its corresponding distributed MIMO-relay design are presented in Section 5.4. In Section 5.5, we run exhaustive computer simulations to assess the performance of the proposed distributed synchronization and MIMO-relay beamforming solution both at the component and link levels in terms of estimation accuracy and throughput, respectively. Finally, we draw out some concluding remarks in Section 5.6.

The notations adopted in this paper are as follows. Vectors and matrices are represented in lower- and upper-case bold fonts, respectively. The shorthand notation $x \sim \mathcal{CN}(m, \sigma^2)$ denotes a complex normal (i.e., Gaussian) distribution with mean m and variance σ^2 . Moreover, $\{\cdot\}^T$ and $\{\cdot\}^H$ denote the conjugate and Hermitian (i.e., transpose conjugate) operators and $\det\{\cdot\}$ returns the determinant of any square matrix. The Euclidean norm of any vector is denoted as $\|\cdot\|$ and \mathbf{I}_N denotes the $(N \times N)$ identity matrix. For any vector \mathbf{x} , $\text{diag}\{\mathbf{x}\}$ refers to the diagonal matrix whose elements are those of \mathbf{x} . For any matrix \mathbf{X} , $[\mathbf{X}]_q$ and $[\mathbf{X}]_{l,k}$ denote its q^{th} column and $(l, k)^{\text{th}}$ entry, respectively. The element-wise product between any two vectors \mathbf{x}_1 and \mathbf{x}_2 is denoted as $\mathbf{x}_1 \odot \mathbf{x}_2$. Moreover, $\{\cdot\}^*$, $\angle\{\cdot\}$, and $|\cdot|$ return the conjugate, angle, and modulus of any complex number, respectively. Finally, $\mathbb{E}\{\cdot\}$ stands for the statistical expectation, j is the imaginary unit (i.e., $j^2 = -1$), and the notation \triangleq is used for definitions.

5.2 System model

Consider a cooperative decode-and-forward (DF) communication system with a source, S , a destination, D , and a MIMO relay of K randomly distributed nodes, R_1, R_2, \dots, R_K , as shown in Fig. 5.1. The K relays are subject to CFOs and TDs due to the presence of different local oscillators. We denote the CFOs of the K relays by $(\bar{\nu}_1, \bar{\nu}_2, \dots, \bar{\nu}_K) \subset [0, \nu_{\max}]^K$ and their respective TDs by $(\bar{\tau}_1, \bar{\tau}_2, \dots, \bar{\tau}_K) \subset [0, \tau_{\max}]^K$. The parameters, ν_{\max} and τ_{\max} , can be set as large as desired within the vicinity of practical CFO and TD values. The true unknown parameters will also carry the

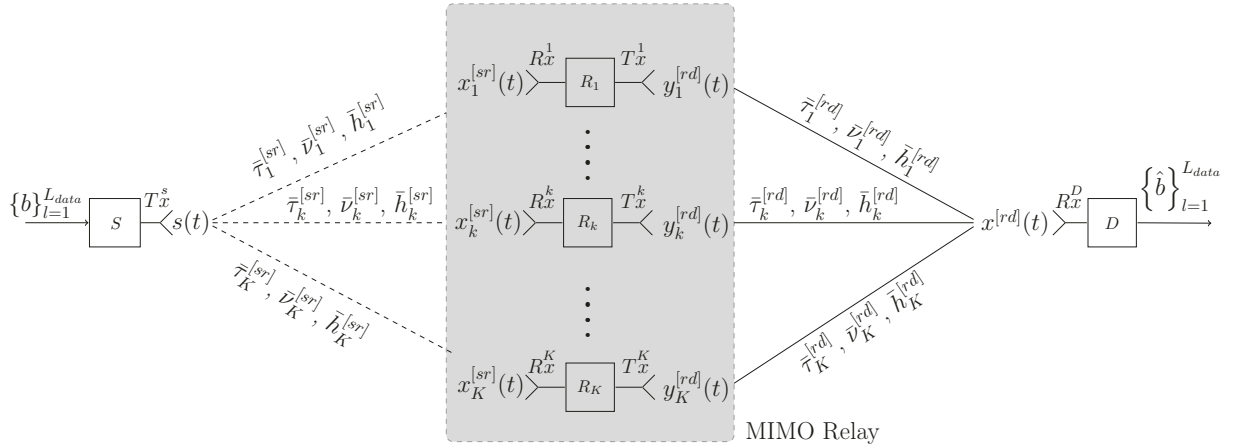


Figure 5.1 – System model for the distributed MIMO-relay beamforming scheme illustrated during the DT (data transmission) cycles.

superscripts $(\cdot)^{[sr]}$ and $(\cdot)^{[rd]}$ to indicate the communication link to which they belong, i.e., S to R_k and R_k to D , respectively. Most importantly, in stark contrast to previous works on multi-node synchronization which have only dealt so far with TCCs, all the nodes and/or the destination are assumed in this work to be mobile, possibly with different velocities. Hence the second-hop's communication link between each relay node R_k and the destination has a TVC characterized by the Doppler spread σ_{D_k} .

During an initial synchronization period, the final destination starts by broadcasting a common training sequence of L symbols, $\mathbf{a}^{[dr]} \triangleq [a^{[dr]}[1], a^{[dr]}[2], \dots, a^{[dr]}[L]]^T$, to all the relays. Hence, every relay node will be able to estimate its own synchronization parameters locally and independently of all others. This approach, in contrast to [25], alleviates the hurdles of estimating closely-spaced TDs and/or CFOs when implemented jointly at the destination. During this pilot transmission (PT)

period, the destination broadcasts the following known signal to all the relays:

$$s^{[dr]}(t) = \sum_{l=0}^{L-1} \mathbf{a}^{[dr]}[l+1]g(t-lT), \quad (5.1)$$

where $g(t)$ is the pulse-shaping function and T is the symbol duration. The continuous-time received signal at the k^{th} relay is given by:

$$x_k^{[dr]}(t) = h_k^{[dr]}(t)s^{[dr]}(t - \hat{\tau}_k^{[dr]})e^{j2\pi\hat{\nu}_k^{[dr]}t} + n_k^{[dr]}(t), \quad (5.2)$$

where $h_k^{[dr]}(t)$ is a flat-fading Rayleigh channel and $n_k^{[dr]}(t)$ is the additive Gaussian noise component assumed to be temporally white. Using its received signal in (5.2), each relay will find the estimates, $\hat{\tau}_k^{[dr]}$ and $\hat{\nu}_k^{[dr]}$, for its channel TD and CFO, $\hat{\tau}_k^{[dr]}$ and $\hat{\nu}_k^{[dr]}$, respectively. The signal in (5.2) is oversampled by a factor $Q = T/T_s$ where T_s is the sampling period. The observation sequence corresponding to the sampling time instants, $\{nT_s\}_{n=0}^{QL-1}$, is given by:

$$x_k^{[dr]}(n) = h_k^{[dr]}(n) \sum_{l=0}^{L-1} \mathbf{a}^{[dr]}[l+1]g(nT_s - lT - \hat{\tau}_k^{[dr]})e^{j2\pi\hat{\nu}_k^{[dr]}\frac{n}{Q}} + n_k^{[dr]}(n), \quad (5.3)$$

where the additive white Gaussian noise is denoted by $n_k^{[dr]}(n) \sim \mathcal{CN}(0, \sigma_{n_k}^2)$. Notice in (5.3) that we keep using the same notation, $\hat{\nu}_k^{[dr]}$, as in (5.2) for the normalized (by T_s) CFO between R_k and D , that is for the sake of simplicity.

In order to rewrite (5.3) in a matrix/vector form, we denote by $\mathbf{x}_k^{[dr]} \triangleq [x_k^{[dr]}(0), x_k^{[dr]}(1), \dots, x_k^{[dr]}(QL-1)]^T$, $\mathbf{h}_k^{[dr]} \triangleq [h_k^{[dr]}(0), h_k^{[dr]}(1), \dots, h_k^{[dr]}(QL-1)]^T$, and $\mathbf{n}_k^{[dr]} \triangleq [n_k^{[dr]}(0), n_k^{[dr]}(1), \dots, n_k^{[dr]}(QL-1)]^T$ the vectors that contain, respectively, the received samples, the channel coefficients, and the noise components. We also introduce the following matrix that is parametrized by the generic TD variable τ :

$$\mathbf{G}(\tau) \triangleq \begin{pmatrix} g(0-T-\tau) & \dots & g(0-LT-\tau) \\ g(T_s-T-\tau) & \dots & g(T_s-LT-\tau) \\ \vdots & \vdots & \vdots \\ g((QL-1)T_s-T-\tau) & \dots & g((QL-1)T_s-LT-\tau) \end{pmatrix}.$$

Starting from (5.3) and resorting to some straightforward algebraic manipulations, it can be shown for $k = 1, 2, \dots, K$ that we have:

$$\mathbf{x}_k^{[dr]} = \mathbf{\Lambda}(\bar{\nu}_k^{[dr]}) \mathbf{\Omega}(\bar{\tau}_k^{[dr]}) \mathbf{h}_k^{[dr]} + \mathbf{n}_k^{[dr]}, \quad (5.4)$$

where:

$$\mathbf{\Omega}(\tau) \triangleq \text{diag}\{\mathbf{G}(\tau) \mathbf{a}^{[dr]}\}, \quad (5.5)$$

$$\mathbf{\Lambda}(\nu) \triangleq \begin{pmatrix} 1 & 0 & \dots & 0 \\ 0 & e^{j2\pi\nu} & 0 & \dots & 0 \\ \vdots & \vdots & \vdots & \vdots & \vdots \\ 0 & \dots & \dots & \dots & e^{j2\pi\nu(QL-1)/Q} \end{pmatrix}. \quad (5.6)$$

For the sake of clarity, we will only focus on the second hop and assume the first hop's estimation and transmission tasks to be ideal. Indeed, as shown in Fig. 5.2, the proposed synchronization algorithm can also be applied at each relay node to obtain the matched filtered samples required to decode the data locally during the data transmission (DT) period. As such, we will drop in (5.4)

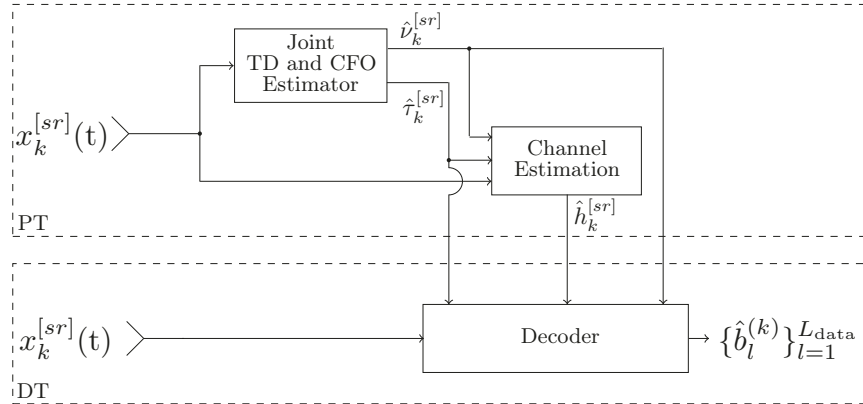


Figure 5.2 – Block diagram of the DF receiver at the k^{th} relay.

and in all the equations of the next section the $[dr]$ superscript thereby leading to:

$$\mathbf{x}_k = \mathbf{\Lambda}(\bar{\nu}_k) \mathbf{\Omega}(\bar{\tau}_k) \mathbf{h}_k + \mathbf{n}_k. \quad (5.7)$$

Yet for the sake of completeness, the entire processing and data signaling structure of the two-hop MIMO-relay beamforming scheme is fully illustrated in Fig. 5.4. And its active building blocks, over the second hop, will be discussed and clarified one by one in the following sections.

5.3 Joint TD and CFO ML estimator

5.3.1 TCC Case

Under the assumption of static channels, all nodes are stationary and as such the Doppler spread is equal to zero. In this case, the system model in (5.7) reduces to:

$$\mathbf{x}_k = h_k \mathbf{\Lambda}(\bar{\nu}_k) \mathbf{G}(\bar{\tau}_k) \mathbf{a} + \mathbf{n}_k, \quad (5.8)$$

where h_k is the channel gain of the communication link between D and R_k . It can be shown that the log-likelihood function (LLF) can be expressed as follows:

$$\mathcal{L}(\nu_k, \tau_k, h_k, \sigma_{n_k}^2) = -\frac{1}{\sigma_{n_k}^2} \|\mathbf{x}_k - h_k \mathbf{\Psi}(\nu_k, \tau_k) \mathbf{a}\|^2 - QL \ln(\pi \sigma_{n_k}^2), \quad (5.9)$$

where

$$\mathbf{\Psi}(\nu_k, \tau_k) = \mathbf{\Lambda}(\nu_k) \mathbf{G}(\tau_k). \quad (5.10)$$

First, we maximize $\mathcal{L}(\nu, \tau, h, \sigma_{n_k}^2)$ with respect to the noise variance. The partial derivative of (5.9) with respect to $\sigma_{n_k}^2$ is given by:

$$\frac{\partial}{\partial \sigma_{n_k}^2} \mathcal{L}(\nu_k, \tau_k, h_k, \sigma_{n_k}^2) = \frac{1}{\sigma_{n_k}^4} \|\mathbf{x}_k - h_k \mathbf{\Psi}(\nu_k, \tau_k) \mathbf{a}\|^2 - \frac{QL}{\sigma_{n_k}^2}.$$

Setting this result to zero and solving for $\sigma_{n_k}^2$ yields the ML estimate for the noise variance:

$$\widehat{\sigma}_{n_k, \text{ML}}^2 = \frac{1}{QL} \|\mathbf{x}_k - h_k \mathbf{\Psi}(\nu_k, \tau_k) \mathbf{a}\|^2, \quad (5.11)$$

which is substituted back in (5.9) to obtain the following ML estimates for the remaining parameters at each relay node:

$$[\hat{\nu}_k, \hat{\tau}_k, \hat{h}_k] = \underset{\nu, \tau, h}{\operatorname{argmin}} \mathcal{L}(\nu, \tau, h), \quad (5.12)$$

where:

$$\mathcal{L}(\nu, \tau, h) = \|\mathbf{x}_k - h\mathbf{\Psi}(\nu, \tau)\mathbf{a}\|^2. \quad (5.13)$$

For any given couple of values for ν and τ , the LLF optimization over h_k reduces to a linear least squares (LS) problem whose solution is given by:

$$\hat{h}_k = \frac{1}{\|\mathbf{\Psi}(\nu, \tau)\mathbf{a}\|^2} \mathbf{a}^H \mathbf{\Psi}(\nu, \tau)^H \mathbf{x}_k. \quad (5.14)$$

By substituting \hat{h}_k for h_k back in (5.13) and after some algebraic manipulations, we obtain the so-called *compressed* LLF (CLLF) which depends solely on ν and τ :

$$\begin{aligned} \mathcal{L}_c(\nu, \tau) &= \frac{1}{\|\mathbf{\Psi}(\nu, \tau)\mathbf{a}\|^2} \mathbf{x}_k^H \mathbf{\Psi}(\nu, \tau)\mathbf{a} \mathbf{a}^H \mathbf{\Psi}(\nu, \tau)^H \mathbf{x}_k. \\ &= \frac{1}{\|\mathbf{\Psi}(\nu, \tau)\mathbf{a}\|^2} \left[\mathbf{a}^H \mathbf{\Psi}^H(\nu, \tau) \mathbf{x}_k \right]^H \left[\mathbf{a}^H \mathbf{\Psi}^H(\nu, \tau) \mathbf{x}_k \right]. \end{aligned} \quad (5.15)$$

Hence, the joint ML estimates of ν_k and τ_k become the solution of the following optimization problem:

$$[\hat{\nu}_k, \hat{\tau}_k] = \underset{\nu, \tau}{\operatorname{argmax}} \mathcal{L}_c(\nu, \tau). \quad (5.16)$$

Moreover, noticing that $\mathbf{a}^H \mathbf{\Psi}^H(\nu, \tau) \mathbf{x}_k$ is a scalar quantity, one can rewrite (5.15) as follows:

$$\mathcal{L}_c(\nu, \tau) = \frac{1}{\|\mathbf{\Psi}(\nu, \tau)\mathbf{a}\|^2} \left| \mathbf{a}^H \mathbf{G}(\tau)^H \mathbf{\Lambda}^H(\nu) \mathbf{x}_k \right|^2. \quad (5.17)$$

Now, we define the vector $\mathbf{v}(\tau) = \mathbf{G}(\tau)\mathbf{a}$ whose elements are obtained by linearly convolving the training sequence, \mathbf{a} , with the delayed shaping pulse $g(t - \tau)$ and then sampling the output at time

instants $\{mT_s\}_{m=0}^{QL-1}$. Therefore, it follows that:

$$\begin{aligned}\mathcal{L}_c(\nu, \tau) &= \frac{1}{\|\mathbf{d}(\nu, \tau)\|^2} |\mathbf{v}(\tau)^H \mathbf{\Lambda}^H(\nu) \mathbf{x}_k|^2 \\ &= \frac{1}{\|\mathbf{d}(\nu, \tau)\|^2} \left| \sum_{m=0}^{QL-1} v_\tau^*[m+1] x_k[m+1] e^{-j2\pi\nu m/Q} \right|^2,\end{aligned}\quad (5.18)$$

where $v_\tau(m)$ is the m^{th} element of the vector $\mathbf{v}(\tau)$. By closely inspecting the expression in (5.18), we observe that the underlying CLLF can be evaluated at each TD candidate value, and all CFO candidate values using fast Fourier transform (FFT) operation.

5.3.2 TVC Case

We start by deriving the LLF that depends on all the unknown parameters observed separately at each relay, i.e., $\nu_k, \tau_k, h_k, \sigma_{n_k}^2$. Since the noise components are assumed to be temporally white and Gaussian distributed, i.e., $\mathbf{n}_k \sim \mathcal{CN}(\mathbf{0}, \sigma_{n_k}^2 \mathbf{I}_{QL})$, each vector \mathbf{x}_k in (5.7) is also Gaussian distributed. Hence, it can be shown that the *actual* LLF at each relay R_k is given by¹:

$$\mathcal{L}(\nu_k, \tau_k, h_k, \sigma_{n_k}^2) = -\ln(\det\{\mathbf{R}_{\mathbf{x}_k \mathbf{x}_k}\}) - \mathbf{x}_k^H \mathbf{R}_{\mathbf{x}_k \mathbf{x}_k}^{-1} \mathbf{x}_k, \quad (5.19)$$

where $\mathbf{R}_{\mathbf{x}_k \mathbf{x}_k} = \mathbb{E}\{\mathbf{x}_k \mathbf{x}_k^H\}$ is the covariance matrix of the zero-mean observation vector \mathbf{x}_k whose expression follows from (5.7) as:

$$\mathbf{R}_{\mathbf{x}_k \mathbf{x}_k} = \mathbf{\Lambda}(\nu_k) \mathbf{\Omega}(\tau_k) \mathbf{R}_{\mathbf{h}_k \mathbf{h}_k} \mathbf{\Omega}(\tau_k)^H \mathbf{\Lambda}(\nu_k)^H + \sigma^2 \mathbf{I}_{QL}, \quad (5.20)$$

where $\mathbf{R}_{\mathbf{h}_k \mathbf{h}_k} = \mathbb{E}\{\mathbf{h}_k \mathbf{h}_k^H\}$. It is obvious that maximizing $\mathcal{L}(\nu_k, \tau_k, h_k, \sigma_{n_k}^2)$ requires the inversion of a large-size ($QL \times QL$) covariance matrix and the computation of its determinant. In the following, we develop a new solution that avoids these costly calculations. Actually, the new solution relies on the two-ray channel approximation² of the covariance matrix of the channel, as described in [80],[81] (please refer to the Appendix in [80] for more details about the underlying second-order Taylor series approximation), which leads to:

$$\mathbf{R}_{\mathbf{h}_k \mathbf{h}_k} \approx \frac{\sigma_{h_k}^2}{2} \mathbf{W} \mathbf{W}^H, \quad (5.21)$$

1. After dropping the constant terms.

2. It is worth mentioning that the two-ray channel approximation holds only when $LF_{D_k} T \ll 1$.

where $\sigma_{h_k}^2$ is channel variance and \mathbf{W} is defined as follows:

$$\mathbf{W} = [\mathbf{w} \ \mathbf{w}^*]. \quad (5.22)$$

The vector \mathbf{w} in (5.22) is given by:

$$\mathbf{w} = \left[1 \ e^{-j\sigma_{D_k} T_s} \ \dots \ e^{-j(QL-1)\sigma_{D_k} T_s} \right]^T.$$

Injecting (5.21) in (5.20) leads to the following overall covariance matrix approximation:

$$\mathbf{R}_{\mathbf{x}_k \mathbf{x}_k} = \frac{\sigma_{h_k}^2}{2} \mathbf{\Lambda}(\nu_k) \mathbf{C}(\tau_k) \mathbf{C}^H(\tau_k) \mathbf{\Lambda}(\nu_k)^H + \sigma_{n_k}^2 \mathbf{I}_{QL}, \quad (5.23)$$

in which the matrix $\mathbf{C}(\tau_k)$ is defined as follows:

$$\mathbf{C}(\tau_k) \triangleq [\mathbf{c}_1(\tau_k) \ \mathbf{c}_2(\tau_k)] = \mathbf{\Omega}(\tau_k) \mathbf{W}. \quad (5.24)$$

To find the inverse of $\mathbf{R}_{\mathbf{x}_k \mathbf{x}_k}$ and its determinant, we start by finding the analytical expressions for the eigenvalues of $\mathbf{C}(\tau_k) \mathbf{C}^H(\tau_k)$ and their corresponding eigenvectors. Clearly, the matrix $\mathbf{C}(\tau_k) \mathbf{C}^H(\tau_k)$ is of rank two (cf. Appendix) and has the same non-zero eigenvalues values as $\mathbf{C}^H(\tau_k) \mathbf{C}(\tau_k)$. Since the latter is a 2×2 matrix, its eigenvalues can be computed analytically. Indeed, it can be shown that:

$$\mathbf{C}^H(\tau_k) \mathbf{C}(\tau_k) = \begin{pmatrix} \alpha(\tau_k) & \varphi(\tau_k) \\ \varphi(\tau_k)^* & \alpha(\tau_k) \end{pmatrix}, \quad (5.25)$$

where:

$$\alpha(\tau_k) = \sum_{n=0}^{QL-1} (\Omega_{n,n}(\tau_k))^2, \quad (5.26)$$

$$\varphi(\tau_k) = \sum_{n=0}^{QL-1} (\Omega_{n,n}(\tau_k))^2 e^{2\sigma_{D_k}(n-1)T_s}. \quad (5.27)$$

From the roots of the characteristic polynomial of the matrix $\mathbf{C}^H(\tau_k) \mathbf{C}(\tau_k)$ in (5.25), the two eigenvalues are obtained as follows:

$$\lambda_1 = \alpha(\tau_k) + |\varphi(\tau_k)| \quad \text{and} \quad \lambda_2 = \alpha(\tau_k) - |\varphi(\tau_k)|. \quad (5.28)$$

Hence the corresponding unit-norm eigenvectors are given by:

$$\mathbf{v}_1 = \frac{1}{\sqrt{2}} \begin{bmatrix} 1 & \frac{\varphi(\tau_k)^*}{|\varphi(\tau_k)|} \end{bmatrix}^T \quad \text{and} \quad \mathbf{v}_2 = \frac{1}{\sqrt{2}} \begin{bmatrix} 1 & -\frac{\varphi(\tau_k)^*}{|\varphi(\tau_k)|} \end{bmatrix}^T.$$

Since λ_1 and λ_2 are also the two non-zero eigen-values of $\mathbf{C}(\tau_k)\mathbf{C}(\tau_k)^H$, the singular value decomposition (SVD) of the matrix $\mathbf{C}(\tau_k)$ is obtained as follows:

$$\mathbf{C}(\tau_k) = \mathbf{U}(\tau_k)\mathbf{\Sigma}(\tau_k)^{1/2}\mathbf{V}(\tau_k)^H, \quad (5.29)$$

where:

$$\mathbf{\Sigma}(\tau_k) \triangleq \text{diag}\{\lambda_1, \lambda_2\} \quad \text{and} \quad \mathbf{V}(\tau_k) \triangleq [\mathbf{v}_1 \quad \mathbf{v}_2]. \quad (5.30)$$

Moreover, since $\mathbf{V}(\tau_k)^H\mathbf{V}(\tau_k) = \mathbf{I}_2$, then $\mathbf{U}(\tau_k) = [\mathbf{u}_1 \quad \mathbf{u}_2]$ can be expressed as follows:

$$\mathbf{U}(\tau_k) = \mathbf{C}(\tau_k)\mathbf{V}(\tau_k)^H\mathbf{\Sigma}(\tau_k)^{-1/2}. \quad (5.31)$$

Therefore, it follows that:

$$\mathbf{u}_1 = \frac{1}{\sqrt{2\lambda_1}} \left(\mathbf{c}_1(\tau_k) + \frac{\varphi(\tau_k)^*}{|\varphi(\tau_k)|} \right), \quad (5.32)$$

$$\mathbf{u}_2 = \frac{1}{\sqrt{2\lambda_2}} \left(\mathbf{c}_2(\tau_k) - \frac{\varphi(\tau_k)^*}{|\varphi(\tau_k)|} \right). \quad (5.33)$$

Now, by injecting (5.29) back into (5.23), it follows that:

$$\mathbf{R}_{\mathbf{x}_k\mathbf{x}_k} = \sigma_{n_k}^2 \left(\frac{\rho_k}{2} \mathbf{B}(\nu_k, \tau_k) \mathbf{\Sigma}(\tau_k) \mathbf{B}(\nu_k, \tau_k)^H + \mathbf{I}_{QL} \right), \quad (5.34)$$

where $\mathbf{B}(\nu_k, \tau_k) = \mathbf{\Lambda}(\nu_k) \mathbf{U}(\tau_k)$ and $\rho_k = \sigma_{h_k}^2 / \sigma_{n_k}^2$ is the signal-to-noise ratio (SNR). Using the Woodbury identity [82], the inverse of (5.34) can be computed analytically as follows:

$$\mathbf{R}_{\mathbf{x}_k\mathbf{x}_k}^{-1} = \frac{1}{\sigma_{n_k}^2} \mathbf{I}_{QL} - \frac{1}{\sigma_{n_k}^2} \mathbf{B} \left(\frac{2}{\rho_k} \mathbf{\Sigma}^{-1} + \mathbf{B}^H \mathbf{B} \right)^{-1} \mathbf{B}^H, \quad (5.35)$$

from which, the matrix and vector arguments have been removed for the sake of simplicity. Next, exploiting the fact that \mathbf{u}_1 and \mathbf{u}_2 are orthogonal with unit norms, the inverse of the covariance

matrix in (5.35) can be written as follows:

$$\mathbf{R}_{\mathbf{x}_k \mathbf{x}_k}^{-1} = \frac{1}{\sigma_{n_k}^2} \mathbf{I}_{QL} - \frac{1}{\sigma_{n_k}^2} \mathbf{B}(\nu_k, \tau_k) \Gamma(\tau_k) \mathbf{B}(\nu_k, \tau_k)^H, \quad (5.36)$$

where:

$$\Gamma(\tau_k) = \text{diag} \left\{ \frac{\rho_k \lambda_1}{2 + \rho_k \lambda_1}, \frac{\rho_k \lambda_2}{2 + \rho_k \lambda_2} \right\}. \quad (5.37)$$

Moreover, from (5.34), it can be shown that the determinant of $\mathbf{R}_{\mathbf{x}_k \mathbf{x}_k}$ is given by:

$$\det\{\mathbf{R}_{\mathbf{x}_k \mathbf{x}_k}\} = \frac{(\sigma_{n_k}^2)^{QL}}{4} (\rho_k \lambda_1 + 2)(\rho_k \lambda_2 + 2). \quad (5.38)$$

Finally, by injecting (5.36) and (5.38) back into (5.19), the LLF reduces to:

$$\mathcal{L}(\nu_k, \tau_k, \sigma_n^2) = -\ln((\rho_k \lambda_1 + 2)(\rho_k \lambda_2 + 2)) + \frac{1}{\sigma_{n_k}^2} \left\| \Gamma(\tau_k)^{1/2} \mathbf{B}(\nu_k, \tau_k)^H \mathbf{x}_k \right\|^2. \quad (5.39)$$

By expanding the norm in (5.39), the LLF can be expressed as follows:

$$\mathcal{L}(\nu_k, \tau_k, \sigma_{n_k}^2) = -\ln((\rho_k \lambda_1 + 2)(\rho_k \lambda_2 + 2)) + \frac{1}{\sigma_{n_k}^2} \sum_{i=1}^2 \frac{\rho_k \lambda_i}{2 + \rho_k \lambda_i} \left| \mathbf{u}_i^H \mathbf{\Lambda}(\nu_k)^H \mathbf{x}_k \right|^2, \quad (5.40)$$

or alternatively as:

$$\begin{aligned} \mathcal{L}(\nu_k, \tau_k, \sigma_{n_k}^2) = & -\ln((\rho_k \lambda_1 + 2)(\rho_k \lambda_2 + 2)) + \frac{1}{\sigma_{n_k}^2} \times \\ & \sum_{i=1}^2 \frac{\rho_k \lambda_i}{2 + \rho_k \lambda_i} \left| \sum_{m=0}^{QL-1} \mathbf{u}_i^*[m+1] e^{-j2\pi\nu \frac{m}{Q}} \mathbf{x}_k[m+1] \right|^2, \end{aligned} \quad (5.41)$$

and the joint ML estimates of ν_k and τ_k , assuming perfect knowledge of the Doppler spread σ_{D_k} , are obtained as the solution to the following two-dimensional optimization problem:

$$[\hat{\nu}_k, \hat{\tau}_k] = \underset{\nu, \tau}{\text{argmax}} \mathcal{L}(\nu, \tau). \quad (5.42)$$

Note here that the estimates of the SNR, ρ_k , and the noise variance, $\sigma_{n_k}^2$, are obtained using the same approach adopted in [80]. Moreover, by closely inspecting the expression in (5.41), we observe that the underlying cost function can be easily evaluated at each candidate value, τ , and all candidate

(normalized) CFO values by taking the FFT of the following vector:

$$\mathbf{z}_i(\tau) = \left[u_i^*[1]x_k[1], u_i^*[2]x_k[2], \dots, u_i^*[QL]x_k[QL] \right]^T. \quad (5.43)$$

Note as well that the candidate values, $\boldsymbol{\nu} = [\nu_1, \nu_2, \dots, \nu_{N_{\text{FFT}}}]^T$, for the unknown CFO parameter are dictated by the size, N_{FFT} , of the underlying FFT:

$$\nu_n = \frac{n-1}{N_{\text{FFT}}}, \quad n = 1, 2, \dots, N_{\text{FFT}}. \quad (5.44)$$

A larger N_{FFT} allows a more refined sampling of the CFO grid and, therefore, a more accurate estimation. Hence, we can easily use the FFT algorithm to evaluate the LLF for all candidate CFO values, $\boldsymbol{\nu}$, at any given candidate delay value, $\boldsymbol{\tau}[r]$, as follows:

$$\mathbf{d}_r = -\log((\rho\lambda_1 + 2)(\rho\lambda_2 + 2)) + \frac{1}{\sigma_n^2} \sum_{i=1}^2 \frac{\rho\lambda_i}{2 + \rho\lambda_i} |\text{FFT}(\mathbf{u}_i \odot \mathbf{x}_k)|^2, \quad r = 1, 2, \dots, N_\tau. \quad (5.45)$$

Hence, the function in (5.41) is evaluated for all possible TD and CFO values at each relay. The result is a $N_{\text{FFT}} \times N_\tau$ matrix defined as:

$$\mathbf{D} = [\mathbf{d}_1, \mathbf{d}_2, \dots, \mathbf{d}_{N_\tau}]. \quad (5.46)$$

Finally the estimates $\hat{\nu}_k$ and $\hat{\tau}_k$ are obtained by fetching the global maximum of the matrix \mathbf{D} .

5.3.3 Cramer rao lower bound (CRLB)

In the TVC case, the CLRb was previously derived in [83] for the Doppler spread estimation. In the following, we extend it to joint CFO and TD estimation for performance benchmarking. Recall that the covariance matrix of the received signal is given by:

$$\mathbf{R}_{\mathbf{x}_k \mathbf{x}_k} = \boldsymbol{\Lambda}(\bar{\nu}_k) \boldsymbol{\Omega}(\bar{\tau}_k) \mathbf{E}\{\mathbf{h}_k \mathbf{h}_k^H\} \boldsymbol{\Omega}(\bar{\tau}_k)^H \boldsymbol{\Lambda}(\bar{\nu}_k)^H + \bar{\sigma}_{n_k}^2 \mathbf{I}_{QL}. \quad (5.47)$$

Let $\boldsymbol{\zeta} = [\bar{\tau}_k, \bar{\nu}_k, \bar{\sigma}_{n_k}^2]^T$ be a vector that contains all the parameters of interest, then the $(k, l)^{th}$ element of the Fisher information matrix (FIM) can be written as follows:

$$[\mathbf{J}(\boldsymbol{\zeta})]_{k,l} = \text{trace} \left[\mathbf{R}_{\mathbf{x}_k \mathbf{x}_k}^{-1} \frac{\partial \mathbf{R}_{\mathbf{x}_k \mathbf{x}_k}}{\partial \boldsymbol{\zeta}_k} \mathbf{R}_{\mathbf{x}_k \mathbf{x}_k}^{-1} \frac{\partial \mathbf{R}_{\mathbf{x}_k \mathbf{x}_k}}{\partial \boldsymbol{\zeta}_l} \right]. \quad (5.48)$$

The CRLBs for the TD and CFO parameters are obtained by finding the inverse of the FIM in (5.48) and then taking its first and second diagonal entries, respectively.

5.3.4 Joint synchronization and Doppler spread estimation

The LLF in (5.41) depends on both the target TD and CFO, but also on the Doppler spread. The latter was assumed thus far to be perfectly known. However, in real life scenarios, the Doppler spread has to be estimated. To reduce the complexity of the tri-dimensional estimation problem, we use a similar approach to the one proposed in [25] in order to find the minimum of some cost function. This approach allows to separate the Doppler estimation problem from the joint synchronization one. As far as the initialization step is concerned, we opt for the TCC technique developed in Subsection 5.3.1 to get initial TD and CFO estimates, i.e., $\hat{\tau}_k^{(0)}$ and $\hat{\nu}_k^{(0)}$. The latter are then injected into the LLF of (5.41) to obtain an initial Doppler spread estimate. This preliminary guess is in its turn injected in the very same LLF function to jointly estimate the TD and CFO. The TCC-based technique is suitable for initialization since it provides good initial estimates for the TVC-based technique. Hence, the latter converges quickly, in few iterations only. The overall estimation technique at each relay R_k is summarized in Algorithm 2. Note that the Doppler estimates can be obtained using

Algorithm 2 Joint estimator for the Doppler, TD, and CFO at each relay R_K

Initialization: Estimate $\hat{\tau}_k^{(0)}$ and $\hat{\nu}_k^{(0)}$ using (5.18)
for $j = 1$ to J **do**
 Estimate $\hat{\sigma}_{D_k}^{(j)}$
 Estimate $\hat{\tau}_k^{(j)}$ and $\hat{\nu}_k^{(j)}$ using (5.41)
end for

(5.41) after injecting the $\hat{\tau}_k^{(j-1)}$ and $\hat{\nu}_k^{(j-1)}$. Unfortunately, at high Doppler values, the TCC CFO estimates may not be reliable and could affect the performance of the overall algorithm. In such a scenario, we can adopt the technique proposed in [80] which is robust to the CFO and, hence, provides accurate Doppler estimates for injection into the next processing iteration.

5.4 Distributed MIMO-relay beamforming

Very often, the synchronization process is performed at the destination where the receiver extracts the estimates of all the parameters. This approach could perform well in practice. However,

it can suffer from prohibitive computational costs since it requires solving a multi-dimensional problem with a cardinality increasing with the number of relaying nodes [84]. Many techniques opt for sub-optimal iterative implementations [25], [85] that could become ineffective in the case of dense networks. In such a case, open-loop synchronization architectures should be adopted instead. Accordingly, the proposed synchronization technique is run at each relay node along with the distributed MIMO-relay beamforming transceiver structure illustrated in Fig. 5.3. During a PT period, each node performs a channel parameter estimation task. During the DT period, each relay will transmit the useful data to the destination while ensuring that the signal is modified properly using the TD, CFO and channel estimates made available during the PT period. Full details of the processing and data signaling structure are shown in Fig. 5.4. Note that the synchronization parameters are

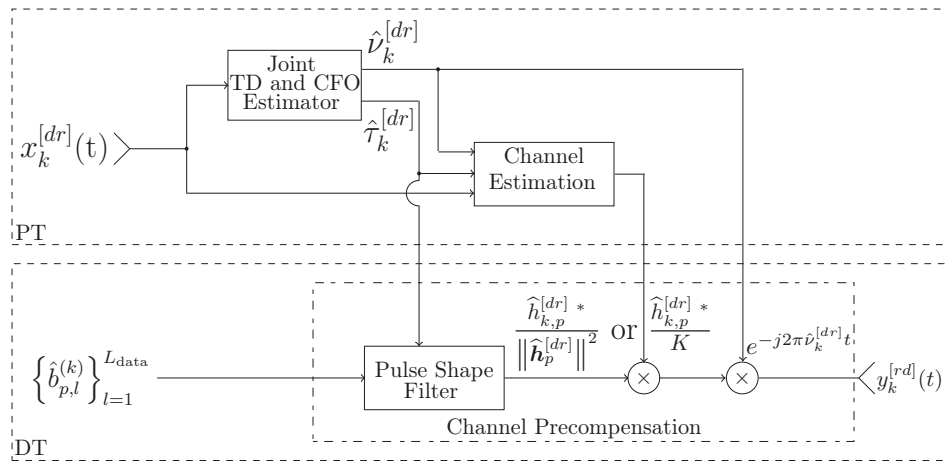


Figure 5.3 – Block diagram of the DF transceiver at the k^{th} relay.

expected to vary with time, but actually at a rate much slower than the channel time-variations. Therefore, as shown in Fig. 5.4, the synchronization parameters will be refreshed once each P consecutive DT periods.

For more details about the proposed communication protocol, we provide an example on how the processing time and data signaling are organized in the time domain. In fact, during the first period, i.e., step (1), the destination broadcasts a training sequence, $\{a_l^{[rd]}\}_{l=1}^{L_{\text{sync}}}$, to all K relaying nodes. Then, the source node starts transmitting its own training sequence, $\{a_l^{[sr]}\}_{l=1}^{L_{\text{sync}}}$, to the relaying nodes during steps (2) and (3). Each relay node estimates the channel parameters $(\hat{\tau}_k^{[rd]}, \hat{\nu}_k^{[rd]})$ and $(\hat{\tau}_k^{[sr]}, \hat{\nu}_k^{[sr]})$ during steps (4) and (5), respectively. At steps (6) and (7), the destination node broadcasts another training sequence, $\{a_l^{[rd]}\}_{l=1}^{L_{\text{ch}}}$, dedicated to channel estimation. At the same time, the source node performs the same procedure by sending the sequence $\{b_{p,l}\}_{l=1}^{L_{\text{data}}}$ during steps (8)

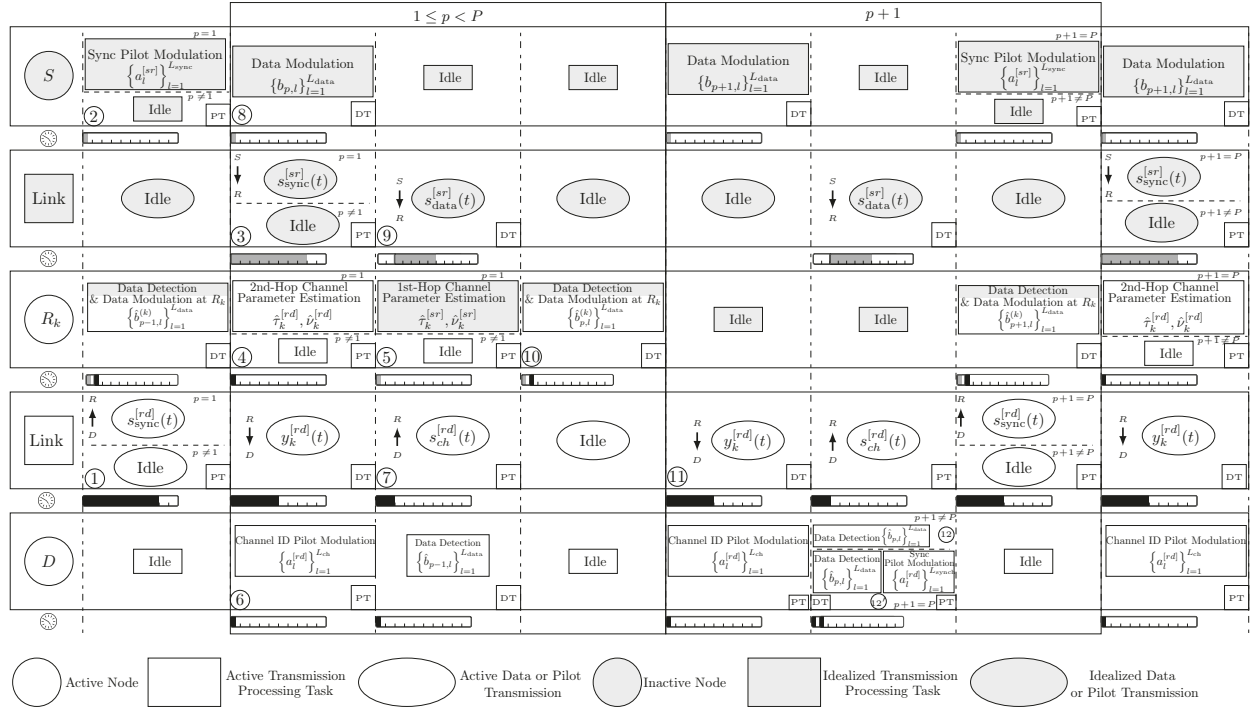


Figure 5.4 – Processing and data signaling structure of the two-hop MIMO-relay beamforming scheme assuming ideal (inactive) first-hop communication.

and (9). At step (10), each relay node uses $\hat{\tau}_k^{[sr]}$ and $\hat{\nu}_k^{[sr]}$ along with $\hat{h}_{k,p}^{[sr]}$ to estimate $\{\hat{b}_{p,l}^{(k)}\}_{l=1}^{L_{\text{data}}}$. The latter will be used along with $\hat{\tau}_k^{[rd]}$, $\hat{\nu}_k^{[rd]}$, and $\hat{h}_{k,p}^{[rd]}$ to generate the transmitted signal $y_k^{[rd]}(t)$ as described in (5.53). The signal $y_k^{[rd]}(t)$ is transmitted during step (11). Finally, the destination node performs a simple decoding procedure during step (12). During the next $P-1$ periods (i.e., $1 < p < P$), steps (1) to (5) are ignored since the channel parameters ($\hat{\tau}_k^{[rd]}$, $\hat{\nu}_k^{[rd]}$) and ($\hat{\tau}_k^{[sr]}$, $\hat{\nu}_k^{[sr]}$) are assumed to be the same over P periods. At the P^{th} period, however, we execute the same steps (6) to (11) but slightly change the final step (12) and, hence, denote it as (12'). In step (12'), once the destination node completes the decoding process, it starts broadcasting again the very same training sequence $\{a_l^{[rd]}\}_{l=1}^{L_{\text{sync}}}$.

Now, as explained above, the destination periodically transmits to all the relays, at each p^{th} period, a training sequence \mathbf{a}_p that only contains L_{ch} pilot symbols, i.e., $\mathbf{a}^{[dr]} = \{a_l^{[dr]}\}_{l=1}^{L_{\text{ch}}}$. The latter are exploited by each relay to update its channel state information (CSI) with respect to the destination. More specifically, the corresponding oversampled signal denoted³ here as $\tilde{\mathbf{x}}_k^{[dr]}$ is processed by relay R_k to find the ML estimate of its own complex-valued channel coefficient of the D -to- R_k

3. Note here that $\tilde{\mathbf{x}}_k^{[dr]}$ is equivalent to $\mathbf{x}_k^{[dr]}$ in (5.7) using, however, another training sequence transmitted specifically for channel estimation purposes.

link during the $\{p^{th}\}_{p=1}^P$ period, as follows :

$$\hat{h}_{k,p}^{[dr]} = \frac{1}{\|\mathbf{r}(\hat{\nu}_k, \hat{\tau}_k)\|^2} \mathbf{r}^H(\hat{\nu}_k, \hat{\tau}_k) \tilde{\mathbf{x}}_k^{[dr]}, \quad k = 1, 2, \dots, K, \quad (5.49)$$

where:

$$\mathbf{r}(\nu, \tau) = \mathbf{\Lambda}(\nu) \mathbf{G}(\tau) \mathbf{a}^{[dr]}. \quad (5.50)$$

To ensure that the signals from all the relays arrive at the receiver coherently and thus combine constructively, the relays must adjust their carrier frequencies, carrier phases, and symbol timings as follows:

- The signal carrying the useful data to be transmitted by the k^{th} relay is delayed as follows:

$$s(t - \hat{\tau}_k^{(\text{comp})}) = \sum_{l=0}^{L_{\text{data}}-1} b_{p,l+1} g(t - lT - \hat{\tau}_k^{(\text{comp})}), \quad (5.51)$$

where $\{b_{p,l}\}_{l=1}^{L_{\text{data}}}$ are the symbols containing the useful data during the p^{th} period assuming here perfect transmission links between the source and the relays, and $\hat{\tau}_k^{(\text{comp})} = \tau_{\text{max}} - \hat{\tau}_k^{[dr]}$.

- The relay node pre-compensates its CFO by de-rotating the signal in (5.51) as follows:

$$e^{-j2\pi \hat{\nu}_k^{[dr]} t} s(t - \hat{\tau}_k^{(\text{comp})}). \quad (5.52)$$

- By relying on the channel reciprocity property of time-division duplex (TDD) schemes, we pre-compensate the channel phase and match its amplitude with the complex channel estimate to generate the following transmit signal $y_k(t)$ at each relay:

$$y_k(t) = \frac{\hat{h}_{k,p}^{[dr]*}}{\|\hat{\mathbf{h}}_p^{[dr]}\|^2} e^{-j2\pi \hat{\nu}_k t} s(t - \hat{\tau}_k^{(\text{comp})}), \quad (5.53)$$

where $\hat{h}_{k,p}^{[dr]}$ is the channel estimate at the k^{th} relay obtained from (5.49) and $\hat{\mathbf{h}}_p^{[dr]} = [\hat{h}_{1,p}^{[dr]}, \hat{h}_{2,p}^{[dr]}, \dots, \hat{h}_{K,p}^{[dr]}]^T$. In (5.53), we need to have the channel estimates over all $D - R$ links available at each relay node for the sole purpose of calculating the square norm of the K -dimensional $D - R$ vector channel. The latter can be fed back by the destination. Alternatively, to avoid any additional overhead, it can be simply approximated by its average value K as follows:

$$y_k(t) \approx \frac{\hat{h}_{k,p}^{[dr]*}}{K} e^{-j2\pi \hat{\nu}_k t} s(t - \hat{\tau}_k^{(\text{comp})}). \quad (5.54)$$

At the destination, the received signal, $x_p^{[rd]}(t)$, which is the superposition of all the pre-synchronized signals transmitted by the K relays, can be expressed as follows:

$$x_p^{[rd]}(t) = \sum_{k=1}^K h_{k,p}^{[rd]}(t) e^{-j2\pi\nu_k t} y_k(t - \tau_k) + w(t), \quad (5.55)$$

where $h_{k,p}^{[rd]}(t)$ is the true TVC pertaining to the k^{th} relay and $w(t)$ is the additive Gaussian noise component received at the destination node. By substituting $y_k(t)$ in (5.55) with its expression in (5.53), the received signal stemming from our decentralized multi-node synchronization scheme and distributed MIMO-relay beamforming design is rewritten as follows:

$$x_p^{[rd]}(t) = \sum_{k=1}^K h_{k,p}^{[rd]}(t) \frac{\hat{h}_{k,p}^{[dr]*}}{\|\hat{\mathbf{h}}_p^{[dr]}\|^2} e^{j2\pi(\hat{\nu}_k^{[dr]} - \nu_k^{[dr]})t} s\left(t - \hat{\tau}_k^{(\text{comp})} - \tau_k^{[dr]}\right) + w(t). \quad (5.56)$$

5.5 Simulation results

In the following, we discuss our simulation results at both the component and link levels when all previous works would stop short from moving to the more time consuming yet much more insightful link level. In all our simulations, we assume as would be expected in practice that the K relays are co-located at about the same distance and moving at the same relative speed from the destination whether the latter is stationary or also in motion itself. Under this assumption, the average SNR and the Doppler frequency are assumed to be the same over all R-D and D-R links. Please note that only in the simulations section did we make the choice of considering the simple case of nearly equal SNR and Doppler values over all second-hop channels that could arise in practice in the case for instance of co-located nodes. We did so only for the sake of simplifying our presentation and discussion of the simulation results. Nevertheless, our solution was designed to cope well with the general case where both the SNR and Doppler frequency values could be different from one second-hop link to another. Beyond the above considerations, co-location could become a required feature among collaborating nodes. For example, it was shown in [86], that multi-hop transmission with co-located cooperating nodes exhibits better coverage especially for higher path loss exponents. Moreover, we know that sensors usually have limited-capacity batteries. And one way to extend their life and allow longer network operation without human intervention is by exploiting wireless energy harvesting (WEH) [87]. Such a solution requires that the sensors be co-located and clustered. In the following, we will

investigate in different scenarios the estimation accuracy of the tested synchronization parameter estimators in terms of the normalized mean square error (NMSE) before assessing their link-level throughput performance.

5.5.1 Component-level simulations

In all component-level simulations, we consider a training sequence, $\mathbf{a}^{[dr]}$, of $L_{\text{sync}} = 128$ QPSK symbols and a square root raised-cosine shaping-pulse filter (SRRC) with a roll-off factor $\rho = 0.3$. In Fig. 5.5, we compare the proposed technique under its two variants with idealized and active Doppler frequency estimation, i.e., ML TVC-PD and ML TVC-DE, against the space alternating generalized expectation maximization (SAGE) algorithm in [25], the sole benchmark available in the literature dealing with multi-node TD and CFO synchronization, and the CRLBs derived in Section III.B in terms of NMSE performance. We observe that all tested techniques perform nearly

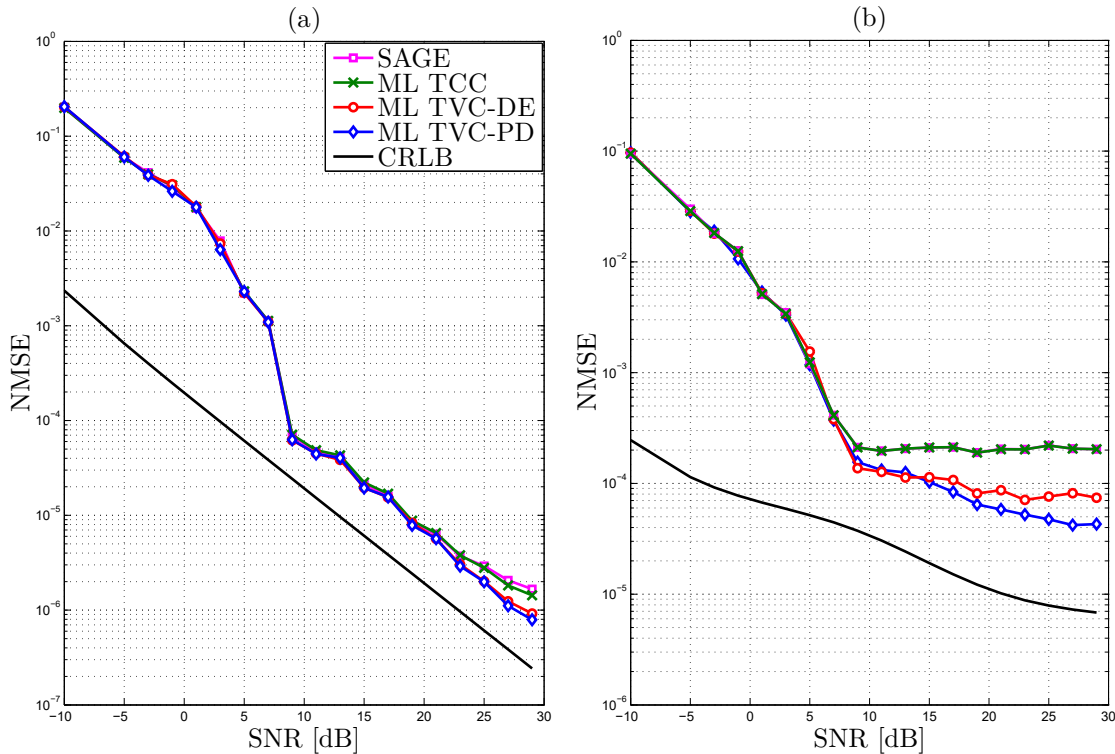


Figure 5.5 – CRLB and NMSE vs SNR of the ML TVC, ML TCC, and SAGE techniques vs the SNR with $F_{D_k} = 15$ Hz and *uniform Jakes'* model for: (a) the TDs and (b) the CFOs.

the same at $F_{D_k} = 15$ Hz with a small advantage for both TVC-PD and TVC-DE measured at high SNR values. On the other hand, SAGE and ML TCC - which perform exactly the same because

they both rely on the TCC assumption - see their performance slightly degrade at high SNR because the channel is not totally constant (i.e., $F_{D_k} \neq 0$ Hz). Besides, we observe that the practical ML TVC-DE version matches its idealized ML TVC-PD counterpart in terms of TD estimation accuracy whereas it exhibits slightly lower CFO estimation performance. In fact, this degradation stems from the Doppler estimation errors that increase at higher Doppler values with an even more detrimental impact on CFO estimation.

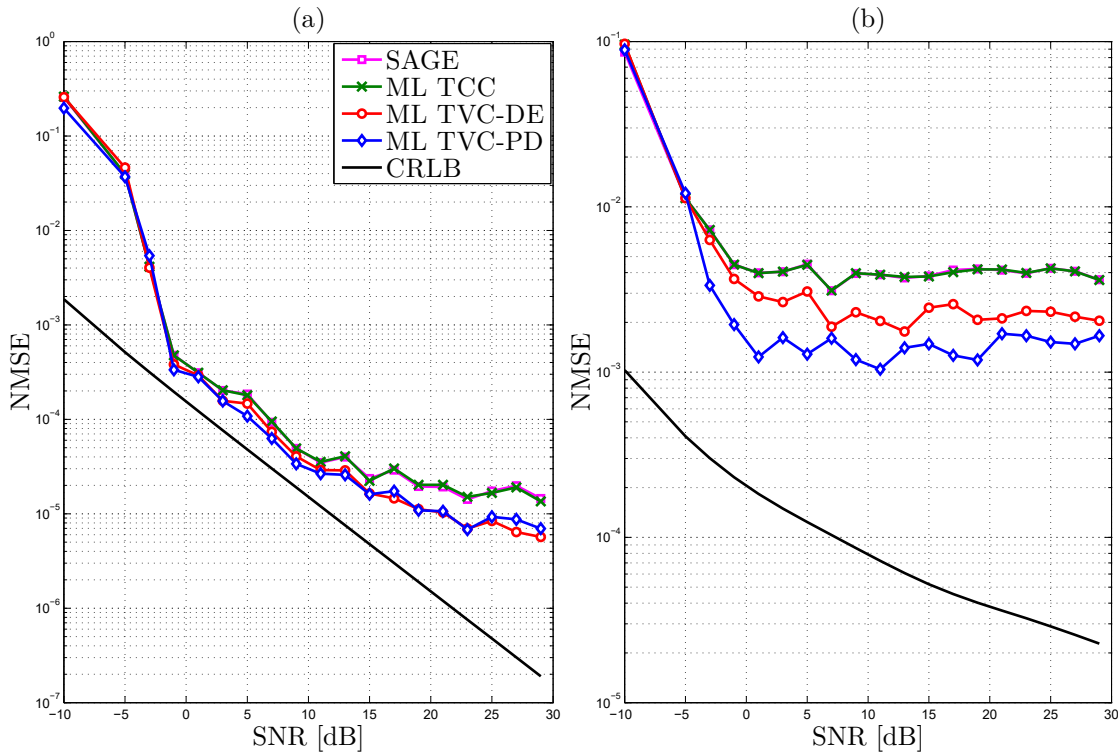


Figure 5.6 – CRLB and NMSE vs SNR of the ML TVC, ML TCC, and SAGE techniques vs the SNR with $F_{D_k} = 100$ Hz and *uniform Jakes'* model for: (a) the TDs and (b) the CFOs.

In Fig. 5.6, we tackle a more challenging case with a significantly higher Doppler frequency $F_{D_k} = 100$ Hz. Here again, we can report the very same qualitative observations made in Fig. 5.5, yet with more prominent performance gaps this time in terms of CFO and TD estimation accuracies, more so at high SNR values, between on one hand ML TVC and the TCC-based techniques (i.e., SAGE and ML TCC) and on the other hand between ML TVC-PD and ML TVC-DE. This is hardly surprising because on one hand SAGE and ML TCC fail to reach the global maximum and exhibit poor performance since the TCC assumption no longer holds at high Doppler. And because, on the other hand, the Doppler estimator selected for joint operation with the new ML TVC technique to illustrate its applicability in real-world operating conditions is specifically tailored to cope with the far more challenging estimation of low Doppler frequencies. Hence, the additional performance

losses resulting from the joint estimation of high Doppler frequencies can be reduced to the same small if not negligible amounts observed at low Doppler in Fig. 5.5; that is by the simple integration of alternative Doppler estimation solutions easily prone to be made relatively much more accurate at high Doppler.

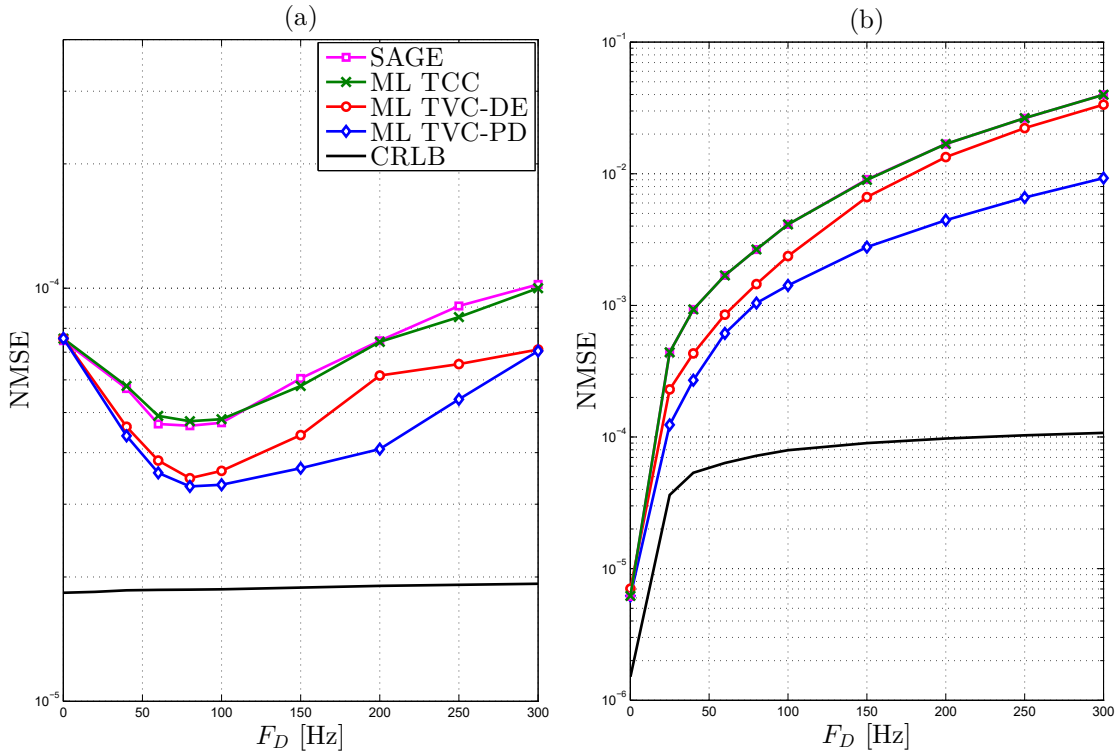


Figure 5.7 – CRLB and NMSE vs F_{D_k} of the ML TVC, ML TCC, and SAGE techniques with $SNR = 10$ dB and *uniform Jakes’* model for: (a) the TDs, and (b) the CFOs.

To better investigate the effect of Doppler frequency on the synchronization accuracy, we plot in Fig. 5.7 the NMSE of all techniques against the Doppler. Obviously both ML TVC-PD and ML TVC-DE outperform the TCC-based techniques (i.e., SAGE and ML TCC) over a wide Doppler range (i.e., $F_{D_k} \leq 300$ Hz). As the Doppler increases, the TCC-based techniques start experiencing serious difficulties to converge to the global maximum that translate into extremely poor TD and CFO estimation accuracies.

In Fig. 5.8, we assess the performance variations of the same tested techniques against the training sequence length. We observe that TVC-PD outperforms both ML TCC and SAGE algorithms in terms of CFO estimation accuracy no matter the number of symbols. Recall that both TVC-PD and TVC-DE rely on a two-ray channel approximation (cf. Section 5.3.2) that holds only when $L_{\text{sync}}F_{D_k}T \ll 1$ [80]. Hence, when increasing the training sequence’s size at small Doppler values, both techniques see their NMSE performance improve. However, the approximation becomes inac-

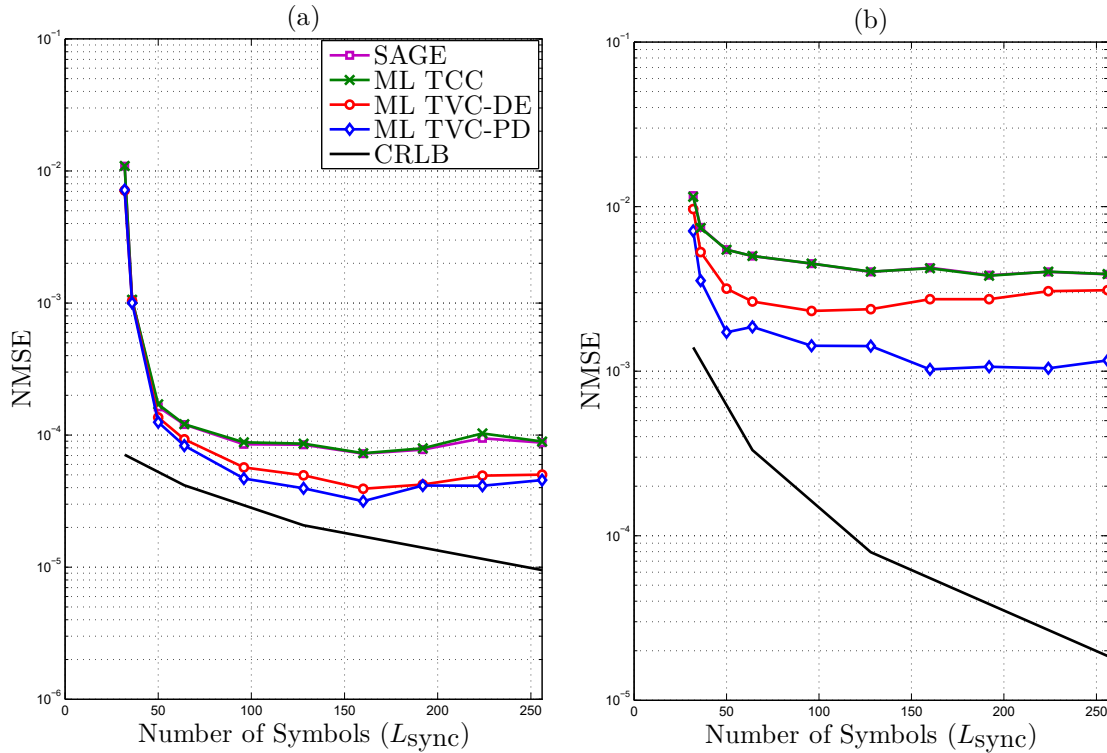


Figure 5.8 – CRLB and NMSE vs the number of pilot symbols L_{sync} of the ML TVC, ML TCC, and SAGE techniques with $SNR = 10$ dB, $F_{D_k} = 100$ Hz, and *uniform Jakes’ model* for: (a) the TDs, and (b) the CFOs.

curate with even longer sequences, more so at higher Doppler, thereby resulting beyond some best trade-off length in counter-effect accuracy losses.

5.5.2 Link-level simulations

Our link-level simulations were run using the key setup parameters listed in Table 5.1.

Table 5.1 – Simulation parameters

Parameters	Symbol	Values
Symbol period	T	1/14 ms
Number of relays	K	{1, 2, 4, 8}
Maximum Doppler shift	$\{F_{D_k}\}_{k=1}^K$	{15, 100, 200, 300} Hz
Oversampling factor	Q	2
Roll-off factor	ρ	0.3
TDs	τ_k	Uniformly random (i.i.d.)
CFOs	ν_k	Uniformly random (i.i.d.)
R_k – D channel	\mathbf{h}_k	Rayleigh random (i.i.d.)

Fig. 5.9 depicts the resulting throughput for three different modulation orders (QPSK, 16-QAM and 64-QAM) and K relays. We consider in Figs. 5.9 (a) and 5.9 (b) the case where all K relay-destination links have the same maximum Doppler frequency shift of 15 and 100 Hz, respectively. For a given modulation order M , the throughput is obtained from the symbol error rate (SER) as follows:

$$\text{Throughput} = \frac{1}{T} \log_2(M)(1 - \text{SER})(1 - R), \quad (5.57)$$

where R is the overhead ratio. Note here that the latter is computed over a period that spans L_{sync} symbols for synchronization and P periods each of which includes $L_{\text{ch}} = 2$ pilot symbols followed by $L_{\text{data}} = 12$ information-bearing symbols. As such, the overhead ratio is given by:

$$R = \frac{L_{\text{sync}} + L_{\text{ch}}P}{L_{\text{sync}} + (L_{\text{ch}} + L_{\text{data}})P}. \quad (5.58)$$

Our simulations were obtained for $L_{\text{sync}} = 128$ and $P = 100$. Note here that the overhead ratio associated with the synchronization period becomes negligible for such large value of P . The latter cannot, however, be increased indefinitely as it is dictated by the required refreshment rate P that better copes with the time variations of the synchronization parameters.

We see from Fig. 5.9 (a) that QPSK transmissions, among the different considered modulations, provide higher throughput for SNR values below 11 dB. When the SNR ranges between 11 dB and 16 dB, 16-QAM becomes more suitable whereas 64-QAM dominates when the SNR exceeds 16 dB. The resulting throughput curve assuming an adaptive (i.e., SNR-dependent) modulation is depicted by the black curve.

In Fig. 5.9 (b), we show the performance of the proposed distributed beamforming scheme at a higher Doppler $F_{D_k} = 100$ Hz (i.e., fast TVCs). In this scenario, QPSK and 16-QAM modulations provide higher throughput over the same SNR ranges reported above at low Doppler whereas 64-QAM dominates when the SNR exceeds 21 dB. We also observe that 64-QAM transmissions suffer from a noticeable performance degradation. Indeed, at lower Doppler values, the phase estimates of (5.49) provide accurate values since the channel varies slowly during the same period. Hence, the decoder at the destination is able to accurately estimate the transmitted symbols. In the case of high mobility, the channel varies rapidly during the same period, leading to a more severe degradation of the channel estimates. The latter affects the decoding process, especially at higher modulations which are more sensitive to phase shifts.

In Fig. 5.10, we compare the performance of ML TVC-PD and ML TVC-DE in terms of through-

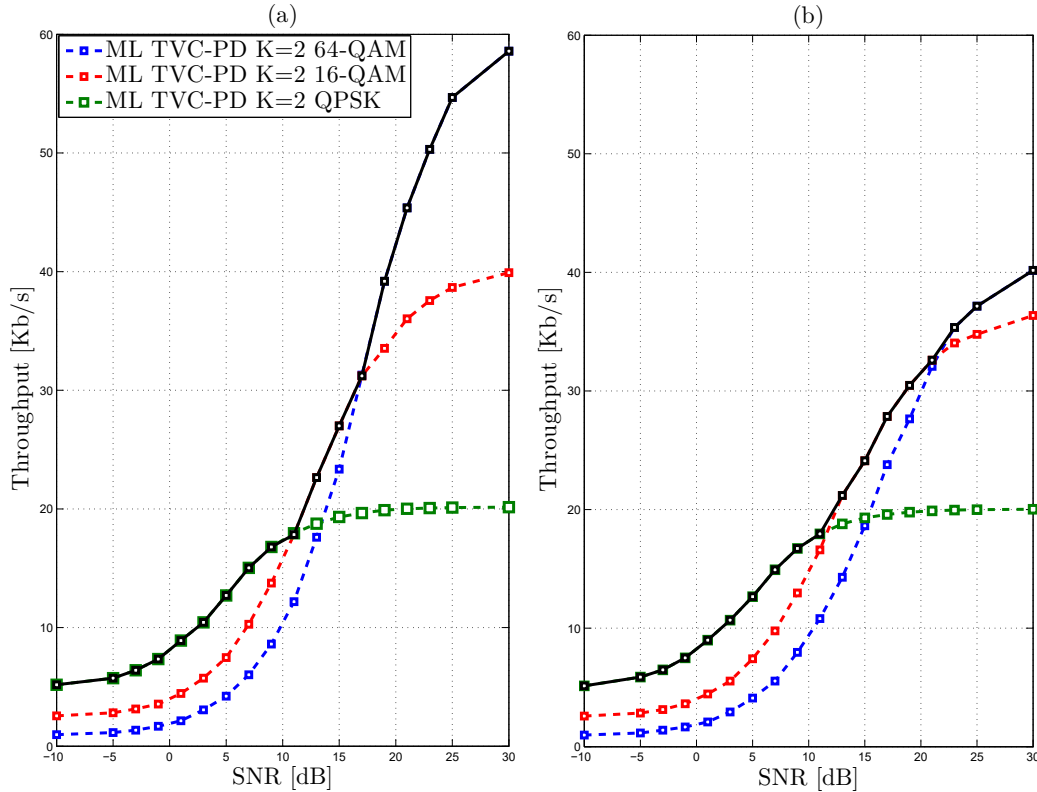


Figure 5.9 – Link-level throughput vs SNR for ML TVC-PD at $K = 2$ relays and a refreshment rate $P = 100$ for: (a) $\{F_{D_k}\}_{k=1}^K = 15$ Hz, and (b) $\{F_{D_k}\}_{k=1}^K = 100$ Hz.

put. The former sees its performance deteriorate against the former only at high SNR. Measured losses are almost negligible at low Doppler, but become noticeable at high Doppler. Yet, as reported previously when discussing the component-level simulation results, such link-level throughput gap can be easily bridged by the integration of an alternative high-range Doppler estimator, thereby making ML TVC-PD an equivalent version to ML TVC-DE and a meaningful one for further comparisons in what follows with existing Doppler-independent TCC-based benchmarks.

In Fig. 5.11, we assess the performance of ML TVC-PD in the more realistic case of an active first-hop scenario, that is to gauge in comparison the usefulness of the results obtained in the idealized case of perfect $D - R$ transmissions. Actually, the impact of active first-hop links is emulated by inserting erroneous symbols at each relay. The latter are generated with a probability resulting from an SNR level 5 dB higher than the one measured at the destination. This is to reflect the fact that relays are expectedly selected at more favorable locations than the destination. We see that the throughput curve of the two-hop scenario exhibits approximately the same performance as the one considering an idealized first-hop communication. Such a result confirms that the throughput of the MIMO-relay beamforming system is mainly dictated by the performance of the relatively

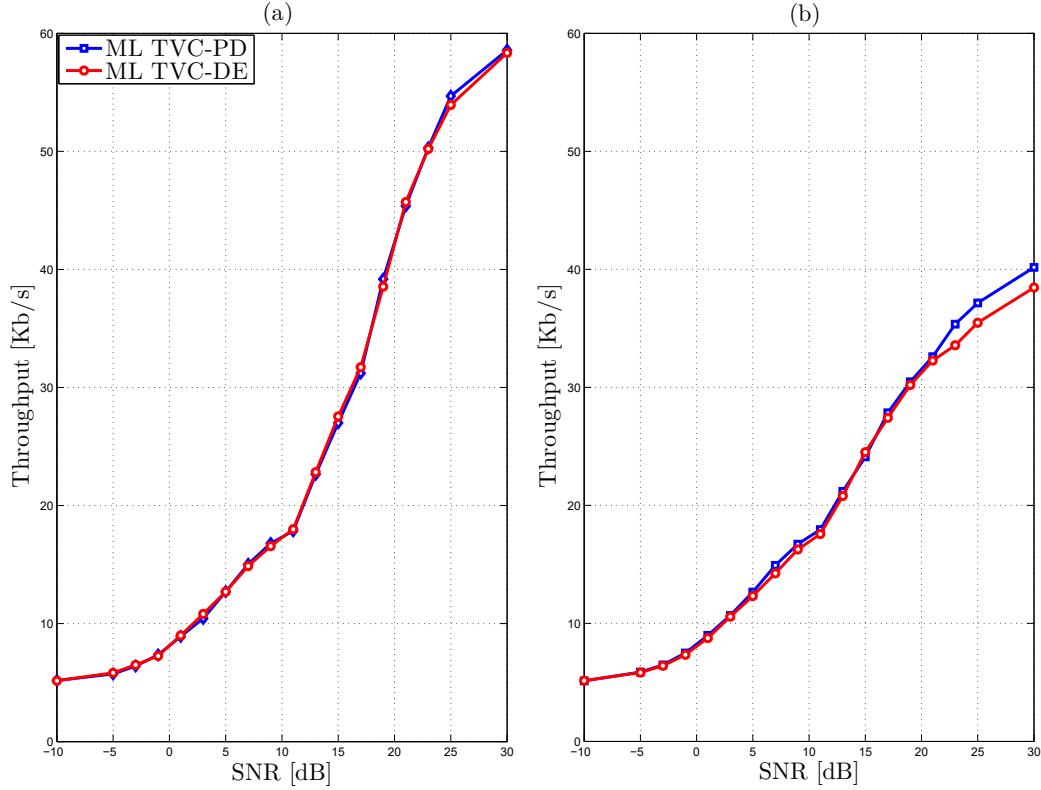


Figure 5.10 – Link-level throughput vs SNR for ML TVC-PD and ML TVC-DE at $K = 2$ relays, $\{F_{D_k}\}_{k=1}^K = 100$ Hz, and a refreshment rate $P = 100$ for: (a) $\{F_{D_k}\}_{k=1}^K = 15$ Hz, and (b) $\{F_{D_k}\}_{k=1}^K = 100$ Hz.

weaker-SNR second-hop.

In Fig. 5.12, we compare the performance of ML TVC-PD, ML TCC, and SAGE in terms of throughput for four different numbers of relays ($K = 1$, $K = 2$, $K = 4$, and $K = 8$) and four different Doppler frequencies (i.e., $\{F_{D_k}\}_{k=1}^K = 15$ Hz, $\{F_{D_k}\}_{k=1}^K = 100$ Hz, $\{F_{D_k}\}_{k=1}^K = 200$ Hz, and $\{F_{D_k}\}_{k=1}^K = 300$ Hz). We see under the TCC assumption (i.e., $F_{D_k} = 15$ Hz) that all techniques perform nearly the same in terms of link-level throughput. They do so the best with QPSK transmissions when the SNR is below 11 dB whereas 16-QAM becomes more suitable at SNR values ranging between 11 and 16 dB. When the SNR exceeds 16 dB, 64-QAM transmissions ultimately become the best choice. At a higher Doppler frequency (i.e., $F_{D_k} = 100$ Hz), we can always report noticeable and constantly increasing throughput gains of ML TVC over TCC-based SAGE and ML TCC at both medium and high SNR levels when increasing the number of relays from 1 to 8. At lower SNR values, all techniques exhibit the same NMSE and consequently the same throughput performances. At even higher Doppler values (i.e., $F_{D_k} = 200$ Hz or $F_{D_k} = 300$ Hz), the relative throughput gains of ML TVC over SAGE and ML TCC become even more significant, again more

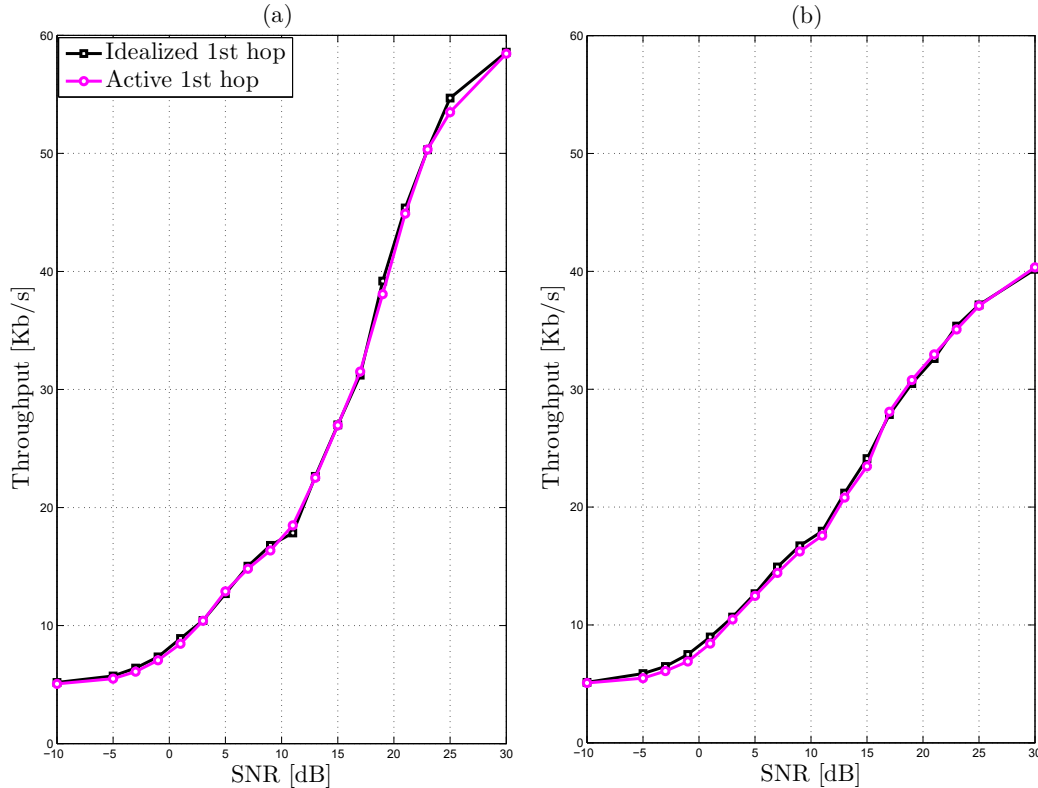


Figure 5.11 – Link-level throughput vs SNR for ML TVC-PD at $K = 2$ relays and a refreshment rate $P = 100$ for: (a) $\{F_{D_k}\}_{k=1}^K = 15$ Hz, and (b) $\{F_{D_k}\}_{k=1}^K = 100$ Hz.

so when the number of relays also increases. These key observations come as a solid confirmation of the very important performance benefits of the proposed distributed MIMO-relay beamforming and multi-node synchronization schemes.

5.6 Conclusion

In this paper, we addressed the problem of time and frequency synchronization in cooperative systems over TVCs. We proposed two different estimation techniques. The first operates under the TVC assumption while the second one works with TCCs. In the first ML TVC-PD approach, we assume perfect knowledge of the Doppler spread to provide accurate TD and CFO synchronization estimates. Whereas we exploit the second ML TCC technique as an initialization scheme for preliminary synchronization then embed both ML TVC-PD and some Doppler estimator in a new iterative version, ML TVC-DE. That is to account for the practical need to estimate at each relay node the Doppler spread upon which relies ML TVC-PD. We also developed a new distributed MIMO-relay

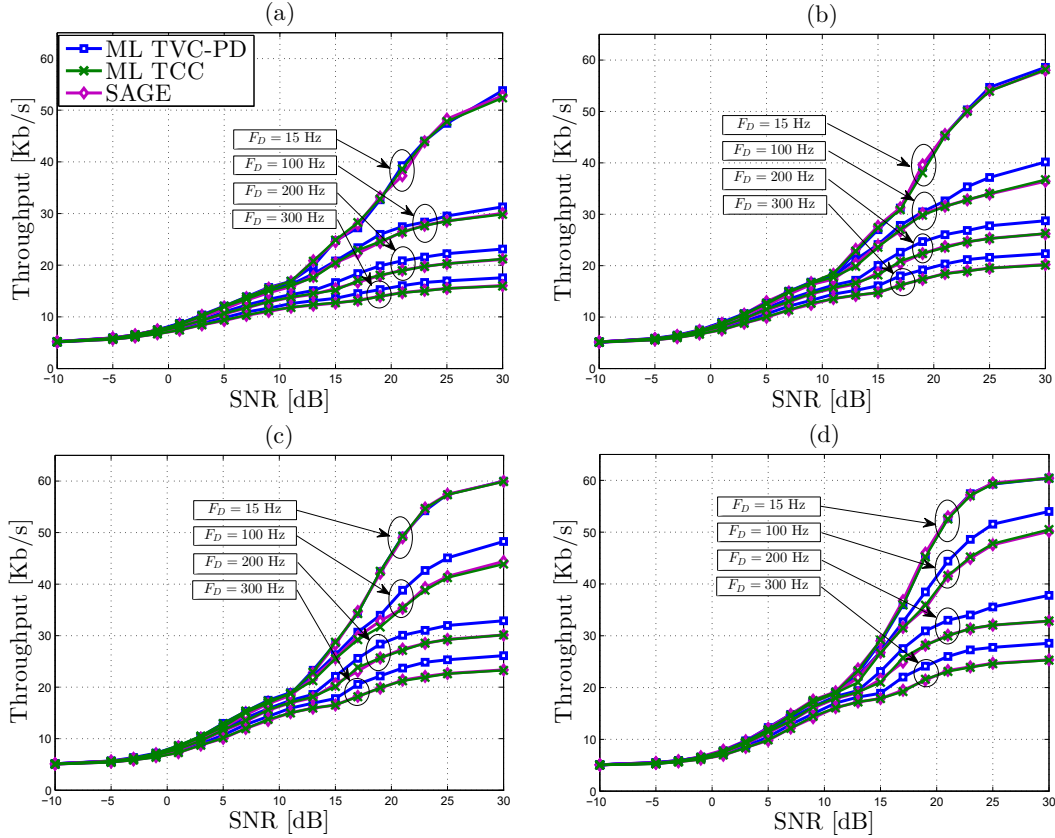


Figure 5.12 – Link-level throughput vs SNR for ML TVC-PD at a refreshment rate $P = 100$ and different Doppler frequencies for: (a) $K = 1$, (b) $K = 2$, (c) $K = 4$, and (d) $K = 8$.

beamforming design that embeds the proposed synchronization technique at each relay node. We showed under the TCC assumption that all techniques exhibit approximately the same performance. However, when the Doppler increases, the TCC-based techniques exhibit poor performance while the new ML TVC continues to provide accurate estimates. Link-level simulations confirm the net advantages of the proposed ML TVC multi-node synchronization technique and the MIMO-relay beamforming scheme in terms of throughput gains, especially at medium and high SNRs, more so at relatively higher Doppler frequencies or with more distributed MIMO-relay beamforming nodes. Future work could investigate a more complex system that includes multiple antennas at each relay nodes and/or multiple receivers.

5.7 Appendices

Appendix 1: [Relationship between the rank of $\mathbf{C}(\tau_k)\mathbf{C}^H(\tau_k)$ and the two-ray approximation]

As stated in [80], by adopting the two-ray approximation model, the approximate channel covariance matrix, $\widehat{\mathbf{R}}_{h_k h_k}$, is of rank two. However, introducing the diagonal matrix $\mathbf{\Omega}(\tau_k)$ (i.e., $\mathbf{C}(\tau_k)\mathbf{C}^H(\tau_k) = \mathbf{\Omega}(\tau_k)\widehat{\mathbf{R}}_{h_k h_k}\mathbf{\Omega}(\tau_k)^H$) does not guarantee that $\mathbf{C}(\tau_k)\mathbf{C}^H(\tau_k)$ remains of rank two. To find the rank of $\mathbf{C}(\tau_k)\mathbf{C}^H(\tau_k)$, we start with the following:

$$\text{rank}(\mathbf{C}(\tau_k)) = \text{rank}(\mathbf{\Omega}(\tau_k)\mathbf{W}) \leq \min\{\text{rank}(\mathbf{\Omega}(\tau_k)), \text{rank}(\mathbf{W})\}. \quad (5.59)$$

We have also:

$$\text{rank}(\mathbf{\Omega}(\tau_k)) + \text{rank}(\mathbf{W}) - QL_{\text{sync}} \leq \text{rank}(\mathbf{\Omega}(\tau_k)\mathbf{W}) = \text{rank}(\mathbf{C}(\tau_k)). \quad (5.60)$$

If $\mathbf{\Omega}(\tau_k)$ is a full rank matrix, then by using (5.59) and (5.60), it follows that:

$$\text{rank}(\mathbf{C}(\tau_k)) = \text{rank}(\mathbf{W}). \quad (5.61)$$

Since $\mathbf{\Omega}(\tau_k)$ is a diagonal matrix, by establishing that $\{[\mathbf{\Omega}(\tau_k)]_{qq} \neq 0\}_{q=1}^{QL_{\text{sync}}}$, we can prove that $\mathbf{\Omega}(\tau_k)$ is a full rank matrix. Now, recall that:

$$\mathbf{\Omega}(\tau) \triangleq \text{diag}\{\mathbf{G}(\tau)\mathbf{a}^{[dr]}\}. \quad (5.62)$$

Hence, the diagonal elements of $\mathbf{\Omega}(\tau)$ are given by:

$$[\mathbf{\Omega}(\tau)]_{qq} = \sum_{l=0}^{L_{\text{sync}}} a^{[dr]}[l+1]g(qT_s - L_{\text{sync}}T - \tau), \quad (5.63)$$

which are always non-zero elements due to the omnipresence in time of ISI components. It follows that $\mathbf{\Omega}(\tau)$ is a diagonal matrix with non-zero elements and, hence, full rank. As seen in Fig. 5.13, the probability that the absolute values of the diagonal element be equal to zeros is zero. Besides, $\mathbf{W} = [\mathbf{w} \ \mathbf{w}^*]$ was proved to be of rank two in [81]. It follows from (5.61) that $\mathbf{C}(\tau_k)$ is also of rank

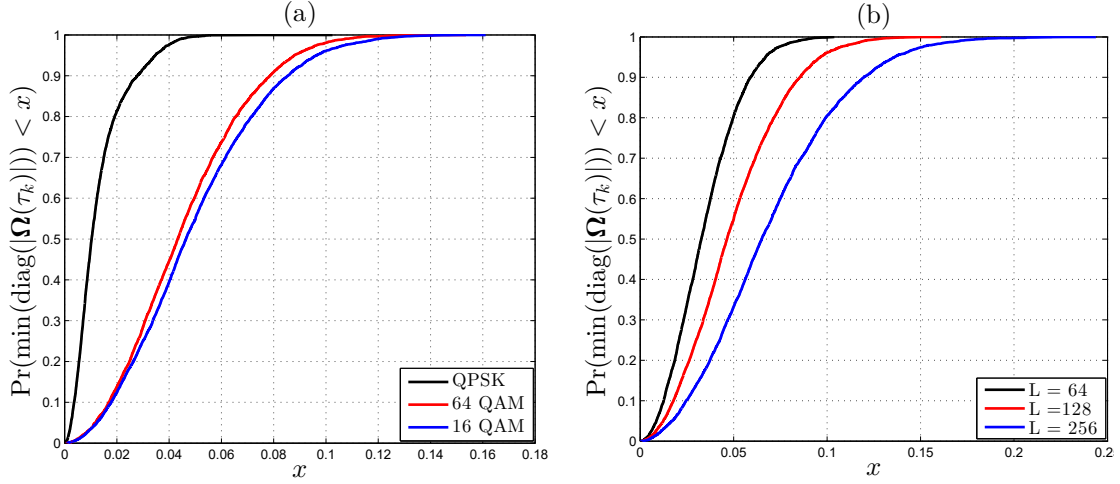


Figure 5.13 – CDF of the minimum of absolute value of $\text{diag}\{\Omega(\tau_k)\}$ for: (a) multiple modulation orders, and (b) multiple sequence lengths.

two. And since for any matrix we have:

$$\text{rank}(\mathbf{C}(\tau_k)\mathbf{C}(\tau_k)^H) = \text{rank}(\mathbf{C}(\tau_k)^H\mathbf{C}(\tau_k)) = \text{rank}(\mathbf{C}(\tau_k)) = \text{rank}(\mathbf{W}), \quad (5.64)$$

we establish that $\mathbf{C}(\tau_k)\mathbf{C}^H(\tau_k)$ is of rank two as well and also prove by the same token that this rank value is entirely related to the two-ray approximation, indeed.

Chapitre 6

Maximum Likelihood Joint Angle and Delay Estimation from Multipath and Multicarrier Transmissions With Application to Indoor Localization Over IEEE 802.11ac Radio

Faouzi Bellili, Souheib Ben Amor, Sofiène Affes, and Ali Ghrayeb
IEEE Transactions on Mobile Computing, vol. 18, no. 5, May 2019

Abstract

In this chapter, we tackle the problem of joint angle and delays estimation (JADE) of multiple reflections of a known signal impinging on multiple receiving antennae. Based on the importance sampling (IS) concept, we propose a new *non-iterative* maximum likelihood (ML) estimator that enjoys guaranteed global optimality and enhanced high-resolution capabilities for both single- and multi-carrier models. The new ML approach succeeds in transforming the original *multi-dimensional* optimization problem into multiple *two-dimensional* ones thereby resulting in huge computational savings. Moreover, it does not suffer from the off-grid problems that are inherent to most existing

JADE techniques. By exploiting the sparsity feature of a carefully designed pseudo-pdf that is intrinsic to the new estimator, we also propose a novel approach that enables the accurate detection of the unknown number of paths over a wide range of practical signal-to-noise ratios (SNRs). Computer simulations show the distinct advantage of the new ML estimator over state-of-the-art JADE techniques both in the single- and multi-carrier scenarios. Most remarkably, they suggest that the proposed IS-based ML JADE is statistically efficient as it almost reaches the Cramér-Rao lower bound (CRLB) even in the adverse conditions of low SNR levels. Using real-world channel measurements collected from four access points (APs) with IEEE 802.11ac standard's setup parameters in an indoor environment, we also show that the proposed ML estimator achieves a localization performance below 15 cm accuracy.

6.1 Introduction

In parametric multipath propagation models, a source signal impinges on an antenna array through a number of rays, each described by an angle-of-arrival (AoA), a time delay (TD), and a path gain. The JADE problem consists then in jointly estimating all the AoAs and their corresponding TDs from a finite number of received samples. The JADE problem arises in many practical situations ranging from military applications (e.g., radar and sonar) to broadband wireless communication systems. Typically, the power to characterize each path with its own angle and delay endows the system with stronger sensorial capabilities leading, for instance, to more robust beamforming techniques [42] and enhanced equalization performance [43]. Moreover, as location-aware services for handhelds are likely to be in high demand for future wireless communication systems, the information about the AoAs and the TDs can be used to design highly-accurate localization techniques [44]-[45]. In this context, in order to cope with dense multipath environments, the so-called *fingerprinting* paradigm which recasts source localization into a pattern recognition problem was envisaged in [46]-[47]. In particular, it was recently shown that *fingerprinting* with location signatures that are characterized by the AoAs and TDs of each candidate location leads to substantial improvements against location signatures that are characterized by the received signal strength (RSS) [48]. In fact, contrarily to the RSS which varies substantially over a wavelength distance (due to constructive and destructive multipath interference), the AoAs together with the associated TDs form a unique fingerprint for each location [47]. Hence, accurate and low-cost estimation of

such multipath parameters can be used along with the *fingerprinting* paradigm to develop very efficient localization algorithms. Alternatively, if multiple access points (APs) are available, they can cooperate to localize a mobile user by using the estimated time difference of arrivals (TDOAs) and AoAs (see [49] and [50] for more details). In this paper, we apply for the very first time the IS technique along with the ML concept to the JADE problem over both OFDM and single-carrier transmissions. Roughly speaking, the major difficulty with IS consists in generating multiple (i.e., vector) realizations according to a given (multi-dimensional) pdf. Much like all the aforementioned IS-based works, we succeed in designing a separable (i.e., factorable) joint angle-delay *pseudo-pdf* which allows a very easy generation of the required vector realizations. Even more, by exploiting the sparsity of the proposed pseudo-pdf, we derive a simple and yet very accurate approach to estimate the number of paths which is also *a priori* unknown in practice and needs to be estimated even before proceeding to angles and delays acquisition. Computer simulations will show the superiority of the proposed IS-based ML estimator over state-of-the-art ML-type and subspace-based JADE techniques in terms of estimation accuracy, resolution capabilities, and computational complexity. Real-world channel measurements collected using IEEE 802.11ac standard's setup parameters in an indoor environment were also used to investigate the online localization capabilities of the proposed algorithm. Results show a localization performance below 15 cm accuracy.

We organize the rest of this paper as follows: We discuss the related background works in Section 2. In section 3, we introduce the OFDM system model. In section 4, we derive the concentrated likelihood function (CLF) of the system whose global maximization is detailed in section 5. In section 6, we derive the IS-ML technique in the special case of single-carrier systems. In section 7, we detail the process of generating the required realizations via the IS concept. In section 8, we provide the necessary implementation details for the proposed IS-based estimator. In section 9, we develop a new approach for the estimation of the number of paths that is inherent to the proposed IS-based JADE algorithm. In section 10, we assess through exhaustive computer simulations the performance of the new estimator and benchmark it against a variety of existing JADE techniques. There, we also assess the localization capabilities of the proposed algorithm using real-world channel measurements. Finally, we draw out some concluding remarks in section 11.

We define beforehand some of the common notations that will be adopted in this paper. Vectors and matrices are represented in lower- and upper-case bold fonts, respectively. Moreover, $\{\cdot\}^T$ and $\{\cdot\}^H$ denote the conjugate and Hermitian (i.e., transpose conjugate) operators and $\det\{\cdot\}$ returns the determinant of any square matrix. The Euclidean norm of any vector is denoted as $\|\cdot\|$ and

\mathbf{I}_N denotes the $(N \times N)$ identity matrix. For any matrix \mathbf{X} , $[\mathbf{X}]_q$ and $[\mathbf{X}]_{l,k}$ denote its q^{th} column and $(l, k)^{th}$ entry, respectively. The kronecker product of any two matrices \mathbf{X} and \mathbf{Y} is denoted as $\mathbf{X} \otimes \mathbf{Y}$. In addition, $\{\cdot\}^*$, $\angle\{\cdot\}$, and $|\cdot|$ return the conjugate, angle, and modulus of any complex number, respectively. The complementary cumulative distribution function (CCDF) of a given random variable (RV), X , is denoted as $F_c(x) \triangleq Pr[X \geq x]$. Finally, $\mathbb{E}\{\cdot\}$ stands for the statistical expectation, j is the pure complex number that verifies $j^2 = -1$, and the notation \triangleq is used for definitions.

6.2 Overview of related works

Unlike JADE, the separate (or disjoint) estimation of either the time delays or the directions of arrival (DOA) has been heavily investigated for decades now. For prior works on DOA-only and TD-only estimation, see [51], [52] and [53], [54] and references therein, respectively. In comparison with disjoint estimation techniques which first estimate the delays and then the corresponding angles, the joint estimation of these space-time parameters (i.e., JADE) is more accurate in cases where multiple rays have nearly equal delays or angles [42]. Moreover, contrarily to JADE, the number of estimated angles in DOA-only estimation schemes must be smaller than the number of antennae. Thus DOA-only estimators would require large-size antenna arrays in highly dense multipath environments.

So far, a number of JADE techniques have been reported in the literature, except the unitary matrix pencil (UMP)-based approach proposed recently [49], all the existing solutions are geared toward single-carrier systems. Roughly speaking, they can be broadly categorized into two major categories: subspace-based and ML-based estimators. Most of the subspace-based techniques are built upon the well-known MUSIC and ESPRIT algorithms [55]-[56]. In practice, subspace-based approaches are more attractive due to their reduced computational load. However, they are usually suboptimal and suffer from severe performance degradation (both in terms of resolution and estimation accuracy) for low SNR levels and/or closely-spaced paths. ML approaches, however, are known to enjoy higher accuracy and enhanced resolution capabilities. Yet, despite their promising advantages, their computational complexity has been often considered as the major culprit for a widespread reluctance of designers to their implementation in practice.

In the specific JADE context, to the best of our knowledge only two ML estimators have been so

far introduced but only for narrowband signals. The very first ML solution was proposed by Wax *et al.* in [57] which is *iterative* in nature and thus will be referred to, hereafter, as the iterative ML (IML) estimator. The other ML solution introduced later in [58] is also *iterative* and based on the space-alternating generalized expectation maximization (SAGE) algorithm. However, like any *iterative* approach, the performance of these two ML estimators is closely tied to the initial knowledge about the unknown parameters, i.e., they will not converge to the global maximum of the log-likelihood function (LLF) if their initial guesses are not reliable. Besides, for both *iterative* ML estimators, a fixed sampling grid is selected to serve as a possible set of all candidate estimates for the unknown TDs and AoAs. Then, by assuming all true (unknown) parameters to be exactly on the selected grid, IML and SAGE attempt to maximize the LLF iteratively. Consequently, they suffer from the inevitable off-grid problem which arises in practical situations where some of the true TDs and/or AoAs do not lie on the sampling grid. For accurate estimation, it is compulsory to use a densely-sampled grid since it reduces the gap between the true parameters and their nearest points on the grid. However, as “there is no free lunch”, the cost of a dense grid sampling is the excessive increase in computational complexity.

These problems, among many others, have spurred a widespread belief that resorting to suboptimal subspace-based solutions is inevitable by trading estimation accuracy for lower complexity. This paper challenges that basic percept by introducing a novel ML JADE technique that beats state-of-the-art subspace-based methods both in terms of accuracy and complexity. Most remarkably, the new ML estimator is statistically efficient since it reaches the CRLB at SNR levels as low as -10 dB.

The proposed estimator builds upon the global maximization theorem of Pincus [59] and the importance sampling (IS) concept [60]. In particular, owing to a very accurate approximation of the concentrated likelihood function (CLF), we transform the original *multi-dimensional* optimization problem into multiple *two-dimensional* optimization ones resulting thereby in tremendous computational savings. Even more, the underlying two-dimensional optimization problems are totally disjoint and, as such, they can be performed separately in practice. From this perspective, the new IS-based ML estimator lends itself to a very attractive parallel computing implementation that can be efficiently executed on nowadays multiprocessor platforms.

The combination of Pincus’ theorem and IS concept has been previously applied to many fundamental estimation problems. To the best of our knowledge, however, this elegant combination was first pioneered by S. Kay and S. Saha in [61] in the context of multiple frequencies estimation. There,

it was shown for the very first time that joint ML estimation of multiple frequencies boils down to the computation of sample mean estimates from a number of realizations generated according to a carefully designed importance function (or pseudo-pdf). Pincus' theorem along with the IS concept were later on applied by S. Kay *et al.* to the estimation of chirp signals' parameters [62], sources' DOAs estimation with antenna arrays [52], as well as, joint angle and Doppler estimation in [63]. They were also successfully applied in the context of joint CFO and channel estimation under: *i*) single-user OFDMA communications [64], and *ii*) multiuser MIMO-OFDM communications with optimal training sequences design [65]. More recently, these powerful tools were leveraged in the context of TDOA-based source localization [66], non-data-aided (NDA) timing recovery [67], as well as, time delays acquisition in multipath environments [54]. In all these works, the combination of Pincus' theorem with the IS approach resulted in remarkable improvements both from estimation performance and computational complexity viewpoints.

6.3 System model

We will derive our estimator for multi-carrier transmissions and the minor changes that need to be accounted for when dealing with a single-carrier system will be briefly highlighted in Section 6.6. To start with, consider an antennae array consisting of P antenna elements immersed in a homogeneous medium in the far field of one source that is transmitting a planar wave. The known transmitted signal is modulated over $M + 1$ subcarriers. After undergoing multiple reflections, it impinges on the receiving antenna array from \bar{Q} different angles $(\bar{\alpha}_1, \bar{\alpha}_2, \dots, \bar{\alpha}_{\bar{Q}})$ with associated time delays $(\bar{\tau}_1, \bar{\tau}_2, \dots, \bar{\tau}_{\bar{Q}}) \subset [0, \tau_{\max}]^{\bar{Q}}$ where τ_{\max} can be as large as desired. Note here that we use the overbar symbol to distinguish the true AoAs and TDs, $\bar{\alpha}_q$ and $\bar{\tau}_q$, from the unknown generic variables, α_q and τ_q , that will be used later in the algorithm¹. We also denote the actual channel frequency response (CFR) over the $\{m^{th}\}_{M=-M/2}^{M/2}$ subcarrier and $\{p^{th}\}_{P=1}^P$ antenna element as $\bar{h}_p(m)$ whose expression was derived in [49] as follows (for more details, the reader is referred to [88]):

$$\bar{h}_p(m) = \sum_{q=1}^{\bar{Q}} \bar{\xi}_q e^{-j2\pi f_c \bar{\tau}_q} e^{-j2\pi m \Delta f \bar{\tau}_q} e^{-j2\pi \varphi_{p,m}(\bar{\alpha}_q)}. \quad (6.1)$$

1. For the same reasons, we use \bar{Q} to denote the true unknown number of paths that will be estimated later in Section VII.

In (6.1), f_c and Δf stand, respectively, for the carrier frequency and subcarrier spacing while $\{\bar{\xi}_q\}_{q=1}^{\bar{Q}}$ stand for the actual path gain coefficients which are assumed to be unknown as well. Moreover, the functions $\varphi_{p,m}(\alpha)$ represent some real-valued angular transformations that depend on the array geometry. Typically, uniform linear arrays (ULAs) and uniform circular arrays (UCAs) remain by far the most studied cases in the open literature. For these two popular configurations, the underlying angular transformations are given by:

$$\varphi_{p,m}(\alpha) = \begin{cases} \frac{d(f_c + m\Delta f)}{c}(p-1)\sin(\alpha), & \text{(ULA)} \\ \frac{d(f_c + m\Delta f)}{c} \frac{\cos(\alpha - 2[p-1]\pi/P)}{2\sin(\pi/P)}, & \text{(UCA)} \end{cases}$$

where $d = \lambda/2$ is the separation between consecutive antenna elements, and c is the speed of light. Given the transmitted signal and the received data, an estimate, $h_p(m)$, for the actual CFR $\bar{h}_p(m)$ in (6.1) can be readily obtained by applying any data-aided (DA) channel estimation technique, e.g., the least-squares method. By doing so, one has access to the following implicit observation model:

$$h_p(m) = \sum_{q=1}^{\bar{Q}} \bar{\gamma}_q e^{-j2\pi m \Delta f \bar{\tau}_q} e^{-j2\pi \varphi_p(\bar{\alpha}_q)} + w_p(m), \quad (6.2)$$

in which we defined $\bar{\gamma}_q \triangleq \bar{\xi}_q e^{-j2\pi f_c \bar{\tau}_q}$ for $q = 1, \dots, \bar{Q}$ that are some unknown but constant coefficients across all the subcarriers and antenna elements. Moreover, $w_p(m)$ are the residual estimation noise components which are assumed to be spatially white and uncorrelated between subcarriers. Statistically, they are modeled by zero-mean complex Gaussian random processes with independent real and imaginary parts each of variance $\sigma^2/2$.

For mathematical convenience, we now group all the unknown multipath parameters in the following three vectors: $\bar{\alpha} = [\bar{\alpha}_1, \bar{\alpha}_2, \dots, \bar{\alpha}_{\bar{Q}}]^T$, $\bar{\tau} = [\bar{\tau}_1, \bar{\tau}_2, \dots, \bar{\tau}_{\bar{Q}}]^T$, and $\bar{\gamma} = [\bar{\gamma}_1, \bar{\gamma}_2, \dots, \bar{\gamma}_{\bar{Q}}]^T$. We further gather the channel estimates in (6.2) across all the antenna elements at each m^{th} subcarrier into a single vector, $\mathbf{h}(m) = [h_1(m), h_2(m), \dots, h_P(m)]^T$, given by:

$$\mathbf{h}(m) = \sum_{q=1}^{\bar{Q}} \mathbf{a}_m(\bar{\alpha}_q) \bar{\gamma}_q e^{-j2\pi m \Delta f \bar{\tau}_q} + \mathbf{w}(m), \quad (6.3)$$

where $\mathbf{w}(m) = [w_1(m), w_2(m), \dots, w_P(m)]^T$ is the corresponding noise vector and:

$$\mathbf{a}_m(\alpha) \triangleq [e^{-j2\pi\varphi_{1,m}(\alpha)}, e^{-j2\pi\varphi_{2,m}(\alpha)}, \dots, e^{-j2\pi\varphi_{P,m}(\alpha)}]^T, \quad (6.4)$$

is the array *steering vector* defined for any direction α . Our goal in the remainder of this paper is to jointly estimate the parameters $\{\bar{\alpha}_q\}_{q=1}^{\bar{Q}}$ and $\{\bar{\tau}_q\}_{q=1}^{\bar{Q}}$ along with \bar{Q} given the $M + 1$ vectors $\{\mathbf{h}(m)\}_{m=-M/2}^{M/2}$.

6.4 Derivation of the concentrated likelihood function (CLF)

In this section, we will derive the *concentrated* likelihood function (CLF) that depends on the parameters of interest only [89], namely $\bar{\boldsymbol{\tau}}, \bar{\boldsymbol{\alpha}}$. In fact, since $\mathbf{w}(m) \sim \mathcal{N}(\mathbf{0}, \sigma^2 \mathbf{I}_P)$, it can be shown that the actual LLF (after dropping the constant terms) is given by²:

$$\mathcal{L}(\boldsymbol{\alpha}, \boldsymbol{\tau}, \boldsymbol{\gamma}) = \sum_{m=-\frac{M}{2}}^{\frac{M}{2}} \left\| \mathbf{h}(m) - \sum_{q=1}^{\bar{Q}} \mathbf{a}_m(\alpha_q) \gamma_q e^{-j2\pi m \Delta f \bar{\tau}_q} \right\|^2. \quad (6.5)$$

where $\boldsymbol{\tau}$, $\boldsymbol{\alpha}$, and $\boldsymbol{\gamma}$ stand for any candidate values for $\bar{\boldsymbol{\tau}}$, $\bar{\boldsymbol{\alpha}}$, and $\bar{\boldsymbol{\gamma}}$, respectively. Now, define the $(M\bar{Q} \times \bar{Q})$ matrix:

$$\boldsymbol{\Phi}(\boldsymbol{\tau}) \triangleq \left[\boldsymbol{\Phi}_{-M/2}(\boldsymbol{\tau})^T \boldsymbol{\Phi}_{-M/2+1}(\boldsymbol{\tau})^T \dots \boldsymbol{\Phi}_{M/2}(\boldsymbol{\tau})^T \right]^T, \quad (6.6)$$

with $\{\boldsymbol{\Phi}_m(\boldsymbol{\tau})\}_{m=-M/2}^{M/2}$ being the following $(\bar{Q} \times \bar{Q})$ diagonal matrix:

$$\boldsymbol{\Phi}_m(\boldsymbol{\tau}) \triangleq \text{diag}(e^{-j\omega_m \tau_1}, e^{-j\omega_m \tau_2}, \dots, e^{-j\omega_m \tau_{\bar{Q}}}), \quad (6.7)$$

2. Note here that, for ease of notation, we do not show explicitly the dependence of the LLF on $\{\mathbf{h}(m)\}_{m=-M/2}^{M/2}$ in the left-hand side of (6.5).

and $\omega_m = 2\pi m\Delta f$. Therefore, by letting $\mathbf{A}_m(\boldsymbol{\alpha}) \triangleq [\mathbf{a}_m(\alpha_1) \ \mathbf{a}_m(\alpha_2) \ \cdots \ \mathbf{a}_m(\alpha_{\bar{Q}})]$ and defining the following array *steering matrix*:

$$\mathbf{A}(\boldsymbol{\alpha}) = \begin{pmatrix} \mathbf{A}_{-M/2}(\boldsymbol{\alpha}) & \mathbf{0} & \cdots & \mathbf{0} \\ \mathbf{0} & \mathbf{A}_{-M/2+1}(\boldsymbol{\alpha}) & & \vdots \\ \vdots & & \ddots & \mathbf{0} \\ \mathbf{0} & \cdots & \mathbf{0} & \mathbf{A}_{M/2}(\boldsymbol{\alpha}) \end{pmatrix}, \quad (6.8)$$

it can be shown that (6.5) is equivalent to:

$$\mathcal{L}(\boldsymbol{\alpha}, \boldsymbol{\tau}, \boldsymbol{\gamma}) = \left\| \mathbf{h} - \mathbf{A}(\boldsymbol{\alpha})\boldsymbol{\Phi}(\boldsymbol{\tau})\boldsymbol{\gamma} \right\|^2, \quad (6.9)$$

where $\mathbf{h} \triangleq [\mathbf{h}(\omega_{-M/2})^T \mathbf{h}(\omega_{-M/2+1})^T \cdots \mathbf{h}(\omega_{M/2})^T]^T$. Maximizing (6.9) jointly with respect to $\boldsymbol{\tau}$, $\boldsymbol{\alpha}$, and $\boldsymbol{\gamma}$ is extremely challenging. Yet, significant computational savings follow from the observation that for any given $\boldsymbol{\tau}$ and $\boldsymbol{\alpha}$, the problem of finding the optimal $\boldsymbol{\gamma}$ becomes a linear least squares (LS) problem [90] whose solution is given by:

$$\hat{\boldsymbol{\gamma}}_{\text{MLE}} = \underbrace{[\mathbf{A}(\boldsymbol{\alpha})\boldsymbol{\Phi}(\boldsymbol{\tau})]^{\dagger}}_{\triangleq \mathbf{D}} \mathbf{h}, \quad (6.10)$$

where \mathbf{D}^{\dagger} is the Moore-Penrose pseudo-inverse of \mathbf{D} given by $\mathbf{D}^{\dagger} = (\mathbf{D}^H \mathbf{D})^{-1} \mathbf{D}^H$. Note here that \mathbf{D} has full column rank and, therefore, $(\mathbf{D}^H \mathbf{D})^{-1}$ always exists. Now, by substituting $\hat{\boldsymbol{\gamma}}_{\text{MLE}}$ for $\boldsymbol{\gamma}$ back in (6.9) and resorting to some straightforward algebraic manipulations, we obtain the so-called *concentrated* likelihood function (CLF) which depends solely on $\boldsymbol{\alpha}$ and $\boldsymbol{\tau}$:

$$\mathcal{L}_c(\boldsymbol{\alpha}, \boldsymbol{\tau}) = \mathbf{h}^H \mathbf{D} (\mathbf{D}^H \mathbf{D})^{-1} \mathbf{D}^H \mathbf{h}, \quad (6.11)$$

The joint ML estimates of $\bar{\boldsymbol{\alpha}}$ and $\bar{\boldsymbol{\tau}}$ are then obtained as the solution to the following reduced-dimension optimization problem:

$$[\hat{\boldsymbol{\alpha}}_{\text{MLE}}, \hat{\boldsymbol{\tau}}_{\text{MLE}}] = \underset{\boldsymbol{\alpha}, \boldsymbol{\tau}}{\operatorname{argmax}} \mathcal{L}_c(\boldsymbol{\alpha}, \boldsymbol{\tau}). \quad (6.12)$$

Once $\hat{\boldsymbol{\alpha}}_{\text{MLE}}$ and $\hat{\boldsymbol{\tau}}_{\text{MLE}}$ are obtained, they can be substituted back in (6.10) in order to find the MLEs for all the unknown path gains, i.e., $\hat{\boldsymbol{\gamma}}_{\text{MLE}}$.

6.5 Global maximization of the CLF

6.5.1 Pincus' theorem and the IS concept

As done previously within the framework of other estimation problems (see [52], [61]-[67], and references therein), we will resort to Pincus' theorem [59] and the powerful IS concept [91] in order to solve the multidimensional optimization problem in (6.12). The theorem proposed by Pincus in [59] simply states that the global maximum of any continuous \tilde{Q} -dimensional function, $f(\boldsymbol{\theta})$, is reached at the vector $\hat{\boldsymbol{\theta}} = [\hat{\theta}_1, \hat{\theta}_2, \dots, \hat{\theta}_{\tilde{Q}}]$ whose $\{q^{th}\}_{q=1}^{\tilde{Q}}$ entry is given by:

$$\hat{\theta}_q = \lim_{\rho \rightarrow +\infty} \frac{\int \dots \int \theta_q e^{\rho f(\boldsymbol{\theta})} d\boldsymbol{\theta}}{\int \dots \int e^{\rho f(\boldsymbol{\theta})} d\boldsymbol{\theta}}. \quad (6.13)$$

The limit involved in (6.13) is approximated for some sufficiently high value ρ_0 of ρ as follows:

$$\hat{\theta}_q = \frac{\int \dots \int \alpha_q e^{\rho_0 f(\boldsymbol{\theta})} d\boldsymbol{\theta}}{\int \dots \int e^{\rho_0 f(\boldsymbol{\theta})} d\boldsymbol{\theta}}. \quad (6.14)$$

Applying this general result to our estimation problem with $\boldsymbol{\theta} \triangleq [\boldsymbol{\alpha}, \boldsymbol{\tau}]^T$ and $f(\boldsymbol{\theta}) \triangleq \mathcal{L}_c(\boldsymbol{\alpha}, \boldsymbol{\tau})$ leads to the following expressions for the required MLEs (each in terms of $2\tilde{Q}$ -dimensional integrals) for $q = 1, 2, \dots, \tilde{Q}$:

$$\hat{\tau}_{q, \text{MLE}} = \int \dots \int \tau_q \bar{\mathcal{L}}_c(\boldsymbol{\alpha}, \boldsymbol{\tau}) d\boldsymbol{\alpha} d\boldsymbol{\tau}, \quad (6.15)$$

$$\hat{\alpha}_{q, \text{MLE}} = \int \dots \int \alpha_q \bar{\mathcal{L}}_c(\boldsymbol{\alpha}, \boldsymbol{\tau}) d\boldsymbol{\alpha} d\boldsymbol{\tau}, \quad (6.16)$$

where $\bar{\mathcal{L}}_c(\boldsymbol{\alpha}, \boldsymbol{\tau})$ is the *normalized CLF* defined as:

$$\bar{\mathcal{L}}_c(\boldsymbol{\alpha}, \boldsymbol{\tau}) \triangleq \frac{e^{\rho_0 \mathcal{L}_c(\boldsymbol{\alpha}, \boldsymbol{\tau})}}{\int \dots \int e^{\rho_0 \mathcal{L}_c(\boldsymbol{\alpha}, \boldsymbol{\tau})} d\boldsymbol{\alpha} d\boldsymbol{\tau}}. \quad (6.17)$$

Intuitively, as ρ_0 tends to infinity, $\bar{\mathcal{L}}_c(\boldsymbol{\alpha}, \boldsymbol{\tau})$ becomes a Dirac-delta function centered at the true maximum of $\mathcal{L}_c(\boldsymbol{\alpha}, \boldsymbol{\tau})$ whose location is indeed given by the set of integrals in (6.15) and (6.16). In our attempt to avoid multi-dimensional grid search, it may appear here at first sight that we

have we ended up dealing with a multi-dimensional integration bearing the very same practical difficulties. By closely inspecting (6.17), however, it turns out that the *normalized CLF*, $\bar{\mathcal{L}}_c(\boldsymbol{\alpha}, \boldsymbol{\tau})$, has all the properties of a pdf since it is nonnegative and integrates to one. Consequently, we will term it in the sequel as “*pseudo-pdf*” since strictly speaking the involved working variables $\boldsymbol{\alpha}$ and $\boldsymbol{\tau}$ are not truly random. Yet, by hypothetically assuming them to be random vectors that are jointly distributed according to $\bar{\mathcal{L}}_c(\boldsymbol{\alpha}, \boldsymbol{\tau})$, the MLEs in (6.15) and (6.16) can be alternatively regarded as statistical expectations, i.e., for $q = 1, 2, \dots, \bar{Q}$, we have:

$$\hat{\tau}_{q,\text{MLE}} = \mathbb{E}_{\boldsymbol{\alpha}, \boldsymbol{\tau}} \{ \tau_q \} \quad \text{and} \quad \hat{\alpha}_{q,\text{MLE}} = \mathbb{E}_{\boldsymbol{\alpha}, \boldsymbol{\tau}} \{ \alpha_q \}. \quad (6.18)$$

Thus, if one is able to generate R realizations, $\{\boldsymbol{\tau}^{(r)}\}_{r=1}^R$ and $\{\boldsymbol{\alpha}^{(r)}\}_{r=1}^R$, using the joint *pseudo-pdf* $\bar{\mathcal{L}}_c(\boldsymbol{\tau}, \boldsymbol{\alpha})$, then it will be very accurate to approximate the expectations in (6.18) by their sample mean estimates as follows:

$$\hat{\tau}_{q,\text{MLE}} = \frac{1}{R} \sum_{r=1}^R \tau_q^{(r)} \quad \text{and} \quad \hat{\alpha}_{q,\text{MLE}} = \frac{1}{R} \sum_{r=1}^R \alpha_q^{(r)}. \quad (6.19)$$

Clearly, as the number of realizations R used in (6.19) increases, the variances of the two sample mean estimates above decrease making them approach the global maximum of the CLF [91]. Unfortunately, the pseudo-pdf $\bar{\mathcal{L}}_c(\boldsymbol{\alpha}, \boldsymbol{\tau})$ is extremely non-linear and as such cannot be practically used to generate $\{\boldsymbol{\tau}^{(r)}\}_{r=1}^R$ and $\{\boldsymbol{\alpha}^{(r)}\}_{r=1}^R$. To sidestep this problem, one can resort to the importance sampling concept [52], [61] and rewrite (6.15) and (6.16) in the following equivalent forms:

$$\hat{\tau}_{q,\text{MLE}} = \int \cdots \int \tau_q \frac{\bar{\mathcal{L}}_c(\boldsymbol{\alpha}, \boldsymbol{\tau})}{\bar{\mathcal{G}}(\boldsymbol{\alpha}, \boldsymbol{\tau})} \bar{\mathcal{G}}(\boldsymbol{\alpha}, \boldsymbol{\tau}) d\boldsymbol{\alpha} d\boldsymbol{\tau}, \quad (6.20)$$

$$\hat{\alpha}_{q,\text{MLE}} = \int \cdots \int \alpha_q \frac{\bar{\mathcal{L}}_c(\boldsymbol{\alpha}, \boldsymbol{\tau})}{\bar{\mathcal{G}}(\boldsymbol{\alpha}, \boldsymbol{\tau})} \bar{\mathcal{G}}(\boldsymbol{\alpha}, \boldsymbol{\tau}) d\boldsymbol{\alpha} d\boldsymbol{\tau}. \quad (6.21)$$

for some $\bar{\mathcal{G}}(\boldsymbol{\alpha}, \boldsymbol{\tau})$ which is another pseudo-pdf — called *importance function* — to be designed as close as possible to $\bar{\mathcal{L}}_c(\boldsymbol{\alpha}, \boldsymbol{\tau})$ while allowing at the same time the easy generation of the required vector realizations $\{\boldsymbol{\tau}^{(r)}\}_{r=1}^R$ and $\{\boldsymbol{\alpha}^{(r)}\}_{r=1}^R$. By doing so, the MLEs in (6.20) and (6.21) are interpreted as expected values of transformed RVs, i.e.:

$$\hat{\tau}_{q,\text{MLE}} = \mathbb{E}_{\boldsymbol{\alpha}, \boldsymbol{\tau}} \{ \eta(\boldsymbol{\tau}, \boldsymbol{\alpha}) \tau_q \} \quad (6.22)$$

$$\hat{\alpha}_{q,\text{MLE}} = \mathbb{E}_{\boldsymbol{\alpha}, \boldsymbol{\tau}} \{ \eta(\boldsymbol{\alpha}, \boldsymbol{\tau}) \alpha_q \}, \quad (6.23)$$

where $\eta(\boldsymbol{\alpha}, \boldsymbol{\tau})$ is defined as the following ratio:

$$\eta(\boldsymbol{\alpha}, \boldsymbol{\tau}) \triangleq \frac{\bar{\mathcal{L}}_c(\boldsymbol{\alpha}, \boldsymbol{\tau})}{\bar{\mathcal{G}}(\boldsymbol{\alpha}, \boldsymbol{\tau})}. \quad (6.24)$$

If $\bar{\mathcal{G}}(\boldsymbol{\alpha}, \boldsymbol{\tau})$ is carefully designed, the expectations in (6.22) and (6.23) can be computed at any desired degree of accuracy (by increasing R) using the corresponding sample mean estimates. The appropriate choice of the importance function, $\bar{\mathcal{G}}(\boldsymbol{\alpha}, \boldsymbol{\tau})$, will be discussed in the following subsection. But before delving into details, we mention beforehand that it must be separable in terms of the \bar{Q} angle-delay pairs $\{(\alpha_q, \tau_q)\}_{q=1}^{\bar{Q}}$ in order to facilitate the process of generating the required R vector realizations. In other words, our ultimate goal is to design $\bar{\mathcal{G}}(\boldsymbol{\alpha}, \boldsymbol{\tau})$ in a way that allows it to be factorized as follows:

$$\bar{\mathcal{G}}(\boldsymbol{\alpha}, \boldsymbol{\tau}) = \prod_{q=1}^{\bar{Q}} \bar{g}_q(\alpha_q, \tau_q). \quad (6.25)$$

This will allow us to interpret $\bar{\mathcal{G}}(\boldsymbol{\alpha}, \boldsymbol{\tau})$ as a multivariate pseudo-pdf that corresponds to a set of *independent* bivariate random variables. Hence, instead of generating realizations for \bar{Q} -dimensional random vectors $\boldsymbol{\alpha}$ and $\boldsymbol{\tau}$ directly using $\bar{\mathcal{G}}(\boldsymbol{\alpha}, \boldsymbol{\tau})$, one can easily generate independent realizations for *bivariate* random variables $\{(\alpha_q, \tau_q)\}_{q=1}^{\bar{Q}}$ using $\{\bar{g}_q(\alpha_q, \tau_q)\}_q^{\bar{Q}}$. In order to reduce the variance of estimation errors, however, it is preferable to design $\bar{\mathcal{G}}(\boldsymbol{\alpha}, \boldsymbol{\tau})$ upon an appropriate approximation of $\bar{\mathcal{L}}_c(\boldsymbol{\alpha}, \boldsymbol{\tau})$.

6.5.2 Approximation of the CLF and appropriate choice for $\bar{\mathcal{G}}(\boldsymbol{\alpha}, \boldsymbol{\tau})$

First, by revisiting (6.11), one can easily recognize that the original CLF, $\mathcal{L}_c(\boldsymbol{\alpha}, \boldsymbol{\tau})$, cannot be directly expressed as a separable function due to the presence of the matrix inverse $(\mathbf{D}^H \mathbf{D})^{-1}$. Fortunately, though, we show in the sequel that $\mathbf{D}^H \mathbf{D}$ can be accurately approximated by a diagonal matrix. In fact, by recalling the expression of \mathbf{D} in (6.10), we notice that the delay coming from the antenna array is negligible when compared with τ_l (i.e., $p d \sin(\alpha_l)/c \ll \tau_l$), it follows that:

$$\mathbf{D} = [\mathbf{I}_M \otimes \mathbf{A}_0(\boldsymbol{\alpha})] \boldsymbol{\Phi}(\boldsymbol{\tau}). \quad (6.26)$$

By using some basic properties of the Kronecker product, the matrix $\mathbf{D}^H \mathbf{D}$ can be written as:

$$\begin{aligned} \mathbf{D}^H \mathbf{D} &= \Phi(\boldsymbol{\tau})^H [\mathbf{I}_{M+1} \otimes \mathbf{A}(\boldsymbol{\alpha})^H] [\mathbf{I}_{M+1} \otimes \mathbf{A}(\boldsymbol{\alpha})] \Phi(\boldsymbol{\tau}), \\ &= \Phi(\boldsymbol{\tau})^H \left(\mathbf{I}_{M+1} \otimes [\mathbf{A}(\boldsymbol{\alpha})^H \mathbf{A}(\boldsymbol{\alpha})] \right) \Phi(\boldsymbol{\tau}). \end{aligned} \quad (6.27)$$

Then, by noticing that $\mathbf{I}_{M+1} \otimes [\mathbf{A}_0(\boldsymbol{\alpha})^H \mathbf{A}_0(\boldsymbol{\alpha})]$ is a block-diagonal matrix, it can be shown that:

$$\mathbf{D}^H \mathbf{D} = \sum_{m=-M/2}^{M/2} \Phi_m(\boldsymbol{\tau})^H \mathbf{A}_0(\boldsymbol{\alpha})^H \mathbf{A}_0(\boldsymbol{\alpha}) \Phi_m(\boldsymbol{\tau}). \quad (6.28)$$

Next, by recalling that the l^{th} column of the steering matrix is $[\mathbf{A}_0(\boldsymbol{\alpha})]_l = \mathbf{a}_0(\alpha_l)$ and since $\Phi_m(\boldsymbol{\tau})$ is a diagonal matrix, we immediately have:

$$\begin{aligned} [\mathbf{A}_0(\boldsymbol{\alpha}) \Phi_m(\boldsymbol{\tau})]_l &= [\Phi_m(\boldsymbol{\tau})]_{l,l} [\mathbf{A}_0(\boldsymbol{\alpha})]_l \\ &= e^{-j\omega_m \tau_l} \mathbf{a}_0(\alpha_l). \end{aligned}$$

The $(l, k)^{\text{th}}$ entry of $\mathbf{D}^H \mathbf{D}$ is thus obtained as:

$$\begin{aligned} [\mathbf{D}^H \mathbf{D}]_{l,k} &= \sum_{m=-M/2}^{M/2} ([\mathbf{A}_0(\boldsymbol{\alpha}) \Phi_m(\boldsymbol{\tau})]_l)^H [\mathbf{A}_0(\boldsymbol{\alpha}) \Phi_m(\boldsymbol{\tau})]_k, \\ &= \sum_{m=-M/2}^{M/2} e^{j\omega_m (\tau_l - \tau_k)} \mathbf{a}_0(\alpha_l)^H \mathbf{a}_0(\alpha_k), \\ &= \sum_{m=-M/2}^{M/2} e^{j\omega_m (\tau_l - \tau_k)} \times \sum_{p=1}^P e^{-j2\pi[\varphi_p(\alpha_k) - \varphi_p(\alpha_l)]}. \end{aligned} \quad (6.29)$$

In particular, all the diagonal elements are expressed as:

$$[\mathbf{D}^H \mathbf{D}]_{k,k} = P(M+1). \quad (6.30)$$

Due to the destructive superposition (for $l \neq k$) of the complex exponentials³ in (6.29), one could expect the off-diagonal entries of $\mathbf{D}^H \mathbf{D}$ to be very small compared to the diagonal ones thereby allowing the following much useful approximation:

$$\mathbf{D}^H \mathbf{D} \approx P(M+1) \mathbf{I}_{\bar{Q}}. \quad (6.31)$$

3. This is reminiscent of multipath fading in wireless channels.

To see this, we define:

$$\beta_{l,k} \triangleq \frac{\left(\sum_{m=-M/2}^{M/2} e^{j\omega_m(\tau_l - \tau_k)} \right) \left(\sum_{p=1}^P e^{-j2\pi[\varphi_p(\alpha_k) - \varphi_p(\alpha_l)]} \right)}{P(M+1)}, \quad (6.32)$$

as the ratio of the off-diagonal over diagonal entries of $\mathbf{D}^H \mathbf{D}$. Then, we generate a large number of couples $(\tau_l, \tau_k) \sim U[0, \tau_{\max}]^2$ and $(\alpha_l, \alpha_k) \sim U[-\pi/2, \pi/2]^2$ and inject them into (6.32) in order to compute the CCDF, $F_c(x) = Pr[|\beta_{l,k}| \geq x]$, depicted in Fig. 6.1. There, it can be seen that

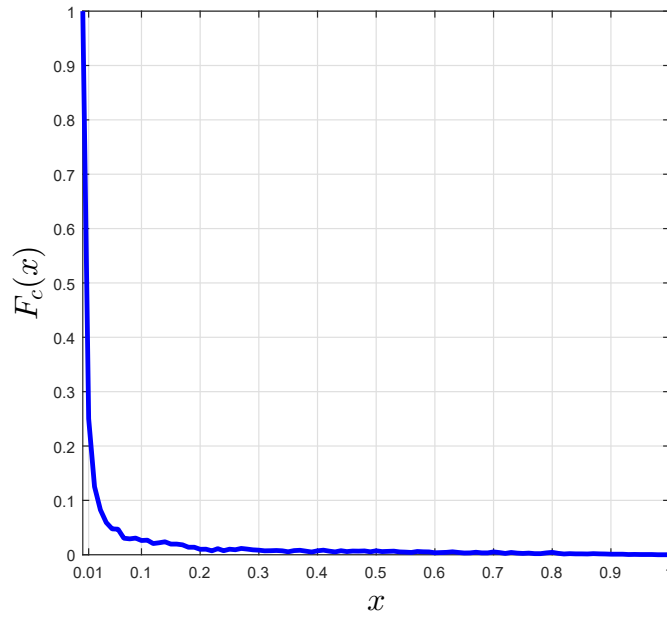


Figure 6.1 – CCDF of the magnitude of the ratio between the off-diagonal and diagonal entries of the matrix $\mathbf{D}^H \mathbf{D}$, using $M + 1 = 245$ subcarriers and a ULA configuration of $P = 6$ receiving antenna elements.

the off-diagonal elements of $\mathbf{D}^H \mathbf{D}$ can indeed be neglected in front of its diagonal ones since $|\beta_{l,k}|$ has an almost-zero probability to exceed 0.1 for all $l \neq k$. Therefore, (6.31) is a valid and accurate approximation for $\mathbf{D}^H \mathbf{D}$ which is used in (6.11) to obtain the following accurate approximation

$$\mathcal{L}_c(\boldsymbol{\alpha}, \boldsymbol{\tau}) \approx \frac{1}{P(M+1)} \mathbf{h}^H \mathbf{D} \mathbf{D}^H \mathbf{h}. \quad (6.33)$$

Recalling from (6.10) that $\mathbf{D} = \mathbf{A}(\boldsymbol{\alpha}) \boldsymbol{\Phi}(\boldsymbol{\tau})$, it follows that:

$$\mathcal{L}_c(\boldsymbol{\alpha}, \boldsymbol{\tau}) \approx \frac{1}{P(M+1)} \left\| \boldsymbol{\Phi}(\boldsymbol{\tau})^H \mathbf{A}(\boldsymbol{\alpha})^H \mathbf{h} \right\|^2. \quad (6.34)$$

Now, by recalling that:

$$\mathbf{h} = \left[\mathbf{h}(-M/2)^T \mathbf{h}(-M/2 + 1)^T \cdots \mathbf{h}(M/2)^T \right]^T, \quad (6.35)$$

and using (6.6) it can be shown that:

$$\Phi(\boldsymbol{\tau})^H \mathbf{A}(\boldsymbol{\alpha})^H \mathbf{h} = \sum_{m=-M/2}^{M/2} [\mathbf{A}_m(\boldsymbol{\alpha}) \Phi_m(\boldsymbol{\tau})]^H \mathbf{h}(m). \quad (6.36)$$

Therefore, it follows from (6.34) that:

$$\begin{aligned} \mathcal{L}_c(\boldsymbol{\alpha}, \boldsymbol{\tau}) \\ \approx \frac{1}{P(M+1)} \sum_{q=1}^{\bar{Q}} \left| \sum_{m=-M/2}^{M/2} [\mathbf{A}_m(\boldsymbol{\alpha}) \Phi_m(\boldsymbol{\tau})]_q^H \mathbf{h}(m) \right|^2. \end{aligned} \quad (6.37)$$

Starting from (6.37) and resorting to some straightforward algebraic manipulations, we obtain the following much useful approximation for the CLF:

$$\mathcal{L}_c(\boldsymbol{\alpha}, \boldsymbol{\tau}) \approx \frac{1}{P(M+1)} \sum_{q=1}^{\bar{Q}} I(\alpha_q, \tau_q), \quad (6.38)$$

where $I(\alpha, \tau)$ is the periodogram of the signal given by:

$$I(\alpha, \tau) = \left| \sum_{p=1}^P \sum_{m=-M/2}^{M/2} e^{-j2\pi\varphi_{p,m}(\alpha)} h_p^*(m) e^{-j2\pi\tau\omega_m} \right|^2, \quad (6.39)$$

in which $h_p(m)$ is the p^{th} element of the vector $\mathbf{h}(m)$. Owing to the decomposition of the *approximate* CLF in (6.38) as the superposition of the separate contributions pertaining to the \bar{Q} angle-delay pairs, we exploit it below as the *importance function* (upon normalization):

$$\bar{\mathcal{G}}(\boldsymbol{\alpha}, \boldsymbol{\tau}) = \frac{\exp \left\{ \rho_1 \sum_{q=1}^{\bar{Q}} I(\alpha_q, \tau_q) \right\}}{\int \cdots \int \exp \left\{ \rho_1 \sum_{q=1}^{\bar{Q}} I(\alpha'_q, \tau'_q) \right\} d\boldsymbol{\alpha}' d\boldsymbol{\tau}'}. \quad (6.40)$$

Note here that the factor $\frac{1}{P(M+1)}$ involved in (6.38) is absorbed in the new design parameter, $\rho_1 \neq \rho_0$, whose appropriate choice will be discussed later in section 6.10. Note as well that $\bar{\mathcal{G}}(\boldsymbol{\alpha}, \boldsymbol{\tau})$ is *separable* in terms of the angle-delay pairs as originally required. Indeed, it can be easily shown

that $\bar{\mathcal{G}}(\boldsymbol{\alpha}, \boldsymbol{\tau})$ factorizes as follows:

$$\bar{\mathcal{G}}(\boldsymbol{\alpha}, \boldsymbol{\tau}) = \prod_{q=1}^{\bar{Q}} \bar{g}_{\bar{\alpha}_q, \bar{\tau}_q}(\alpha_q, \tau_q), \quad (6.41)$$

where

$$\bar{g}_{\bar{\alpha}, \bar{\tau}}(\alpha, \tau) = \frac{e^{\rho_1 I(\alpha, \tau)}}{\iint e^{\rho_1 I(\alpha', \tau')} d\alpha' d\tau'}. \quad (6.42)$$

is a common bivariate distribution for all angle/delay pairs. Therefore, in order to generate vector realizations $\boldsymbol{\alpha}^{(r)}$ and $\boldsymbol{\tau}^{(r)}$ using the multidimensional distribution $\bar{\mathcal{G}}(\boldsymbol{\alpha}, \boldsymbol{\tau})$, one can easily generate \bar{Q} independent couples $(\alpha_q^{(r)}, \tau_q^{(r)})$ using $\bar{g}_{\bar{\alpha}_q, \bar{\tau}_q}(\alpha, \tau)$ then construct $\boldsymbol{\alpha}^{(r)} = [\alpha_1^{(r)}, \alpha_2^{(r)}, \dots, \alpha_{\bar{Q}}^{(r)}]$ and $\boldsymbol{\tau}^{(r)} = [\tau_1^{(r)}, \tau_2^{(r)}, \dots, \tau_{\bar{Q}}^{(r)}]$. The process of generating $\{(\alpha_q^{(r)}, \tau_q^{(r)})\}_{q=1}^{\bar{Q}}$ using $\bar{g}_{\bar{\alpha}, \bar{\tau}}(\alpha, \tau)$ is explained in some depth later in Section 6.7.

6.6 Special case of single-carrier systems

Assume that a known modulated signal $s(t)$ is transmitted by the source. After sampling the continuous-time received signal at time instants $\{t_m = mT_s\}_{m=0}^{(M-1)}$ where T_s is the sampling period, one obtains the following M samples over each p th antenna:

$$x_p(t_m) = \sum_{q=1}^{\bar{Q}} \bar{\xi}_q s(t_m - \bar{\tau}_q) e^{j\pi\varphi_p(\bar{\alpha}_q)} + w_p(t_m), \quad (6.43)$$

for $m = 0, 2, \dots, M-1$. By collecting the samples across all the antenna elements at each m^{th} time index, $\mathbf{x}(t_m) = [x_1(t_m), x_2(t_m), \dots, x_P(t_m)]^T$, one obtains:

$$\mathbf{x}(t_m) = \sum_{q=1}^{\bar{Q}} \mathbf{a}_0(\bar{\alpha}_q) \bar{\xi}_q s(t_m - \bar{\tau}_q) + \mathbf{w}(t_m), \quad (6.44)$$

in which $\mathbf{a}_0(\bar{\alpha}_q)$ obtained from (6.4) by setting $m = 0$. Then, by using Parseval's identity, it can be shown that the actual LLF is expressed as follows in the case of single-carrier systems:

$$\mathcal{L}_{\text{SC}}(\boldsymbol{\alpha}, \boldsymbol{\tau}, \boldsymbol{\gamma}) \approx \sum_{m=0}^{M-1} \left\| \mathbf{x}(\omega_m) - \sum_{q=1}^{\bar{Q}} \mathbf{a}_0(\alpha_q) \gamma_q e^{-j\omega_m \tau_q} s(\omega_m) \right\|^2, \quad (6.45)$$

where $\{\mathbf{x}(\omega_m)\}_m$ and $\{s(\omega_m)\}_m$ are, respectively, the DFTs of $\{\mathbf{x}(t_m)\}_m$ and $\{s(t_m)\}_m$ and $\{\omega_m = \frac{m}{MT_s}\}_{m=0}^{M-1}$ is the m^{th} frequency bin. By following the same derivations as done in the OFDM model in the previous sections, it can be shown that the CLF of SC systems is expressed as follows:

$$\mathcal{L}_c^{\text{SC}}(\boldsymbol{\alpha}, \boldsymbol{\tau}) = \mathbf{x}^H \mathbf{D} (\mathbf{D}^H \mathbf{D})^{-1} \mathbf{D}^H \mathbf{x}, \quad (6.46)$$

where $\mathbf{x} \triangleq [\mathbf{x}(\omega_1)^T \mathbf{x}(\omega_2)^T \cdots \mathbf{x}(\omega_M)^T]^T$ and the matrix \mathbf{D} is given by:

$$\mathbf{D} = [\mathbf{I}_M \otimes \mathbf{A}_0(\boldsymbol{\alpha})] \boldsymbol{\Phi}(\boldsymbol{\tau}). \quad (6.47)$$

Then, it is easy to show that $\mathbf{D}^H \mathbf{D}$ can also be approximated by a diagonal matrix thereby leading to the same expression for the importance function already obtained in and (6.41) and (6.42). The only difference being in the expression of the periodogram which is now given by:

$$I_{\text{sc}}(\boldsymbol{\alpha}, \boldsymbol{\tau}) = \left| \sum_{p=1}^P e^{j\pi\varphi_p(\boldsymbol{\alpha})} \sum_{m=0}^{M-1} s(\omega_m) x_p^*(\omega_m) e^{-j2\pi\tau\omega_m} \right|^2, \quad (6.48)$$

in which $x_p(\omega_m)$ is the p^{th} element of the vector $\mathbf{x}(\omega_m)$. The remaining derivations hold exactly the same for both single- and multi-carrier systems.

6.7 Generation of the required realizations

A well-known general result from probability theory is that the joint distribution, $\bar{g}_{\bar{\alpha}, \bar{\tau}}(\boldsymbol{\alpha}, \boldsymbol{\tau})$, can be factorized as the product of marginal and conditional pdfs, in two equivalent forms, as follows:

$$\bar{g}_{\bar{\alpha}, \bar{\tau}}(\boldsymbol{\alpha}, \boldsymbol{\tau}) = \bar{g}_{\bar{\tau}}(\boldsymbol{\tau}) \bar{g}_{\bar{\alpha}|\bar{\tau}}(\boldsymbol{\alpha}|\boldsymbol{\tau}), \quad (6.49)$$

$$\bar{g}_{\bar{\alpha}, \bar{\tau}}(\boldsymbol{\alpha}, \boldsymbol{\tau}) = \bar{g}_{\bar{\alpha}}(\boldsymbol{\alpha}) \bar{g}_{\bar{\tau}|\bar{\alpha}}(\boldsymbol{\tau}|\boldsymbol{\alpha}), \quad (6.50)$$

where $\bar{g}_{\bar{\tau}}$ [resp., $\bar{g}_{\bar{\alpha}}(\boldsymbol{\alpha})$] is the marginal pdf of $\boldsymbol{\tau}$ [resp. $\boldsymbol{\alpha}$] and $\bar{g}_{\bar{\tau}|\bar{\alpha}}(\boldsymbol{\tau}|\boldsymbol{\alpha})$ [resp., $\bar{g}_{\bar{\alpha}|\bar{\tau}}(\boldsymbol{\alpha}|\boldsymbol{\tau})$] is the conditional pdf of $\boldsymbol{\tau}$ given $\boldsymbol{\alpha}$ [resp., $\boldsymbol{\alpha}$ given $\boldsymbol{\tau}$]. The two identities in (6.49) and (6.50) suggest the following two respective alternatives to generate the required realizations:

1. ALTERNATIVE 1: generate $\tau_q^{(r)}$ using $\bar{g}_{\bar{\tau}}(\boldsymbol{\tau})$ and then use $\bar{g}_{\bar{\alpha}|\bar{\tau}}(\boldsymbol{\alpha}|\boldsymbol{\tau} = \tau_q^{(r)})$ to generate $\alpha_q^{(r)}$.

2. ALTERNATIVE 2: generate $\alpha_q^{(r)}$ using $\bar{g}_{\bar{\alpha}}(\alpha)$ and then use $\bar{g}_{\bar{\tau}|\bar{\alpha}}(\tau|\alpha = \alpha_q^{(r)})$ to generate $\tau_q^{(r)}$.

In practice, however, “ALTERNATIVE 2”, is not a good option since $\bar{g}_{\bar{\alpha}}(\alpha)$ cannot allow resolution of closely-spaced angles inevitably embodied by a single main lobe even in the total absence of noise. Fig. 6.2(b) illustrates this phenomenon in single-carrier systems for a modulated signal (with symbol duration T) propagating via two paths with delays $\bar{\tau}_1 = 4T$ and $\bar{\tau}_2 = 5T$ and angular separation $|\bar{\alpha}_1 - \bar{\alpha}_2| = 6^\circ$.

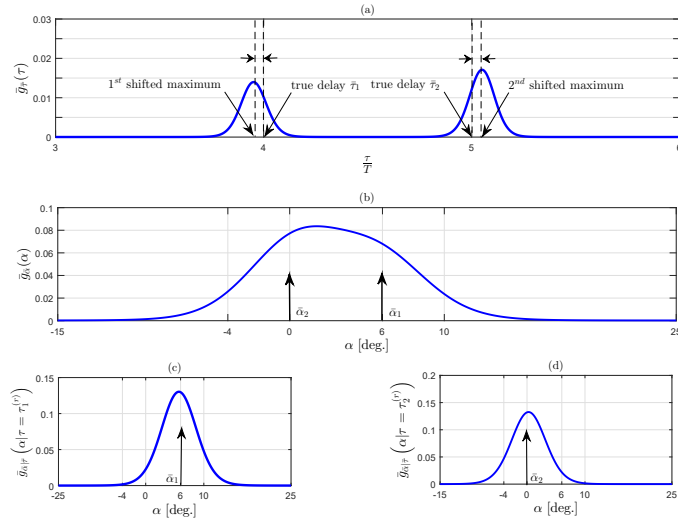


Figure 6.2 – Marginal and conditional pdfs illustrated in a single-carrier system, ULA, $P = 5$, $\bar{Q} = 2$ and SNR = 30 dB: (a) marginal pdf of τ , (b) marginal pdf of α , (c) conditional pdf of α given $\tau_1^{(r)}$, and (d) conditional pdf of α given $\tau_2^{(r)}$.

In contrast, it is found that $\bar{g}_{\bar{\tau}}(\tau)$ always exhibits \bar{Q} main lobes around the true unknown TDs, $\{\bar{\tau}_q\}_{q=1}^{\bar{Q}}$, even if the latter are associated to closely-spaced angles as depicted in Fig. 6.2(a). Moreover, as will be seen in Section VIII, $\bar{g}_{\bar{\tau}}(\tau)$ is able to resolve closely-spaced delays even if the two paths are also *extremely* closely spaced in the angular domain (typically, $|\bar{\alpha}_1 - \bar{\alpha}_2| = 0.5^\circ$). For these reasons, we opt for “ALTERNATIVE 1” and first evaluate $\bar{g}_{\bar{\tau}}(\tau)$ as follows:

$$\bar{g}_{\bar{\tau}}(\tau) = \int \bar{g}_{\bar{\alpha},\bar{\tau}}(\alpha, \tau) d\alpha, \quad (6.51)$$

which is then used to generate the r^{th} vector of delay realizations, $\boldsymbol{\tau}^{(r)} = [\tau_1^{(r)}, \tau_2^{(r)}, \dots, \tau_{\bar{Q}}^{(r)}]^T$, as will be explained shortly. Now, for the same angular separation (i.e., $|\alpha_1 - \alpha_2| = 6^\circ$) and as depicted in Figs. 6.2(c) and (d), each $\{q^{th}\}_{q=1}^{\bar{Q}}$ conditional angle pdf:

$$\bar{g}_{\bar{\alpha}|\bar{\tau}}(\alpha|\tau = \tau_q^{(r)}) = \frac{\bar{g}_{\bar{\alpha},\bar{\tau}}(\alpha, \tau_q^{(r)})}{\bar{g}_{\bar{\tau}}(\tau_q^{(r)})}, \quad (6.52)$$

is found to exhibit exactly a single main lobe around the true angle $\bar{\alpha}_q$ associated to $\bar{\tau}_q$. Next, we recall the following lemma [92] that will be used to generate the required realizations:

Lemma 1: Let $X \in \mathcal{X}$ be any RV with pdf $f_X(x)$ and CDF $F_X(x)$ and denote the inverse CDF as $F_X^{-1}(\cdot) : [0, 1] \rightarrow \mathcal{X}$, $u \rightarrow x$ s.t. $F_X(x) = u$. Then, for any uniform RV, $U \in [0, 1]$, the RV $\tilde{X} = F_X^{-1}(U)$ is distributed according to $f_X(\cdot)$.

In principle, $\bar{g}_{\bar{\tau}}(\tau)$ can be used along with the result of LEMMA 1 to generate the required delay realizations $\{\tau_q^{(r)}\}_{r=1}^R \sim \bar{g}_{\bar{\tau}}(\tau)$ for every $q = 1, 2, \dots, \bar{Q}$ as follows:

1. Generate R realizations $\{u_q^{(r)}\}_{r=1}^R \sim U[0, 1]$,
2. Obtain $\tau_q^{(r)} = \bar{G}_{\bar{\tau}}^{-1}(u_q^{(r)})$ where $\bar{G}_{\bar{\tau}}(\cdot)$ is the CDF associated to $\bar{g}_{\bar{\tau}}(\tau)$.

However, depending on the SNR level, the direct use of the marginal pdf $\bar{g}_{\bar{\tau}}(\tau)$ faces the following major problems in practice:

- At low SNR levels, $\bar{g}_{\bar{\tau}}(\tau)$ exhibits non-negligible secondary lobes, as depicted in Fig. 6.3(b) with SNR = -5 dB, which translate into spurious slopes in the CDF, $\bar{G}_{\bar{\tau}}(\tau)$, as seen from Fig. 6.3(a). Consequently, any realization $u \sim U[0, 1]$ that falls within the range of such spurious slopes (along the y -axis) will result in a delay realization $\tau = \bar{G}_{\bar{\tau}}^{-1}(u)$ that does not correspond to any of the true delays (i.e., an *outlier*). This phenomenon is also illustrated in Fig. 6.3(a) for the two typical realizations u' and u'' . Such outliers affect severely the performance of the estimator. In order to obtain *outliers-free* realizations, it is possible to rid $\bar{g}_{\bar{\tau}}(\tau)$ from its secondary lobes by choosing a sufficiently large value for the design parameter ρ_1 [cf. (6.42)]. Taking a large value for ρ_1 , however, renders the main lobes in $\bar{g}_{\bar{\tau}}(\tau)$ extremely narrow making it more likely that the true delays lie outside their very short spans. Consequently, all the *outliers-free* realizations will be shifted, thereby resulting in an inevitable estimation bias.
- At sufficiently high SNR levels, however, the secondary lobes are naturally absent and thus a small value for ρ_1 can be chosen. Yet, the difference in main lobes' sizes results in out-of-proportion slopes in the CDF. As such, an unbalanced number of realizations will be generated under the different main lobes. As a brute-force remedy, one could be tempted by choosing an extremely large value of R to guarantee that a sufficient number of realizations be generated under each main lobe; not without having to pay a significant extra cost in terms of increased complexity though.

To sidestep all the aforementioned problems, we describe hereafter a simple procedure that allows one to generate all the realizations around the true delays and angles thereby avoiding systematically

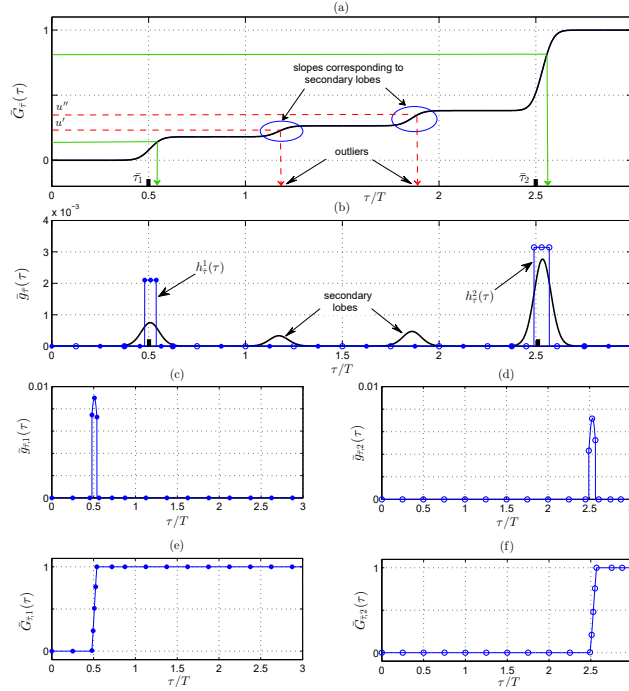


Figure 6.3 – Pseudo-pdfs in a single-carrier system illustrated for $\bar{Q} = 2$ and SNR = -5 dB: (a) marginal CDF of τ , (b) marginal pdf of τ , (c) local pdf of τ around $\bar{\tau}_1$, (d) local pdf of τ around $\bar{\tau}_2$, (e) local CDF of τ around $\bar{\tau}_1$, and (f) local CDF of τ around $\bar{\tau}_2$.

the problem of outliers. Moreover, it ensures that the realizations are generated in exactly the same number under each of the main lobes irrespectively of their relative sizes. To do so, we begin by extracting — through a broad line search — some initial estimates of the unknown true TDs as follows:

$$[\hat{\tau}_1^{(0)}, \hat{\tau}_2^{(0)}, \dots, \hat{\tau}_{\bar{Q}}^{(0)}] = \underset{\tau}{\operatorname{argmax}_{\bar{Q}}} \bar{g}_{\tau}(\tau), \quad (6.53)$$

where $\operatorname{argmax}_{\bar{Q}}\{\cdot\}$ returns the positions of the \bar{Q} largest peaks of any objective function. This initial broad line search is performed using a relatively large grid step $\Delta_{\bar{\tau}}$. Since the main lobes of $\bar{g}_{\tau}(\tau)$ are shifted [cf. Fig. 6.2(a)], note that (6.53) does not provide the delay MLEs even by taking an arbitrarily small value for $\Delta_{\bar{\tau}}$. Then, initial estimates for the associated AoAs are obtained as:

$$\hat{\alpha}_q^{(0)} = \underset{\alpha}{\operatorname{argmax}} \bar{g}_{\hat{\alpha}_q|\hat{\tau}_q}(\alpha|\tau = \hat{\tau}_q^{(0)}), \quad q = 1, \dots, \bar{Q}. \quad (6.54)$$

Likewise, the initial line search in (6.54) is performed with a large grid step $\Delta_{\hat{\alpha}}$. To force $\{\tau_q^{(r)}\}_{r=1}^R$ and $\{\alpha_q^{(r)}\}_{r=1}^R$ to be generated in the vicinity of $\bar{\tau}_q$ and $\bar{\alpha}_q$, respectively, we fix the following \bar{Q} local

intervals:

$$\begin{aligned} D_{\hat{\tau}_q^{(0)}} &= \left[\hat{\tau}_q^{(0)} - \delta_{\bar{\tau}}, \hat{\tau}_q^{(0)} + \delta_{\bar{\tau}} \right], \\ D_{\hat{\alpha}_q^{(0)}} &= \left[\hat{\alpha}_q^{(0)} - \delta_{\bar{\alpha}}, \hat{\alpha}_q^{(0)} + \delta_{\bar{\alpha}} \right], \end{aligned}$$

which are centered at $\hat{\tau}_q^{(0)}$ and $\hat{\alpha}_q^{(0)}$. The sizes of such local delay and angle intervals are governed by the design parameters $\delta_{\bar{\tau}}$ and $\delta_{\bar{\alpha}}$ whose values will be specified in Section VIII. We also define the associated delay and angle *impulse* functions as follows:

$$h_{\hat{\tau}_q^{(0)}}(\tau) = \begin{cases} h_{\bar{\tau}}^q & \text{for } \tau \in D_{\hat{\tau}_q^{(0)}}, \\ 0 & \text{otherwise;} \end{cases} \quad (6.55)$$

$$h_{\hat{\alpha}_q^{(0)}}(\alpha) = \begin{cases} h_{\bar{\alpha}}^q & \text{for } \alpha \in D_{\hat{\alpha}_q^{(0)}}, \\ 0 & \text{otherwise;} \end{cases} \quad (6.56)$$

In the specific case of $\bar{Q} = 2$, the two delay *impulse* functions are illustrated in Fig. 6.3(b) with dotted and circled lines. The q^{th} delay and angle pseudo-pdfs (referred to hereafter as *local* pseudo-pdfs) that will be used to generate the realizations in $D_{\hat{\tau}_q^{(0)}} \times D_{\hat{\alpha}_q^{(0)}}$ are given by:

$$\bar{g}_{\bar{\tau},q}(\tau) = h_{\bar{\tau}}^q(\tau) \bar{g}_{\bar{\tau}}(\tau), \quad (6.57)$$

$$\bar{g}_{\bar{\alpha}|\bar{\tau},q}(\alpha|\tau) = h_{\bar{\alpha}}^q(\alpha) \bar{g}_{\bar{\alpha}|\bar{\tau}}(\alpha|\tau), \quad (6.58)$$

for $q = 1, 2, \dots, \bar{Q}$. The constants $h_{\bar{\tau}}^q$ and $h_{\bar{\alpha}}^q$ in (6.55) and (6.56) are computed such that the local pseudo-pdfs in (6.57) and (6.58) sum up to one thereby yielding:

$$h_{\bar{\tau}}^q = \left(\int_{\hat{\tau}_q^{(0)} - \delta_{\bar{\tau}}}^{\hat{\tau}_q^{(0)} + \delta_{\bar{\tau}}} \bar{g}_{\bar{\tau}}(\tau) d\tau \right)^{-1}. \quad (6.59)$$

$$h_{\bar{\alpha}}^q = \left(\int_{\hat{\alpha}_q^{(0)} - \delta_{\bar{\alpha}}}^{\hat{\alpha}_q^{(0)} + \delta_{\bar{\alpha}}} \bar{g}_{\bar{\alpha}|\bar{\tau}}(\alpha|\tau) d\alpha \right)^{-1}. \quad (6.60)$$

Note here that by applying the impulse functions in (6.57) and (6.58) we obtain a separate (i.e., isolated) local angle/delay pseudo-pdf for each q^{th} path. Therefore, in practice, the processes of generating the required realizations locally around each true delay/angle couple, $(\bar{\alpha}_q, \bar{\tau}_q)$, can be implemented separately and run in parallel with a much faster and less complex execution.

For better illustration, the isolated local delay pseudo-pdfs, $\bar{g}_{\bar{\tau},1}(\tau)$ and $\bar{g}_{\bar{\tau},2}(\tau)$, in the specific case of $\bar{Q} = 2$ are depicted in Figs. 6.3(c) and (d), respectively. Further, as seen from Figs. 6.3(e) and 6.3(f), the associated local CDFs, $\bar{G}_{\bar{\tau},1}(\tau)$ and $\bar{G}_{\bar{\tau},2}(\tau)$, exhibit a single slope that is located around the corresponding true delay. Therefore, by applying the result of LEMMA 1, every uniform realization $u_q^{(r)} \in [0, 1]$ will yield a delay realization $\tau_q^{(r)} \in D_{\bar{\tau}_q^{(0)}} [i.e., \text{in the vicinity of } \bar{\tau}_q]$. For the same reasons, all the angle realizations that are generated using the q^{th} isolated conditional pdfs fall in the vicinity of $\bar{\alpha}_q$.

6.8 Implementation details

6.8.1 Local generation of the required realizations

In this section, we give all the necessary details for an easy and practical implementation of the newly proposed IS-based ML JADE algorithm. Without loss of generality, we consider the case of a ULA with $\alpha = 0$ corresponding to the broadside axis. Hence, the candidate angles are confined within $[-\pi/2, \pi/2]$ and recall that $\tau \in [0, \bar{\tau}_{\max}]$ where $\bar{\tau}_{\max}$ can be freely chosen as high as desired. The starting point of the algorithm is the evaluation of the periodogram, $I(\alpha_i, \tau_j)$ at multiple grid points (α_i, τ_j) with relatively large discretization steps $\Delta_{\bar{\alpha}}^{\text{broad}}$ and $\Delta_{\bar{\tau}}^{\text{broad}}$. Then, by approximating integrals with discrete sums, we evaluate the joint pdf in (6.42), $\bar{g}_{\bar{\alpha}, \bar{\tau}}(\alpha, \tau)$, at every grid point (i.e., $\forall (\alpha_i, \tau_j) \in [-\pi/2, \pi/2] \times [0, \bar{\tau}_{\max}]$) as follows:

$$\bar{g}_{\bar{\alpha}, \bar{\tau}}(\alpha_i, \tau_j) = \frac{\exp\{\rho_1 I(\alpha_i, \tau_j)\}}{\sum_i \sum_j \exp\{\rho_1 I(\alpha_i, \tau_j)\} \Delta_{\bar{\tau}}^{\text{broad}} \Delta_{\bar{\alpha}}^{\text{broad}}}, \quad (6.61)$$

from which the marginal delay pdf is computed as follows:

$$\bar{g}_{\bar{\tau}}(\tau_j) = \sum_i \bar{g}(\alpha_i, \tau_j) \Delta_{\bar{\alpha}}^{\text{broad}}, \quad \forall \tau_j \in [0, \tau_{\max}]. \quad (6.62)$$

The initial delay estimates, $\{\hat{\tau}_q^{(0)}\}_{q=1}^{\bar{Q}}$, are the discrete delay points that correspond to the largest \bar{Q} maxima of (6.62). Then, for every $q = 1, 2, \dots, \bar{Q}$, the conditional pdf of the q^{th} angle corresponding to $\hat{\tau}_q^{(0)}$ is directly obtained as:

$$\bar{g}_{\hat{\alpha}|\hat{\tau}}(\alpha_i|\tau = \hat{\tau}_q^{(0)}) = \frac{\bar{g}_{\hat{\alpha},\hat{\tau}}(\alpha_i, \hat{\tau}_q^{(0)})}{\bar{g}_{\hat{\tau}}(\hat{\tau}_q^{(0)})}, \quad \forall \alpha_i \in [-\frac{\pi}{2}, \frac{\pi}{2}]. \quad (6.63)$$

The initial estimate, $\hat{\alpha}_q^{(0)}$, for the q^{th} AoA is the discrete point, α_i , that corresponds to the maximum of (6.63). Then, the process of generating the realizations in the intervals $D_{\hat{\tau}_q^{(0)}}$ and $D_{\hat{\alpha}_q^{(0)}}$ amounts to performing the following steps for every $q = 1, 2, \dots, \bar{Q}$:

- **step 1:** Evaluate the joint pdf, $\bar{g}_{\hat{\alpha},\hat{\tau}}(\alpha, \tau)$, *locally* at new discrete points $(\alpha'_i, \tau'_j) \in D_{\hat{\alpha}_q^{(0)}} \times D_{\hat{\tau}_q^{(0)}}$ as in (6.61); yet with smaller grid steps $\Delta_{\hat{\tau}}^{\text{small}} < \Delta_{\hat{\tau}}^{\text{broad}}$ and $\Delta_{\hat{\alpha}}^{\text{small}} < \Delta_{\hat{\alpha}}^{\text{broad}}$.
- **step 2:** Compute the q^{th} local marginal delay pdf at every point $\tau'_j \in D_{\hat{\tau}_q^{(0)}}$ as in (6.62), i.e.:

$$\bar{g}_{\hat{\tau},q}(\tau'_j) = \sum_i \bar{g}(\alpha'_i, \tau'_j) \Delta_{\hat{\alpha}}^{\text{small}} \quad \forall \tau'_j \in D_{\hat{\tau}_q^{(0)}}. \quad (6.64)$$

- **step 3:** Compute the q^{th} local delay CDF as follows:

$$\bar{G}_{\hat{\tau},q}(\tau'_j) = \sum_{l \leq j} \bar{g}_{\hat{\tau},q}(\tau'_l) \Delta_{\hat{\tau}}^{\text{small}} \quad \forall \tau'_j \in D_{\hat{\tau}_q^{(0)}}. \quad (6.65)$$

- **step 4:** Generate R realizations $\{u_q^{(r)}\}_{r=1}^R \sim U[0, 1]$ and invert $\bar{G}_{\hat{\tau},q}(\cdot)$ via linear interpolation in order to obtain the local delay realizations $\tau_q^{(r)} = \bar{G}_{\hat{\tau},q}^{-1}(u_q^{(r)})$ for $r = 1, 2 \dots R$.
- **step 5:** For $r = 1, 2, \dots, R$, obtain immediately the local pdf of the q^{th} AoA conditioned on $\tau_q^{(r)}$ from the local joint pdf (already evaluated in “STEP 1”) as follows:

$$\bar{g}_{\hat{\alpha}|\hat{\tau}}(\alpha'_i|\tau = \tau_q^{(r)}) = \frac{\bar{g}_{\hat{\alpha},\hat{\tau}}(\alpha'_i, \tau_q^{(r)})}{\bar{g}_{\hat{\tau},q}(\tau_q^{(r)})}, \quad \forall \alpha'_i \in D_{\hat{\alpha}_q^{(0)}}.$$

- **step 6:** Evaluate the q^{th} local angle CDF, $\bar{G}_{\hat{\alpha},q}(\alpha'_i)$, similarly to $\bar{G}_{\hat{\tau},q}(\tau'_j)$ in (6.65) and generate the r^{th} angle realization, $\alpha_q^{(r)} = \bar{G}_{\hat{\alpha},q}^{-1}(u_q^{(r)})$, using linear interpolation as well.

6.8.2 Estimations of the TDs and AoAs

Using the same arguments of [52], [61], after generating all the required realizations, more accurate IS-based parameter estimates are obtained by applying the *circular* instead of the *linear* sample mean estimate. In fact, the latter simply averages out all the realizations and outlier seeds will result in an inevitable estimation bias. As will be shown later in this paper, however, the circular mean succeeds in selecting the best angle and delay realizations in terms of Euclidean distance to the true multipath-resolution parameters. The circular mean [93], ch. 2,3 of any transformation $f(\Phi)$ of a given random variable $\Phi \in [-\pi, \pi]$ with distribution $p_\Phi(\phi)$ is obtained as follows:

$$\hat{\phi} = \angle \frac{1}{R} \sum_{r=1}^R f(\phi^{(r)}) e^{j\phi^{(r)}}, \quad (6.66)$$

where $\phi^{(r)} \sim p_\Phi(\cdot)$ are R realizations of Φ . Note here that the original realizations $\tau_q^{(r)}$ and $\alpha_q^{(r)}$ are, respectively, in $[0, \tau_{\max}]$ and $[-\pi/2, \pi/2]$ for ULAs ($[0, 2\pi]$ for UCAs). Therefore, one needs to transform both of them into the interval $[-\pi, \pi]$ in order to successfully apply the circular mean. To that end, we use the transformations $\phi_1(\tau_q^{(r)}) = 2\pi(\tau_q^{(r)}/\tau_{\max} - 1/2) \in [-\pi, \pi]$ and $\phi_2(\alpha_q^{(r)}) = 2\alpha_q^{(r)} \in [-\pi, \pi]$ for ULAs⁴. The circular mean is first applied using $\phi_1(\tau_q^{(r)})$ and $\phi_2(\alpha_q^{(r)})$ and the true TDs and AoAs are then estimated using the inverse transformations $\phi_1^{-1}(x) = \tau_{\max} \left(\frac{1}{2} + \frac{1}{2\pi}x \right)$ and $\phi_2^{-1}(x) = \frac{1}{2}x$ as follows:

$$\hat{\tau}_q = \tau_{\max} \left(\frac{1}{2\pi} \angle \left[\sum_{r=1}^R \eta(\boldsymbol{\alpha}^{(r)}, \boldsymbol{\tau}^{(r)}) e^{j2\pi \left(\frac{\tau_q^{(r)}}{\tau_{\max}} - \frac{1}{2} \right)} \right] + \frac{1}{2} \right), \quad (6.67)$$

$$\hat{\alpha}_q = \frac{1}{2} \angle \left[\sum_{r=1}^R \eta(\boldsymbol{\alpha}^{(r)}, \boldsymbol{\tau}^{(r)}) e^{j(2\alpha_q^{(r)} - \pi)} \right]. \quad (6.68)$$

Now by using (6.17) and (6.40) in (6.24), the weighting coefficient $\eta(\boldsymbol{\alpha}^{(r)}, \boldsymbol{\tau}^{(r)})$ can be explicitly expressed as follows:

$$\eta(\boldsymbol{\alpha}^{(r)}, \boldsymbol{\tau}^{(r)}) = \frac{\mu \exp \left\{ \rho_0 \mathcal{L}_c(\boldsymbol{\alpha}^{(r)}, \boldsymbol{\tau}^{(r)}) \right\}}{\exp \left\{ \rho_1 \sum_{q=1}^Q I(\alpha_q^{(r)}, \tau_q^{(r)}) \right\}}, \quad (6.69)$$

4. Note here that we will keep presenting the AoA estimates for ULA configurations and the results for UCAs are quite similar. The only difference is that the corresponding transformation is $\phi_2(\alpha_q^{(r)}) = \alpha_q^{(r)} - \pi$ and its inverse in (6.68) is $\phi_2^{-1}(x) = x + \pi$.

where

$$\mu = \frac{\int \cdots \int \exp \left\{ \rho_1 \sum_{q=1}^{\bar{Q}} I(\alpha_q, \tau_q) \right\} d\boldsymbol{\alpha} d\boldsymbol{\tau}}{\int \cdots \int \exp \left\{ \rho_0 \mathcal{L}_c(\boldsymbol{\alpha}, \boldsymbol{\tau}) \right\} d\boldsymbol{\alpha} d\boldsymbol{\tau}}. \quad (6.70)$$

Actually, by defining the quantity:

$$\Psi(\boldsymbol{\alpha}, \boldsymbol{\tau}) \triangleq \rho_0 \mathcal{L}_c(\boldsymbol{\alpha}, \boldsymbol{\tau}) - \rho_1 \sum_{q=1}^{\bar{Q}} I(\alpha_q, \tau_q), \quad (6.71)$$

and using the same arguments in [52], one can use the following *normalized* weighting coefficient:

$$\bar{\eta}(\boldsymbol{\alpha}^{(r)}, \boldsymbol{\tau}^{(r)}) = \exp \left\{ \Psi(\boldsymbol{\alpha}^{(r)}, \boldsymbol{\tau}^{(r)}) - \max_{1 \leq r \leq R} \Psi(\boldsymbol{\alpha}^{(r)}, \boldsymbol{\tau}^{(r)}) \right\}, \quad (6.72)$$

instead of $\eta(\boldsymbol{\tau}^{(r)}, \boldsymbol{\alpha}^{(r)})$ in order to greatly reduce the computational load with no changes in the final results. Actually we further show in this paper the following interesting result:

Lemma 2: The circular-mean estimates, $\hat{\boldsymbol{\tau}} = [\hat{\tau}_1, \hat{\tau}_2, \dots, \hat{\tau}_{\bar{Q}}]$ and $\hat{\boldsymbol{\alpha}} = [\hat{\alpha}_1, \hat{\alpha}_2, \dots, \hat{\alpha}_{\bar{Q}}]$, obtained in (6.67) and (6.68) by using the normalized factor in (6.72) correspond to the vector realizations that jointly minimize the Euclidean distance to the true delay and angle parameters, i.e.:

$$[\hat{\boldsymbol{\tau}}, \hat{\boldsymbol{\alpha}}] = \underset{\boldsymbol{\tau}^{(r)}, \boldsymbol{\alpha}^{(r)}}{\operatorname{argmin}} \left(\|\boldsymbol{\tau}^{(r)} - \bar{\boldsymbol{\tau}}\|^2 + \|\boldsymbol{\alpha}^{(r)} - \bar{\boldsymbol{\alpha}}\|^2 \right). \quad (6.73)$$

Proof: see Appendix A.

In the sequel, we shall suggest other tricks that result in tremendous additional computational savings and make the proposed estimator always reach the CRLB. In fact, it is found that the initial estimates $\hat{\tau}_q^{(0)}$ and $\hat{\alpha}_q^{(0)}$ are shifted, respectively, by at most ϵ_τ and ϵ_α from the true delays and angles⁵ (i.e., $|\hat{\tau}_q^{(0)} - \bar{\tau}_q| \leq \epsilon_\tau$ and $|\hat{\alpha}_q^{(0)} - \bar{\alpha}_q| \leq \epsilon_\alpha$). In principle, the IS-based estimates in (6.67) and (6.68) are able to return the exact (non-shifted) MLEs by using an extremely large number of realizations. Indeed, using exhaustive simulations, it was found that the exact MLEs are obtained with $R_0 = 20000$ realizations that are generated locally using $\delta_{\bar{\tau}} = 2\epsilon_\tau$ and $\delta_{\bar{\alpha}} = 2\epsilon_\alpha$. These typical values for $\delta_{\bar{\tau}}$ and $\delta_{\bar{\alpha}}$ are chosen so that the corresponding local intervals $D_{\hat{\tau}_q^{(0)}} = [\hat{\tau}_q^{(0)} - \delta_{\bar{\tau}}, \hat{\tau}_q^{(0)} + \delta_{\bar{\tau}}]$

5. Note here that ϵ_τ and ϵ_α depend on the bandwidth of the known transmitted signal and their expressions will be given later in Section 6.10 for both single- and multi-carrier systems.

and $D_{\hat{\alpha}_q^{(0)}} = [\hat{\alpha}_q^{(0)} - \delta_{\hat{\alpha}}, \hat{\alpha}_q^{(0)} + \delta_{\hat{\alpha}}]$ include the true values of the unknown parameters since they verify $|\hat{\tau}_q^{(0)} - \bar{\tau}_q| \leq \delta_{\bar{\tau}}/2$ and $|\hat{\alpha}_q^{(0)} - \bar{\alpha}_q| \leq \delta_{\bar{\alpha}}/2$. This ensures that a portion of the $R_0 = 20000$ realizations are indeed generated on both sides of each true TD and AoA as required by the IS concept. However, using such a very large number of realizations results in a very high computational load. In order to greatly reduce complexity, the algorithm is run in a two-stage⁶ multi-resolution implementation where, in each stage, a far smaller number of realizations is generated over a far narrower lock span around the target parameters.

- STAGE I: Generate $R_1 \ll R_0$ realizations, $\{\tau_q^{(r)}\}_{r=1}^{R_1}$ and $\{\alpha_q^{(r)}\}_{r=1}^{R_1}$, in the aforementioned local intervals $D_{\hat{\tau}_q^{(0)}}$ and $D_{\hat{\alpha}_q^{(0)}}$ and obtain the estimates $\hat{\tau}_q$ and $\hat{\alpha}_q$ as in (6.67) and (6.68).
- STAGE II: Regenerate $R_2 \ll R_0$ new realizations $\{\tau_q'^{(r)}\}_{r=1}^{R_2}$ and $\{\alpha_q'^{(r)}\}_{r=1}^{R_2}$ over narrower intervals that are centered around the estimates $\hat{\tau}_q$ and $\hat{\alpha}_q$ obtained in “STAGE I”, i.e., $D_{\hat{\tau}_q}' = [\hat{\tau}_q - \delta_{\bar{\tau}}', \hat{\tau}_q + \delta_{\bar{\tau}}']$ and $D_{\hat{\alpha}_q}' = [\hat{\alpha}_q - \delta_{\bar{\alpha}}', \hat{\alpha}_q + \delta_{\bar{\alpha}}']$ with $\delta_{\bar{\tau}}' = \delta_{\bar{\tau}}/10$ and $\delta_{\bar{\alpha}}' = \delta_{\bar{\alpha}}/10$. Then, compute the AoA MLEs using the new angle realizations, $\{\boldsymbol{\alpha}'^{(r)} = [\alpha_1'^{(r)}, \alpha_2'^{(r)}, \dots, \alpha_Q'^{(r)}]\}_{r=1}^{R_2}$, and the delay estimates, $\hat{\boldsymbol{\tau}} = [\hat{\tau}_1, \hat{\tau}_2, \dots, \hat{\tau}_Q]^T$, obtained in “STAGE I” as follows:

$$\hat{\alpha}_{q,\text{MLE}} = \frac{1}{2} \angle \left[\sum_{r=1}^{R_2} \bar{\eta}(\boldsymbol{\alpha}'^{(r)}, \hat{\boldsymbol{\tau}}) e^{j(2\alpha_q'^{(r)} - \pi)} \right]. \quad (6.74)$$

All the AoA MLEs obtained in (6.74), i.e., $\hat{\boldsymbol{\alpha}}_{\text{MLE}} = [\hat{\alpha}_{1,\text{MLE}}, \hat{\alpha}_{2,\text{MLE}}, \dots, \hat{\alpha}_{Q,\text{MLE}}]^T$, are then used in conjunction with the new delay realizations, $\{\boldsymbol{\tau}'^{(r)} = [\tau_1'^{(r)}, \tau_2'^{(r)}, \dots, \tau_Q'^{(r)}]\}_{r=1}^{R_2}$, to find the TD MLEs as follows:

$$\hat{\tau}_{q,\text{MLE}} = \tau_{\max} \left(\frac{1}{2\pi} \angle \left[\sum_{r=1}^{R_2} \bar{\eta}(\boldsymbol{\tau}'^{(r)}, \hat{\boldsymbol{\alpha}}_{\text{MLE}}) e^{j2\pi \left(\frac{\tau_q'^{(r)}}{\tau_{\max}} - \frac{1}{2} \right)} \right] + \frac{1}{2} \right). \quad (6.75)$$

Finally, we emphasize the fact that the generated angle and delay realizations are not constrained to be on the grid points due to the use of the linear interpolation in “STEP 4” and “STEP 6”. Therefore, unlike all the existing JADE estimators, the new IS-based ML technique does not suffer from the *off-grid* problems as the MLEs obtained in (6.74) and (6.75) are not also constrained to be on the considered sampling grid (cf. Section I for more details).

6. An N -stage multi-resolution extension would be straightforward.

6.9 Estimating the number of paths

All the existing JADE techniques as well as the new IS-based one require the *a priori* knowledge of the number of paths \bar{Q} . In practice, however, this parameter is also unknown and needs to be estimated even before proceeding to AoAs and TDs acquisition. In this contribution, we also propose a new heuristic approach that allows the exact estimation of \bar{Q} over a wide range of practical SNRs. As will be seen shortly, the new approach is intrinsic to the new IS-based estimator and entails almost no additional complexity. In fact, it relies on the sparsity feature inherent to the marginal delay pdf, $\bar{g}_{\bar{\tau}}(\tau_i)$, depicted in Fig. 6.3(b). Indeed, by properly selecting the *sparsity-promoting* design parameter ρ_1 , it is possible to reduce the sizes of the secondary lobes that are due to the noise contribution. In this way, one obtains a pseudo-pdf whose energy is almost totally concentrated under the main lobes that are located around the true delays. Precisely, just after evaluating $\bar{g}_{\bar{\tau}}(\tau_i)$ in (6.62) over $[0, \tau_{\max}]$, the following two simple steps are performed:

1. STEP 1: Get the points, $\{\hat{\tau}_q^{\circ}\}_{q=1}^{Q_{\text{tot.}}}$, corresponding to all the peaks in $\{\bar{g}_{\bar{\tau}}(\tau_i) \mid \forall \tau_i \in [0, \tau_{\max}]\}$ with $Q_{\text{tot.}}$ being the total number of peaks. Note here that $Q_{\text{tot.}}$ is always greater than \bar{Q} due to the presence of secondary lobes.
2. STEP 2: Sort the squared magnitudes, $\{|\bar{g}_{\bar{\tau}}(\hat{\tau}_q^{\circ})|^2\}_{q=1}^{Q_{\text{tot.}}}$, corresponding to $\{\hat{\tau}_q^{\circ}\}_{q=1}^{Q_{\text{tot.}}}$ and obtain an estimate, \hat{Q} (for the actual number of paths) as the first number of peaks, Q , whose combined energy fractions is above a certain threshold, i.e.:

$$\rho(Q) = \frac{\sum_q^Q |\bar{g}_{\bar{\tau}}(\hat{\tau}_q^{\circ})|^2}{\sum_q^{Q_{\text{tot.}}} |\bar{g}_{\bar{\tau}}(\hat{\tau}_q^{\circ})|^2} \geq \kappa, \quad (6.76)$$

$$\rho(Q-1) = \frac{\sum_q^{Q-1} |\bar{g}_{\bar{\tau}}(\hat{\tau}_q^{\circ})|^2}{\sum_q^{Q_{\text{tot.}}} |\bar{g}_{\bar{\tau}}(\hat{\tau}_q^{\circ})|^2} < \kappa, \quad (6.77)$$

where κ is some threshold level to be designed offline as explained subsequently.

First, it is worth mentioning here that the procedure described above could not be deduced from any of the existing JADE estimators since none of them has a *sparsity-promoting* design parameter like our new IS-based estimator. In practice, they are hence compelled to use one of the traditional more complex signal detection schemes like [94] in order to estimate \bar{Q} .

As mentioned above, the threshold level, κ , can be easily optimized offline in order to obtain the lowest possible \bar{Q} -estimation error for all the practical values of \bar{Q} . To do so, for each \bar{Q} , the mean value of the ratio in (6.76), denoted here as $\bar{\rho}(Q) \triangleq \mathbb{E}\{\rho(Q)\}$, is evaluated by Monte-Carlo

simulations for all $1 \leq Q \leq Q_{\text{tot.}}$. Then, the appropriate value for κ is selected based on these mean values as suggested by Fig. 6.4 (note here that Fig. 6.4(b) depicts a zoom of Fig. 6.4(a) around the specified region along the y -axis). These results are obtained from 10000 Monte-Carlo runs for every \bar{Q} at an SNR = -10 dB.

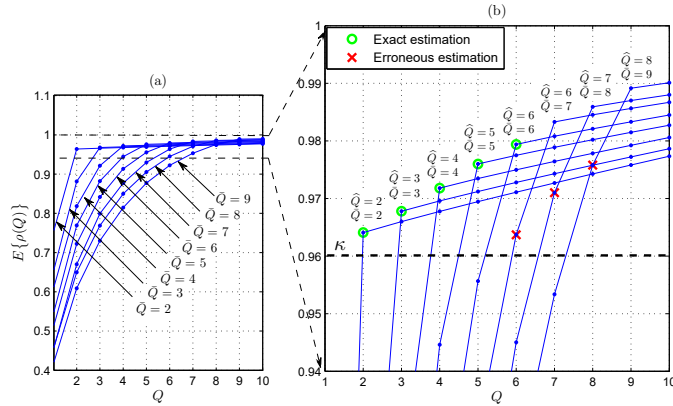


Figure 6.4 – The mean value of $\rho(Q)$ for different values of \bar{Q} , SNR = -10 dB, ULA with $P = 5$ receiving antennas.

As suggested by Fig. 6.4(b), at such extremely low SNR level, an appropriate choice for the threshold level would be $\kappa = 0.96$. In fact, with such threshold, it is seen for $\bar{Q} = 2$ that the first value Q at which $\rho(Q)$ exceeds $\kappa = 0.96$ (on average) is $Q = 2$, i.e., “exact estimation”. The same observation holds for $\bar{Q} = 3, 4, 5$ and 6 as seen from Fig. 6.4(b). For $\bar{Q} = 7$, however, the first value Q that verifies (6.76) on average is $Q = 6$, i.e., “under-estimation” and the same observation holds as well for $\bar{Q} = 8$ and $\bar{Q} = 9$. It will be seen later that the proposed path detection technique outperforms the two well-known existing solutions, namely MDL and AIC [94], especially when the number of paths to be detected is larger than the number of receiving antennas.

6.10 Simulation results

6.10.1 Impact of parameters ρ_0 and ρ_1

We first provide some hints about the appropriate choice of the parameters ρ_0 and ρ_1 . We mention beforehand that (unlike ρ_0) ρ_1 is actually a design parameter that should be carefully chosen.

- Choice of ρ_0 : As suggested by Pincus' theorem, the value of this parameter should be infinite so as to reflect the infinite limit involved in Pincus' theorem [59]. In practice, however, one needs to work with a finite yet sufficiently high value which is optimized offline depending on the observed behaviour of the estimator. In fact, it is found that for low values for ρ_0 , the estimator exhibits very poor estimation performance as seen in Fig. 6.5 below for both single- and multi-carrier systems. By increasing ρ_0 , the estimation accuracy improves remarkably. And starting from a lower threshold, $\bar{\rho}_0$, the performance holds the same; any value for $\rho_0 > \bar{\rho}_0$ can be used. As seen from Fig. 6.5 (a) and (b), the lower threshold on ρ_0 is found to be $\bar{\rho}_0 = 300$; above which the estimator performs well (i.e., close to the CRLB) both in terms of TDs and AoAs estimation.
- Choice of ρ_1 : The main role of this design parameter is to control the spans of the main lobes in $\bar{g}_{\bar{\tau}}(\tau)$ and $\bar{g}_{\bar{\alpha}|\bar{\tau}}(\alpha|\tau)$ that appear, respectively, around the true (unknown) AoAs and TDs, $\{\bar{\alpha}_q\}_{q=1}^{\bar{Q}}$ and $\{\bar{\tau}_q\}_{q=1}^{\bar{Q}}$. Taking a large value for ρ_1 renders the main lobes in $\bar{g}_{\bar{\tau}}(\tau)$, for instance, extremely narrow making it more likely that the true delays lie outside their very short spans. Since the realizations pertaining to each q^{th} delay, $\bar{\tau}_q$, are generated under the associated main lobe, they will be all shifted from $\bar{\tau}_q$ resulting in an inevitable estimation bias. Therefore, contrarily to ρ_o , there is an upper threshold, $\bar{\rho}_1$, that should not be exceeded by ρ_1 as shown in Fig. 6.6 below. There, we see that the upper threshold on ρ_1 is $\bar{\rho}_1 = 40$ as the performance of the estimator deteriorates greatly for $\rho_1 > 40$; especially in terms of delay estimation.

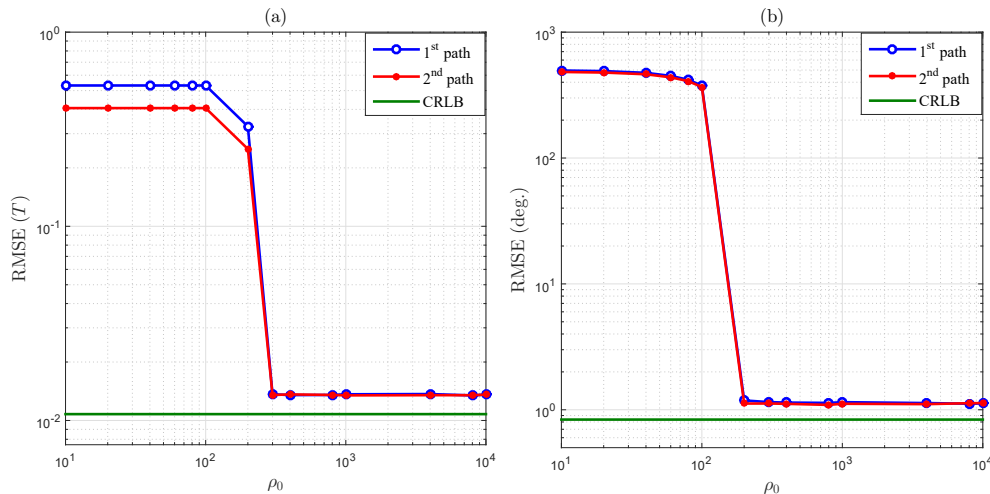


Figure 6.5 – Impact of the parameter, ρ_0 , on the performance of the proposed IS-based estimator at SNR = -10 dB: (a) and (b) multi-carrier, $M = 244$.

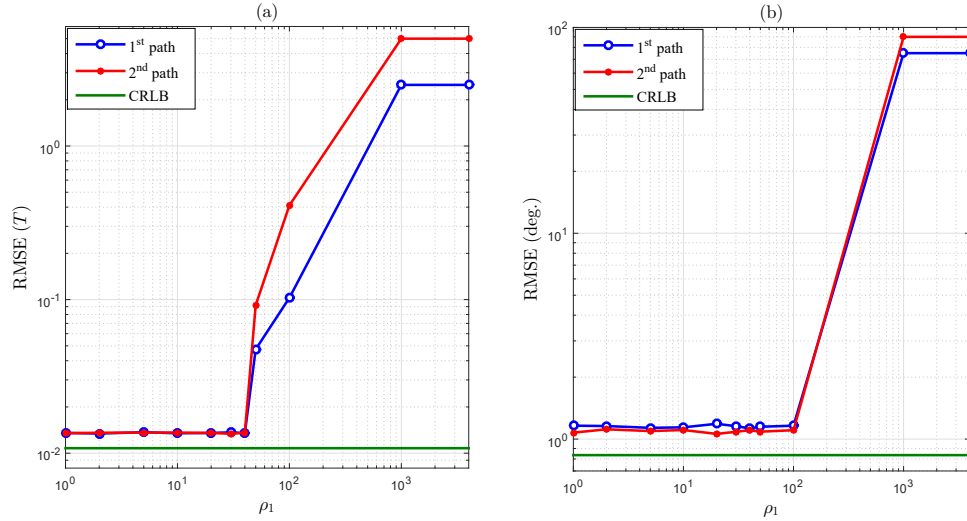


Figure 6.6 – Impact of the parameter, ρ_1 , on the performance of the proposed IS-based estimator at SNR = -10 dB: (a) and (b) multi-carrier, $M = 244$.

In Fig. 6.7, we gauge our proposed approach for estimating the number of paths, \bar{Q} , against the two widely used signal detection schemes, namely MDL and AIC [94]. There, it is seen that the proposed approach outperforms both benchmarks in terms of the probability of detection error. This is mainly due to the use of the sparsity-promoting design parameter, ρ_1 , whose appropriate selection allows to reduce the contributions of the spurious lobes stemming from the background noise. We emphasize, however, the fact that both MDL and AIC are applicable only when the actual number of paths, \bar{Q} , is smaller than the number of receiving antenna elements P since their cost functions can be evaluated for $1 \leq Q \leq P$ only.

In the remaining simulations, we assess the performance of the proposed IS-based ML estimator in terms of the root mean square error (RMSE) which is defined for each q^{th} TD and AoA as follows:

$$\text{RMSE} = \sqrt{\frac{\sum_{m=1}^{M_c} \left(\hat{\tau}_{q, \text{MLE}}^{[m]} - \bar{\tau}_q \right)^2}{M_c}},$$

$$\text{RMSE}(\text{deg.}) = \sqrt{\frac{\sum_{m=1}^{M_c} \left(\hat{\alpha}_{q, \text{MLE}}^{[m]} - \bar{\alpha}_q \right)^2}{M_c}},$$

where $M_c = 5000$ is the total number of Monte-Carlo runs, in all simulations, and $\hat{\tau}_{q, \text{MLE}}^{[m]}$ and $\hat{\alpha}_{q, \text{MLE}}^{[m]}$ are, respectively, the estimates of $\bar{\tau}_q$ and $\bar{\alpha}_q$ during the m^{th} Monte-Carlo run.

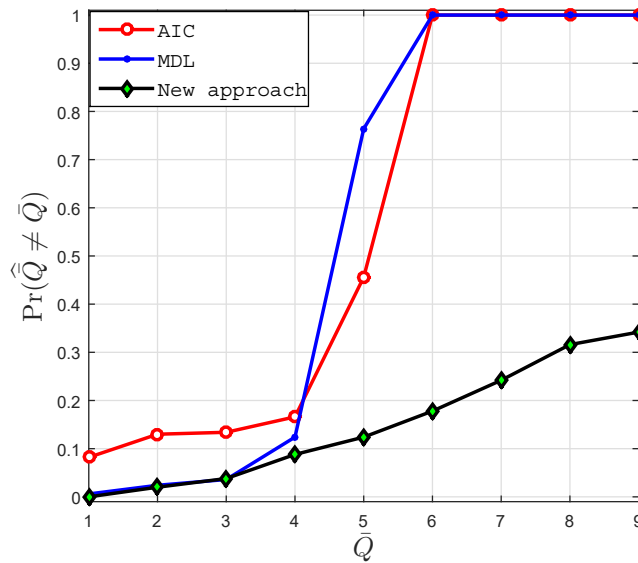


Figure 6.7 – Error Probability on detecting the number of paths for a multicarrier-carrier system employing $M + 1 = 245$ subcarriers at $\text{SNR} = 0$ dB with $P = 5$ and $\rho_1 = 4$.

6.10.2 AoA and TD estimation accuracies: multi-carrier case

We consider the IEEE 802.11ac standard’s setup parameters with a bandwidth $B = 80$ MHz and $P = 6$ antenna elements. In this case, the subcarrier spacing is $\Delta F = 312.5$ KHz thereby leading to $M + 1 = 245$ useful subcarriers within the considered bandwidth. According to the IEEE 802.11ac standard, there are 8 subcarriers allocated for other purposes that cannot be exploited for JADE. That is why we are left with only 245 useful subcarriers out of the 256 available in the considered setup.

MATLAB-based simulations

We will compare our estimator the unitary matrix pencil (UMP) JADE algorithm introduced recently in [49], [50] and which remains so far the only technique that is geared specifically towards multicarrier systems. The two estimators will also be gauged against the CRLB developed in [50] and used here as an overall benchmark that reflects, for every considered setup, the best achievable performance ever. The design parameter, ρ_1 , required by our algorithm was $\rho_1 = 4$, and ρ_0 which must be sufficiently high was set to $\rho_0 = 8000$. Moreover, we fix $\delta_{\bar{\tau}} = 0.2/B$ and $\delta_{\bar{\tau}} = 0.2^\circ$. It was also found that $R_1 = R_2 = 1000$ generated realizations (during “STAGE I” and “STAGE II”) provide

sufficiently accurate IS-based MLEs for both the TDs and AoAs as will be seen from the subsequent simulations.

We begin by simulating the two estimators in a relatively *comfortable* situation where the paths are widely separated both in time and space. The results are shown in Fig. 6.8 for two equi-powered paths that are located at directions $\bar{\alpha}_1 = 20^\circ$ and $\bar{\alpha}_2 = 45^\circ$ with respective delays $\bar{\tau}_1 = 2/B$ and $\bar{\tau}_2 = 5/B$. There it is seen that the proposed IS-based ML estimator (referred to here as “New

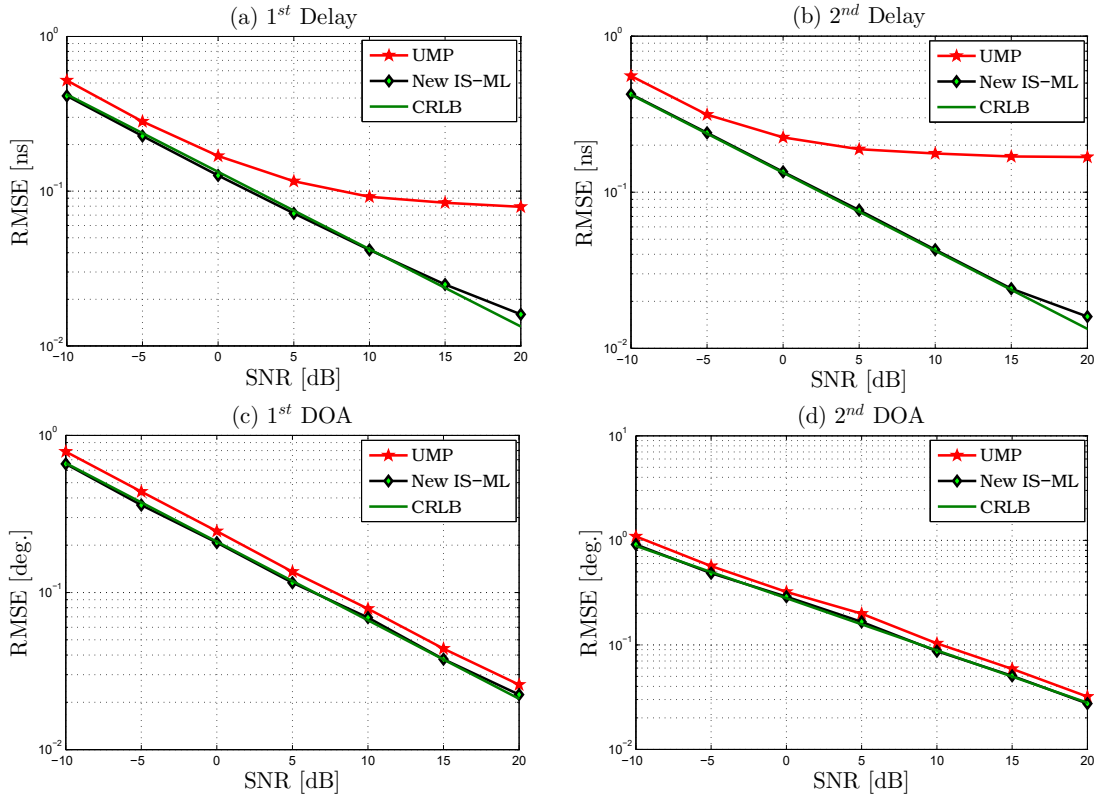


Figure 6.8 – RMSE for the TDs and AoAs with $M + 1 = 245$ subcarriers, for large angular and delay separations.

IS-ML”) outperforms UMP in terms of TDs estimation, although the two estimators exhibit almost the same performance in terms of angle estimation over the entire SNR range. Most remarkably, the proposed IS-based ML estimator reaches the CRLB both in terms of delay and angle estimations thereby confirming its statistical efficiency.

We also assess the performance of both estimators in a more challenging scenario where the paths have closely-spaced angles or delays. To do so, we consider in Fig. 6.9 three paths in a situation where the two paths that have small angular separation are well separated in the delay line and vice versa. More specifically, the paths are located at directions $\bar{\alpha}_1 = 10^\circ$, $\bar{\alpha}_2 = 44.5^\circ$ and $\bar{\alpha}_3 = 45^\circ$ with

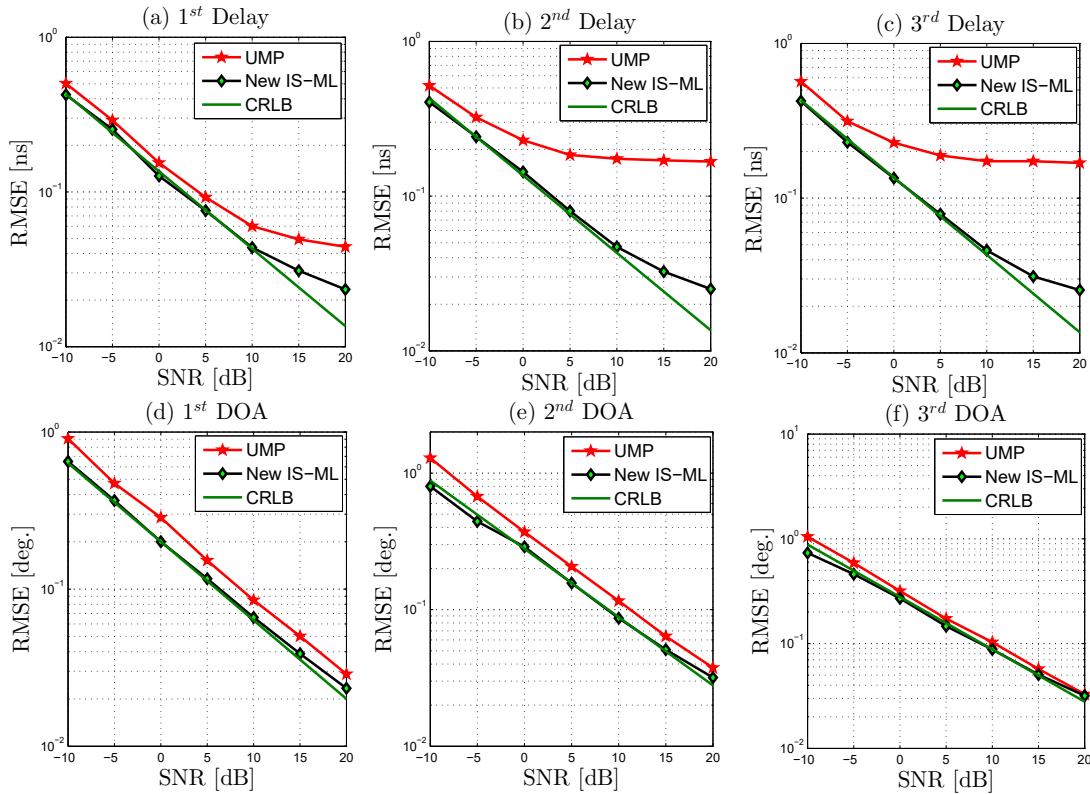


Figure 6.9 – RMSE for the TDs and AoAs with $M = 245$ subcarriers, for paths with closely-spaced angles and large delay separations and vice versa.

respective delays $\bar{\tau}_1 = 2/B$, $\bar{\tau}_2 = 3/B$ and $\bar{\tau}_3 = 8/B$. Here again, it is seen that the proposed IS-based ML estimator exhibits a huge performance advantage in terms of delays estimation as compared to UMP.

Localization with real-world measurements

Here, we evaluate the localization performance of the proposed algorithm using real-world measurements in the form of measured channel frequency responses (CFRs) that were obtained in [50] using the IEEE 802.11ac standard's setup parameters. In the tested scenario, a multilateral localization system is considered wherein a mobile unit (MU) broadcasts a reference/known signal to a number of access points (APs). Each AP forwards the recorded observations to a central unit (CU). The latter extracts the required CFR measurements (corresponding to each AP) and then feeds them to the new IS-based ML JADE technique which is itself executed locally at the CU. The obtained IS-based AoA and TDOA estimates from all APs are then blended together to find

the physical location of the MU. If the need be, the computed coordinates can be fed back to the MU from the central unit. According to the measurement setup depicted in [50], Fig. 5], the APs (denoted as AP1, AP2, AP3, and AP4) and the MU were positioned at (146.2, -172.6) cm, (841.6, -213.2) cm, (907.7, 338.2) cm, (19.1, 333.4) cm, and (462.1, 161.4) cm, respectively. It is worth mentioning here that two of the APs have no line of sight (LOS) component to the MU. Moreover, as explained in [50], 310 different channel measurements were collected over a bandwidth of $B = 80$ MHz using the Agilent ENA E5071C network analyzer and a uniform linear array of six antennas at each AP, all configured according to the IEEE 802.11ac standard's setup parameters.

To localize the MU, we consider the hybrid Time Difference of Arrival (TDOA) and AoA localization technique proposed in [50], Section IIV] with the TDOA being time difference of arrival between each AP and a reference AP (here chosen to be AP1). Indeed, it was shown that the hybrid TDOA and AoA localization procedure outperforms the procedures that are based on either AoA or TDOA only. This hybrid localization approach, however, requires the knowledge of the covariance matrix \mathbf{Q} of all the estimated angles and delays in order to reduce the effect of outlier AoA or TDOA estimates. In [50], \mathbf{Q} was obtained from the different estimates corresponding to the different 310 channel measurements. In the sequel, we shall refer to this procedure as the covariance-based localization technique. It should be emphasized, however, that this is a somewhat non practical solution since the MU needs to be localized using a single set of channel measurements. In this situation, one can use the same hybrid localization procedure by simply setting $\mathbf{Q} = \mathbf{I}$ which is referred to hereafter as the covariance-free procedure in the sequel. If the underlying JADE algorithm is already outlier free, then the more practical covariance-free method will also be accurate.

Fig. 6.10 depicts the location estimates obtained from the TDOA and AoA estimates returned by both UMP and the proposed IS-based ML estimator. By inspecting Figs. 6.10(a) and (c), it is seen that both UMP and the new IS-ML algorithms yield accurate location estimates when used in conjunction with the covariance-based localization procedure. Indeed, all the corresponding location estimates are scattered in the close vicinity of the true MU position. A distinct advantage for the proposed IS-ML algorithm over UMP is, however, observed when the more practical covariance-free localization procedure is used (i.e., using a single channel measurement). In fact, as seen from Figs. 6.10(b) and (d), while all IS-based estimated locations remain very close to the true MU position, UMP exhibits many outlier locations which are roughly 80 cm and 30 cm away from the MU along the x - and y - axes, respectively. This is mainly due to some inaccurate TDOA and AoA estimates for UMP.

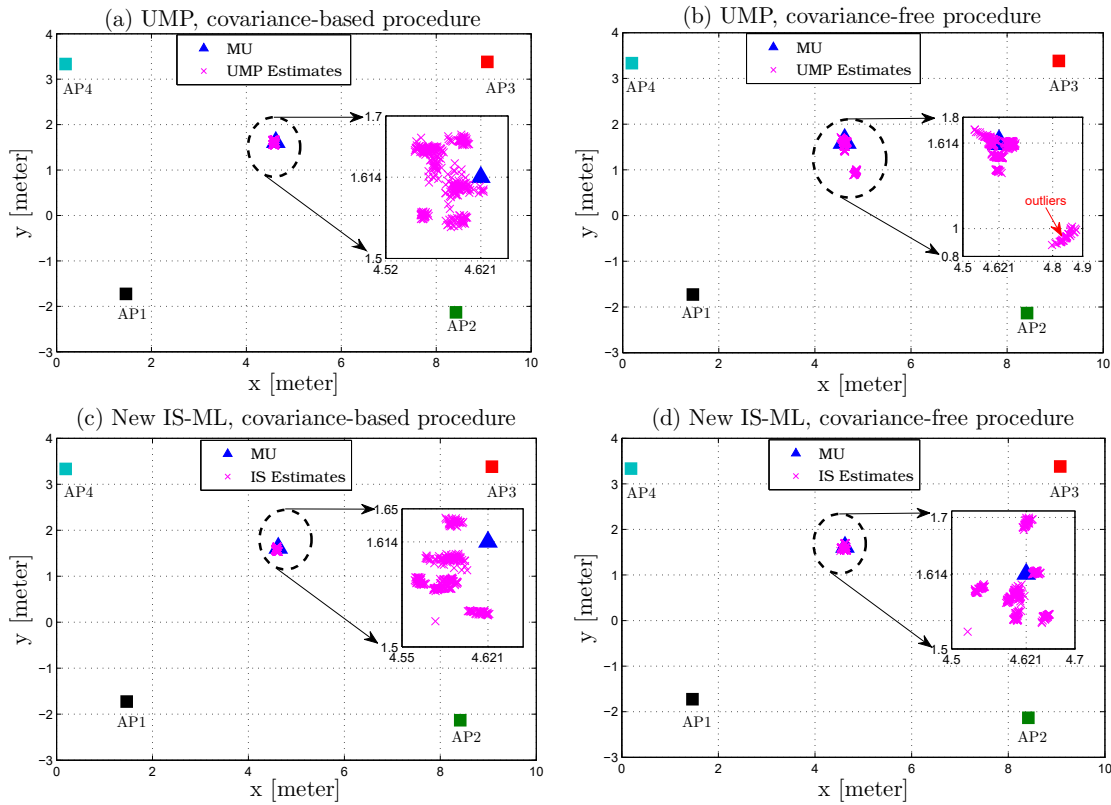


Figure 6.10 – Constellation of the location estimates in the XY plane for: (a) UMP with weighting matrix, (b) UMP without weighting matrix, (c) IS ML with weighting matrix, (d) IS ML without weighting matrix.

For better illustration, we plot in Fig. 6.11 the empirical complementary distribution function (CDF) of the position error:

$$e_z = \sqrt{(\hat{x} - x)^2 + (\hat{y} - y)^2}. \quad (6.78)$$

where (x, y) and (\hat{x}, \hat{y}) are the true coordinates of the MU and their estimates, respectively.

As seen from Fig. 6.11 (a), both UMP and IS ML techniques yield remarkably small localization errors which are smaller than 10 cm at all times, when used with the covariance-based localization procedure. Fig. 6.11 (b) depicts the CDF when the more practical covariance-free localization procedure is applied using the TDOA and AoA estimates provided by each algorithm. There, it is seen that IS-ML still provides a localization error smaller than 10 cm in 90% of the cases (and never exceed 15 cm) while UMP localization errors are higher than 70 cm in 10% of the cases.

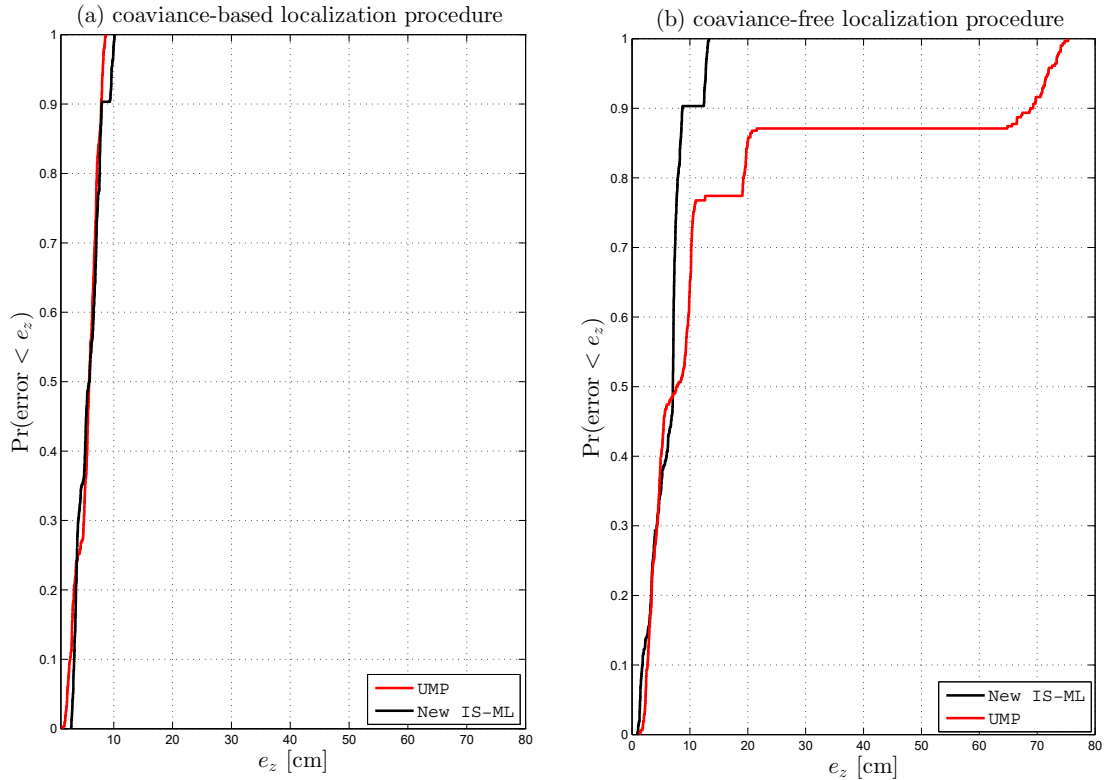


Figure 6.11 – CDF of the position error e_z for both IS-ML and UMP: (a) covariance-based localization procedure (b) covariance-free localization procedure.

6.10.3 AoA and TD estimation accuracies: single-carrier case

In what follows, we will compare our new IS-based ML estimator to the most known JADE techniques that were developed for single-carrier systems. Specifically, we consider the two most powerful subspace-based methods, namely, TST-MUSIC [55] and SI-JADE [56] along with the only two existing ML-type methods which are IML [57] and SAGE [58]. All the estimators are also gauged against the CRLB [56] as an overall benchmark that reflects, for every considered setup, the best achievable performance ever. In all subsequent simulations, we consider a ULA consisting of $P = 5$ receiving antenna elements with half-wavelength spacing, and $M = 128$ received samples. Moreover, as a fast visual reminder, subspace-based and ML techniques are plotted with dashed and solid lines, respectively.

As done for the multicarrier case, we begin by simulating all the estimators in a relatively *comfortable* situation where the paths are widely separated both in time and space. The results are shown in Fig. 6.12 for a linear chirp signal that is sampled at its Nyquist rate and we consider — as representative example — two equi-powered paths that are located at directions $\bar{\alpha}_1 = -15^\circ$ and

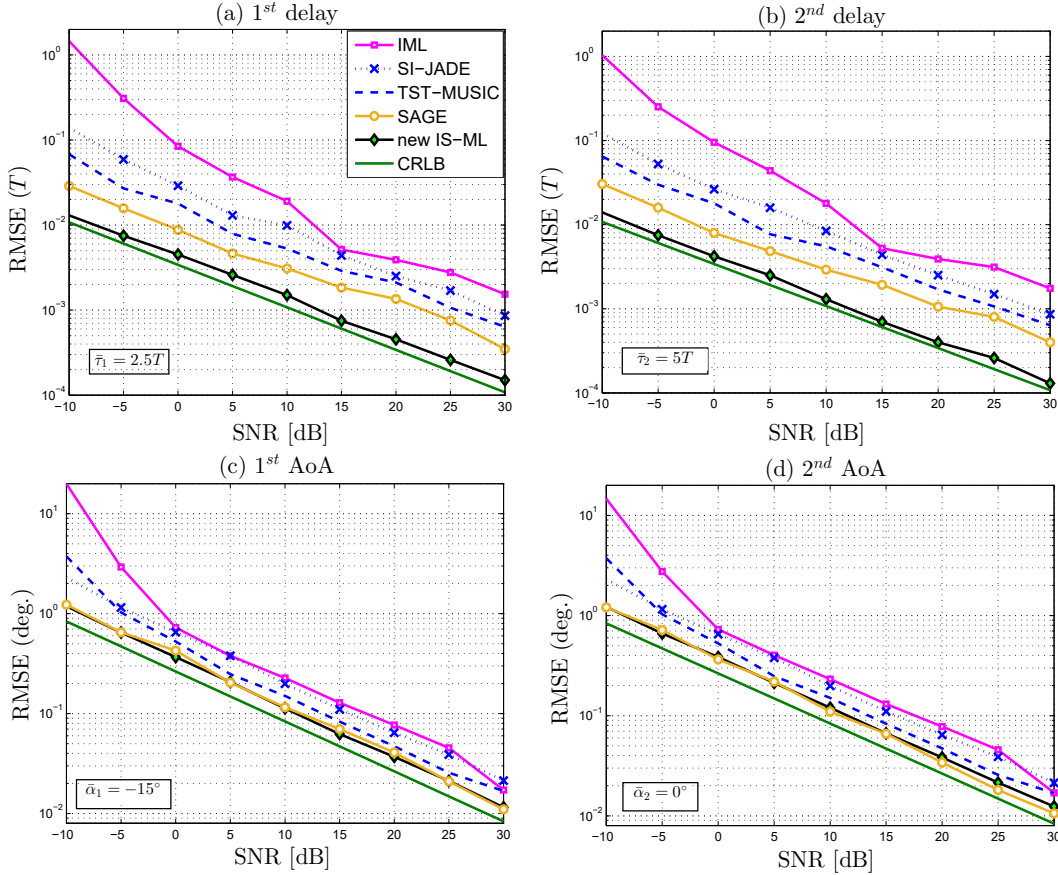


Figure 6.12 – RMSE for the TDs and AoAs with $M = 128$ samples for *large* angular and delay separations.

Table 6.1 – Complexity assessment of the considered JADE algorithms (cf. Table 6.2).

Algorithm	Complexity	Complexity ratio
IS-ML	$(P+1)M \log(M) + (G_1+G_2)PM + (G_1+G_2)P(K_1+K_2) + 2[(K_1+K_2)+M] + (G_2+1)^2Q[(K_2+1)^2+6] + 3R[2(MPQ+Q^2)+Q^3] + 12R$	1.00
SAGE	$[(2PM+2P+1)K+Q(M(2P+1)(G+1)+2Q)Q + N_{\text{iter}}^{\text{SAGE}}Q[2(Q+1)P+2(Q+3)(P+M)+Q+K+M(2P+1)(K+2+G)+Q+2]]$	12.19
IML	$(P+1)M \log(M) + Q[(2P+P^2)+M(Q+P+P^2+1)+(P^3+P)]K + N_{\text{iter}}^{\text{IML}}[M(G+2PQ^2+Q^3+2QP+Q+2+Q^2)+Q^3+PQ^3+2PK]$	2.99
TST-MUSIC	$N_{\text{S-MUSIC}}[N_{\text{burst}}P^2M_{\text{burst}}+P^3+(P+P^3)K+P^3M_{\text{burst}}] + N_{\text{T-MUSIC}}[N_{\text{burst}}M_{\text{burst}}^2P+M_{\text{burst}}^3+(M_{\text{burst}}^3+M_{\text{burst}})G+PM_{\text{burst}}^3]$	22.40
SI-JADE	$(P+1)M \log(M) + [P_1m_2+(m_1P_1m_2(M-m_1+1))]m_2m_1+m_2(M-m_1+1)(2m_1P^2+4m_1P_1)4N_{\text{row}}^2N_{\text{col}}+2N_{\text{col}}^3+4(m_1P_1)^2Q+7Q^3$	3.29
UMP	$(WU)^2(P-W+1)(M-U+1)+17W^3U^3/3+2W^2U^2(P-W+1)(M-U+1)+8/3Q^3+2Q^2(2WU-W-U)+17Q^3$	1.15

$\bar{\alpha}_2 = 0^\circ$ with respective delays $\bar{\tau}_1 = 2.5 T$ and $\bar{\tau}_2 = 5 T$ wherein $T = T_s$.

For such large angle/delay separations, ML-type SAGE offers an AoA estimation performance as superior as ours, at the cost, however, of about 13 times higher complexity as will be shown at the end of this section. The other ML-type solution (i.e., IML), on the other hand, is severely affected in performance at lower SNR values due to noise amplification since it requires the division of the frequency-domain received signal by $s(\omega_m)$. To circumvent this problem, it was suggested in [57] that only the frequency bins $\{\omega_m\}_m$ for which $\{|s(\omega_m)|^2\}_m$ are significantly greater than the noise power σ^2 be used. Typically, the authors impose a threshold of 30 dB, i.e., only the frequency-domain observations, $\{\mathbf{x}(\omega_m)\}_m$, for which $10 \log_{10}(|s(\omega_m)|^2/\sigma^2) \geq 30$ dB are exploited during

the estimation process. Obviously, as the SNR decreases (i.e., σ^2 increases), the number of useful observations decreases affecting thereby the overall performance of IML.

In the following, the known transmitted signal is a block of $K = 64$ BPSK symbols — each of period T — that are pulse-shaped with a raised-cosine filter of *excess* bandwidth $\Delta f = 0.3$. In this case, $T_s = T/2$ is the largest sampling period that verifies the Nyquist rate for all the excess bandwidth values (or roll-off factors). We then assess the performance of all the estimators in a more challenging scenario where the paths have closely-spaced angles or delays. To do so, we consider in Fig. 6.13 three paths in a situation where the two paths that have small angular separation are well separated in the delay line and vice versa. More specifically, the paths are located at directions $\bar{\alpha}_1 = -3^\circ$, $\bar{\alpha}_2 = 0^\circ$ and $\bar{\alpha}_3 = 0.5^\circ$ with respective delays $\bar{\tau}_1 = 2.25 T$, $\bar{\tau}_2 = 2.5 T$ and $\bar{\tau}_3 = 5 T$.

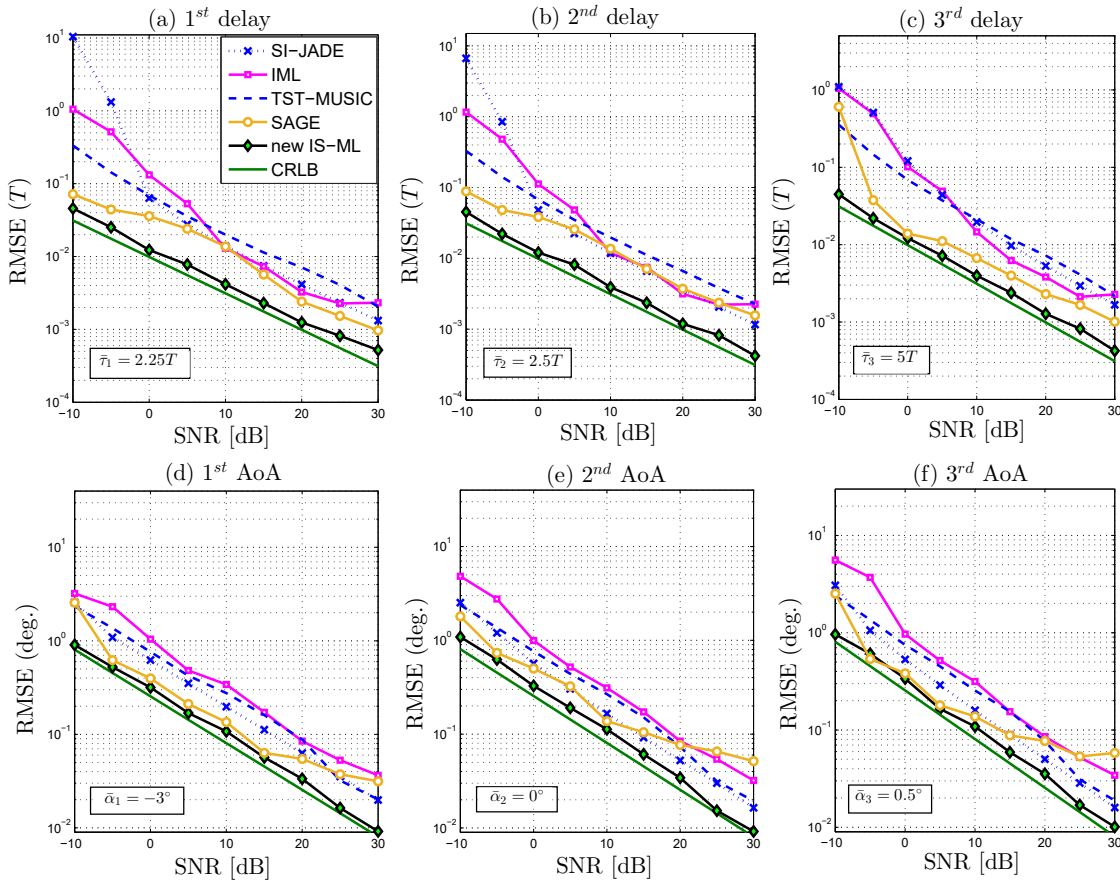


Figure 6.13 – RMSE for the TDs and AoAs with $M = 128$ samples for paths with closely-spaced angles and large delay separations and vice versa.

It is seen that the behavior of TST-MUSIC remains almost unchanged compared to the *comfortable* situation of Fig. 6.12. This is hardly surprising since TST-MUSIC was designed specifically for such type of situations [55]. In fact, it applies the traditional MUSIC algorithm several times by alter-

nating between temporal and spatial spectral estimations in order to use the angular (resp. delay) separation to resolve multipath components that are closely spaced in the delay (resp. angular) domain. The performance of SI-JADE, however, deteriorate at low SNR levels. The improvements of IML in terms of AoA estimation as compared to Fig. 6.12 (at low SNR values) is due to the improved spectral content, $s(\omega)$, of the RRC waveform as compared to the chirp signal of Fig. 6.12. In contrast, our new IS-based estimator is oblivious to the shape of the transmitted waveform and continues to achieve the CRLB over the entire SNR range.

6.10.4 Complexity assessment

In Table 6.1, we computed the total number of operations (i.e., $+$, \times , \div) required by each technique. Please refer to Table 6.2 for the definition of the various parameters. For SAGE and IML, which are iterative in nature, we computed the average number of iterations, $\bar{N}_{\text{iter}}^{\text{SAGE}}$ and $\bar{N}_{\text{iter}}^{\text{IML}}$, they took until convergence by means of Monte-Carlo simulations at a fixed SNR = 0 dB. Then, $\bar{N}_{\text{iter}}^{\text{SAGE}}$ and $\bar{N}_{\text{iter}}^{\text{IML}}$ are used as multiplicative factors to their complexities measured over a single iteration. For the sake of clarity, we introduced $P_1 = m_1(P - m_2 + 1)$, $N_{\text{row}} = m_1(P - m_2 + 1)$, and $N_{\text{col}} = 2m_2(M - m_1 + 2)$. The results in Table 6.1 were obtained by fixing the number of generated realizations required by the proposed IS-ML JADE to $R = 1000$ as was the case in all experiments discussed in the simulations section. The number of samples and antenna elements were set to $M = 128$ and $P = 5$, respectively.

Table 6.2 – Definition of the Complexity Analysis Parameters in Table 6.1

Parameter	Description
K_1, G_1, K_2, G_2	Number of grid points for IS-ML
R	Number of generated realizations for IS-ML
$N_{\text{burst}}, M_{\text{burst}}$	Number and size of the data bursts for TST-MUSIC
$N_{\text{S-MUSIC}}, N_{\text{T-MUSIC}}$	Number of MUSIC blocks in the space and time domains
$\bar{N}_{\text{iter}}^{\text{SAGE}}$	Number of iterations for IML
$\bar{N}_{\text{iter}}^{\text{SAGE}}$	Number of iterations for SAGE
K, G	Number of grid points for IML and SAGE
m_1, m_2	Stacking parameters for SI-JADE
U, W	Pencil parameters for UMP

We see from Table 6.1 that the new IS-based ML JADE estimator exhibits remarkable computational savings compared to TST-MUSIC and the two existing ML estimators. For instance, with the

simulation setup considered in Fig. 6.12 (i.e., $P = 5$, $M = 128$, and $\bar{Q} = 2$), IML, SAGE, and TST-MUSIC are, respectively, 3, 12, and 22 times more complex than IS-ML.

6.11 Conclusion

In this paper, we proposed a new non-iterative and statistically efficient ML solution for the joint estimation of the time delays and angles-of-arrival of overlapping reflections of a signal with a known waveform. Based on the importance sampling concept, this new ML JADE technique applies to both single- and multi-carrier models and enjoys guaranteed global optimality with super-resolution capabilities. Typically, it is able to resolve multipath components with simultaneous angle and delay separations as low as $\Delta\bar{\alpha} = 0.5^\circ$ and $\Delta\bar{\tau} = 0.25 T$ while achieving the CRLB even at SNR levels as low as -10 dB. By exploiting the sparsity feature of a pseudo-pdf that is *intrinsic* to the new algorithm, we also proposed a new approach that can accurately estimate the unknown number of paths. Computer simulation results show the clear superiority of the new IS-based ML estimator over state-of-the-art JADE techniques both in accuracy and complexity. Simulations with real channel measurements in an indoor environment also show the high accuracy of the IS-based ML JADE technique in real-world localization applications.

6.12 Appendices

Appendix 1: [Proof of Lemma 2]

Owing to the very essence of maximum likelihood theory, among all generated realizations $\{\boldsymbol{\alpha}^{(r)}\}_{r=1}^R$ and $\{\boldsymbol{\tau}^{(r)}\}_{r=1}^R$, it is the closest (in Euclidean distance) pair of vector realizations, $\boldsymbol{\alpha}^{(r_0)}$ and $\boldsymbol{\tau}^{(r_0)}$, to the true angle-delay parameters, that maximizes the CLF. In other words, we have:

$$\mathcal{L}_c(\boldsymbol{\alpha}^{(r_0)}, \boldsymbol{\tau}^{(r_0)}) > \mathcal{L}_c(\boldsymbol{\alpha}^{(r)}, \boldsymbol{\tau}^{(r)}), \quad \text{for } 1 \leq r \neq r_0 \leq R \quad (6.79)$$

with

$$r_0 = \underset{1 \leq r \leq R}{\operatorname{argmin}} \left(\|\boldsymbol{\alpha}^{(r)} - \bar{\boldsymbol{\alpha}}\|^2 + \|\boldsymbol{\tau}^{(r)} - \bar{\boldsymbol{\tau}}\|^2 \right). \quad (6.80)$$

Now, recall that ρ_0 can be freely chosen as high as desired. Therefore, after optimizing the choice of ρ_1 as discussed previously, a sufficiently high value of ρ_0 can be chosen such that:

$$\rho_0 \mathcal{L}_c(\boldsymbol{\alpha}^{(r)}, \boldsymbol{\tau}^{(r)}) \gg \rho_1 \sum_{q=1}^{\bar{Q}} I(\alpha_q^{(r)}, \tau_q^{(r)}) \quad \text{for } 1 \leq r \leq R. \quad (6.81)$$

Note here that $\mathcal{L}_c(\boldsymbol{\alpha}, \boldsymbol{\tau}) = \mathbf{x}^H \mathbf{D}(\mathbf{D}^H \mathbf{D})^{-1} \mathbf{D}^H \mathbf{x}$ is always strictly positive since $\mathbf{D}(\mathbf{D}^H \mathbf{D})^{-1} \mathbf{D}^H$ is a positive definite matrix and $I(\alpha_q^{(r)}, \tau_q^{(r)})$ is also always positive. Therefore, a choice of ρ_0 that satisfies the condition in (6.81) is always possible. Under such particular choice of ρ_0 and as suggested by (6.81), we have from eq. (56) in the main paper:

$$\begin{aligned} \Psi(\boldsymbol{\alpha}^{(r)}, \boldsymbol{\tau}^{(r)}) &= \rho_0 \mathcal{L}_c(\boldsymbol{\alpha}^{(r)}, \boldsymbol{\tau}^{(r)}) - \rho_1 \sum_{q=1}^{\bar{Q}} I(\alpha_q^{(r)}, \tau_q^{(r)}), \\ &\approx \rho_0 \mathcal{L}_c(\boldsymbol{\alpha}^{(r)}, \boldsymbol{\tau}^{(r)}). \end{aligned} \quad (6.82)$$

Therefore, by recalling (6.79), it follows that:

$$\max_{1 \leq r \leq R} \Psi(\boldsymbol{\alpha}^{(r)}, \boldsymbol{\tau}^{(r)}) = \rho_0 \mathcal{L}_c(\boldsymbol{\alpha}^{(r_0)}, \boldsymbol{\tau}^{(r_0)}). \quad (6.83)$$

Hence, using (6.82) and (6.83) back into eq. (57) of the main paper, it follows that:

$$\bar{\eta}(\boldsymbol{\alpha}^{(r)}, \boldsymbol{\tau}^{(r)}) = e^{\rho_0 \beta^{(r)}}, \quad (6.84)$$

where

$$\beta^{(r)} \triangleq \mathcal{L}_c(\boldsymbol{\alpha}^{(r)}, \boldsymbol{\tau}^{(r)}) - \mathcal{L}_c(\boldsymbol{\alpha}^{(r_0)}, \boldsymbol{\tau}^{(r_0)}). \quad (6.85)$$

Now, since we have:

$$\beta^{(r_0)} = \mathcal{L}_c(\boldsymbol{\alpha}^{(r_0)}, \boldsymbol{\tau}^{(r_0)}) - \mathcal{L}_c(\boldsymbol{\alpha}^{(r_0)}, \boldsymbol{\tau}^{(r_0)}) = 0, \quad (6.86)$$

it follows from (6.84) that:

$$\bar{\eta}(\boldsymbol{\alpha}^{(r_0)}, \boldsymbol{\tau}^{(r_0)}) = 1. \quad (6.87)$$

Owing to (6.79), however, we have:

$$\beta^{(r)} < 0, \quad \text{for all } r \neq r_0. \quad (6.88)$$

And since $\rho_0 \gg 1$, it immediately follows that:

$$\bar{\eta}(\boldsymbol{\alpha}^{(r)}, \boldsymbol{\tau}^{(r)}) = e^{\rho_0 \beta^{(r)}} \approx 0, \quad \text{for all } r \neq r_0. \quad (6.89)$$

In conclusion, we have for all $1 \leq r \leq R$:

$$\bar{\eta}(\boldsymbol{\alpha}^{(r)}, \boldsymbol{\tau}^{(r)}) = \begin{cases} 1 & \text{for } r = r_0 \\ 0 & \text{otherwise.} \end{cases} \quad (6.90)$$

Then, injecting (6.90) in eqs. (52) and (53) of the main paper, the circular-mean estimates for the angle and delay parameters are obtained as follows:

$$\hat{\tau}_q = \tau_{\max} \left(\frac{1}{2\pi} \angle \left\{ e^{j2\pi \left(\frac{\tau_q^{(r_0)}}{\tau_{\max}} - \frac{1}{2} \right)} \right\} + \frac{1}{2} \right), \quad (6.91)$$

$$\hat{\alpha}_q = \frac{1}{2} \angle \left\{ e^{j(2\alpha_q^{(r)} - \pi)} \right\}. \quad (6.92)$$

But owing to the transformations applied right after eq. (51) in the main paper, we always have:

$$2\pi \left(\frac{\tau_q^{(r_0)}}{\tau_{\max}} - \frac{1}{2} \right) \in [-\pi, \pi], \quad (6.93)$$

$$2\alpha_q^{(r)} - \pi \in [-\pi, \pi], \quad (6.94)$$

and hence it follows that:

$$\angle \left\{ e^{j2\pi \left(\frac{\tau_q^{(r_0)}}{\tau_{\max}} - \frac{1}{2} \right)} \right\} = 2\pi \left(\frac{\tau_q^{(r_0)}}{\tau_{\max}} - \frac{1}{2} \right), \quad (6.95)$$

and

$$\angle \left\{ e^{j(2\alpha_q^{(r)} - \pi)} \right\} = (2\alpha_q^{(r)} - \pi) \quad (6.96)$$

Plugging (6.95) and (6.96) back into (6.91) and (6.92), it immediately follows that:

$$\widehat{\tau}_q = \tau_q^{(r_0)}, \quad q = 1, 2, \dots, \bar{Q} \quad (6.97)$$

$$\widehat{\alpha}_q = \alpha_q^{(r_0)}, \quad q = 1, 2, \dots, \bar{Q}. \quad (6.98)$$

By recalling (6.80), it turns out that the vector realizations $\boldsymbol{\tau}^{(r_0)} = [\tau_1^{(r_0)}, \tau_2^{(r_0)}, \dots, \tau_{\bar{Q}}^{(r_0)}]$ and $\boldsymbol{\alpha}^{(r_0)} = [\alpha_1^{(r_0)}, \alpha_2^{(r_0)}, \dots, \alpha_{\bar{Q}}^{(r_0)}]$ selected by the circular mean as ML estimates, in (6.97) and (6.98), minimize the combined Euclidean distance to all the true angle/delay parameters. In other words, under appropriate choice of ρ_0 , the circular mean succeeds in selecting the best angle/delay realizations instead of simply averaging all the realizations as in the linear mean.

Chapitre 7

Other Contributions within this Thesis

Abstract

During my Ph.D. program, i had the chance to be involved in the IMT-2020 evaluation process of the 5G SRITs and RITs technologies. The Wireless Lab was one of the few if not the only academic team in Canada to have been involved in ITU-R WP 5D activities for the evaluation of candidates for 4G standards (IMT-Advanced) in 2009-2010 and 5G (IMT-2020) in 2018-2020. Most recent mandate covered the RITs and/or SRITs of 3GPP, TSDSI, ETSI DECT, and NuFront and we are currently continuing with re-evaluation of DECT and NuFront. We were actually among the few independent evaluation groups (IEG)s to have demonstrated that these two candidates could not pass step 4 of the evaluation process. I also have been given an opportunity by my supervisor, Prof. Sofiène Affes, to mentor graduate and undergraduate students in their research projects.

7.1 Evaluation of radio interface technology (RIT) and set of RITs (SRITs) candidates to the new ITU-R WP 5D IMT-2020 (5G) standards within the CEG¹ and ISED² mandates

7.1.1 Introduction

One of the strongest driving forces for wireless technology evolution today is 5G, also known as IMT-2020 [1], which promises to encompass several radio interface technologies (RITs) or sets thereof (SRITs), including 3GPP and ETSI/DECT among others. These IMT-2020 standard candidates, made available very recently for evaluation, are to be assessed for compliance to minimum requirements [68],[69]. 5G promises to deliver by 2020 ultra-high-speed wireless data transmission services at much lower costs and latencies while providing much higher rates, spectrum efficiencies, and coverage. In order to ensure the most cost/spectrum-efficient deployment of these new-generation wireless technologies in a few years from now, their performance has to be reliably assessed by simulations in the more realistic way. The capabilities of IMT-2020 also include: very high peak data rate, very high and guaranteed user experienced data rate, and quite high mobility while providing satisfactory quality of service. It also includes features such as enabling massive connections in very-high-density scenarios, very high energy efficiency for network and device side, high spectrum and bandwidth flexibility, and ultra-high reliability. Multiple key features are to be assessed such as packet throughput, cell spectrum efficiency, packet loss rate, and latency. These features will give valuable insights to identify i) areas where enhancements can be made, ii) introduce these enhancements and evaluate them, iii) support equipment manufacturers and operators in their standardization effort to integrate these enhancements if deemed valuable. The comparison of the selected 5G technologies is performed on a fair basis using a common simulation platform.

It is from this perspective, that the Wireless Lab team (mandated by ISED and CEG), has worked on developing a common simulation platform design for the 3GPP and ETSI/DECT RIT candidates for 5G. The characteristics chosen for evaluation by simulation include peak 5th percentile user spectral efficiency, average spectral efficiency, connection density, reliability, and mobility

1. Canadian Evaluation Group

2. Innovation, Science, and Economic Development Canada

[68]. The obtained results were included in the final report of the CEG contribution to the working party 5D (WP 5D) meetings.

7.1.2 Simulation process

Usage scenarios and test environments

There are three usage scenarios for IMT-2020 as follows:

- eMBB: This usage scenario will come with new application areas and requirements in addition to existing mobile broadband applications for improved performance and an increasingly seamless user experience. This usage scenario covers a range of cases, including wide-area coverage and hotspot, which have different requirements.
- mMTC: This usage scenario is characterized by a very large number of connected devices typically transmitting a relatively low volume of non-delay-sensitive data.
- URLLC: This usage scenario has stringent requirements for capabilities such as throughput, latency and availability. Some examples include wireless control of industrial manufacturing or production processes, remote medical surgery, distribution automation in a smart grid, transportation safety, etc.

A test environment reflects a combination of geographic environment and usage scenario. There are five selected test environments for IMT-2020 as follows:

- Indoor Hotspot-eMBB: An indoor isolated environment at offices and/or in shopping malls based on stationary and pedestrian users with very high user density.
- Dense Urban-eMBB: An urban environment with high user density and traffic loads focusing on pedestrian and vehicular users.
- Rural-eMBB: A rural environment with larger and continuous wide area coverage, supporting pedestrian, vehicular and high-speed vehicular users.
- Urban Macro-mMTC: An urban macro environment targeting continuous coverage focusing on a high number of connected machine type devices.
- Urban Macro-URLLC: An urban macro environment targeting ultra-reliable and low latency communications.

Network layout

The guidelines in [95] describe multiple use cases which were all implemented in the system-level simulator.

- Indoor scenario: The documentation in [95] gives the details about the indoor placement of the hotspots. However, no details were provided about the network layout nor the UEs placement. In our simulator, it is assumed that the UEs are uniformly distributed over the whole area and each site include 1 TRxPs.
- Hexagonal one-layer layout: Following [95], the dense urban-eMBB rural-eMBB, urban macro-mMTC and urban macro-URLLC are evaluated using macro-layer base stations that are placed in a regular grid with a hexagonal layout (with three TRxPs per site). In our simulator both, TRxP per site or 3 TRxPs per site are available.
- Hexagonal two-layer layout: This configuration contains Two layers. The macro-layer base stations are placed in a regular grid, following hexagonal layout with three TRxPs per site. For the micro layer, there are 3 micro sites randomly dropped in each macro TRxP area. In our simulator both, TRxP per site or 3 TRxPs per site are available.
- Dense Urban-eMBB (500km/h mobility): In the case of high mobility (500 km/h), additional evaluations can be envisaged using linear cell layout configuration(s) as defined in Annex 2 of [95].

Evaluation criteria

The evaluation criteria that requires system- and link-level simulations are listed below. Note that the ITU requires other evaluation criteria (analytical and by inspection) that can be found in [68].

- 5th percentile user spectral efficiency: the 5% point of the CDF of the normalized user throughput. It is defined for the purpose of evaluation in the eMBB usage scenario. The minimum requirements for various test environments are summarized in Table 7.1.

Table 7.1 – 5th percentile user spectral efficiency

Test environment	Downlink (bit/s/Hz)	Uplink (bit/s/Hz)
Indoor Hotspot – eMBB	0.3	0.21
Dense Urban – eMBB	0.225	0.15
Rural – eMBB	0.12	0.045

- Average spectral efficiency: the aggregate throughput of all users over a certain period of time divided by the channel bandwidth and the number of TRxPs. It is measured in bit/s/Hz/TRxP and the minimum requirements for various test environments are summarized in Table 7.2.

Table 7.2 – Average spectral efficiency

Test environment	Downlink (bit/s/Hz/TRxP)	Uplink (bit/s/Hz/TRxP)
Indoor Hotspot – eMBB	9	6.75
Dense Urban – eMBB	7.8	5.4
Rural – eMBB	3.3	1.6

- Connection density: the total number of devices fulfilling a specific quality of service (QoS) per unit area (per km²). The target QoS is to support delivery of a message of a certain size within a certain time and a success probability, as specified in [95]. This requirement is defined for the purpose of evaluation in the mMTC usage scenario and the minimum requirement for connection density is 1 000 000 devices per *km*².
- Reliability: the success probability of transmitting a packet within a required maximum time. This requirement is defined for the purpose of evaluation in the URLLC usage scenario and the minimum requirement for the reliability is $1 - 10^{-5}$ success probability.
- Mobility: is the maximum mobile station speed at which a defined QoS can be achieved. The minimum requirements for various test environments are summarized in Table 7.3.

Table 7.3 – Traffic channel link data rates normalized by bandwidth.

Test environment	Normalized traffic channel link data rate (bit/s/Hz)	Mobility
Indoor Hotspot – eMBB	1.5	10
Dense Urban – eMBB	1.12	30
Rural – eMBB	0.8	120
	0.45	500

Evaluation summary

Multiple standard candidates were submitted to WP 5D for evaluation. In Table 7.4, we provide summary of the performance criteria evaluated for each submitted technology. To be approved, each candidate needs to fulfill the minimum requirement of each of the evaluation criteria mentioned above.

Table 7.4 – Technologies covered by the CEG for WP 5D

Proponent	IMT-2020 SUBMISSION						
	3GPP		China	South Korea	TSDSI	ETSI-DECT	NuFront
Document Reference	RIT [70]	SRIT [71]	[72]	[73]	[74]	[75]	[76]
Status	Evaluated	Evaluated	Not evaluated (WP 5D has determined that the 3GPP evaluation applies to this candidate)	Not evaluated (WP 5D has determined that the 3GPP evaluation applies to this candidate)	Not evaluated (After de-activation of certain features, TSDSI RIT became sufficiently similar to 3GPP RIT)	Partial evaluation (only the DECT component RIT)	Partial evaluation
Average spectral efficiency	✓	✓				N/A	Missing data
5% spectral efficiency	✓	✓				N/A	Missing data
Mobility	✓	✓				N/A	Missing data
Reliability	✓	N/A				✓	Missing data
Connection density	✓	✓				Missing data	Missing data

In table 7.5, we provide the 3GPP NR RIT technology compliance template for technical Performance requiring evaluation by simulation. We concluded that 3GPP NR RIT satisfies all of the minimum requirements. Moreover, as mentioned in [96], the CEG believes that the NR RIT submission satisfies all of the minimum requirements (including analytical and by inspection evaluations) as specified in Reports ITU-R M.2410 [68], M.2411 [69], and M.2412 [95].

In table 7.6, we provide the 3GPP SRIT technology compliance template for technical performance requiring evaluation by simulation. The SRIT submission of 3GPP includes two components: LTE RIT and NR RIT. We concluded that 3GPP SRIT satisfies all of the minimum requirements. Note that the LTE component does not support URLLC scenario and hence the reliability was not evaluated. Moreover, as mentioned in [96], the CEG believes that the SRIT submission satisfies all of the minimum requirements (including analytical and by inspection evaluations).

In table 7.7, only the DECT component RIT of the ETSI-DECT SRIT submission was evaluated and the following observations were drawn:

- The DECT component applies only to UMa-URLLC and UMa-mMTC. Therefore, no evaluations applying to the eMBB usage scenario could be implemented (eMBB is covered by 3GPP NR RIT in the ETSI-DECT submission).
- The DECT component RIT fulfils the reliability criterion for the UMa-URLLC test environment.
- The assumptions required to simulate mMTC environment are very specific to the DECT component RIT and in spite of several e-mail exchanges with the proponent, proved to be too numerous and too complicated to execute. These assumptions certainly go far beyond what is provided as an evaluation methodology in report ITU-R M.2412. Ultimately, with the network going from cellular layout to mesh layout, and interactions required between the two, we were not able to perform simulations before the WP 5D 34th meeting. Some examples of the assumptions required to be made:

- Device-to-device channel and interference models for shortest path selection and data relaying.
- Criteria required to establish the number of hops and path from the user equipment via other user devices to reach the base stations.
- RSSI sensitivity threshold to determine device-to-device connectivity.
- Device-to-device data relaying, modulation, coding, and resource allocation schemes.

In the final report, the CEG was not able to conclude whether the DECT component RIT passes the connection density requirements, which in turn implies that it is unclear if this component meets the overall criterion of fulfilling the requirements of at least two test environments.

After the de-activation of additional features such as pulse shaping and power boosting (decision made during the WP 5D meeting # 33), TSDSI became sufficiently similar to the 3GPP RIT. It was also decided during the same meeting that the evaluation configuration with bandwidths such as 60 MHz at a frequency of 3.5 GHz and an inter-site distance of 12 km were not directly relevant to the evaluation process.

Table 7.5 – Compliance template for technical performance requiring evaluation by simulation for 3GPP NR RIT technology

Minimum technical performance requirements, ITU-R M.2410-0	Category			Required value	Value	Requirement met?	Comments ³
	Usage scenario	Test environment	Downlink or uplink				
5.2.4.3.4 5th percentile user spectral efficiency (bit/s/Hz) (4.4)	eMBB	Indoor Hotspot – eMBB	Downlink	0.3	0.380	<input checked="" type="checkbox"/> Yes <input type="checkbox"/> No	FDD/ TDD Table 11.2.12-1 Conf. A
			Uplink	0.21	0.357	<input checked="" type="checkbox"/> Yes <input type="checkbox"/> No	
	eMBB	Dense Urban – eMBB	Downlink	0.225	0.307	<input checked="" type="checkbox"/> Yes <input type="checkbox"/> No	FDD/ TDD Table 11.2.12-3 Conf. A
			Uplink	0.15	0.288	<input checked="" type="checkbox"/> Yes <input type="checkbox"/> No	
	eMBB	Rural – eMBB	Downlink	0.12	0.201-0.334	<input checked="" type="checkbox"/> Yes <input type="checkbox"/> No	FDD/ TDD Table 11.2.12-5 Conf. A
			Uplink	0.045	0.093-0.108	<input checked="" type="checkbox"/> Yes <input type="checkbox"/> No	
5.2.4.3.5 Average spectral efficiency (bit/s/Hz/ TRxP) (4.5)	eMBB	Indoor Hotspot – eMBB	Downlink	9	9.120	<input checked="" type="checkbox"/> Yes <input type="checkbox"/> No	
			Uplink	6.75	7.538	<input checked="" type="checkbox"/> Yes <input type="checkbox"/> No	
	eMBB	Dense Urban – eMBB	Downlink	7.8	7.923	<input checked="" type="checkbox"/> Yes <input type="checkbox"/> No	
			Uplink	5.4	6.756	<input checked="" type="checkbox"/> Yes <input type="checkbox"/> No	
	eMBB	Rural – eMBB	Downlink		10.664-12.027	<input checked="" type="checkbox"/> Yes <input type="checkbox"/> No	FDD/ TDD Table 11.2.12-5 Conf. A
						<input checked="" type="checkbox"/> Yes <input type="checkbox"/> No	
			Uplink	1.6	2.041-5.037	<input checked="" type="checkbox"/> Yes <input type="checkbox"/> No	
					3.836	<input checked="" type="checkbox"/> Yes <input type="checkbox"/> No	
5.2.4.3.9 Connection density (devices/km ²) (4.8)	mMTC	Urban Macro – mMTC	Uplink	1 000 000	34 378 000 (ISD=500m)	<input checked="" type="checkbox"/> Yes <input type="checkbox"/> No	11.2.13
					1 422 700 (ISD=1 732m)		
5.2.4.3.11 Reliability (4.10)	URLLC	Urban Macro –URLLC	Uplink or Downlink	1 – 10 ⁻⁵ success probability of transmitting a layer 2 PDU (protocol data unit) of size 32 bytes within 1 ms in channel quality of coverage edge	99.999% or greater on the DL and UL	<input checked="" type="checkbox"/> Yes <input type="checkbox"/> No	11.1.14
5.2.4.3.13 Mobility: Traffic channel link data rates (bit/s/Hz) (4.11)	eMBB	Indoor Hotspot – eMBB	Uplink	1.5 (10 km/h)	LoS: 2.297	<input checked="" type="checkbox"/> Yes <input type="checkbox"/> No	FDD/ TDD Conf. A Table 11.2.15-1
					LoS: 1.746 NLoS: 1.457	<input checked="" type="checkbox"/> Yes <input type="checkbox"/> No	
	eMBB	Dense Urban – eMBB	Uplink	1.12 (30 km/h)	LoS: 2.718	<input checked="" type="checkbox"/> Yes <input type="checkbox"/> No	FDD/ TDD Conf. A Table 11.2.15-3
					NLoS: 1.924-2.495	<input checked="" type="checkbox"/> Yes <input type="checkbox"/> No	
	eMBB	Rural – eMBB	Uplink	0.45 (500 km/h)	Not evaluated	<input checked="" type="checkbox"/> Yes <input type="checkbox"/> No	FDD/ TDD Conf. A Table 11.2.15-5

Table 7.6 – Compliance template for technical performance requiring evaluation by simulation for 3GPP SRIT technology

Minimum technical performance requirements, ITU-R M.2410-0	Category			Required value	Value	Requirement met?	Comments ⁴
	Usage scenario	Test environment	Downlink or uplink				
5.2.4.3.4 5th percentile user spectral efficiency (bit/s/Hz) (4.4)	eMBB	Indoor Hotspot – eMBB	Downlink	0.3	0.380	<input checked="" type="checkbox"/> Yes <input type="checkbox"/> No	11.1.12.2 for LTE comp RIT
			Uplink	0.21	0.357	<input checked="" type="checkbox"/> Yes <input type="checkbox"/> No	
	eMBB	Dense Urban – eMBB	Downlink	0.225	0.307	<input checked="" type="checkbox"/> Yes <input type="checkbox"/> No	
			Uplink	0.15	0.288	<input checked="" type="checkbox"/> Yes <input type="checkbox"/> No	
	eMBB	Rural – eMBB	Downlink	0.12	0.201-0.334	<input checked="" type="checkbox"/> Yes <input type="checkbox"/> No	
			Uplink	0.045	0.093-0.108	<input checked="" type="checkbox"/> Yes <input type="checkbox"/> No	
5.2.4.3.5 Average spectral efficiency (bit/s/Hz/ TRxP) (4.5)	eMBB	Indoor Hotspot – eMBB	Downlink	9	9.120	<input checked="" type="checkbox"/> Yes <input type="checkbox"/> No	11.1.12.2 for LTE comp RIT
			Uplink	6.75	7.538	<input checked="" type="checkbox"/> Yes <input type="checkbox"/> No	
	eMBB	Dense Urban – eMBB	Downlink	7.8	7.923	<input checked="" type="checkbox"/> Yes <input type="checkbox"/> No	
			Uplink	5.4	6.756	<input checked="" type="checkbox"/> Yes <input type="checkbox"/> No	
	eMBB	Rural – eMBB	Downlink	3.3	10.664-12.027	<input checked="" type="checkbox"/> Yes <input type="checkbox"/> No <input type="checkbox"/> Yes <input type="checkbox"/> No	
			Uplink	1.6	2.041-5.037	<input checked="" type="checkbox"/> Yes <input type="checkbox"/> No	
		LMLC		3.836	<input checked="" type="checkbox"/> Yes <input type="checkbox"/> No		
5.2.4.3.9 Connection density (devices/km ²) (4.8)	mMTC	Urban Macro – mMTC	Uplink	1 000 000	34 378 000 (ISD=500m) 1 422 700 (ISD=1 732m)	<input checked="" type="checkbox"/> Yes <input type="checkbox"/> No	11.1.13
5.2.4.3.11 Reliability (4.10)	URLLC	Urban Macro – URLLC	Uplink or Downlink	1 – 10 ⁻⁵ success probability of transmitting a layer 2 PDU (protocol data unit) of size 32 bytes within 1 ms in channel quality of coverage edge	NR component RIT: 99.999% or greater on the DL and UL LTE component RIT: N/A	<input checked="" type="checkbox"/> Yes <input type="checkbox"/> No	11.1.14
5.2.4.3.13 Mobility: Traffic channel link data rates (bit/s/Hz) (4.11)	eMBB	Indoor Hotspot – eMBB	Uplink	1.5 (10 km/h)	LoS: 2.297	<input checked="" type="checkbox"/> Yes <input type="checkbox"/> No	11.1.15
			Uplink	1.12 (30 km/h)	LoS: 1.746 NLoS: 1.457	<input checked="" type="checkbox"/> Yes <input type="checkbox"/> No	
	eMBB	Rural – eMBB	Uplink	0.8 (120 km/h)	LoS: 2.718	<input checked="" type="checkbox"/> Yes <input type="checkbox"/> No	
			Uplink	0.45 (500 km/h)	NLoS: 1.924-2.495 Not evaluated	<input checked="" type="checkbox"/> Yes <input type="checkbox"/> No	

Table 7.7 – Compliance template for technical performance requiring evaluation by simulation for ETSI-DECT SRIT technology

Minimum technical performance requirements, ITU-R M.2410-0	Category			Required value	Value	Requirement met?	Comments ⁵
	Usage scenario	Test environment	Downlink or uplink				
5.2.4.3.4 5th percentile user spectral efficiency (bit/s/Hz) (4.4)	eMBB	Indoor Hotspot – eMBB	Downlink	0.3		<input type="checkbox"/> Yes <input type="checkbox"/> No	
			Uplink	0.21		<input type="checkbox"/> Yes <input type="checkbox"/> No	
	eMBB	Dense Urban – eMBB	Downlink	0.225		<input type="checkbox"/> Yes <input type="checkbox"/> No	
			Uplink	0.15		<input type="checkbox"/> Yes <input type="checkbox"/> No	
	eMBB	Rural – eMBB	Downlink	0.12		<input type="checkbox"/> Yes <input type="checkbox"/> No	
			Uplink	0.045		<input type="checkbox"/> Yes <input type="checkbox"/> No	
5.2.4.3.5 Average spectral efficiency (bit/s/Hz/ TRxP) (4.5)	eMBB	Indoor Hotspot – eMBB	Downlink	9		<input type="checkbox"/> Yes <input type="checkbox"/> No	
			Uplink	6.75		<input type="checkbox"/> Yes <input type="checkbox"/> No	
	eMBB	Dense Urban – eMBB	Downlink	7.8		<input type="checkbox"/> Yes <input type="checkbox"/> No	
			Uplink	5.4		<input type="checkbox"/> Yes <input type="checkbox"/> No	
	eMBB	Rural – eMBB	Downlink	3.3		<input type="checkbox"/> Yes <input type="checkbox"/> No	
			Uplink	1.6		<input type="checkbox"/> Yes <input type="checkbox"/> No	
5.2.4.3.9 Connection density (devices/km ²) (4.8)	mMTC	Urban Macro – mMTC	Uplink	1 000 000	Unable to evaluate too many assumptions required.	<input type="checkbox"/> Yes <input type="checkbox"/> No	Mesh- and cellular-network layouts have to be synchronized somehow. No procedure in ITU-R M.2412
5.2.4.3.11 Reliability (4.10)	URLLC	Urban Macro – URLLC	Uplink or Downlink	1 – 10 ⁻⁵ success probability of transmitting a layer 2 PDU (protocol data unit) of size 32 bytes within 1 ms in channel quality of coverage edge	>99.999%	<input checked="" type="checkbox"/> Yes <input type="checkbox"/> No	DECT component RIT only.
5.2.4.3.13 Mobility: Traffic channel link data rates (bit/s/Hz) (4.11)	eMBB	Indoor Hotspot – eMBB	Uplink	1.5 (10 km/h)		<input type="checkbox"/> Yes <input type="checkbox"/> No	
			Uplink	1.12 (30 km/h)		<input type="checkbox"/> Yes <input type="checkbox"/> No	
	eMBB	Rural – eMBB	Uplink	0.8 (120 km/h)		<input type="checkbox"/> Yes <input type="checkbox"/> No	
			Uplink	0.45 (500 km/h)		<input type="checkbox"/> Yes <input type="checkbox"/> No	

Outcome of WP 5D meeting #35e

A total of fourteen independent evaluation groups (IEGs), including the CEG, were expected to be involved in the evaluation process. One IEG did not provide an evaluation report, and hence

thirteen final evaluation reports (including the CEG's [96]) were submitted and recorded at ITU-R under Steps 4 and 5 of the evaluation process. The Wireless Lab participated, as a member of Canadian delegation (c.f., Fig. 7.1), in the WP 5D meeting #34 in Geneva. The latter took place in February 2020 to discuss and summarize the final evaluation results submitted by the IEGs. The



Figure 7.1 – INRS Professor Sofiène Affes and his two students Oussama Ben Smida and Souheib Ben Amor (2nd to 4th from the right), accompanied by Venkatesh Sampath from Ericsson Canada (right) and Serge Bertuzzo from Bell Canada (left), at the ITU meeting in Geneva in February 2020. [3]

WP 5D meeting #35e reviewed the results of Step 4 (Evaluation of candidate RITs or SRITs by independent evaluation groups). It was agreed during the meeting that the 3GPP RIT and SRIT proposals, China, Korea, and TSDSI are considered as qualified RIT/SRITs of Step 6. Hence, they were forwarded to further consideration in Step 7.

In the following is the outcome of Step 7:

- The RITs and SRITs proposed by 3GPP, China and Korea are grouped into the technology identified in ITU as “3GPP 5GSRIT” and “3GPP 5GRIT” as developed by 3GPP. Both technologies passed Step 7.
- The TSDSI RIT also passed Step 7 as “TSDSI RIT”.
- The WG Technology Aspects failed to reach an agreement on how to summarize the Step 4 results for ETSI-DECT and Nufront submissions. In the closing plenary of WP 5D Meeting

#35e (23 June – 9 July), the meeting agreed on option 2 (Fig. 7.2) and provide a one-time extension on an exception basis for both candidates

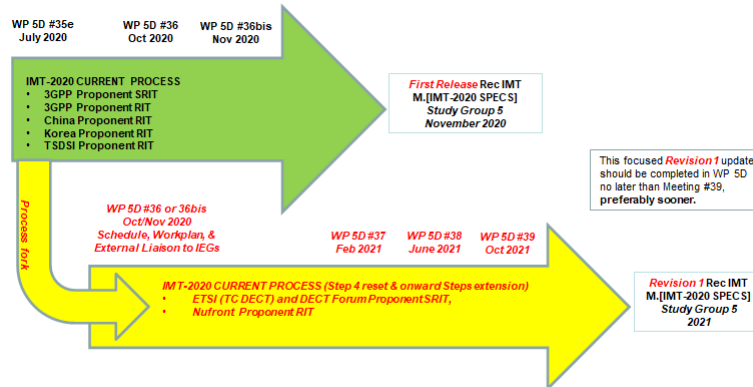


Figure 7.2 – Next steps for the development of IMT-2020 radio interface Recommendations [4]

7.2 Contributions to students’ mentoring within this thesis

During my Ph.D. program, I have been given an opportunity by my supervisor, Prof. Sofiène Affes, to mentor three undergraduate and two graduate students. The research topics cover multiple fields from signal processing to hardware implementation.

7.2.1 Blind maximum likelihood jade in multipath environment using importance sampling

In this project, Mrs. Maha Abdelkhalek, PhD student at INRS and recipient of a PhD Excellence Grant from the Government of Tunisia, was able to solve the problem of joint angles and time delays estimation (JADE) in a non-data aided (NDA) scenario where the transmitted signal is unknown at the receiver. The importance sampling (IS) technique is used to reduce the multidimensionality of the maximization problem without recurring to an iterative option. This work was published in a conference version in [97]. Right now, we are working on the submission of a journal paper version and simultaneously trying to exploit the importance sampling technique to solve more complex problems related to synchronization and localization applications.

7.2.2 Terahertz propagation performance evaluation for indoor environment

In this project, Mrs. Nagma Elburki, PhD student at INRS and recipient of a CBIE Excellence PhD Grant, was able to evaluate the path-loss models that can be adopted for indoor communications in the Terahertz (THz) frequency band. Three different models were investigated versus distance; namely, the ITU, the log-distance (LD), and the multi-wall COST 231 models. This work was published in a conference version in [98]. Right now, we are investigating the use of machine learning tools for pathloss prediction in the THz frequency band.

7.2.3 Synchronization of UAV swarms for indoor applications under obstacle-avoidance restrictions

This project, incepted for the initiation of undergraduate students to research, involved Mr. Sheevam Sharma, BSc student at UBC and recipient of one of only two yearly INRS 2020 Research Excellence Scholarship Program for Undergraduate Internships. Mr. Sharma was able to get quickly acquainted with a novel research-oriented UAV equipment (crazyflie drones) recently made available at the Wireless Lab. He was able to work with multiple UAV frameworks to ensure full synchronization between the UAVs in swarm flight. Right now, we are investigating new synchronization techniques for UAV swarm flights.

7.2.4 Implementation of D2D communication between multiple IoT devices

This project, incepted for the initiation of undergraduate students to research, involved Mr. Nicholas Andrianos, BSc student at UBC and recipient of one of only two yearly INRS 2020 Research Excellence Scholarship Program for Undergraduate Internships. Mr. Andrianos was able to get quickly acquainted with an already established research field that includes WSN (Micaz sensors, c.f., experimental demonstration [99] in [100]). He was able, using a simulation platform, to unicasts the RSSI values from multiple nodes to the BS 7.3. Once received at the base station, the sink displays the RSSI and source to a console. The RSSI can then be extracted to an external file for analysis or as an input for a further calculation at the base. Right now, we are trying to upload the solution directly into the Micaz sensors. During the internship, Mr. Andrianos also was able to get quickly acquainted with a novel research-oriented IoT equipment (Arduino rovers) recently made

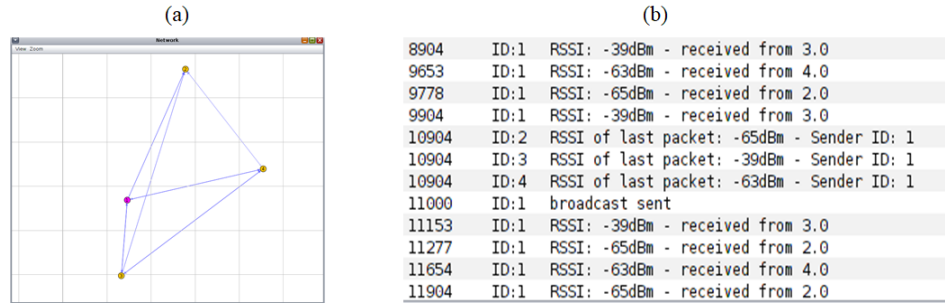


Figure 7.3 – BS receiving RSSI values from multiple nodes: (a) Network topology and (b) RSSI values displayed at the BS

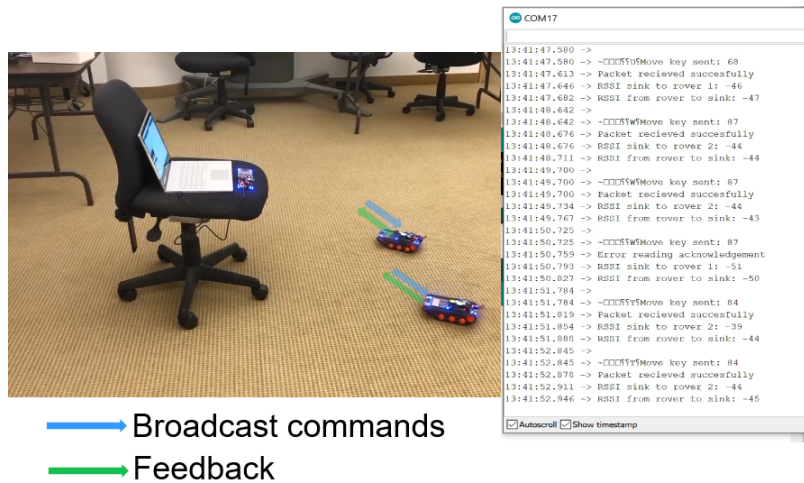


Figure 7.4 – Real-world demo using Arduino rovers

available at the Wireless Lab. He was to extract the RSSI from multiple nodes and at the same time send a predefined path, in broadcast mode, to all the rovers in the network 7.4. Right now, we are investigating new localization techniques using the RSSI values gathered at the BS.

7.2.5 Online indoor localization techniques of mobile units over non-line-of-sight transmission links

This project was an initiation to research for undergraduate students, Mrs. Wen Xin, BSc student at McGill University and recipient of an NSERC USRA/INRS Research Excellence Scholarship Program for Undergraduate Internships, was able to provide a new solution to the problem of joint angles and time delays estimation (JADE) in a data aided (DA). An alternative Monte-Carlo technique, instead of the IS approach, was used to reduce the multidimensionality of the

maximization problem without recurring to an iterative option. Right now, we are in the process of preparing a scientific paper related to this topic.

Chapitre 8

Conclusion and Future Work

8.1 Major research contributions

In this thesis, we proposed multiple joint estimation techniques to acquire the information of key channel parameters. Mainly, we made three contributions.

In chapter 4, we addressed the problem of time-varying channel estimation over SIMO OFDM transmissions in multipath propagation environments. The proposed approach is based on a polynomial approximation of the complex path gains and takes advantage of all the observation - both at pilot and non-pilot positions - to enhance the channel estimation capabilities. To do so, we develop a new SIMO DA ML estimator - which turns out to be a generalized extension of the SISO DA LS estimator in [2] - for the sole purpose of initializing at relatively rare pilot insertion instants (pilot to data or overhead ratio can be as low as 0.16%) of another new SIMO NDA ML version when operated at the remaining data samples, resulting in the ultimately advocated new hybrid ML-EM estimator of fast time-varying OFDM channels. Moreover, by further developing a new regularized DA ML (RDM) variant of either SISO DA LS in [2] or its proposed SIMO DA ML extension, we were able to further reduce the number of pilots and break the strict requirement of more pilots than paths in [2], and, hence, decrease the overhead and increase the per-carrier throughput. We show through exhaustive simulations that the proposed hybrid ML-EM solution outperforms both SISO DA LS in [2] and its proposed SIMO DA ML extension in terms of component-level channel identification accuracy. The latter translates into significant gains in terms of link-level BER and

per-carrier throughput performances, especially at medium-to-high per-carrier SNR values more so at relatively higher Doppler or faster SIMO OFDM channel variations. This contribution resulted in the publication of the work [C6] for SISO configuration and [C7,J6] for SIMO configuration.

In chapter 5, we addressed the problem of time and frequency synchronization in cooperative systems over TVCs. We proposed two different estimation techniques. The first operates under the TVC assumption while the second one works with TCCs. In the first ML TVC-PD approach, we assume perfect knowledge of the Doppler spread to provide accurate TD and CFO synchronization estimates. Whereas we exploit the second ML TCC technique as an initialization scheme for preliminary synchronization then embed both ML TVC-PD and some Doppler estimator in a new iterative version, ML TVC-DE. That is to account for the practical need to estimate at each relay node the Doppler spread upon which relies ML TVC-PD. We also developed a new distributed MIMO-relay beamforming design that embeds the proposed synchronization technique at each relay node. We showed under the TCC assumption that all techniques exhibit approximately the same performance. However, when the Doppler increases, the TCC-based techniques exhibit poor performance while the new ML TVC continues to provide accurate estimates. Link-level simulations confirm the net advantages of the proposed ML TVC multi-node synchronization technique and the MIMO-relay beamforming scheme in terms of throughput gains, especially at medium and high SNRs, more so at relatively higher Doppler frequencies or with more distributed MIMO-relay beamforming nodes. Future work could investigate a more complex system that includes multiple antennas at each relay nodes and/or multiple receivers. This contribution resulted in the publication of the work [C3] for time and frequency synchronization in cooperative systems over TVCs and [C5,J4] for the development of new distributed MIMO-relay beamforming design.

In chapter 6, we proposed a new non-iterative and statistically efficient ML solution for the joint estimation of the time delays and angles-of-arrival of overlapping reflections of a signal with a known waveform. Based on the importance sampling concept, this new ML JADE technique applies to both single- and multi-carrier models and enjoys guaranteed global optimality with super-resolution capabilities. Typically, it is able to resolve multipath components with simultaneous angle and delay separations as low as $\Delta\bar{\alpha} = 0.5^\circ$ and $\Delta\bar{\tau} = 0.25 T$ while achieving the CRLB even at SNR levels as low as -10 dB. By exploiting the sparsity feature of a pseudo-pdf that is *intrinsic* to the new algorithm, we also proposed a new approach that can accurately estimate the unknown number of paths. Computer simulation results show the clear superiority of the new IS-based ML

estimator over state-of-the-art JADE techniques both in accuracy and complexity. Simulations with real channel measurements in an indoor an environment also show the high accuracy of the IS-based ML JADE technique in real-world localization applications. This contribution resulted in the publication of the work [C4] for the detection of the number of paths over Wireless channels and [J5] for the joint angle and delay estimation from multipath and multicarrier transmissions.

In chapter 7, we summarize other achievements accomplished during the PhD program. The latter include the work mandated by Innovation, Science and Economic Development Canada (ISED) and the Canadian Evaluation Group (CEG). During this project, we covered the RITs and SRITs of 3GPP and we are currently continuing with re-evaluation of DECT and NuFront. Our work during this project was included in the CEG final report submitted to the WP 5D 34th meeting.

8.2 Future research directions

Our research work in this thesis tackles the problem of joint estimation of multiple channel parameters. The following research directions can be further investigated.

8.2.1 Channel coefficient estimation

Massive MIMO technology is already included in 5G standards such as 3GPP 5G NR. A possible extension of the EM solution to mmWave massive MIMO technology is worth investigating as it provides accurate estimates with low overhead.

8.2.2 Multi-node time and frequency synchronization with multiple destination nodes

Synchronization in a distributed network is a crucial task which becomes more challenging in the presence of multi-destination nodes. Monte Carlo approaches such as Markov chain Monte Carlo (MCMC) methods can be used to solve the resulting multi-dimensional synchronization problem.

8.2.3 Joint azimuth, elevation and, delay estimation

Generally, the joint estimation of the azimuth, elevation angles and TDs can provide a 3D positioning of the target. To reduce the high dimensionality of the optimization problem, we can opt for the IS technique to provide accurate estimates at a reduced complexity.

8.3 List of publications

8.3.1 Technical reports

[T12] The Wireless Lab (EMT Centre - INRS), Evaluation of 3GPP candidate radio interface technology (RIT) and set of RITs (SRITs) for IMT-2020 (5G) within the CEG mandate, Report PR-03, Mar. 2020. (Confidential)

[T11] Canadian Evaluation Group, Evaluation report received from the Canadian Evaluation Group (CEG) on the candidate IMT-2020 radio interface technology proposals, WP 5D, (30), 2020.

[T10] The Wireless Lab (EMT Centre - INRS), Evaluation Report of INRS for CEG, version 9, Feb. 2020. (Confidential)

[T9] The Wireless Lab (EMT Centre - INRS), Evaluation Report of INRS for CEG, version 8, Feb. 2020. (Confidential)

[T8] The Wireless Lab (EMT Centre - INRS), Evaluation Report of INRS for CEG, version 7, Jan. 2020. (Confidential)

[T7] The Wireless Lab (EMT Centre - INRS), Evaluation Report of INRS for CEG, version 6, Jan. 2020. (Confidential)

[T6] Canadian Evaluation Group, Interim evaluation Report on the candidate proposals for IMT-2020 submitted to Working Party 5D - Report with provisional results, (CEG) WP 5D, (28), 2019.

[T5] The Wireless Lab (EMT Centre - INRS), Evaluation Report of INRS for CEG, version 5, Nov. 2019. (Confidential)

[T4] The Wireless Lab (EMT Centre - INRS), Evaluation Report of INRS for CEG, version 4, Oct. 2019. (Confidential)

[T3] The Wireless Lab (EMT Centre - INRS), Evaluation Report of INRS for CEG, version 3, Sep. 2019. (Confidential)

[T2] The Wireless Lab (EMT Centre - INRS), Evaluation Report of INRS for CEG, version 2, Sep. 2019. (Confidential)

[T1] The Wireless Lab (EMT Centre - INRS), Evaluation report of INRS for CEG, version 1, Sep. 2019. (Confidential)

8.3.2 Submitted/accepted journal papers

[J6] S. Ben Amor, S. Affes, F. Bellili, and N. Jayakody, "ML-Type EM-Based Estimation of Fast Time-Varying Frequency-Selective Channels Over SIMO OFDM Transmissions", *IEEE Access*, vol. 7, no. 1, pp. 148265-148277, October 2019.

[J5] F. Bellili, S. Ben Amor, S. Affes, and A. Ghayeb, "Maximum Likelihood Joint Angle and Delay Estimation from Multipath and Multicarrier Transmissions With Application to Indoor Localization Over IEEE 802.11ac Radio," *IEEE Trans. on Mobile Computing.*, vol. 18, no. 5, pp. 1116-1132, May 2019.

[J4] S. Ben Amor, S. Affes, F. Bellili, U. Vilaipornsawai, L. Zhang, and P. Zhu, "Multi-Node ML Time and Frequency Synchronization for Distributed MIMO-Relay Beamforming over Time-Varying Flat-Fading Channels," *IEEE Trans. on communications*, vol. 67, no. 4, pp. 2702-2715, April 2019.

[J3] F. Bellili, S. Ben Amor, S. Affes, and A. Ghayeb, "Low-Complexity DOA Estimation from Short Data Snapshots for ULA Systems Using the Annihilating Filter Technique", *EURASIP Journal on Advances in Signal Processing*, vol. 2017, no. 48, pp. 1-16, June 2017.

[J2] F. Bellili, A. Methenni, S. Ben Amor, and S. Affes, "Time Synchronization of Turbo-Coded Square-QAM Modulated Transmissions: Closed-Form Cramér-Rao Lower Bounds and Code-Aided ML Estimators," *IEEE Trans. on Vehicular Technology*, vol. PP, no. 99, pp. 1-14, June 2017.

[J1] F. Bellili, C. Elguet, S. Ben Amor, S. Affes, and A. Stephenne, "Code-Aided DOA Estimation from TurboCoded QAM Transmissions: Analytical CRLBs and Maximum Likelihood Estimator ," *IEEE Trans. on Wireless Comm.*, vol. 16, no. 5, pp. 2850-2865, May 2017.

8.3.3 Accepted conference papers

[C9] N. Elburki, S. Ben Amor, and S. Affes, "TeraHertz Propagation Performance Evaluation for Indoor Environment," in Proc IEEE CCECE'2020, London, Canada, April 26-29, 2020.

- [C8] M. Abdelkhalek, S. Ben Amor, and S. Affes, "Blind Maximum Likelihood JADE in Multipath Environment Using Importance Sampling," in Proc. IEEE CAMSAP'2019, Le Gosier, Guadeloupe, French West Indies, December 15-18, 2019.
- [C7] S. Ben Amor, S. Affes, and F. Bellili, "EM-Based ML Estimation of Fast Time-Varying Multipath Channels for SIMO OFDM Systems," in Proc. of IEEE GLOBECOM'2019, Waikoloa, HI, USA, December 9-13, 2019.
- [C6] S. Ben Amor, S. Affes, and F. Bellili, "ML EM Estimation of Fast Time-Varying OFDM-Type Channels," in Proc. of IEEE IWCMC'2019, Tangier, Morocco, 24-28 June 2019. Invited Paper.
- [C5] S. Ben Amor, S. Affes, F. Bellili, U. Vilaipornsawai, L. Zhang, and P. Zhu, "Joint ML Time and Frequency Synchronization for Distributed MIMO-Relay Beamforming," in Proc. of IEEE WCNC'2019, Marrakech, Morocco, April 15-18, 2019.
- [C4] S. Ben Amor, S. Affes, and A. Ghayeb, "Detection of the Number of Paths over Wireless Channels: A Maximum Likelihood Approach," in Proc. of ETIC'2019, Dewathang, Bhutan, March 8-10, 2019.
- [C3] S. Ben Amor, S. Affes, F. Bellili, U. Vilaipornsawai, L. Zhang, and P. Zhu, "ML Time-Delay and CFO Synchronization for MIMO-Relay Beamforming over Time-Varying Channels," in Proc. of IEEE GLOBECOM'2018, Abu Dhabi, UAE, Dec.9-13, 2018.
- [C2] F. Bellili, S. Ben Amor, A. Methenni, and S. Affes, "Low-Cost Code-Aided ML Timing Recovery from Turbo-Coded QAM Transmissions," in Proc. of IEEE PIMRC'2017, Montreal, Canada, Oct. 8-13, 2017.
- [C1] S. Ben Amor, F. Bellili, S. Affes, U. Vilaipornsawai, L. Zhang and P. Zhu, "Joint Time and Frequency Synchronization for Distributed Beamforming in Decode-and-Forward Relaying Systems Using Importance Sampling," in Proc. of IEEE ICUWB'2017, Salamanca, Spain, Sep. 12-15, 2017.

Références

- [1] M Series. IMT Vision–Framework and overall objectives of the future development of IMT for 2020 and beyond. *Recommendation ITU*, 2083, 2015.
- [2] Hussein Hijazi and Laurent Ros. Polynomial estimation of time-varying multipath gains with intercarrier interference mitigation in OFDM systems. *IEEE Transactions on Vehicular Technology*, 58(1):140–151, 2008.
- [3] Audrey-Maude Vézina. A team at the INRS participates in the evaluation of new 5G technologies, July 2020. inrs.ca [Online; posted 15-July-2020].
- [4] WP 5D. Agreed ‘way forward’ Option 2 for ETSI (TC DECT) and DECT Forum proponent and Nufront proponent candidate technology submissions for IMT-2020. *WP 5D*, (52), 2020.
- [5] Sofiene Affes and Paul Mermelstein. Adaptive space-time processing for wireless CDMA. In *Adaptive Signal Processing*, pages 283–321. Springer, 2003.
- [6] Mohamed Ali Boujelben, Faouzi Bellili, Sofiène Affes, and Alex Stéphenne. SNR estimation over SIMO channels from linearly modulated signals. *IEEE Transactions on Signal Processing*, 58(12):6017–6028, 2010.
- [7] Imen Mrissa, Faouzi Bellili, Sofiène Affes, and Alex Stéphenne. A context-aware cognitive SIMO transceiver for enhanced throughput on the downlink of LTE HetNet. *wireless communications and mobile computing*, 16(11):1414–1430, 2016.
- [8] Faouzi Bellili, Achref Methenni, Souheib Ben Amor, Sofiène Affes, and Alex Stephenne. Time synchronization of turbo-coded square-QAM-modulated transmissions: Code-aided ML estimator and closed-form Cramer–Rao lower bounds. *IEEE Transactions on Vehicular Technology*, 66(12):10776–10792, 2017.
- [9] 3GPP TS 38.211. NR; Physical channels and modulation, 2018.
- [10] Paolo Banelli, Stefano Buzzi, Giulio Colavolpe, Andrea Modenini, Fredrik Rusek, and Alessandro Ugolini. Modulation formats and waveforms for 5G networks: Who will be the heir of OFDM?: An overview of alternative modulation schemes for improved spectral efficiency. *IEEE Signal Processing Magazine*, 31(6):80–93, 2014.
- [11] Zijian Tang, Rocco Claudio Cannizzaro, Geert Leus, and Paolo Banelli. Pilot-assisted time-varying channel estimation for OFDM systems. *IEEE Transactions on Signal Processing*, 55(5):2226–2238, 2007.
- [12] Yasamin Mostofi and Donald C Cox. ICI mitigation for pilot-aided OFDM mobile systems. *IEEE Transactions on Wireless Communications*, 4(2):765–774, 2005.

- [13] Stefano Tomasin, Alexei Gorokhov, Haibing Yang, and J-P Linnartz. Iterative interference cancellation and channel estimation for mobile OFDM. *IEEE Transactions on Wireless Communications*, 4(1):238–245, 2005.
- [14] Habib Senol, Erdal Panayirci, and H Vincent Poor. Nondata-aided joint channel estimation and equalization for OFDM systems in very rapidly varying mobile channels. *IEEE transactions on signal processing*, 60(8):4236–4253, 2012.
- [15] Souheib Ben Amor, Sofène Affes, and Faouzi Bellili. ML EM estimation of fast time-varying OFDM-type channels. In *2019 15th International Wireless Communications & Mobile Computing Conference (IWCMC)*, pages 1–6. IEEE, 2019.
- [16] Ami Wiesel, Jason Goldberg, and Hagit Messer-Yaron. SNR estimation in time-varying fading channels. *IEEE Transactions on Communications*, 54(5):841–848, 2006.
- [17] Faouzi Bellili, Rabii Meftehi, Sofène Affes, and Alex Stéphenne. Maximum likelihood SNR estimation of linearly-modulated signals over time-varying flat-fading SIMO channels. *IEEE Transactions on Signal Processing*, 63(2):441–456, 2014.
- [18] Faouzi Bellili, Alex Stéphenne, and Sofiene Affes. SNR estimation of QAM-modulated transmissions over time-varying SIMO channels. In *2008 IEEE International Symposium on Wireless Communication Systems*, pages 199–203. IEEE, 2008.
- [19] Hussein Hijazi and Laurent Ros. Joint data QR-detection and Kalman estimation for OFDM time-varying Rayleigh channel complex gains. *IEEE Transactions on Communications*, 58(1):170–178, 2010.
- [20] Hussein Hijazi, Eric Pierre Simon, Martine Liénard, and Laurent Ros. Channel estimation for MIMO-OFDM systems in fast time-varying environments. In *2010 4th international symposium on communications, control and signal processing (ISCCSP)*, pages 1–6. IEEE, 2010.
- [21] Ruizhe Yang, Siyang Ye, Pengbo Si, Yinglei Teng, and Yanhua Zhang. Iterative channel estimation and detection for high-mobility MIMO-OFDM systems: mitigating error propagation by exploiting error information. *Wireless Personal Communications*, 84(3):1907–1931, 2015.
- [22] Arthur P Dempster, Nan M Laird, and Donald B Rubin. Maximum likelihood from incomplete data via the EM algorithm. *Journal of the Royal Statistical Society: Series B (Methodological)*, 39(1):1–22, 1977.
- [23] Andrew Sendonaris, Elza Erkip, and Behnaam Aazhang. User cooperation diversity. Part I. System description. *IEEE transactions on communications*, 51(11):1927–1938, 2003.
- [24] Yindi Jing and Hamid Jafarkhani. Network beamforming using relays with perfect channel information. *IEEE Transactions on Information Theory*, 55(6):2499–2517, 2009.
- [25] Ali A Nasir, Hani Mehrpouyan, Steven D Blostein, Salman Durrani, and Rodney A Kennedy. Timing and carrier synchronization with channel estimation in multi-relay cooperative networks. *IEEE Transactions on Signal Processing*, 60(2):793–811, 2011.
- [26] Huiming Wang, Xiang-Gen Xia, and Qinye Yin. Computationally efficient equalization for asynchronous cooperative communications with multiple frequency offsets. *IEEE transactions on wireless communications*, 8(2):648–655, 2009.

- [27] Yung-Szu Tu and Gregory J Pottie. Coherent cooperative transmission from multiple adjacent antennas to a distant stationary antenna through AWGN channels. In *Vehicular Technology Conference. IEEE 55th Vehicular Technology Conference. VTC Spring 2002 (Cat. No. 02CH37367)*, volume 1, pages 130–134. IEEE, 2002.
- [28] Ali A Nasir, Salman Durrani, Hani Mehrpouyan, Steven D Blostein, and Rodney A Kennedy. Timing and carrier synchronization in wireless communication systems: a survey and classification of research in the last 5 years. *EURASIP Journal on Wireless Communications and Networking*, 2016(1):180, 2016.
- [29] Xiao Li, Chengwen Xing, Yik-Chung Wu, and SC Chan. Timing estimation and resynchronization for amplify-and-forward communication systems. *IEEE Transactions on Signal Processing*, 58(4):2218–2229, 2009.
- [30] Xiao Li, Yik-Chung Wu, and Erchin Serpedin. Timing synchronization in decode-and-forward cooperative communication systems. *IEEE Transactions on Signal Processing*, 57(4):1444–1455, 2008.
- [31] Hani Mehrpouyan and Steven D Blostein. Bounds and algorithms for multiple frequency offset estimation in cooperative networks. *IEEE Transactions on Wireless Communications*, 10(4):1300–1311, 2011.
- [32] The-Hanh Pham, Arumugam Nallanathan, and Ying-Chang Liang. Joint channel and frequency offset estimation in distributed mimo flat-fading channels. *IEEE Transactions on Wireless Communications*, 7(2):648–656, 2008.
- [33] Jong-Ho Lee and Seong-Cheol Kim. Time and frequency synchronization for ofdma uplink system using the sage algorithm. *IEEE Transactions on Wireless Communications*, 6(4):1176–1181, 2007.
- [34] Michele Morelli. Timing and frequency synchronization for the uplink of an ofdma system. *IEEE Transactions on Communications*, 52(2):296–306, 2004.
- [35] Suhanya Jayaprakasam, Sharul Kamal Abdul Rahim, and Chee Yen Leow. Distributed and collaborative beamforming in wireless sensor networks: Classifications, trends, and research directions. *IEEE Communications Surveys & Tutorials*, 19(4):2092–2116, 2017.
- [36] Haifen Yang, Dong Liu, Yutao Fan, Cheng Qian, Zhi Zheng, and Bo Yan. Variable directional perturbation with one-bit feedback for collaborative beamforming. In *2016 IEEE/CIC International Conference on Communications in China (ICCC)*, pages 1–5. IEEE, 2016.
- [37] François Quitin, Muhammad Mahboob Ur Rahman, Raghuraman Mudumbai, and Upamanyu Madhow. Distributed beamforming with software-defined radios: frequency synchronization and digital feedback. In *2012 IEEE Global Communications Conference (GLOBECOM)*, pages 4787–4792. IEEE, 2012.
- [38] Maria Antonietta Alvarez and Umberto Spagnolini. Distributed time and carrier frequency synchronization for dense wireless networks. *IEEE Transactions on Signal and Information Processing over Networks*, 4(4):683–696, 2018.
- [39] Ruisi He, Bo Ai, Gongpu Wang, Ke Guan, Zhangdui Zhong, Andreas F Molisch, Cesar Briso-Rodriguez, and Claude P Oestges. High-speed railway communications: From GSM-R to LTE-R. *Ieee vehIcular technology magazine*, 11(3):49–58, 2016.

- [40] Ilaria Thibault, Giovanni E Corazza, and Lina Deambrogio. Phase synchronization algorithms for distributed beamforming with time varying channels in wireless sensor networks. In *2011 7th International Wireless Communications and Mobile Computing Conference*, pages 77–82. IEEE, 2011.
- [41] Wayes Tushar, David B Smith, Andrew Zhang, Tharaka A Lamahewa, and Thushara Abhayapala. Distributed transmit beamforming: Phase convergence improvement using enhanced one-bit feedback. In *2012 IEEE Wireless Communications and Networking Conference (WCNC)*, pages 528–532. IEEE, 2012.
- [42] A-J Van Der Veen. Algebraic methods for deterministic blind beamforming. *Proceedings of the IEEE*, 86(10):1987–2008, 1998.
- [43] Jiunn-Tsair Chen and Yeong-Cheng Wang. Performance analysis of the parametric channel estimators for MLSE equalization in multipath channels with AWGN. *IEEE Transactions on Communications*, 49(3):393–396, 2001.
- [44] Brian R Phelan, Erik H Lenzing, and Ram M Narayanan. Source localization using unique characterizations of multipath propagation in an urban environment. In *2012 IEEE 7th Sensor Array and Multichannel Signal Processing Workshop (SAM)*, pages 189–192. IEEE, 2012.
- [45] Stuart A Golden and Steve S Bateman. Sensor measurements for Wi-Fi location with emphasis on time-of-arrival ranging. *IEEE Transactions on Mobile Computing*, 6(10):1185–1198, 2007.
- [46] Chahé Nerguizian, Charles Despins, and Sofiène Affès. Geolocation in mines with an impulse response fingerprinting technique and neural networks. *IEEE transactions on wireless communications*, 5(3):603–611, 2006.
- [47] Ariel Jaffe and Mati Wax. Single-site localization via maximum discrimination multipath fingerprinting. *IEEE Transactions on Signal Processing*, 62(7):1718–1728, 2014.
- [48] Chen Feng, Wain Sy Anthea Au, Shahrokh Valaee, and Zhenhui Tan. Received-signal-strength-based indoor positioning using compressive sensing. *IEEE Transactions on mobile computing*, 11(12):1983–1993, 2011.
- [49] Abdo Gaber and Abbas Omar. A study of wireless indoor positioning based on joint TDOA and DOA estimation using 2-D matrix pencil algorithms and IEEE 802.11 ac. *IEEE Transactions on Wireless Communications*, 14(5):2440–2454, 2014.
- [50] Abdo Gaber and Abbas Omar. Utilization of multiple-antenna multicarrier systems and NLOS mitigation for accurate wireless indoor positioning. *IEEE Transactions on Wireless Communications*, 15(10):6570–6584, 2016.
- [51] Nuri Yilmazer, Seckin Ari, and Tapan K Sarkar. Multiple snapshot direct data domain approach and ESPRIT method for direction of arrival estimation. *Digital Signal Processing*, 18(4):561–567, 2008.
- [52] Huigang Wang, Steven Kay, and Supratim Saha. An importance sampling maximum likelihood direction of arrival estimator. *IEEE transactions on signal processing*, 56(10):5082–5092, 2008.
- [53] Abdo Gaber and Abbas Omar. A study of tdoa estimation using matrix pencil algorithms and ieee 802.11 ac. In *2012 Ubiquitous Positioning, Indoor Navigation, and Location Based Service (UPINLBS)*, pages 1–8. IEEE, 2012.

- [54] Ahmed Masmoudi, Faouzi Bellili, Sofiène Affes, and Alex Stephenne. A maximum likelihood time delay estimator in a multipath environment using importance sampling. *IEEE Transactions on Signal Processing*, 61(1):182–193, 2012.
- [55] Yung-Yi Wang, Jiunn-Tsair Chen, and Wen-Hsien Fang. TST-MUSIC for joint DOA-delay estimation. *IEEE Transactions on Signal Processing*, 49(4):721–729, 2001.
- [56] A-J Van der Veen, Michaela C Vanderveen, and Arogyaswami Paulraj. Joint angle and delay estimation using shift-invariance techniques. *IEEE Transactions on Signal Processing*, 46(2):405–418, 1998.
- [57] Mati Wax and Amir Leshem. Joint estimation of time delays and directions of arrival of multiple reflections of a known signal. *IEEE Transactions on Signal Processing*, 45(10):2477–2484, 1997.
- [58] Bernard H Fleury, Martin Tschudin, Ralf Heddergott, Dirk Dahlhaus, and K Ingeman Pedersen. Channel parameter estimation in mobile radio environments using the SAGE algorithm. *IEEE Journal on selected areas in communications*, 17(3):434–450, 1999.
- [59] Martin Pincus. Letter to the Editor—A Closed Form Solution of Certain Programming Problems. *Operations Research*, 16(3):690–694, 1968.
- [60] Reuven Y Rubinstein and Dirk P Kroese. *Simulation and the Monte Carlo method*, volume 10. John Wiley & Sons, 2016.
- [61] Steven Kay and Supratim Saha. Mean likelihood frequency estimation. *IEEE Transactions on Signal Processing*, 48(7):1937–1946, 2000.
- [62] Supratim Saha and Steven M Kay. Maximum likelihood parameter estimation of superimposed chirps using Monte Carlo importance sampling. *IEEE Transactions on Signal Processing*, 50(2):224–230, 2002.
- [63] Huigang Wang and Steven Kay. Maximum likelihood angle-Doppler estimator using importance sampling. *IEEE Transactions on Aerospace and Electronic Systems*, 46(2):610–622, 2010.
- [64] Jianwu Chen, Yik-Chung Wu, SC Chan, and Tung-Sang Ng. Joint maximum-likelihood CFO and channel estimation for OFDMA uplink using importance sampling. *IEEE transactions on vehicular technology*, 57(6):3462–3470, 2008.
- [65] Jianwu Chen, Yik-Chung Wu, Shaodan Ma, and Tung-Sang Ng. Joint CFO and channel estimation for multiuser MIMO-OFDM systems with optimal training sequences. *IEEE transactions on signal processing*, 56(8):4008–4019, 2008.
- [66] Gang Wang and Hongyang Chen. An importance sampling method for TDOA-based source localization. *IEEE Transactions on Wireless Communications*, 10(5):1560–1568, 2011.
- [67] Ahmed Masmoudi, Faouzi Bellili, Sofiène Affes, and Alex Stephenne. A non-data-aided maximum likelihood time delay estimator using importance sampling. *IEEE Transactions on Signal Processing*, 59(10):4505–4515, 2011.
- [68] Report ITU-R M. 2410-0. Minimum requirements related to technical performance for IMT-2020 radio interface (s). *Recommendation ITU*, 2017.

- [69] Report ITU-R M. 2411-0. Requirements, evaluation criteria and submission templates for the development of IMT-2020. *Recommendation ITU*, pages 2410–0, 2017.
- [70] 3GPP. Acknowledgement of candidate RIT submission from 3GPP proponent Step 3 of the IMT-2020 process. *WP 5D*, (14), 2019.
- [71] 3GPP. Acknowledgement of candidate SRIT submission from 3GPP proponent under Step 3 of the IMT-2020 process. *WP 5D*, (13), 2019.
- [72] China. Acknowledgement of candidate RIT submission from China (People’s Republic of) under Step 3 of the IMT-2020 process. *WP 5D*, (15), 2019.
- [73] Korea. Acknowledgement of candidate RIT submission from Korea (Republic of) under Step 3 of the IMT-2020 process. *WP 5D*, (16), 2019.
- [74] TSDSI. Acknowledgement of candidate RIT submission from TSDSI under Step 3 of the IMT-2020 process. *WP 5D*, (19), 2019.
- [75] DECT Forum ETSI. Acknowledgement of candidate SRIT submission from ETSI (TC DECT) and DECT Forum under Step 3 of the IMT-2020 process. *WP 5D*, (17), 2019.
- [76] Nufront. Acknowledgement of candidate RIT submission from Nufront under Step 3 of the IMT-2020 process. *WP 5D*, (18), 2019.
- [77] Steven M Kay. *Fundamentals of statistical signal processing*. Prentice Hall PTR, 1993.
- [78] Gene H Golub, Per Christian Hansen, and Dianne P O’Leary. Tikhonov regularization and total least squares. *SIAM journal on matrix analysis and applications*, 21(1):185–194, 1999.
- [79] Fei Wang, Sanjay Chawla, and Wei Liu. Tikhonov or lasso regularization: Which is better and when. In *2013 IEEE 25th International Conference on Tools with Artificial Intelligence*, pages 795–802. IEEE, 2013.
- [80] Mehrez Souden, Sofiène Affes, Jacob Benesty, and Rim Bahroun. Robust Doppler spread estimation in the presence of a residual carrier frequency offset. *IEEE Transactions on Signal processing*, 57(10):4148–4153, 2009.
- [81] Faouzi Bellili, Yassine Selmi, Sofiène Affes, and Ali Ghrayeb. A low-cost and robust maximum likelihood joint estimator for the Doppler spread and CFO parameters over flat-fading Rayleigh channels. *IEEE Transactions on Communications*, 65(8):3467–3478, 2017.
- [82] K. B. Petersen and M. S. Pedersen. The Matrix Cookbook, 11 2012. URL "<http://www2.imm.dtu.dk/pubdb/p.php?3274>". Version 20121115.
- [83] Cihan Tepedelenlioğlu. Performance analysis of velocity (Doppler) estimators in mobile communications. In *2002 IEEE International Conference on Acoustics, Speech, and Signal Processing*, volume 3, pages III–2201. IEEE, 2002.
- [84] Yuan Tian, Xia Lei, Yue Xiao, and Shaoqian Li. ML synchronization algorithm and estimation bounds for cooperative systems. In *2010 Second Pacific-Asia Conference on Circuits, Communications and System*, volume 1, pages 379–382. IEEE, 2010.

- [85] Yuan Tian, Xia Lei, Yue Xiao, and Shaoqian Li. SAGE based joint timing-frequency offsets and channel estimation in distributed MIMO systems. *Computer communications*, 33(17): 2125–2131, 2010.
- [86] Syed Ali Hassan and Mary Ann Ingram. The benefit of co-locating groups of nodes in cooperative line networks. *IEEE communications letters*, 16(2):234–237, 2011.
- [87] Prodromos-Vasileios Mekikis, Angelos Antonopoulos, Elli Kartsakli, Aris S Lalos, Luis Alonso, and Christos Verikoukis. Information exchange in randomly deployed dense WSNs with wireless energy harvesting capabilities. *IEEE Transactions on Wireless Communications*, 15(4): 3008–3018, 2016.
- [88] Abdo Nasser Ali Gaber. *Wireless indoor positioning based on TDOA and DOA estimation techniques using IEEE 802.11 standards*. PhD thesis, Faculty of Electrical Engineering and Information Technology, Otto von Guericke University Magdeburg, 5 2015.
- [89] Petre Stoica and Arye Nehorai. On the concentrated stochastic likelihood function in array signal processing. *Circuits, Systems and Signal Processing*, 14(5):669–674, 1995.
- [90] Gene H Golub and Victor Pereyra. The differentiation of pseudo-inverses and nonlinear least squares problems whose variables separate. *SIAM Journal on numerical analysis*, 10(2):413–432, 1973.
- [91] Michael Evans and Timothy Swartz. *Approximating integrals via Monte Carlo and deterministic methods*, volume 20. OUP Oxford, 2000.
- [92] Steven Kay. *Intuitive probability and random processes using MATLAB®*. Springer Science & Business Media, 2006.
- [93] Kantilal Varichand Mardia. *Statistics of directional data*. Academic press, 2014.
- [94] Mati Wax and Thomas Kailath. Detection of signals by information theoretic criteria. *IEEE Transactions on acoustics, speech, and signal processing*, 33(2):387–392, 1985.
- [95] Report ITU-R M. 2412-0. Guidelines for evaluation of radio interface technologies for IMT-2020. *Recommendation ITU*, 2017.
- [96] Canadian Evaluation Group. Evaluation Report received from the Canadian Evaluation Group (CEG) on the candidate IMT-2020 radio interface technology proposals. *WP 5D*, (30), 2020. URL <https://www.itu.int/md/R19-WP5D-C-0090>.
- [97] Maha Abdelkhalek, Souheib Ben Amor, and Sofiène Affes. Blind maximum likelihood jade in multipath environment using importance sampling. In *2019 IEEE 8th International Workshop on Computational Advances in Multi-Sensor Adaptive Processing (CAMSAP)*, pages 391–395. IEEE, 2019.
- [98] Nagma Elburki, Souheib Ben Amor, and Sofiène Affes. Terahertz propagation performance evaluation for indoor environment. In *2020 IEEE Canadian Conference of Electrical and Computer Engineering (CCECE)*. IEEE, 2020.
- [99] Mohamed Guadane, Abdelaziz Samet, and Sofiène Affes. Real-world evaluation of localisation algorithms for wireless networks. In *2017 IEEE 28th Annual International Symposium on Personal, Indoor, and Mobile Radio Communications (PIMRC)*. IEEE, 2017.

- [100] Sofiène Affes. *Proceedings of the 2017 IEEE 28th Annual International Symposium on Personal, Indoor, and Mobile Radio Communications (PIMRC)*. 10 2017. ISBN 978-1-5386-3531-5.